Aerospace Research in Bulgaria

30

Sofia, 2018

C o n t e n t s

С Ъ Д Ъ Р Ж А Н И Е

EXAMINATION OF THE RELATIONSHIP BETWEEN SOLAR ACTIVITY AND EARTH SEISMICITY DURING THE WEAK SOLAR CYCLE 23

Mohamed Semeida[1], Sara Khodairy[1], Mahmoud El Hadidy[1],
Rabab Abdel Hamed[1], Shahinaz Youssef[2],
Penka Stoeva[3], Alexey Stoev[3]

[1]*National Research Institute of Astronomy and Geophysics, Helwan, Egypt*
[2]*Astronomy, Space Science and Meteorology Department, Cairo University, Cairo, Egypt*
[3]*Space Research and Technology Institute - Bulgarian Academy of Sciences*
e-mail: m_semeida@yahoo.com; penm@abv.bg

Abstract

The relations between sunspot number, sunspot areas, solar 10.7 cm radio flux, solar proton events and earthquakes of magnitude $M \geq 5$ and $M \geq 8$ during the time interval between 1996 and 2008 of the solar cycle 23 have been analyzed in this work. We have found that there is a direct relation between solar activity and Earth seismic activity for $M \geq 5$ and $M \geq 8$, near the maximum of the Solar cycle 23, and an inverse relation between them at the descending phase of the cycle.

Introduction

Most of the studies about the relation between solar activity and earthquakes have a cyclicity of about 11 and 22 years like the solar activity cycles. The solar cycle 23 seems to be of a great interest for the researchers due to many peculiarities. Some scientists believe that solar activity can cause earthquakes, volcanoes or extreme weather, and solar activity, presented by sunspots, radio noise and geomagnetic indices, plays a significant but by no means exclusive role in the triggering of earthquakes.

It is well known that various kinds of solar transient activities such as solar flares, disappearing filaments and coronal mass ejections (CMEs) are responsible for strong interplanetary disturbances and corresponding geomagnetic disturbances. Terrestrial effect of these activities as abrupt accelerations in the Earth's angular velocity or surges of telluric currents in the Earth's crust are the actual coupling mechanisms which trigger quakes. Scientists also found that, earthquakes occur frequently around the years of minimum solar activity. Generally, the earthquake activities are relatively less during the peak of the solar activity cycle, some say, around the period of polarity reversal. And also, the earthquake frequency in the period of solar activity minimum is closely related to the maximum annual means of sunspot numbers, the maximum annual means of solar 10.7 cm radio flux and solar

proton events of the whole solar cycle. The relation between earthquakes and solar proton events is closer than the others [1].

Most of earthquakes are induced by the mutual squeeze and collision of the earth crustal plates. However, many geophysicists do not deny that any disaster cannot be attributed to the Earth's own motion. The Sun is the energy source of the Earth. Amendments of its activity influence and modulate the motion and change the whole Earth or its certain part. Therefore, many studies about the relation between solar activity and earthquake activity have come out. Generally, most of these studies investigate the relation between the recurrent variation of sunspot number and earthquake activity. Sytinskiy [2, 3] carried out a series of research on the influence of solar activity on the earth's seismicity. Simpson [4] found that maximum quake frequency occurs at times of moderately high and fluctuating solar activity. Lursmanashvili [5] carried out series of research on the influence of solar activity on the Earth's seismicity and speak about a possibility of influence of the Sun activity on earthquake distribution in the Caucasus. The team led by Zhang, G. Q. and Odintsov [1, 6] studied the long period tendency in global earthquake geomagnetic activity and some simple relationships between solar activity and global number of earthquakes with magnitude equal and larger than 4 (M $\geq$ 4). The authors Zhang, G. Q., Dorman, L. I. and Gerontidou [1, 7, 8] found that internal effects such as subsidence, volcanic and tectonic effects are not the only reason of earthquake but also earthquakes can be triggered by some external effects such as cosmic rays, magnetic field and solar activity. The team led by Courtillot, V. [9] explained that the radiations emitted from the Sun not only have very serious effects on the Earth's atmosphere, but also affect the Earth's surface. Low level clouds, ocean temperatures, land temperatures, tropospheric temperatures, and earthquakes are shown as evidences. Khain, V. E. and Khalilov, E. N. [10] found that the periodicity of solar activity have an influence upon the periodicity of geodynamic processes. Marilia, T. and Anibal, A. [11] inspected possible influence of solar cycles on earthquakes using statistical analyses. Their results show that a significant increase in earthquake events in some of the tectonic plates is linked to solar maxima. The team led by Nikouravan, B. [12] studied in details the relationship between sunspot number, solar 10.7 cm radio flux, solar irradiance, solar proton events and earthquake events in Iran.

Data used

The studied solar cycle is 23rd solar cycle since 1755, when extensive recording of sunspot activity began. The solar cycle lasted 12.6 years, began in May 1996 and ended in January 2008. The maximum smoothed sunspot number (monthly number of sunspots averaged over a twelve-month period) observed during the solar cycle was 120.8 (March 2000), and the minimum was 1.7. There were a total of 805 days without sunspots during this cycle [13]. Sunspot number (annual mean or yearly average) are taken from SIDC web site (Solar Influence Data Analysis

Center), data for solar proton events (>100 MEV) are taken from NOAA/NGDC (National Geophysical Data Center) web site, sunspot area data from Royal Observatory, Greenwich USAF/NOAA Sunspot Data site, and 10.7 solar radio flux (yearly average observed flux) data were taken from Space Weather Canada (Natural Resources Canada) web site for the 1996–2008 time period. Earthquake activity data had been collected from National Earthquake Information Center – NEIC / U.S. Geological Survey – USGS, with magnitude $M \geq 5$ for the same time period. This solar cycle has 7 141 total number of earthquakes, 6 059 earthquakes with $M \geq 5$, 930 earthquakes with $M \geq 6$, 140 earthquakes with $M \geq 7$ and 12 earthquakes with $M \geq 8$.

Large earthquakes, with $M = 8.1$ took place in 1998, 1 with $M = 8$ took place in 2000, 1 with $M = 8.4$ took place in 2001, 1 with $M = 8.3$ took place in 2003, 2 with $M = 8.1$, 9.1 took place in 2004, 2 with $M = 8$, 8.3 took place in 2006 and 4 with $M = 8.1$, 8.1, 8, and 8.5 took place in 2007, as shown in Table 1. Here we divide the data into two categories according to the magnitude of earthquakes ($M \geq 5$ and $M \geq 8$) and compare them with the corresponding solar data. It has been carried out some statistical analysis showing the relation between the solar activity and the corresponding earthquake activity.

Table 1 illustrates the 12 large earthquakes occurred during solar cycle 23 (from May 1996 to January 2008) and show their time, depth, magnitude, latitude and longitude.

Table 1. Large earthquakes during solar cycle 23

No.	Year	Month	Day	Hour	Min.	Depth	Magnitude	Latitude	Longitude
1	1998	3	25	3	12	20.1	8.1	-63.90	149.61
2	2000	11	16	4	54	27.6	8	-3.99	153.26
3	2001	6	23	20	33	32	8.4	-16.38	-73.50
4	2003	9	25	19	50	27	8.3	41.86	143.87
5	2004	12	23	14	59	3.5	8.1	-49.33	161.42
6	2004	12	26	0	58	30	9.1	3.30	95.98
7	2006	5	3	15	26	55	8	-20.15	-174.10
8	2006	11	15	11	14	10	8.3	46.58	153.27
9	2007	1	13	4	23	10	8.1	46.23	154.55
10	2007	4	1	20	39	10	8.1	-8.43	157.06
11	2007	8	15	23	40	39	8	-13.38	-76.61
12	2007	9	12	11	10	34	8.5	-4.44	101.37

Results and discussion

(1) Solar activity and the number of earthquakes with M ≥ 5 during solar cycle 23

Carrying out some statistical analysis and drawing graphs, we show the relationship between solar activity data and the number of earthquakes with M ≥ 5 during the 1996–2008 period (Fig. 1). It is also evident that in 2000 sunspot number is maximal and the earthquake number is maximal, in 2002 the sunspot number is in maximum but the earthquake number is in minimum, and in 2007 the earthquake number is in maximum when the sunspot number is in minimum.

Fig. 2 illustrates the relation between GEOS proton fluence > 100 MEV and earthquake number with M ≥ 5. We see that in 1997, 2000, 2003 the earthquake number and the GEOS proton fluence > 100 MEV are in maximum and in 2007 the GEOS proton fluence > 100 MEV is in minimum and the earthquake number is in maximum.

On Fig. 3 is illustrated the relation between the mean annual solar flux and earthquake number with M ≥ 5. It shows that in 2000 the earthquakes number and the mean annual solar flux were in maximum, but in 2007 the mean annual solar flux was in minimum and the earthquake number is in maximum.

On Fig. 4 is illustrated the relation between both observed and corrected sunspot area and the earthquake number with M ≥ 5. It shows that in 2005 the earthquakes number is in minimum when the sunspot area is in maximum and in 2007 the sunspot area and the earthquake number is in maximum.

From Fig. 1–4 we see that for earthquakes M ≥ 5 near the maximum of the cycle 23 there is a direct relation between sunspot number, mean annual 10.7 cm solar radio flux, mean annual GEOS proton fluence and earthquake number.

Also, at the maximum of the cycle there is an inverse relation between the sunspot number and earthquake number, and a direct relation between GEOS proton fluence and earthquake number. Finally, at the descending phase of the cycle there is an inverse relation between sunspot number, mean annual solar flux, GEOS proton

fluence and earthquake number and a direct relation between sunspots area and earthquake number.
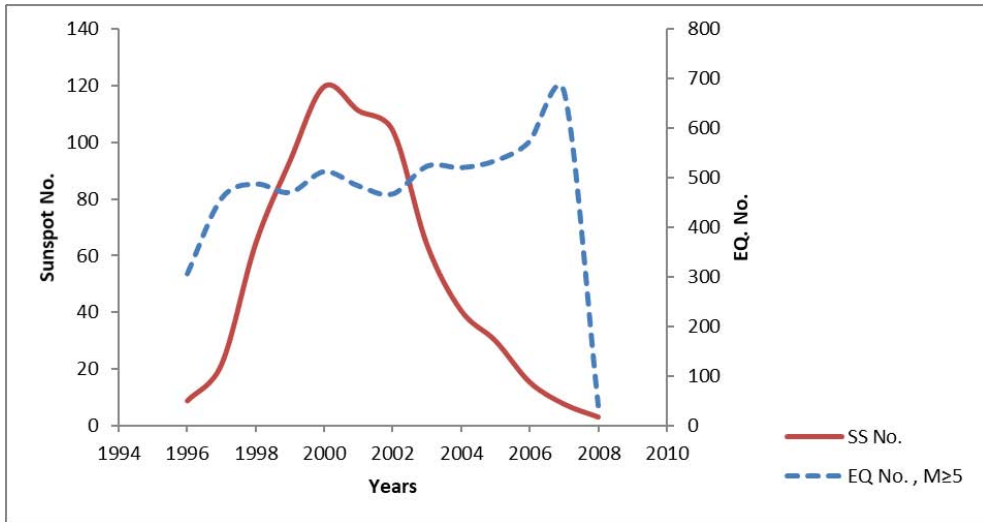
Fig. 1. Relation between sunspot number and the number of earthquakes
with magnitude M ≥ 5 during the solar cycle 23

Fig. 2. Relation between GEOS proton fluence > 100 MEV and the number of earthquakes
with magnitude M ≥ 5 during the solar cycle 23

Fig. 3. Relation between mean annual solar flux and the number of earthquakes
with magnitude M ≥ 5 during the solar cycle 23.

Fig. 4. Relation between both observed and corrected sunspot area and the number
of earthquakes with M ≥ 5 during solar cycle 23

10

(2) Solar activity and the number of earthquakes with M $\geq$ 8 during solar cycle 23

Carrying out some statistical analysis and drawing graphs, we have shown the relationship between the solar activity data and earthquake number with M $\geq$ 8 during the 1996–2008 period in Fig. 5. We see that in 2000 the sunspot number and the earthquake number are in maximum and in 2004 and 2007 the sunspot number is in minimum but the earthquake number is in maximum. Fig. 6 illustrates the relation between GEOS proton fluence > 100 MEV and earthquake number with M $\geq$ 8 and show that in 2001 the earthquake number and the GEOS proton fluence > 100 MEV are in maximum; in 1998, 2002 the GEOS proton fluence > 100 MEV and earthquake number are in minimum and in 2004 and 2007 the earthquake number is in maximum when the GEOS proton fluence > 100 MEV is in minimum. Fig. 7 illustrates the relation between mean annual solar flux and earthquake number with M $\geq$ 8 and show that in 2001 the earthquake number and the mean annual solar flux are in maximum, in 2002 mean annual solar flux is in maximum and earthquake number is in minimum, and in 2007 the earthquake number is in maximum and the mean annual solar flux is in minimum. Fig. 8 illustrates the relation between both observed and corrected sunspot area and earthquake number with M $\geq$ 8 and show that in 2004 the earthquake number is in maximum when the sunspot area is in minimum and in 2007 the sunspot area and earthquake number are in maximum.

From Fig. 5–8 we obtain that for earthquakes with M $\geq$ 8, there is a direct relation between the sunspot number, mean annual solar flux, GEOS proton fluence and earthquake number and an inverse relation during the descending phase of the cycle. Also, there is an inverse relation between the sunspot area in units of millionths of the sun's visible hemisphere and the earthquake number near the maximum of the solar cycle, and a direct relation during the descending phase of the solar cycle.
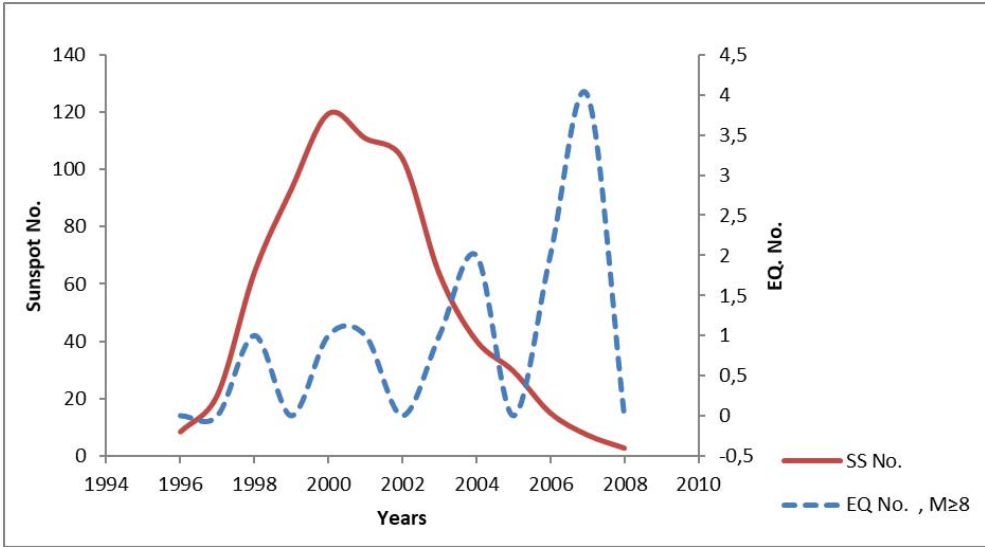
Fig. 5. Relation between the sunspot number and the number of earthquakes
with M ≥ 8 during solar cycle 23
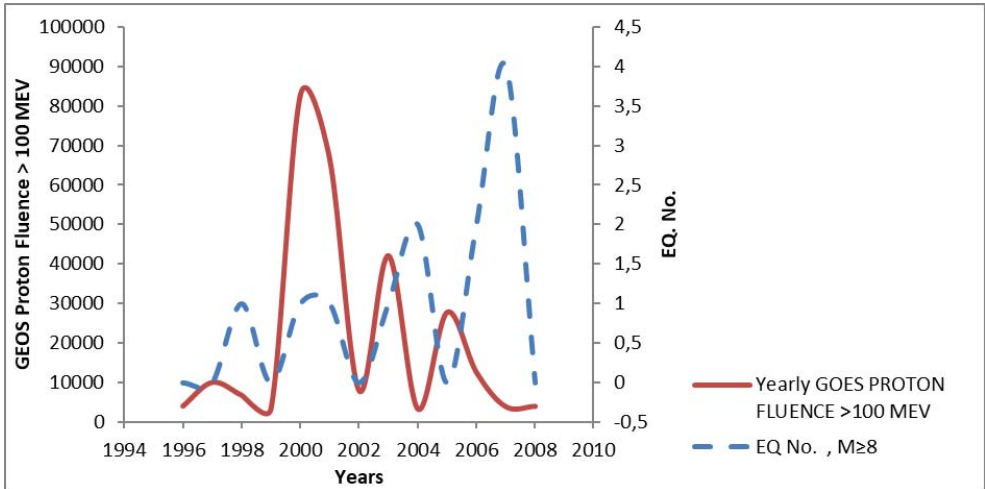
Fig. 6. Relation between the GEOS proton fluence > 100 MEV and the number
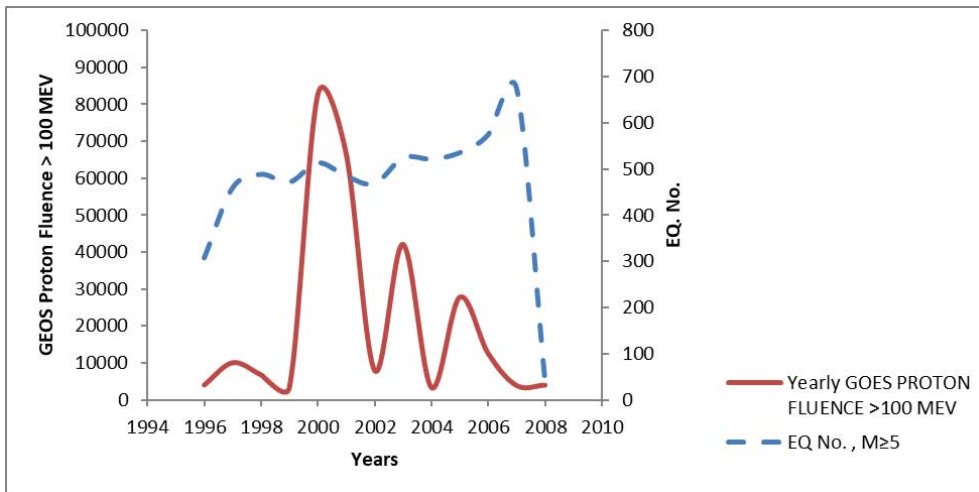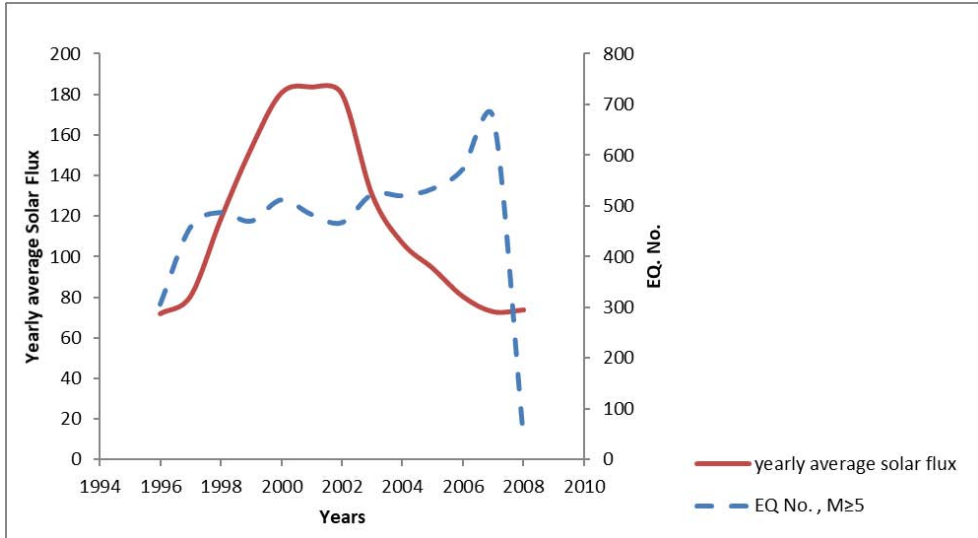*of earthquakes with M ≥ 8 during solar cycle 23*

12
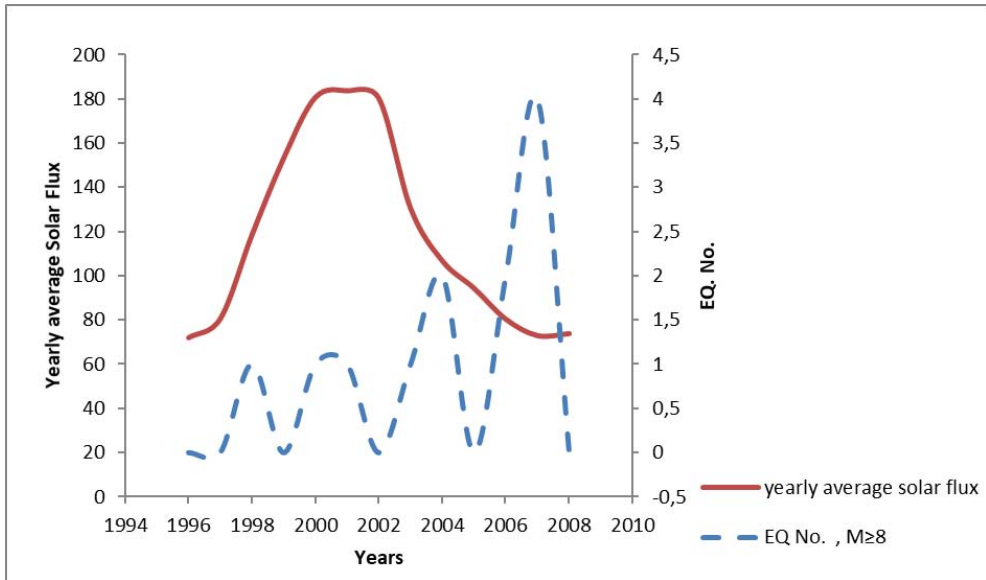
Fig. 7. Relation between the mean annual solar flux and the number of earthquakes with M $\geq$ 8 during solar cycle 23

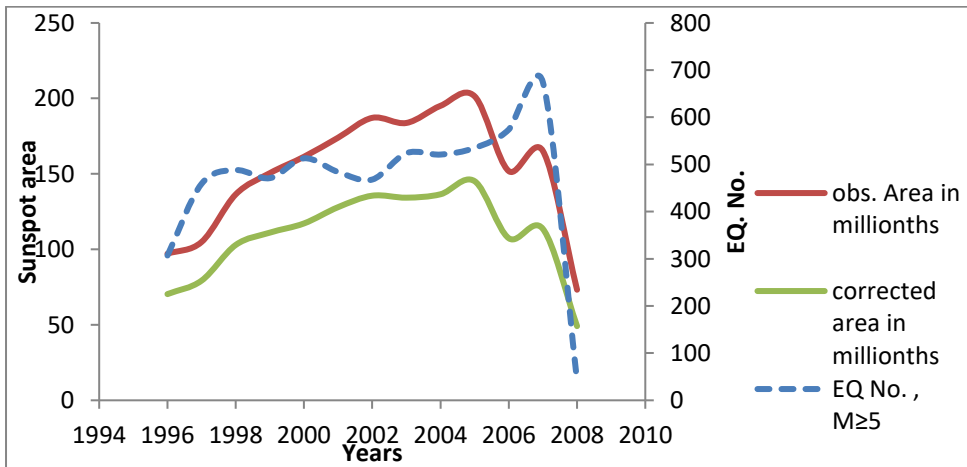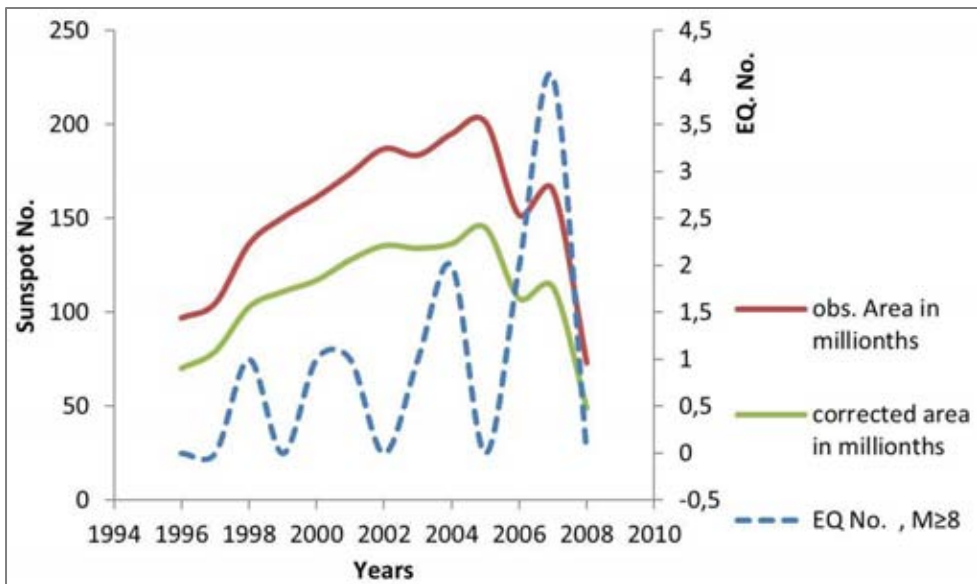*Fig. 8. Relation between both observed and corrected sunspot area and the number of earthquakes with M $\geq$ 8 during solar cycle 23*

Conclusion

Youssef, 2003 [14] show that solar cycle 23 is a weak solar cycle of 11.7 years duration and has two peaks in 2000 and 2002. In the case of earthquakes of magnitude ≥ 5, the number of earthquakes shows a peak at the minimum between cycles 23 and 24 as shown in Fig. 1.

There is a coincidence between the first activity peak of our studied cycle 23 in the year 2000 and the number of earthquakes. In the case of earthquakes of magnitude ≥ 8, the cycle 23 has three peaks of maximum, descending branch and post the weak cycle (Fig. 5).

The proton fluence occurring at the 1st maximum of this cycle is coincident with the 2nd earthquake peak. It is clear that protons have great influence on triggering earthquake particularly for this cycle, which can be explained by the injection of solar protons into the Van Allen belts and hence in polar regions. Strong ionospheric electric currents can induce telluric currents in the earth's crust and deep into the magma perhaps at the epicenter of the earthquake.

So, the Earth Internal Effects (EIE_s) are not the only reason for earthquakes. Solar activity also influences the processes going on the Earth. Our investigation show that the maximum of earthquakes frequently occur around the years of minimum in the solar activity cycle.

References

1. Zhang, Gui-Qing. Relationship between global seismicity and solar activities. ACTA SEISMOLOGICA SINICA, 1998, 11, 4, 495–500.
2. Sytinskiy, A. D. The influence of solar activity on earth seismicity. Akad. Nauk. SSSR, Dokl., 1973, 208(5), 1078–81.
3. Sytinskiy, A.D., On the relation between earthquakes and activity, Fizika Zemli, 1989, 2, 13–30.
4. Simpson, J. F. Solar activity as a triggering mechanism for earthquakes. Earth and Planetary Science Letters, 1968, 3, 417–25.
5. Lursmanashvili, O.V. Possible influence of solar activity on the distribution of the earthquakes in the Caucasus. Akad. Nauk Gruz. SSR Soobshch., 1972, 65, 2, 309–12.
6. Odintsov, S., K. Boyarchuk, K. Georgieva, B. Kirov, and D. Atanasov, Long-period trends in global seismic and geomagnetic activity and their relation to solar activity. Physics and Chemistry of the Earth, Parts A/B/C, 2006, 31, 1–3, 88–93.
7. Dorman, L. I. Cosmic rays in the Earth's atmosphere and underground, Vol. 303: Kluwer Academic Pub., 2004.
8. Gerontidou, M., Vassilaki, A., Mavromichalaki, H., and Kurt, V. Frequency distributions of solar proton events. Journal of Atmospheric and Solar-Terrestrial Physics, 2002, 64, 5–6, 489–96.
9. Courtillot, V., Y. Gallet, J. L. Le Mouël, F. Fluteau, and A. Genevey, Are there connections between the Earth's magnetic field and climate?, Earth Planet. Sci. Lett., 2007, 253, 3, 328–39.

10. Khain, V. E. and E. N. Khalilov, About possible Influence of solar activity upon seismic and volcanic activities: Long-Term forecast. Science without Borders, Transactions of the International Academy of Science H and E, 2007, l.3, SWB, Innsbruck, ISBN 978-9952-451-01-6 ISSN 2070-0334.
11. Tavares, M. and A. Azevedo, Influences of solar cycles on earthquakes. Natural Science, 2011, 3, 6, 436–43.
12. Nikouravan, B., P. Saied, and M. Somayeh. The effect of solar cycle's activities on earthquake: a conceptual idea for forecasting. Disaster Advances, 2013, 6, 4.
13. Kane, R. P. Some Implications Using the Group Sunspot Number Reconstruction. Solar Physics, 2002, 205, 2, 383–401.
14. Yousef, S. Cycle 23, the first of weak solar cycles series and the serious implications on some Sun-Earth connections, ESA Publications Division, 2003, ISBN 92-9092-845-X, 177–180.

ИЗСЛЕДВАНЕ НА ВРЪЗКАТА МЕЖДУ СЛЪНЧЕВАТА АКТИВНОСТ И СЕИЗМИЧНОСТТА НА ЗЕМЯТА ПО ВРЕМЕ НА СЛАБИЯ 23-ти СЛЪНЧЕВ ЦИКЪЛ

М. Семеида, С. Ходайри, М. Ел Хадиди, Р. Хамед, Ш. Юсеф, П. Стоева, А. Стоев

Резюме

В тази работа е изследвана връзката между броя на слънчевите петна, площта на слънчевите петна, слънчевото радиоизлъчване при дължина на вълната 10.7 cm, слънчевите протонни събития и земетресенията с магнитуд M ≥ 5 и M ≥ 8, в интервала 1996–2008 г. от 23-ия слънчев цикъл. Намерена е пряка връзка между слънчевата активност и земната сеизмична активност при M ≥ 5 и M ≥ 8 близо до максимума на 23-ия слънчев цикъл и обратна връзка по време на низходящата фаза на слънчевия цикъл.

STUDY OF WASTE DISPOSAL THERMAL RADIATION USING SATELLITE DATA AND CONSIDERING SOLAR INFLUENCE

Adlin Dancheva, Simeon Asenovski

Space Research and Technology Institute – Bulgarian Academy of Sciences
e-mail: adlin.dancheva@space.bas.bg; asenovski@space.bas.bg

Abstract
In the present article distribution of the waste disposal thermal radiation caused by biochemical processes of decomposition is examined. Using thermal channels of the Landsat 8 (OLI) the waste disposal spectral characteristics are obtained. All this data is compared with solar activity during the same period and differences between internal thermal radiation and solar influences are discussed.

Introduction

With the permanent increasing of human population, a serious problem concerning air and water pollution and also soil contamination arises. This is the problem of waste disposals sites (WDS) and its influence on the surrounding environment [1, 2]. These disposals are main source of methane emissions (CH_4), which is one of the greenhouse gases with strong influence on the atmosphere and prerequisite of the greenhouse effect with anthropogenic character. Waste gases are organic products, a result from decomposition of waste in anaerobic conditions. They are composed mainly from methane (CH_4) and carbon dioxide (CO_2) [3, 4].

The areas occupied by waste disposals are rapidly growing, as in some cases they are unregulated. For example in 2012, 481 kg solid waste per single person for the population in European Union is generated [5].

This research focuses on *Suhodol* waste disposal close to the Bulgarian capital, Sofia. Officially this disposal was formed 30 years ago with purpose of Sofia municipality waste collecting. Its exploitation is achieved in two stages, and the first stage was until 1995.

The main goal of this work is calculating the surface temperature caused by waste internal thermal radiation and determining the places where the temperature is the highest (thermal points). Several time intervals are examined.

In Fig. 1 is shown the location of the waste disposal *Suhodol*, Sofia. The object is in geographic coordinates 23°12′03′′ E and 42°41′26′′ N (WGS 84, UTM 34N).

Fig. 1. Location of the waste disposal Suhodol, Sofia.

Materials and methods

Current investigation uses thermal channels of Landsat 5–7 ETM+ and Landsat 8 OLI/TIRS, as for the calculation of thermal radiation is used band 6 of Landsat ETM+ with wave length 10.40÷12.50 μm and band 10 with wave length 10.6÷11.9 μm. Images for four years and for two different seasons (winter and summer) are considered. In Table 1 are described the images.

We can write a general formula for Landsat 4–8: [6–9]

$$(1) \qquad T_{[K]} = a * ln^{-1} \left(\frac{b}{c*Q+d} + 1 \right)$$

Where *a*, *b*, *c*, and *d* are the constants for the different types of Landsat images, *T* is the pixel temperature (K), *Q* is the spectral brightness coefficient of the

surface in the thermal channel Landsat (4–8) satellite images are downloaded from web page https://earthexplorer.usgs.gov/.

Table 1. Used Landsat satellite images

Date	Satellite
31.01.2004	Landsat 7 ETM+
18.08.2004	Landsat 5 TM
28.01.2006	Landsat 5 TM
23.07.2006	Landsat 5 TM
02.01.2009	Landsat 5 TM
23.07.2009	Landsat 7 ETM+
02.01.2017	Landsat 7 ETM+
21.07.2017	Landsat 8 OLI

After the georeferencing procedure of the thermal images the cutting out of the rectangular sections in each image covering the vicinity of the geographic coordinates is carried out. The time series {Q1, Q2, . . . , Qn} of the images in the thermal channel of each WDS are extracted. The data from the image is converted into the surface temperature {T1, T2, . . . , Tn} using transformation:

(2) $$T_{[C^0]} = a * Ln^{-1}\left(\frac{b}{c*Q+d} + 1\right) - 273.15 \quad ,$$

where:
a is the K_2 = Thermal conversion constant for the band (K2_CONSTANT_BAND_n from the metadata);
b is K_1 = Thermal conversion constant for the band (K1_CONSTANT_BAND_n from the metadata);
c is M_l = Radiance multiplicative scaling factor for the band (RADIANCE_MULT_BAND_n from the metadata);
d is L_{λ} = Spectral radiance ($W/(m2 * sr * \mu m)$);
Q = L1 pixel value in DN;
T = TOA (Top of Atmosphere) Brightness Temperature

The time series for WDS are formed together with the mask for clouds and "blankness" and are entered into the database. The time series of images for temperature for each landfill or WDS is systematized [10].

18

Results

Presented results are for the following days: 18.08.2004, 31.01.2004, 23.07.2006, 28.01.2006, 23.07.2009, 02.01.2009, 02.01.2017 and 21.07.2017. We have tracked the internal thermal radiation of the *Suhodol* waste disposal for four different years. In Fig. 2 land surface temperature (LST) of waste disposal *Suhodol* is presented. Hot spots are situated in the center of the landfills. A temperature variation of 4°C between the center and surrounding area is observed. Average surface temperature is −7°C while the core temperature of the landfills reaches −4°C.

In Fig 3 the temperature for 18.08.2004 is calculated. In the summer there is an increased rotting activity which increases the temperature of this area. Hot spots move beyond the limits of the landfill. The average surface temperature is +26°C while the temperature within the landfill reaches +31°C.

During the winter of 2006 the average surface temperature is −6°C, and within the landfill it reaches −4°C. The hot spots move toward the center and the north parts of the observed object (Fig. 4).

In 23.07.2006 the same temperature displacement as in July 2004 is detected. The highest temperature is again at the center of the object in question as well as in its north part (+34°C).
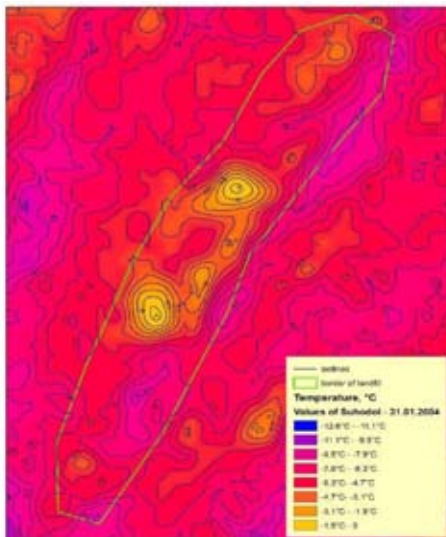
Fig. 2. LST of Suhodol – 31.01.2004
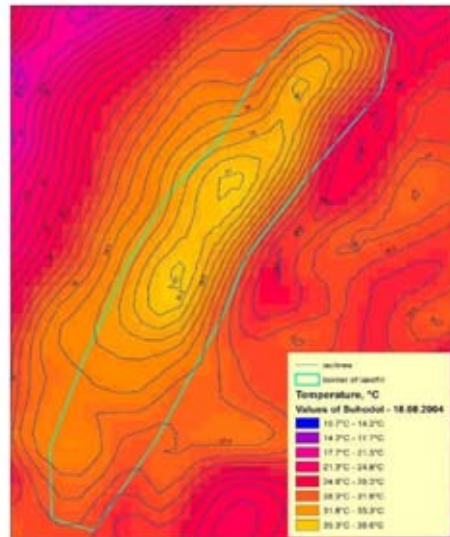
Fig. 3. LST of Suhodol – 18.08.2004
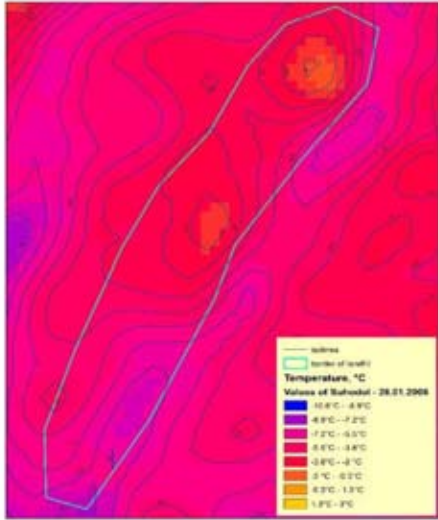
Fig. 4. LST of Suhodol – 28.01.2006
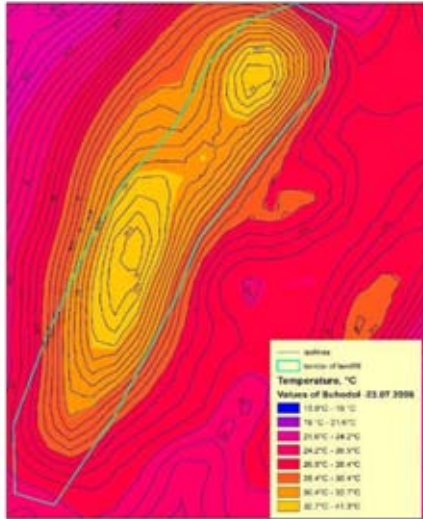
Fig. 5. LST of Suhodol – 23.07.2006
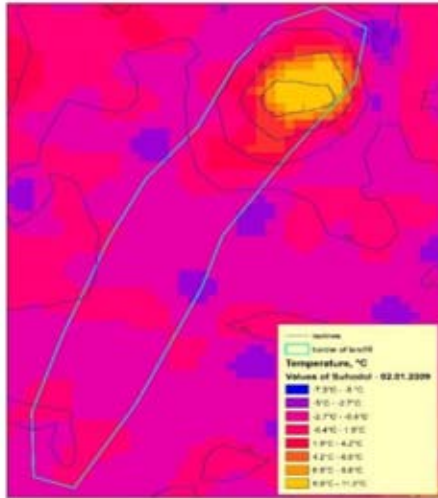
Fig. 6. LST of Suhodol – 02.01.2009
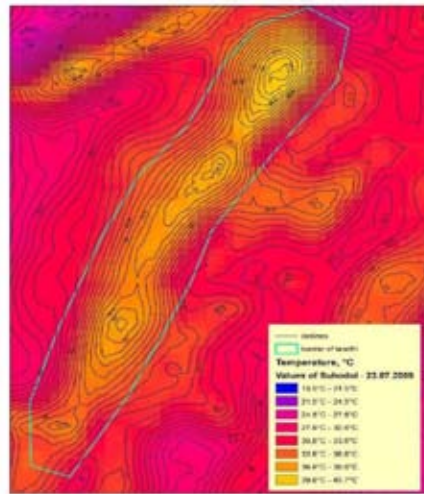
Fig. 7. LST of Suhodol – 23.07.2009

20
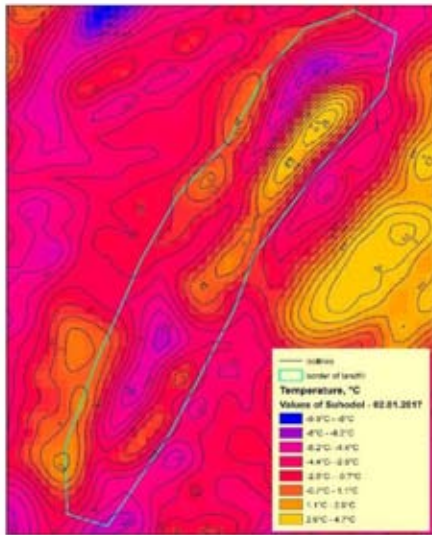
Fig. 8. LST of Suhodol –02.01.2017
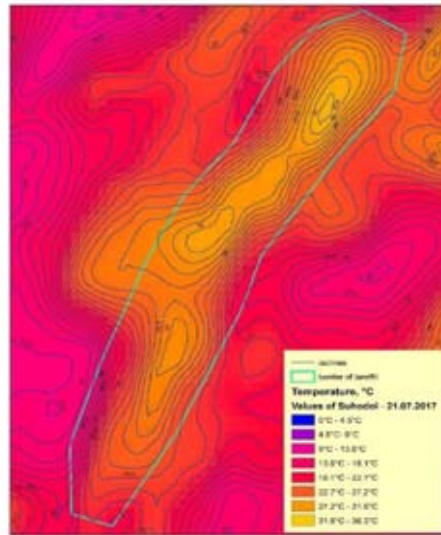
Fig. 9. LST of Suhodol – 21.07.2017

In Fig. 6 is shown that the hot spots are entirely in the northern part of the investigated object. The average surface temperature is –0.5°C, while within the landfill it is +1°C. In the end of the July 2009 (Fig. 7) a major change in landfill temperature is observed. The highest values are found in the northern part - +38.5°C. The average temperature is +29°C.

In January 2017 significant displacement of the hotspot compared to previous years is observed. The temperature difference between the object and surrounding area is 2°C. In Fig. 8 are presented calculated temperature values for 21.07.2017. The temperature has the highest values in the northern part of the landfill +33°C.
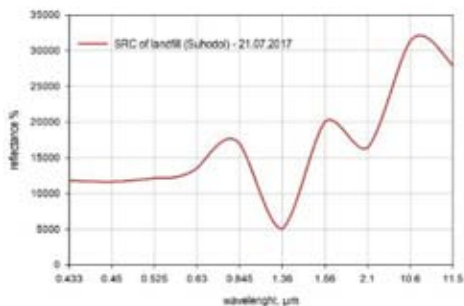
Fig. 10. Spectral reflectanse characteristics of landfill
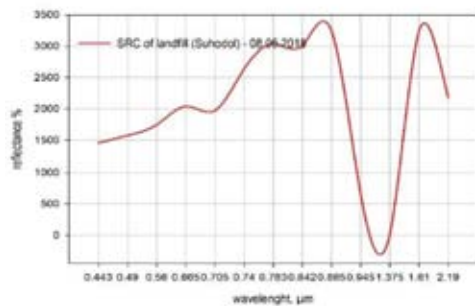
Fig.11. Spectral reflectanse characteristics of lanfill

21

For comparison, landfill spectral characteristic with different sensors are made. In Fig. 10 and 11 spectral reflective characteristics of the waste disposal *Suhodol* for 21.07.2017 and 08.06.2018 are presented. The used sensors are Landsat 8 and Sentinel 2 (Copernicus, ESA, https://scihub.copernicus.eu).

Solar activity

Land surface temperature (LST) is one of the most usable parameters in studying the physical and chemical processes and phenomena that involve energy balance in hydrology, biology meteorology etc. Short and long-term variation of LST depends strongly on the amount the solar energy that reaches the Earth's surface and therefore on the diurnal variation, seasons and climate zones. One of the most reliable indicators for the estimation of the solar energy that reaches the Earth is solar irradiance (W/m^2) and the solar f10.7 index (2 800 MHz) which correlates with the sunspot number and Ultra Violet (UV) radiation. F10.7 radio emissions are very sensitive to the processes in the upper chromosphere and at the base of the solar corona. It is present in solar flux units (sfu), where 1 sfu = 10^{-22} W m^{-2} Hz^{-1}.

In Fig. 12 and Fig. 13 are shown the variations of the total solar irradiance (W.m^{-2}) (http://spot.colorado.edu/~koppg/TSI/) for the last several years that reach the outer part of the Earth's atmosphere and solar radio index 10.7 cm (sfu) (https://omniweb.gsfc.nasa.gov). It can be seen that during the period of last solar minimum, i.e. 2016–2018, the values of both indicators are smaller than those measured in previous years.
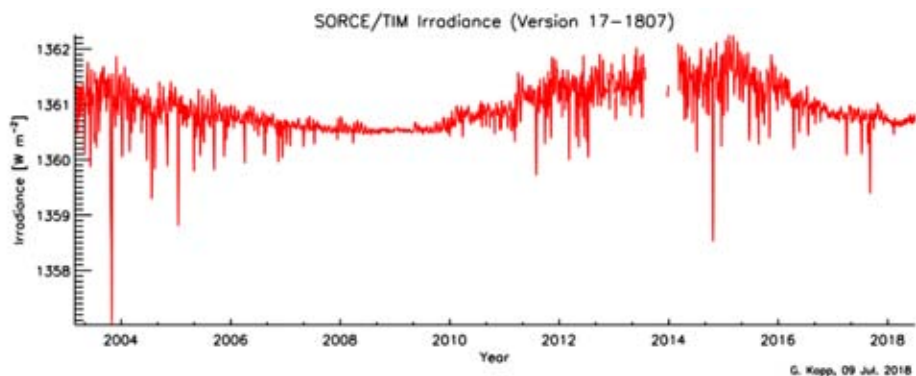
Fig. 12. Variation of the total solar irradiance
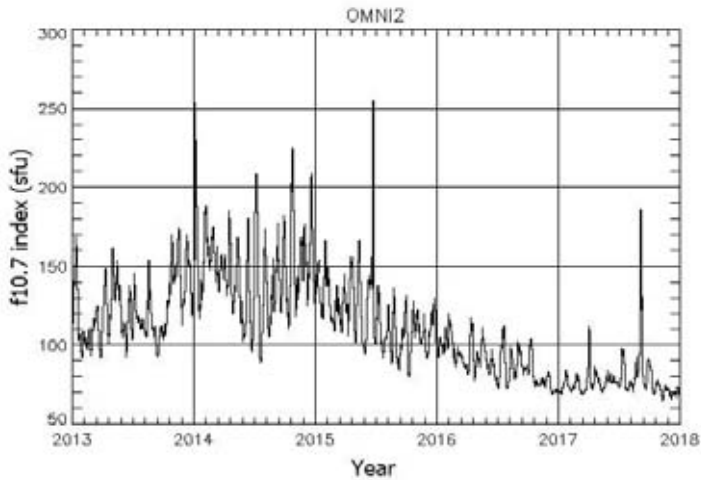
Fig. 13. Variation of the solar radio flux at 10.7 cm

Conclusion

This work presents a study of *Suhodol* waste disposal and its thermal radiation caused by biochemical processes of decomposition using satellite data. The results can be summarized in the following statements:

- In 18.08.2004 an increased rotting activity is observed which increases the temperature of the landfill. Hot spots move beyond the limits of the landfill.
- During the winter of 2006 the hot spots move toward the center and northern parts of the observed object.
- In 23.07.2006 the same temperature displacement as in July 2004 is detected. The highest temperature is again at the center of the object in question as well as in its north part (+34° C).
- In January 2009 the hot spots are entirely in the northern part of the investigated object while in the end of the July 2009 a major change in landfill temperature is observed.
- In January 2017 significant displacement of the hotspot compared to previous years is observed. The temperature difference between the object and surrounding area is 2° C. The temperature has the highest values in the northern part of the landfill - +33° C.
- According to the F10.7 index and Solar irradiance, solar energy reaching the surface during the period of last solar minimum - 2016–2018, is less than the measured in previous years. The observed landfill temperature variation do not show measurable dependence with solar activity.

References

1. Казарян, М. Л., А. А. Рихтер, М. А. Шахраманьян, Р. Недков. Космический мониторинг объектов захоронения твердых бытовых отходов и промышленных отходов (тбо и по): теоретико-методические и социально-экономические аспекты. М.: Научная мысль, ИНФРА-М, 2018, ISBN:978-5-16-014435-1 (print), 978-5-16-106965-3 (online), DOI: dx.doi.org/10.12737

2. Nedkov, R., M. Dimitrova, M. Zaharinova, and I. Ivanova. Web monitoring of fires on Balkans based on satellite data during July and August 2007. Ecological Engineering and Environment Protection, 2008, 1, 13–19. ISSN 1311-8668

3. Shakhramanyan, M., Richter, A., Kazaryan, M., Nedkov, R., Borisova, D., Stankova, N., Ivanova, I., Zaharinova, M. Evaluation of chemical process parameters in waste disposal sites by satellite images. Ecological Engineering and Environment Protection, 2017, 1, 22–28. ISSN 1311-8668

4. Ganev, I., A. Tcanova, Neotralization and oxidation of landfill gas, Energy forum 2006, https://inis.iaea.org/collection/NCLCollectionStore/_Public/38/105/38105235.pdf

5. EEA, Resource efficiency and waste, https://www.eea.europa.eu/bg/signals/signali-2014-g/statii/otpadatsite-problem-ili-resurs

6. Richter, A., M. Kazaryan, M. Shakhramanyan, R. Nedkov, D. Borisova, N. Stankova, I. Ivanova, and M. Zaharinova, Estimation of thermal characteristics of Waste disposal sites using Landsat satellite images. Comptes rendus de l'Academie bulgare des Sciences, 2017, 70, 2.

7. Nedkov, R. Quantitative assessment of forest degradation after fire using ortogonalized satellite images from Sentinel-2. Comptes rendus de l'Academie bulgare des Sciences, 2018, 71, 1, 83–86. ISSN 2367–5535

8. Richter, A., M. Kazaryan, M. Shakhramanyan, R. Nedkov, D. Borisova, N. Stankova, I. Ivanova, and M. Zaharinova. Quality enhancement of satellite images and its application for identification of surroundings of waste disposal sites. Proc. SPIE 10444, 5th International Conference on Remote Sensing and Geoinformation of the Environment (RSCy2017), 10444, SPIE, 2017. DOI:10.1117/12.2277309

9. Landsat 8 Data Users Handbook. 2016, v. 2. USGS, https://landsat.usgs.gov/sites/default/files/documents/Landsat8DataUsersHandbook.pdf

10. Kuenzer, C. et al. Spaceborne thermal infrared observation – an overview of most frequently used sensors for applied research, in: Kuenzer, C. and S., Dech, (eds) Thermal Infrared Remote Sensing SE-7. Springer Netherlands (Remote Sensing and Digital Image Processing), 131–148. DOI:10.1007/978-94-007-6639-6_7.

11. Fjelsted, L., et al. Assessment of a landfill methane emission screening method using an unmanned aerial vehicle mounted thermal infrared camera – A field study. Waste Management and Research, 2018, DOI:10.1016/j.wasman.2018.05.031

12. Iacoboaea, C., F. Petrescu, Landfill monitoring using remote sensing: a case study of Glina, Romania, Waste Management and Research, 2013, 31, 10, 1075–80, DOI:10.1177/0734242X13487585

13. Windahl, E., K. Beurs, An intercomparison of Landsat land surface temperature retrieval methods under variable atmospheric conditions using in situ skin temperature, International Journal of Applied Earth Observation and Geoinformation, 2016, 51, 11–27, DOI:10.1016/j.jag.2016.04.003

ИЗПОЛЗВАНЕ НА СПЪТНИКОВИ ДАННИ ЗА ИЗСЛЕДВАНЕ НА СОБСТВЕНОТО ТОПЛИННО ИЗЛЪЧВАНЕ НА СМЕТИЩА С ОТЧИТАНЕ НА ВЛИЯНИЕТО НА СЛЪНЦЕТО

А. Данчева, С. Асеновски

Резюме

В настоящата работа се изследва разпределението на собственото топлинно излъчване на сметища, предизвикано от биохимични процеси на разлагане. Използвани са топлинните канали на сензора Landsat 8 (OLI). Получени са спектрални характеристики на сметища от сензорите Landsat 8 и Sentinel 2. На базата на спътникови данни за слънчевата активност са отчетени разликите между собственото топлинно излъчване и влиянието на Слънцето. Получени са резултати за различни времеви сезони от различни по своето пространствено разпределение сметища.

SOLAR CYCLE BY A LOOK OF HIGH SPEED SOLAR WIND STREAMS VARIATION

Simeon Asenovski

Space Research and Technology Institute – Bulgarian Academy of Sciences
e-mail: asenovski@space.bas.bg

Abstract

In this paper are presented variation of the solar wind parameters during last four solar cycles (21÷24) with focus on the high speed solar wind streams (HSS) condition. The averaged values of the parameters for every cycle are calculated and discussed. The results show that Earth is under the HSS influence more than 50% of the total time in each of the last four solar cycles. This fact determines the importance of the studding the behavior of the HSS.

Introduction

High speed solar wind streams (HSS) are one of the solar wind components which originate from unipolar open magnetic field areas known as coronal holes [1, 2]. HSS cause relatively weak, but recurrent and long-lasting geomagnetic storms [3]. The variations of geomagnetic activity closely follow the variations of the number and intensity of HSS within the solar cycle [4]. Coronal holes are the largest and in most geoeffective position during the sunspot declining phase [4], when the second maximum in the geomagnetic activity is observed. In Fig. 1 is presented an SDO/AIA image (Solar Dynamics Observatory/ Atmospheric Imaging Assembly) of the coronal hole CH869 on 15 June 2018. CH869 have been rotated into an Earth facing position on June 19–21.
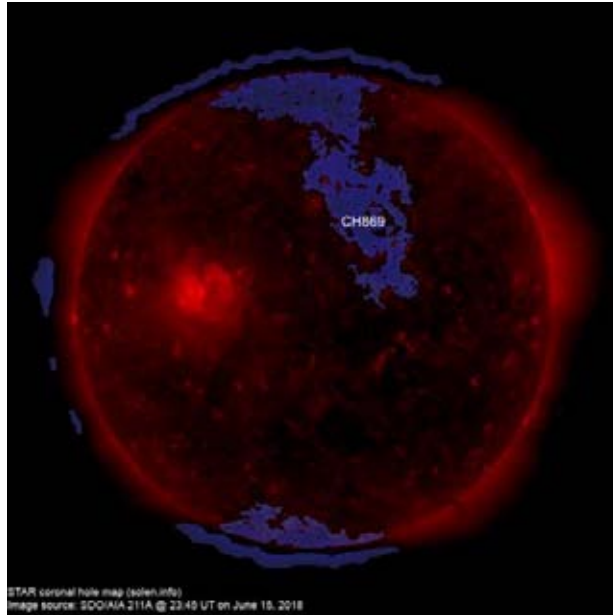
Fig. 1. SDO/AIA image of the coronal hole CH869 at 23:45UT
on 15 June 2018 (http://www.solen.info/solar/)

Solar cycle (SC) is generally associated with the 11 year sunspot cycle (Schwabe, 1843) and numerous studies concerning Sun and solar-terrestrial physics are related with it. In Table 1 are presented duration of the last eight SC (17÷24). The 24th is supposed to end within 2018 with duration approximately of ~11 years.

Table 1. Duration of the last eight Solar cycles (17÷24)

Cycle	Started	Finished	Duration (years)
Solar cycle 17	1933 September	1944 February	10.4
Solar cycle 18	1944 February	1954 April	10.2
Solar cycle 19	1954 April	1964 October	10.5
Solar cycle 20	**1964 October**	**1976 June**	**11.7**
Solar cycle 21	**1976 June**	**1986 September**	**10.3**
Solar cycle 22	**1986 September**	**1996 May**	**9.7**
Solar cycle 23	**1996 May**	**2008 January**	**11.7**
Solar cycle 24	**2008 January**	**2018**	**~ 11**

In the current study, the focus will be on the HSS during the last four SC (21÷24). Here the differences of the main parameters (Temperature [K], Speed [km/s], Density [cm-3], Magnetic field [nT]) during the cycles will be discussed. In Fig. 2 are shown the variations of the sunspot number for these cycles. As it can be seen, the last 24th SC is characterized with the lowest values of the sunspot number during the course of the whole cycle in comparison with the other cycles.
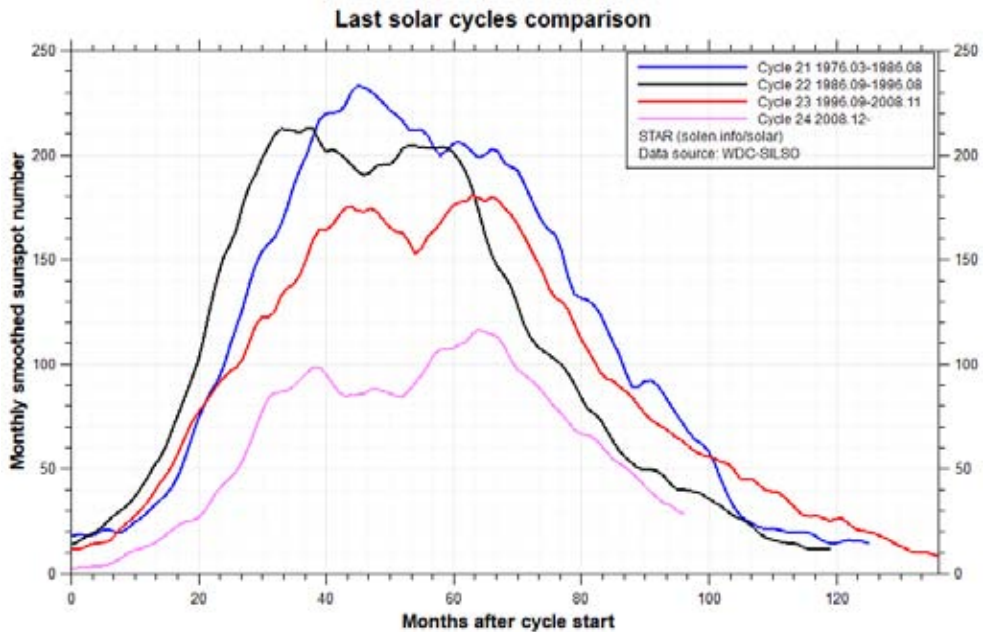
Fig. 2. Comparison of the monthly smoothed sunspot number variation for the last four SC (21-24) (http://www.solen.info/solar/)

Parker suggested that the properties of solar wind flow depend on the solar activity cycle [7]. Several years later series of space probe experiments, as Lunik and Venera [8], Explorer 10 [9] and Venus Mariner 2 [10] confirmed the Parker's theory.

Data

In attempt to identify the periods when Earth is under the influence of the HSS the hourly values of the plasma parameters gathered in OMNI data base are used (http://omniweb.gsfc.nasa.gov/) [11]. The criteria for identifying a HSS include an increase of the solar wind speed by at least 100 km/s in no more than one day to at least 450 km/s for at least five hours [12].

Results

In Tables 2–5 are shown the averaged values of the main solar wind parameters (Different magnetic field components [nT], Temperature of the plasma [K], Density [N/c], Speed [km/s], Flow pressure [nPa]) for the last four SC for different solar wind conditions – Slow solar wind with speed less than 450 km/s, fast solar wind with speed over 450 km/s but different from HSS, coronal mass ejection (CME) and HSS. For every SC are presented the total numbers of hours in which Earth is under the influence of these conditions. The last three rows have shown the averaged values of the geomagnetic *Dst* index and the sunspot number *R*.

Table 2. Averaged values of the main solar wind properties during SC21

	Slow SW V ≤ 450 km/s	Fast SW V > 450 km/s	CME	HSS
Hours	6 120	900	143	7 878
Scalar B, nT	5.41	5.45	11.13	5.85
Bx, nT	–0.22	–0.02	0.30	–0.36
By, nT	0.37	-0.05	–0.45	0.34
Bz, nT	0.12	0.12	–0.56	0.22
T, K	64 495	184 070	69 757	178 230
Dens, N/c	10.78	5.20	8.67	5.60
Speed, km/s	370.45	520.92	394.45	512.18
Pressure, nPa	2.75	2.65	2.54	2.66
R	15.73	21.57	28.44	13.49
Dst, nT	–5.70	–14.03	–27.41	–17.79

At SC21 the number of hours in which HSS is observed is 7 878 which is more than 50 % of the total time of the cycle. Here we can see that the average temperature during HSS is significantly larger than the temperature of the slow solar wind and comparable with the temperature of the fast solar wind. Here it must be noticed what is the difference between fast solar wind and HSS. According to the criteria of HSS there is a requirement concerning duration which is at least five hours. Normally the averaged sunspot number is the largest during the condition of CME.

Table 3. Averaged values of the main solar wind properties during SC22

	Slow SW V ≤ 450 km/s	Fast SW V > 450 km/s	CME	HSS
Hours	3 289	271	105	7 161
Scalar B, nT	5.50	6.73	9.45	5.90
Bx, nT	–0.43	–0.09	–1.52	0.15
By, nT	0.04	–0.51	–0.68	0.03
Bz, nT	0.24	–0.39	–0.61	0.00
T, K	54 590	148 250	73 523	146 090
Dens, N/c	11.83	7.45	7.08	6.14
Speed, km/s	367.02	486.46	422.70	507.98
Press,	2.96	3.41	2.36	2.78
R	18.46	16.99	20.87	16.81
Dst, nT	–4.41	–16.79	-	–19.98

Similarly to SC21, with its 7 161 hours the next SC22 is characterized with more than 50 % of the total time of the cycle in which to the Earth reach HSS. During this time the average density and flow pressure have the lowest values in comparison to the values when it is observed slow and fast solar wind as well as CME.

Table 4. Averaged values of the main solar wind properties during SC23

	Slow SW V ≤ 450 km/s	Fast SW V > 450 km/s	CME	HSS
Hours	7 283	342	132	9 811
Scalar B, nT	3.86	4.58	8.42	4.68
Bx, nT	0.46	–1.61	0.46	–0.19
By, nT	–0.57	1.13	–0.41	0.08
Bz, nT	0.05	0.08	1.13	0.02
T, K	42 251	124 360	61 981	132 840
Dens, N/c	7.02	3.88	5.54	4.06
Speed, km/s	347.06	519.55	399.77	517.74
Press,	1.46	2.03	1.57	1.87
R	5.16	10.32	8.98	4.97
Dst, nT	–1.98	–13.32	–6.25	–12.42

During SC23, time of HSS (9 811 hours) is more than 75 % the total time. This fact determines condition of relatively high temperature, low density and pressure. During the period when Earth is under the slow solar wind the average temperature of the plasma reach its lowest value of 42 251 K.

The general picture has been slightly changed for the last SC24. While the relative duration of the HSS for the cycle remains more than 50 % of the total time,

the most of the parameters differ from the previous cycle. Here can be noticed that the average speed drop under 500 km/s for HSS while the temperature increase more than 200 000 K.

Table 5. Averaged values of the main solar wind properties during SC24

	Slow SW V ≤ 450 km/s	Fast SW V > 450 km/s	CME	HSS
Hours	7 981	655	128	8 690
Scalar B, nT	5.01	5.12	12.68	5.55
Bx, nT	0.10	−1.12	−0.76	0.27
By, nT	−0.02	0.97	0.12	−0.09
Bz, nT	−0.13	−0.21	−0.58	−0.11
T, K	90 625	262 550	80 164	205 240
Dens, N/c	10.33	4.47	8.34	6.97
Speed, km/s	362.73	511.37	402.60	463.32
Press,	2.39	2.19	2.51	2.53
R	10.29	7.85	12.87	11.07
Dst, nT	−6.34	−25.42	−29.84	−17.76

Conclusion

This work presents a study for variation of the solar wind parameters for the different state, as slow and fast solar wind, coronal mass ejection and high solar wind speed. The averaged parameters are calculated and discussed for the last four solar cycles (21÷24). The result can be summarized in the following statements:
- The time in which Earth is under the HSS influence is more than 50 % of the total time in each of the last four solar cycles.
- At SC23 the HSS influence is more than 75 % of the total time.
- Slow solar wind temperature during SC23 reach its lowest value of 42 251 K.
- The averaged parameters of the fast solar wind and HSS have similar values.
- During the last SC24 the averaged HSS speed drops under 500 km/s while HSS temperature increases more than 200 000 K.

References

1. Tsurutani, B. T., W. D. Gonzalez, A. L. C. Gonzalez, F. Tang, J. K. Arballo, M. Okada, Interplanetary origin of geomagnetic activity in the declining phase of the solar cycle, J. Geophys. Res., 1995, 100, 21717.
2. Tsurutani, B. T., W. D. Gonzalez, A. L. C. Gonzalez, F. L. Guarnieri, N. Gopalswamy, M. Grande, Y. Kamide, Y. Kasahara, G. Lu, I. Mann, R. McPherron, F. Soraas, and V. Vasyliunas. Corotating solar wind streams and recurrent geomagnetic activity: A review. J. Geophys. Res., 2006, 111, A07S01, DOI:10.1029/2005JA011273.
3. Borovsky, J. E., M. H. Denton, Differences between CME-driven storms and CIR-driven storms, J. Geophys. Res., 2006, 111, A7.
4. Richardson, I. G., H. V. Cane. Solar wind drivers of geomagnetic storms during more than four solar cycles, J. of Space Weather & Space Clim., 2012, A01, DOI:10.1051/swsc/2012001.
5. Phillips, J. L., S. J. Bame, W. C. Feldman, J. T. Gosling, C. M. Hammond, D. J. McComas, B. E. Goldstein, M. Neugebauer, E. E. Scime, and S. T. Suess. Ulysses Solar Wind Plasma Observations at High Southerly Latitudes, Science, 1995, l268, 1030–33.
6. Schwabe, T. Sonnen-beobachtungen im jahre 1843, Astr. Nachrichten, 1843, 21, 233–236.
7. Parker, E. N. Interaction of the Solar Wind with the Geomagnetic Field, Physics of Fluids, 1958, 1, 171–87.
8. Gringauz, K. I., V. G. Kurt, V .I. Moroz, and I. S. Shklovskii. Results of Observations of Charged Particles Observed Out to R = 100, 000 km, with the Aid of Charged-Particle Traps on Soviet Space Rockets, Astronomicheskii Zhurnal, 1960, 37, 716.
9. Bonetti, A., H. S. Bridge, A. J. Lazarus, B. Rossi, and F. Scherb. Explorer 10 Plasma Measurements, Journal of Geophysical Research, 1963, 68, 4017.
10. Neugebauer, M., C. W. Snyder. Solar Plasma Experiment, Science, 1962, 138, 1095–97.
11. King, J. H., N. E. Papitashvili. Solar wind spatial scales in and comparisons of hourly wind and ACE plasma and field data, J. Geophys. Res., 2005, 110, 2104, 2005.
12. Richardson, I. G., H. V. Cane. Regions of abnormally low proton temperature in the solar wind (1965–1991) and their association with ejecta, J. Geophys. Res., 1995, 100, A12, 23397–412.

СЛЪНЧЕВИЯ ЦИКЪЛ ОТ ГЛЕДНА ТОЧКА НА ВАРИАЦИИТЕ НА ВИСОКОСКОРОСТНИТЕ ПОТОЦИ СЛЪНЧЕВ ВЯТЪР

С. Асеновски

Резюме

В работата са представени вариациите на параметрите на слънчевия вятър за последните четири слънчеви цикъла (21÷24) с подчертано внимание на условията на високоскоростен слънчев вятър. Средните стойности на параметрите за всеки цикъл са пресметнати и дискутирани. Резултатите показват, че Земята е под въздействието на високоскоростен слънчев вятър повече от 50 % за всеки от последните четири слънчеви цикъла. Този факт обуславя важността от изследване на поведението на тези потоци.

SOME SPECIFICS OF THE DISTRIBUTION OF ELECTROMAGNETIC POLLUTION ON THE TERRITORY OF SOFIA MUNICIPALITY

Teodora Andreeva-Nesheva[1], Dimitar Teodossiev[1], Iliya Iliev[2]

[1]Space Research and Technology Institute – Bulgarian Academy of Sciences
[2]Technical University of Sofia, Faculty of Telecommunications
e-mail: teoandreeva1@gmail.com

Abstract

Some results from measurements of electromagnetic radiation in the frequency range between 110 kHz and 7 GHz on the territory of Sofia Municipality are presented and the observed deviations of the measured levels from the adopted maximal allowed values are discussed. The development of methods for evaluation and optimization of electromagnetic emissions in urbanized environments is suggested and justified, as well as the construction of a monitoring and control system for electromagnetic radiation and background noise in strongly urbanized territories, such as Sofia Municipality.

Introduction

One of the environmental energy pollution factors are electromagnetic fields. As a result of the exclusively wide application of electromagnetic energy in various human activity domains, the available sources of the Earth's natural electric and magnetic fields, atmospheric electricity and Galactic and solar radio radiation are supplemented by electromagnetic fields of artificial origin. It is a fact that, in a number of cases, their level exceeds significantly the level of electromagnetic fields originating from natural sources.

In technical literature, serious concern for the increase of electromagnetic radiation (EMR) and from there – of the total background noise (BN) is expressed. Various EMR man-induced sources exist – TV and radio-transmitters, radar antennae, basic mobile operator stations and more. Recent scientific research shows that the levels of EMR and BN are already reaching sufficiently high values to cause disturbances in the electromagnetic compatibility of the available radio equipment, mostly in urban environment, where their concentration is highest. This calls for the need to apply specific methods to measure, monitor and forecast the increase of EMR and BN.

In a strongly developed urban environment where total BN is increased, the so-called "hot points" or "hot areas" may appear where the electromagnetic field

level exceeds the health norms set by regulation. This requires developing effective and reliable methods to forecast the EM circumstances in the vicinity of the typical communication sources and to assess the compliance with EMR admissible level norms.

The measurement, continuous monitoring, composing of a database and evaluation of the parameters of the electromagnetic fields in urban environment are an important aspect of EMR to achieve healthy living environment. Although no direct scientific evidence of any relation between EM fields and human diseases is available, it is necessary to undertake all precautionary measures against the uncontrolled increase of EMR levels.

To assess the actual circumstances and the characteristic features of the distribution of EMR in strongly urbanized urban environment, it is required to perform a series of preliminary measurements in various points of the territory of Sofia Municipality (SM), various 24-hour intervals, various meteorological circumstances and various distances to the irradiating antenna [1–8].

Objective of the study

The major objective of this study is to present and analyse some specifics in the distribution of EMR levels in the districts of SM, which is characterized by different concentration of ground-based sources (TV and radio-transmitters, radar antennae, basic mobile operator stations and more), operation in the frequency range of $680 \div 2500$ MHz, and also by different urbanization degree and relief. The presented analysis of the results from the carried out measurements in different points of the territory of SM featuring different urbanization degree was made while implementing the first stage of Contract No. ДН 07/19/2016 with the Scientific Research Fund, "Methods for Evaluation and Optimization of Electromagnetic Radiation in Urbanized Environments".

Methodology

The study is based on the experience and the developed methods as a result of the successfully concluded European Project under the SEE-ERA-NET Programme "Development of Method and Strategy for Monitoring of Electromagnetic Pollution in the West Balkan Region", implemented by SRTI-BAS as a leading organization with partners from Republic of North Macedonia, Slovenia, and Croatia in 2009 [2].

The measurements were performed in accordance with Regulation No. 9 from 1991 of the Ministry of Health applying a control method according to the Bulgarian State Standard (BSS) 17137–90 (БДС 17137–90).

Used equipment

Two sets of dedicated mobile equipment were used. The first one is "SPECTRAN", produce of the German company AARONIA AG, including unit "SPECTRAN HF 6060 for measurement in the range between 1 MHz and 7 GHz, with directed antenna of the HyperLOG 6080 type. The results from the measurements are visualized in real time and are recorded on HP Compaq 6720s laptop, with installed software of the producing company, providing to carry out adjustments, measurements, visualization and storage of the results.

The second device is the autonomous station NARDA AMB 8057-03 intended for electromagnetic monitoring of the environment in the frequency range from 110 kHz to 7 GHz, which provides for continuous autonomous control of electromagnetic radiation, even in points hardly accessible for observation. Data is transferred automatically to the server hosting the database, whereas possibility for remote control of the device is also provided. The results from the measurements are stored in dedicated database containing information about EMR characteristics, distribution by frequency and location (coordinates of the measurement points in geographic information system – GIS).

The mobile equipment Narda AMB 8057-3 provides possibilities for visualization and reviewing of the information from the measurements for a chosen interval of time, date, week or twenty-four-hour period for the entire frequency range (110 kHz ÷ 7 GHz), a chosen subinterval of the frequency range (110 kHz ÷ 7 GHz), peak values or averaged value for a definite frequency, chosen time interval of the twenty-four-hour period, for observation of fine effects in the distribution of the irradiated power for a given frequency, whereas the maximal admissible radiation level for this frequency is marked by a red line.

Both devices are furnished with dedicated software for data storage, visualization and processing and with a solar panel providing power supply when operating in autonomous mode, as well as the possibility to transmit the measured data to a dedicated server located at a distance from the measurement point.

Experimental results

The results from the measurements of EMR intensity at two characteristic points of SM are presented and analysed. One is located in the ideal centre of Sofia, a building of SM located in 5, Serdika Street, and the other one is located in Bankya District. The first measurement point is packed with a lot of administrative buildings and radiating antennae, accordingly, and the other point is characterised by low construction and quite diverse relief, but also by a basic mobile operator station in its immediate vicinity.

Measurements on the territory of Bankya District, in a private house, in two premises on the second floor of the house, located about 22 m away from another

house, with antennae of a basic mobile operator station assembled on the roof. The measurements were carried out by mobile equipment "SPECTRAN HF 6060", in the range of 700÷2 500 MHz, using antenna of the HyperLOG 7060 type, over the time interval between 10:30 and 11:30 h a.m., in October, in dry weather and air temperature of about 25º C.

The results from the measurements of the intensity of the energy flow in the premises – sitting room on the second floor of the house located in 10, Radost Street, are presented on the following graph which shows the measured values in microwatts per square centimetre for the time interval between 11:17 and 11:35 h a.m., i.e. measurement in the course of 18 minutes.
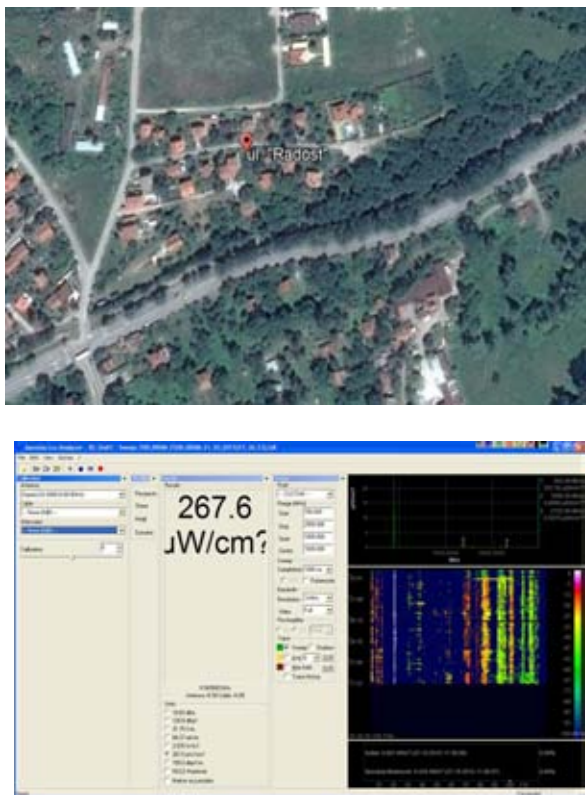
Fig. 1. Satellite photo of the territory of Bankya District, where the measurements of the density of EMR energy flow were carried out and the results of the measurements on a screenshot of the laptop to which the measurement device "SPECTRAN HF 6060" was connected

The results on the laptop's screen show the maximal levels of the irradiated power for the individual frequencies during the measurements. Maximum measured EMR levels are of about 267 µW/cm^2 at frequency of 943 MHz are observed.

The next graph, Fig. 2, shows the averaged values of the results from the measured density of the energy flow in the premises – sitting room on the second floor of the house, in µW/cm^2 over time interval between 11:17 and 11:35 h a.m.
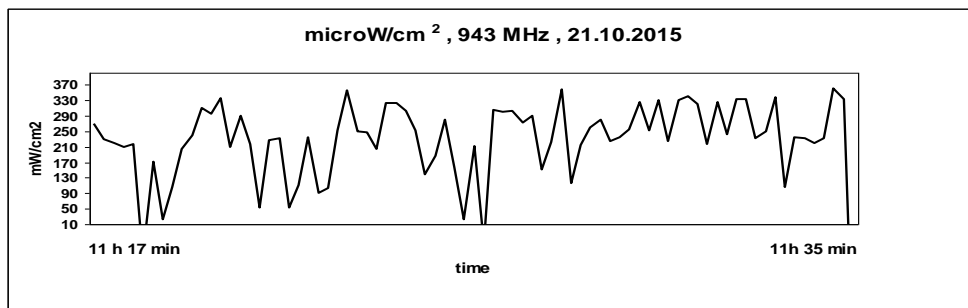
Fig. 2. Averaged values of the results from measuring the density of EMR energy flow over this time period

It may be seen that the average level of irradiated power is about 244.22 µW/cm^2, which is more than 20 times greater than the norm allowed by standard, 10 µW/cm^2. Of this order and a little bit greater were also the values measured on the terrace of the same floor. This point is located about 22–25 meters off the basic station's irradiating antennae, measured along a direct line.

Measurements in the ideal centre of Sofia, in the building of SM in 5, Serdika Street, in front of the office of Sofia's Chief Architect.

Using the mobile equipment Narda AMB 8057-3, which provides for continuous autonomous control of electromagnetic radiation, long-lasting uninterrupted measurements of EMR from various sources in the frequency range of 110 kHz ÷ 7 GHz were carried out, including on business days and holidays, for a period of nearly four months (March – June). Date transmission to the place where the server was located, its recording and storage in the database was performed automatically. The results from the measurements in the database contain information about the characteristics, the distribution by frequency and the location of the measurement point (coordinates of the measurement points in GIS).

Some results from EMR measurements are shown on the next Fig. 3 which illustrates clearly the characteristic course of the changes in EMR intensity over the entire frequency range depending on the intensity of the irradiating antenna and the number of used mobile communication units.
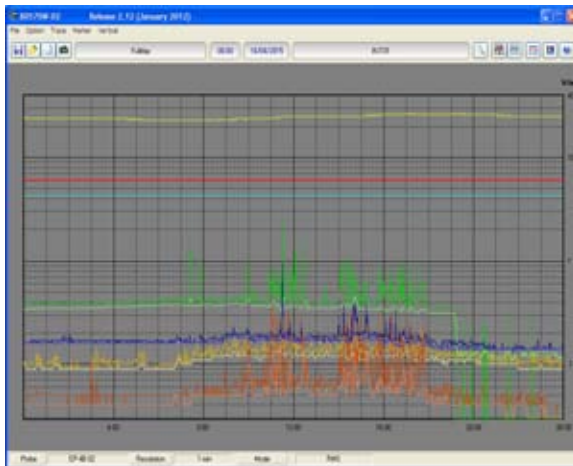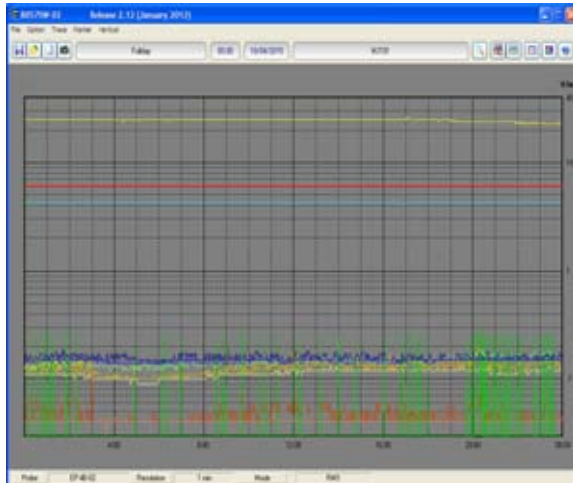
Fig. 3. Results from the measurements carried out by the autonomous measurement device Narda AMB 8057-3. Data from 24–hour continuous measurements for one holiday and one normal business day is presented.

The measured values of electromagnetic fields in the range 110 kHz ÷ 7 GHz for HOLIDAYS feature smooth constant course for all frequencies, much below the admissible field value of 6 V/m, while in the time period between 07:00 h a.m. and 06:00 h p.m. for BUSINESS DAYS, the expected course is observed, with increased EMR intensity in the intervals between 02:00 and 06:00 h p.m. The analysis of the data shows that, irrespective of the increased EMR levels for business days, no cases of exceeding or even nearing the maximal allowed norm for this frequency range are observed.

Conclusion

The urbanization degree of a given territory, the number of irradiation antennae, their power and location has material influence on EMR intensity and BN level. The cases of exceeding the maximal allowed norms according to BSS in some individual points of SM are rather an exception. The primary reasons for available single cases of exceeding the allowed norms may be discrepancies during the approval of the city regulation plan for the respective district and lack of coordination between the construction supervision bodies and the bodies controlling the assembly of new irradiating antennae.

These results and conclusions prove the need of development of EMR evaluation and optimization methods in urbanized environments. Based on this, it is necessary to undertake construction of a System for Monitoring and Control of Electromagnetic Pollution on the Territory of SM using autonomous stations of the type of Narda AMB 8057-3, connected to a GIS. This system will provide data to State and Municipal bodies enabling to control and manage EMR and BN, as well to inform the citizens about environmental EMR.

The basic components of this System for Monitoring and Control of Electromagnetic Pollution on the Territory of SM aiming to manage the information about environment, to plan and develop infrastructure and to provide for sustainable development of Sofia include:

- Sufficient number of available ground-based stations of the type of the mobile equipment NARDA AMB 8057, located in different points of SM (one for each metropolitan district may be envisaged), operating in a connected mode and measuring within the frequency range of 10 Hz ÷ 7 GHz;

- The data from the antennae shall be recorded automatically on a special server in digital form and an option for their visualization for any chosen time interval in the required form shall be provided;

- A dedicated database referred to the GIS, with definite modes and access levels intended to inform the public, as well as to be used by the Municipal and State bodies during the preparation, planning and taking of different managerial decisions;

- Composing of maps of SM territory, referred to GIS, on the overall and by individual districts, presenting the distribution of EMR and BN levels over a definite period, using dedicated software developed for the purpose;

- Composing of maps of SM territory, referred to GIS, with forecast EMR levels, based on recorded data about the location and the powers irradiated by the SM-licensed antennae of firms and State organizations using the dedicated software;

- Establishment of a control centre furnished with data collection server; management of the station network; database in GIS system; preparation of information for the population; preparation of information and analyses on the request of Municipal and State bodies; provision of information about EMR levels to SM for a remuneration on the request of external clients.

- Preparation for application of a version of this system for the needs of other Municipalities on the territory of the country.

The System for Monitoring and Control of Electromagnetic Pollution on the Territory of SM should provide for development, adaptation and superstructuring, accounting for future recommendations and requirements of the EU and other international organizations, such as the World Health Organization (WHO), the International Commission on Non-Ionizing Radiation Protection (ICNIRP).

References

1. Contract № ДН 07/19/2016, Project „Methods for Evaluation and Optimization of Electromagnetic Radiations in Urban Areas".
2. Getsov, P., D. Teodosiev, E. Roumenina, M. Israel, G. Mardirossian, G. Sotirov, S. Velkoski, P. Gajesek, D. Simunic, and K. Iliev. Development of a Strategy and Methods for Monitoring of Electromagnetic Pollution in the Environment of the Western Balkans, Scientific results of the SEE-ERA.NET Pilot Joint Call, Edited by J. Machačová, K. Rohsmann, 2009, 95–101. ISBN 978-3-200-01567-8
3. Baltiiski, P., I. Iliev, B. Kehaiov, V. Poulkov, and T. Cooklev. Long-Term Spectrum Monitoring with Big Data Analysis and Machine Learning for Cloud-Based Radio Access Networks, Wireless Personal Communications, Springer, http://link.springer.com/article/10.1007/s11277-015-2631-8, may 2015.
4. Manassas, A., A. Boursianis, and T. Samaras. Continuous electromagnetic radiation monitoring in the environment: analysis of the results in Greece, Radiation Protection Dosimetry, Oxford Journals, 2012.
5. Joyner, K., M. J. Van Wyk, and J. T. Rowley. National surveys of radiofrequency field strengths from radio base stations in Africa, Radiation Protection Dosimetry, 2014, 158, 3, 251–62.

6. Mahfouz, Z., L. Verloock, W. Joseph, and E. Tanghe, Comparison of temporal realistic Telecommunication base station exposure with worst-case estimation in two countries, Radiation Protection Dosimetry, 2013, 1–8.
7. Gotsis, A., N. Papanikolaou, and D. Komnakos. Non-ionizing electromagnetic radiation monitoring in Greece, Annals of telecommunications, Springer, February 2008, 63, 1–2, 109–23.
8. Röösli, M. et al.. Statistical analysis of personal radiofrequency electromagnetic field measurements with nondetects, Bioelectromagnetics, 2008, 29.

НЯКОИ ОСОБЕНОСТИ В РАЗПРЕДЕЛЕНИЕТО НА ЕЛЕКТРОМАГНИТНОТО ЗАМЪРСЯВАНЕ НА ТЕРИТОРИЯТА НА СТОЛИЧНА ОБЩИНА

Т. Андреева-Нешева, Д. Теодосиев, И. Илиев

Резюме

Представени са някои резултати от измервания на електромагнитните излъчвания, в честотния диапазон от 110 kHz до 7 GHz на територията на Столична община и са дискутирани наблюдавани отклонения в измерените нива, от приетите пределно допустими норми. Предложено и аргументирано е разработването на методи за оценка и оптимизиране на електромагнитните излъчвания в урбанизирани среди и изграждането на система за мониторинг на ЕМИ и ФШ в силно урбанизирани територии, като Столична община.

MAPPING OF FOREST COVER CHANGE BY POST-CLASSIFICATION COMPARISON AND MULTITEMPORAL CLASSIFICATION OF SPOT DATA – A BULGARIAN CASE STUDY

Petar Dimitrov[1], Pontus Olofsson[2], Georgi Jelev[1], Ilina Kamenova[1]

[1]*Space Research and Technology Institute – Bulgarian Academy of Sciences*
[2]*Dept. of Earth & Environment, Boston University*
e-mail: petarkirilov@mail.bg, gjelev@space.bas.bg

Abstract

The paper presents the results of forest cover change mapping in two study areas in Bulgaria (in mountainous and plain-hilly terrain) for period of about 20 years. A comparison was made of two approaches for classification of multitemporal SPOT HRV/HRVIR data with 20 m spatial resolution. The first approach was the post-classification comparison, i.e. pixel-by-pixel comparison of forest/non-forest maps produced by separate classifications of the images from the two ends of the time period. The second approach was a direct multitemporal classification of an image stack comprised of the two-date image data. Following international guidance, instead of counting pixels in the map to obtain the area of forest loss and gain, the areas were estimated by applying an unbiased estimator to sample data collected by stratified random sampling. The map was used to stratify the study areas. Producer's, user's and overall accuracy were also estimated using the sample data. A comparison of accuracy and area estimates, and confidence intervals of estimates, showed that the map produced by direct multitemporal classification was more accurate. It yielded consistently higher class-specific accuracies than the map made by post-classification comparison. As expected, the accuracies of the change classes – forest disturbance and reforestation – were significantly lower than that of the stable classes regardless of the change detection approach. Finally, practical issues and guidelines for future forest change detection studies were discussed.

Introduction

Bulgarian forestry and agriculture have been experiencing transformations for several decades as a result of the transition to market economy, demographic processes, and the adoption of the EU Common Agricultural Policy (CAP). These transformations are accompanied with change in land use and land cover. Abandonment of pastures in mountainous and semi-mountainous regions and their natural reforestation were widespread in 1990s [1]. More recently, the opposite changes may be occasionally observed, namely that young forests are cleared and land is back transformed into pastures, a process which is stimulated by the CAP payments for maintaining pastures in good condition. In the meantime illegal logging increases as well as the development activity in forest areas (e.g. construction of new

ski resorts and facilities) [2]. In addition to these factors, forest disturbance due to wildfires and pest infestation are not uncommon and may affect significant area [3–5].

Mapping of areas of forest cover gain and loss in Bulgaria using traditional forest inventory data is practically impossible because of the lack of archived georeferenced data. Remote sensing is an alternative data source, which provides both high spatial resolution and historical perspective. In this context, the study has been initiated to evaluate the possibilities of using 20 m SPOT HRV/HRVIR imagery for change detection in Bulgarian forests. It was carried out as a pilot study in two test areas and the aim was to provide guidelines for future applications of SPOT data for forest change detection at country level. The SPOT data were selected because of the long image archive dating back to 1980s and the higher spatial resolution as compared to Landsat.

A major concern in every forest change mapping effort is the selection of digital change detection method. A variety of digital change detection techniques utilising satellite image data has become available in the recent decades to monitor ecosystem changes, including forest cover gain and loss [6]. Although sophisticated methods to continuously detect changes over a period of time have been proposed (e.g. [7]) the bi-temporal change detection, i.e. using an image from each end of the time interval of interest, is still widely used when dense image time series cannot be compiled. Two of the most common bi-temporal change detection methods are post-classification comparison (PCC) [8, 9] and multitemporal classification (MTC) [10–12]. The first method involves application of spectral classification on each image independently and then pixel-by-pixel comparison to detect changes in land cover type [6]. The second method applies spectral classification on an image stack, combining data from both dates. The relative performance of the two methods has rarely been evaluated. One example is Mas [13] who compared quantitatively the two methods applying them to Landsat MSS data to map changes in five land cover classes in a tropical region. He found that the post-classification comparison produced significantly higher accuracy than multitemporal classification did. On the other hand, the team led by Olofsson [14], in a comparison of forest cover change maps across Romania, reported considerably lower accuracy due to large commission errors in the map generated by post-classification comparison compared to multitemporal classification. Using simulated data Almutairi and Warner [15] showed that the two methods perform very similarly with the multitemporal classification approach being slightly more accurate.

The objectives of this study are: 1) to assess how accurately forest cover change in Bulgaria can be mapped using 20 m SPOT HRV/HRVIR imagery, and 2) to evaluate the relative performance of post-classification comparison and multitemporal classification as change detection methods. The paper should be regarded as a Bulgarian case study and we do not try to generalize our results regarding the two change detection methods over other regions or image types.

Study area

Two study areas with contrasting physiography and land use patterns are selected (Fig. 1). They represent wide range of conditions in terms of topography, forest types and land-use patterns and are representative for a large part of Bulgaria.
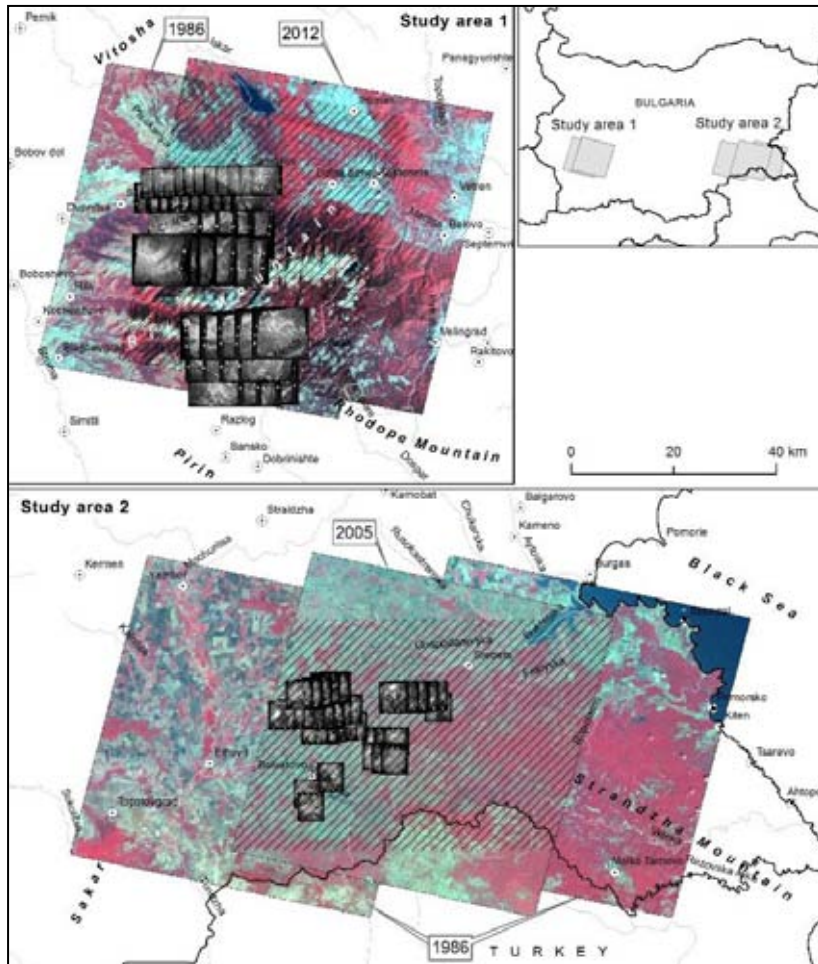
Fig. 1. Maps of the two study areas showing the SPOT imagery
and the panchromatic aerial photographs used in the study.
The change detection was carried out for the hatched areas.

Study area 1 covers the *Rila* Mountains (2925 m a.s.l.) and the surrounding basins. It features high relief, extensive natural coniferous forests and land use dominated by forestry, nature conservation, tourism, and agriculture. The main

species in the coniferous forests are Scots pine, Norway spruce, and Mountain (dwarf) pine. Steep slopes and deeply incised valleys are characteristic for Study area 1 and allow for testing the change detection algorithms in complicated topographic setting. The main factors for the forest change in the area are timber industry, infrastructure and development projects, including for ski resorts, natural regeneration of trees on abandoned pastures, and wildfires.

Study area 2 is located in the western part of the *Strandzha* Mountains where hilly relief predominates. Forests are mostly broadleaved (Turkey oak, Hungarian oak, *Quercus polycarpa*, etc.) with some sparse coniferous plantations. Agricultural lands are widespread and dominate in the west part of Study area 2. The changes in the forest cover are mostly the result of timber industry (logging and establishment of forest plantations), forest succession on abandoned land, and wildfires. The eastern part of the area is characterized by extensive forests while the western part is more fragmented with land use dominated by agriculture and settlements.

Data and methods

SPOT data

In each study area, changes were investigated using two SPOT images – a base image dated 1986 and a second image dated 2012 (Study area 1) or 2005 (Study area 2) (Table 1). To cover the entire Study area 2, two SPOT scenes were needed in 1986. The scenes were acquired at the same time by the two SPOT 1 HRV instruments. Scenes acquired in the end of the summer (August or September) are used because in this season forest can be easily distinguished from most grasslands and crops. In spring, this discrimination is challenging, particularly for the broadleaved and young coniferous stands. The SPOT data were provided at Level 1A and were orthorectified in ERDAS IMAGINE using ASTER GDEM v2. Firstly, the three base scenes were processed using ground control points (GCP) taken from the 2010 Digital Orthophoto Map of Bulgaria. In Study area 1, GCP measured in the field were also used to check the reliability of the orthophoto map in mountainous area. The number of control and checkpoints and the error of orthorectification are shown in Table 2. The total error for each image is less than one pixel. Secondly, the "modern" scenes in the two study areas were orthorectified using the same (SPOT) sensor model in ERDAS IMAGINE and the same DEM data but the control points were automatically generated by the image-to-image matching module AutoSync and the already corrected base scenes as a reference. Checkpoints were not used and the accuracy not tested. All images were resampled to 20 m using the nearest neighbour method. The SWIR band of the SPOT 4 image (Study area 1) was not used in the analysis.

Table 1. SPOT scenes used in the study

SPOT scene ID	Date	Satellite	Study area
10882658609070929252X	7 Sept 1986	SPOT 1	Study area 1
40892651209240831232I	24 Sept 2012	SPOT 4	Study area 1
10952658608180913511X	18 Aug 1986	SPOT 1	Study area 2
10962658608180913492X	18 Aug 1986	SPOT 1	Study area 2
20962650508120915521X	12 Aug 2005	SPOT 2	Study area 2

Table 2. Results from the orthorectification of the base SPOT scenes. The Root Mean Square Error in pixels for the x-axis (RMSEx), for the y-axis (RMSEy), and the total error (RMSEt) are shown. Errors are calculated using the checkpoints.

SPOT scene ID	Study area	Number of control points	Number of check points	RMSEx	RMSEy	RMSEt
10882658609070929252X	Study area 1	50	8	0.4342	0.3371	0.5496
10952658608180913511X	Study area 2	32	7	0.4663	0.4391	0.6405
10962658608180913492X	Study area 2	33	7	0.2470	0.2240	0.3334

As part of preprocessing the SPOT data, DN-values were transformed to top of the atmosphere (TOA) reflectance using Equation (1):

$$(1) \qquad \rho_\lambda = \frac{\pi \times L_\lambda \times d^2}{ESUN_\lambda \times \cos \theta_S},$$

where L_λ is the spectral radiance (W/(m^2 sr μm)), d is the Earth-Sun distance for the image acquisition date (astronomical units), $ESUN_\lambda$ is the solar exoatmospheric spectral irradiances for each band (W/(m^2 μm)), and θ_s is the Sun zenith angle. The spectral radiance L_λ for each band is calculated using the gain and offset values provided with the image metadata. There one can find also the $ESUN_\lambda$ values for the SPOT bands. After the calculation of the TOA reflectance values the radiometric inconsistency between the two 1986 scenes in Study area 2 were much reduced (Fig. 2) and they were mosaicked without further relative normalisation.

Auxiliary image data

High resolution aerial photos were used as a reference data and for collecting training and test datasets for the change detection procedure. To characterize the latter time point, we used the Digital Orthophoto Maps of Bulgaria for 2006 and 2010. The data were available for the entire territory of the two study areas. They represent image tiles in true colour and sub-meter spatial resolution.
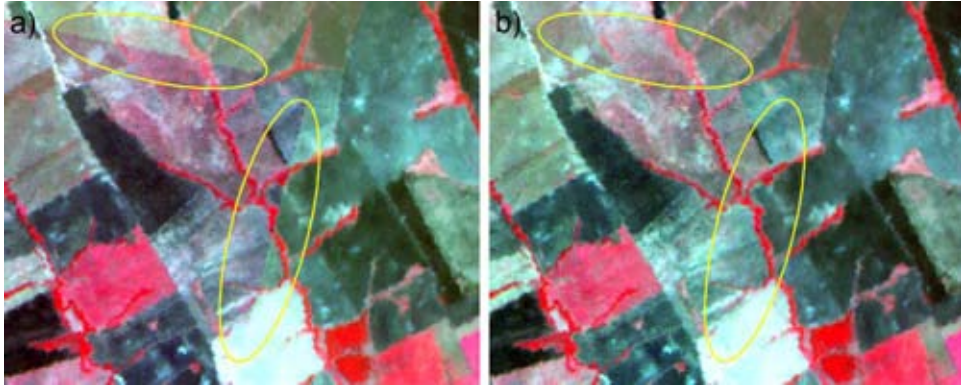
Fig. 2. Excerpts from mosaics of the two 1986 scenes for Study area 2 produced by using a) raw DN data and b) top of the atmosphere reflectance data. The seam line is highlighted.

To characterize the base time point we used archive black and white aerial photographs acquired in 1988 (Study area 1) and 1986 (Study area 2). Unfortunately, these data were available only for part of the territory of the two study areas. The aerial photographs were orthorectified in ERDAS IMAGINE. The coverage of the orthorectified images is shown in Fig. 1. The accuracy of the orthorectified images is summarized in Table 3.

Table 3. Accuracy statistics of the orthorectified black and white aerial photographs

Study area	Photogrametric block number/year	Number of frames	Number of checkpoints	RMSE (m)		
				X	Y	Z
Study area 1	1/1988	11	20 (16)*	2.19	2.47	5.13
	2/1988	21	11	1.49	1.82	6.99
	3/1988	12	17	3.31	4.28	9.72
Study area 2	1/1986	18	16	0.83	1.36	3.09
	2/1986	6	7	0.66	1.17	1.69
	3/1986	6	4	0.58	1.07	2.73
	4/1986	2	2	0.98	0.34	3.13

* the number of checkpoints on the z axis is shown in parenthesis.

Methods

Image classification was selected for the change detection because this method not only can detect changes in the scene but also characterize the type of change. A simple classification scheme with four classes of land cover transition was used: forest disturbance, reforestation, permanent forest, and permanent non forest. The image classification technique is used in two ways in change detection studies. The first approach is the post-classification comparison where the image for each

date is classified separately to produce forest/non forest maps; the two maps are then compared to produce the change detection map. The second approach involves stacking the two images (from the beginning and the end of the period) and classifying them as a single dataset; the change detection map is thus produced in one step. Regardless of the approach the SPOT image data were classified using the Support Vector Machines (SVM) method. The model parameterization and the classification were applied in EnMAP-Box software [16]. The program was set to search for the optimal values of the Gaussian RBF Kernel parameter g and the regularization parameter C. The search range was set initially to 0.001÷1 500 and expanded if the number of support vectors was small. The training procedures for the two change detection approaches are outlined in the next sections.

Approach 1: Post-classification comparison

To train the classifier we used a set of pixels collected in two steps. First, each study area was stratified into forest and non-forest using the CORINE Land Cover dataset and 1 000 random points were generated in each stratum. The type of land cover (forest vs. non-forest) for each point and each date was determined through visual interpretation of the auxiliary high resolution image data and the SPOT imagery. To assign the point to one of the classes we visually interpreted the land cover in a square plot with size 40 m centred at the point. The plots which are at the border of forest and non-forest patches were discarded. Using this sample of pixels we performed preliminary classifications and determined regions/land cover types which were incorrectly classified. Based on this knowledge we manually added more points in these problematic regions/land cover types. The reason for this approach is that in order to distinguish between spectrally similar classes the SVM is focusing on the training samples that lie at the edge of the class distributions [17]. That is why we need to provide more training samples representing ambiguous land cover types. The final number of training samples used in each classification is shown in Table 4.

Table 4. Number of training pixels per class for the four SPOT image classifications

Study area	Date (year)	Forest	Non forest
Study area 1	1986	928	832
	2012	1018	764
Study area 2	1986	707	1002
	2005	796	937

To produce the forest/non-forest maps we used the entire sample to train the classifier (Table 4). Then, the same data were used for assessing the accuracy of the individual forest/non-forest maps by applying 10-fold cross validation. For each date and study area we made 10 classifications each time using 90 % of the available

sample for training and the rest 10 % for validation. Pixels used for accuracy assessment are not repeated between iterations. We then calculated the overall accuracy, Kappa, User's accuracy and Producer's accuracy as an average of these measures from the ten iterations.

Finally the forest/non-forest maps from the two time points were compared and forest change maps produced for each study area. The maps were further processed to eliminate class patches smaller than 1 ha. In this way many forest disturbance or reforestation patches, which most probably resulted from miss-registration errors were removed. To estimate the area and accuracy of map categories of the change map, an independent sample was selected by stratified random sample with the strata defined by the map classes. A total of 150 sample units were used in each study area. The number was subjectively chosen and the main criterion was the time needed to collect the reference data for each classification approach and study area (600 sample units in total). The overall sampling intensity was distributed between the classes using Equation (2) [18]:

$$(2) \qquad n_i = p_i \times \left(\frac{n}{2}\right) + \left(\frac{1}{k}\right) \times \left(\frac{n}{2}\right),$$

where n_i is the number of points for class i, p_i is the proportion of the mapped area of class i, n is the overall sampling intensity (in this case n = 150), and k is the number of classes (in this case k = 4). Error-adjusted estimates of the areas of the thematic classes and map accuracy statistics (including 95 % confidence intervals) were produced following the recommendations of Olofsson et al. [14, 19].

Approach 2: Multitemporal classification

In the multitemporal classification, training data for the four classes – forest disturbance, reforestation, permanent forest, and permanent non-forest – were needed. As the territories occupied by the first two classes are small (and unknown) it was not feasible to distribute training pixels randomly. To guaranty that sufficient number of pixels was selected to characterise the small classes we searched the entire study areas systematically and selected training pixels manually. The study areas were covered with 10 km × 10 km grid and within each cell we tried to select a minimum of 4 (maximum 8) pixels from each class. In fact, several cells possessed no forest disturbance or reforestation patches which could be visually identified. As in Approach 1, preliminary classification was performed and additional training samples were added after examining the results. The numbers of training pixels used in Study area 1 were 118, 152, 96, and 116 for permanent forest, permanent non-forest, forest disturbance, and reforestation respectively. In Study area 2 the corresponding numbers were 125, 128, 72, and 102. Similarly to Approach 1, the forest change maps were post-processed in order to remove patches smaller

than 1 ha. The accuracy of the forest change maps was assessed using stratified random sample with the strata defined by the map classes. 150 points (different from those of Approach 1) were used in each study area. The same methods as specified above were used to produce the error-matrix, area estimates, and the accuracy estimates.

Results

Approach 1: Post-classification comparison

The results from the accuracy assessment of the forest/non-forest maps (Table 5) show that the SVM classifier produced very accurate forest/non-forest maps in all four cases. The overall accuracy is between 95 % and 97 % for different dates and study areas. The forest change maps produced by comparison of these forest/non-forest maps are shown in Fig. 3 and the error matrices for the two study areas are presented in Table 6. The overall (error-adjusted) accuracy of the forest change maps is 85 % and 92 % for Study area 1 and Study area 2 respectively. These values are also relatively high, even though they are, as expected, lower than the accuracies of the individual forest/non-forest classifications. The class accuracies, however review more complex picture. The User and Producer Accuracies of the "Permanent forest" and "Permanent non-forest" classes are generally high in the two study areas – between 87 % and 97 %. However the User Accuracy of the change classes – "Forest disturbance" and "Reforestation" is very low, ranging from 50 % to 65 % and the Producer Accuracy is even lower (between 26 % and 52 %). This indicates that the PCC failed to accurately map the forest change. More severe is the problem in Study area 1 where forest disturbance is confused with permanent non-forest and reforestation is confused with both permanent land cover classes (Table 6). Similar is the situation in Study area 2, but here reforestation is mainly confused with permanent non-forest. In fact Producer Accuracies of the change classes are not significant except for "Reforestation" in Study area 2. The high errors for the change classes are likely to result in strong bias of the mapped class areas and this is suggested also from the estimated (error-adjusted) areas, which deviate markedly from the mapped areas (Table 7). It should be pointed out that the confidence intervals of the estimated areas are very wide, which make the estimates not very useful. For the forest disturbance class the estimated areas are not significantly different from 0 (i.e. the margin of error is ≥ 100, Table 7). The error-adjusted areas of forest change (Table 7) show that reforestation prevails over forest disturbance in both study areas. The reforested area in Study area 1 is estimated to 277 km^2 (11 % of the area), while in Study area 2 it is estimated to 212 km^2 (7 % of the area).

Table 5. Results from the 10-fold cross validation of the four forest/non-forest classifications

Study area/Date	Overall accuracy (%)	Kappa (%)	User Acc.		Prod. Acc.		Average number of test pixels per iteration		
			F	NF	F	NF	Total	F	NF
Study area 1									
1986	94.6	89.1	94.9	94.5	94.9	94.2	176	93	83
2012	96.1	91.9	95.6	96.7	97.7	94.0	178	102	76
Study area 2									
1986	97.4	94.5	97.3	97.5	96.3	98.1	171	71	100
2005	97.4	94.7	97.2	97.7	97.1	97.5	173	80	94

Table 6. Accuracy assessment of the post-classification comparison (Approach 1) change maps of the two study areas. The error matrices are expressed as estimated area proportions. Map categories are the rows while the reference categories are the columns. Accuracy measures are presented with a 95% confidence interval. Wi = proportion of area of class i in the map, ni = number of sample pixels of class i.

	Permanent forest	Permanent non-forest	Forest disturbance	Refores-tation	W_i	n_i	User Acc.	Prod. Acc.
Study area 1: Overall accuracy = 0.854 ± 0.058								
Permanent forest	0.480	0.009	0.000	0.046	0.536	58	0.897±0.079	0.927±0.039
Permanent non-forest	0.008	0.328	0.016	0.024	0.376	47	0.872±0.096	0.938±0.057
Forest disturbance	0.005	0.000	0.006	0.001	0.011	20	0.500±0.225	0.258±0.946
Reforestation	0.025	0.012	0.000	0.040	0.077	25	0.520 ±0.2	0.363±0.404
Study area 2: Overall accuracy = 0.918 ± 0.042								
Permanent forest	0.248	0.007	0.007	0.007	0.269	39	0.923±0.085	0.925±0.042
Permanent non forest	0.000	0.624	0.000	0.029	0.653	67	0.955±0.050	0.971±0.025
Forest disturbance	0.003	0.001	0.007	0.000	0.011	20	0.650±0.214	0.504±0.903
Reforestation	0.017	0.011	0.000	0.039	0.067	24	0.583±0.201	0.521±0.441

Fig. 3. Forest change maps of Study area 1 (1986 – 2012) and Study area 2 (1986 – 2005) produced by post-classification comparison. Classifications are cleaned-up removing patches smaller than 1 ha.

Table 7. Class areas according to change maps (Mapped areas) and estimated areas with 95 % confidence intervals (CI). Margin of error is the ratio of confidence interval to estimated area expressed as percentage. Map bias is the difference of mapped and estimated area.

		Mapped area [km²]	Estimated area [km²]	Map bias [km²]	± 95% CI [km²]	Margin of error [%]
PCC	**Study area 1**					
	Permanent forest	1336.9	1293.0	44	121	9
	Permanent non forest	938.4	872.6	66	107	12
	Forest disturbance	27.8	53.9	–26	56	104
	Reforestation	193.4	277.1	–84	127	46
	Study area 2					
	Permanent forest	755.7	753.9	2	74	10
	Permanent non forest	1834.1	1804.4	30	105	6
	Forest disturbance	30.3	39.1	–9	39	100
	Reforestation	189.1	211.8	–23	108	51
MTC	**Study area 1**					
	Permanent forest	1269.5	1241.1	28	121	10
	Permanent non forest	976.5	912.7	64	117	13
	Forest disturbance	27.3	63.1	–36	61	97
	Reforestation	223.2	279.6	–56	111	40
	Study area 2					
	Permanent forest	861.2	897.8	–37	117	13
	Permanent non forest	1766.2	1703.5	63	133	8
	Forest disturbance	33.8	71.3	–38	68	95
	Reforestation	148.1	136.6	12	61	45

Approach 2: Multitemporal classification

Figure 4 shows the forest change maps resulting from the multitemporal classifications. Visually, results are very similar to those obtained with the post-classification comparison approach. A closer look reviews that, in general, forest disturbance and reforestation patches identified by the two approaches spatially coincide, at least for the largest patches. The overall accuracy of the forest change maps is 87 % and 91 % for Study area 1 and Study area 2 respectively (Table 8). These figures are similar to those for the PCC change maps. As may be expected, the pattern of class accuracies for the MTC is the same as that for the PCC with the accuracy of the permanent land cover classes being higher than the accuracy of the change classes. The User and Producer Accuracies of the "Permanent forest" and "Permanent non forest" classes are between 85 % and 96 %. The MTC approach performed better compared with the PCC in terms of accuracy of the "Reforestation" class (from 54 % to 80 %), the measures being significant for both study areas (Table 8).
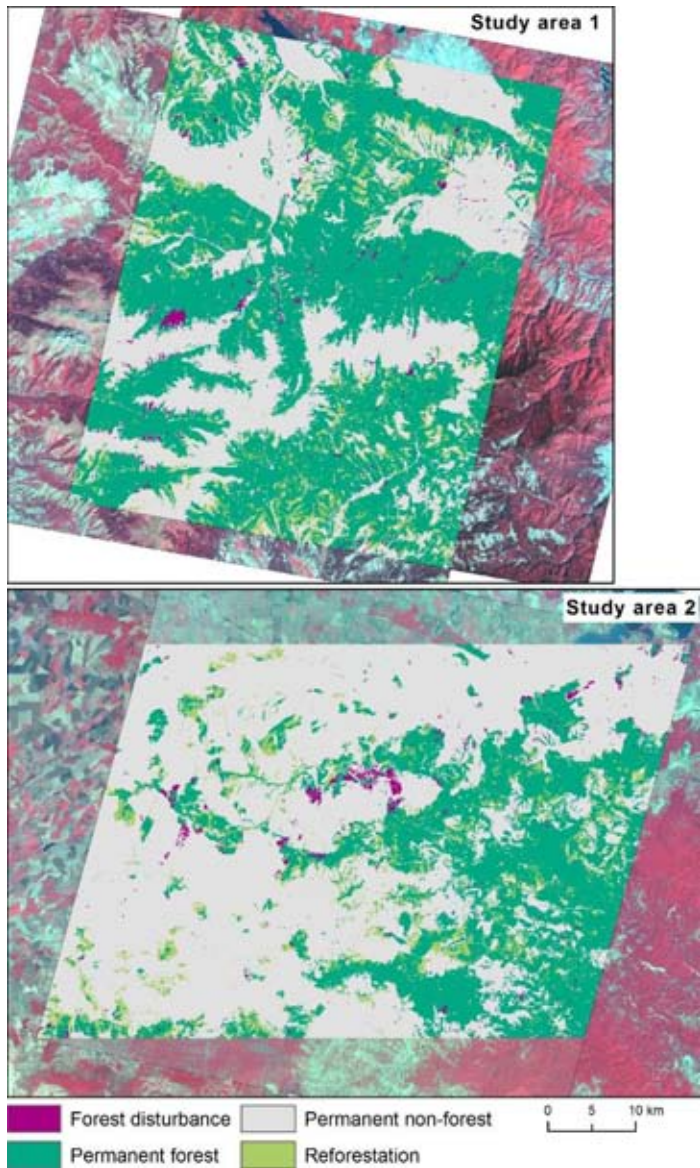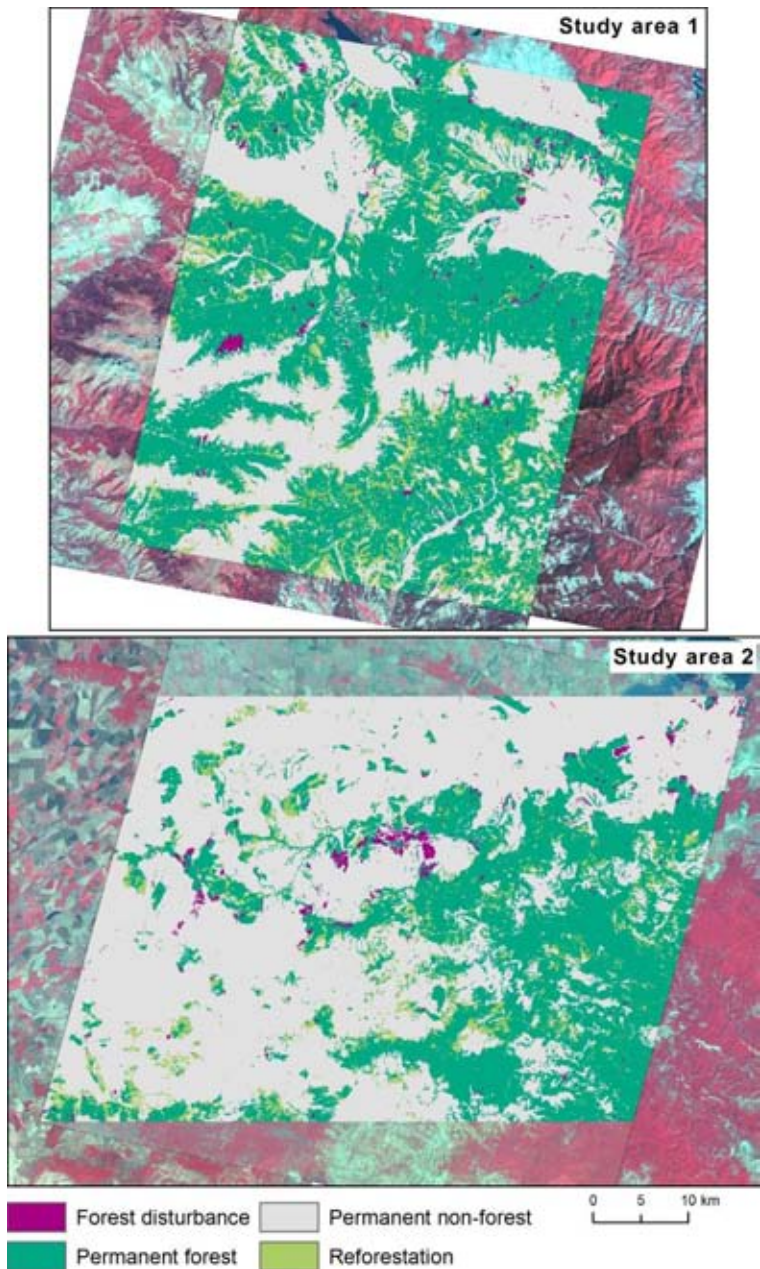
Fig. 4. Forest change maps of Study area 1 (1986–2012) and Study area 2 (1986–2005) produced by multitemporal classification. Classifications are cleaned-up removing patches smaller than 1 ha.

Table 8. Accuracy assessment of the multitemporal classification (Approach 2) change maps of the two study areas. The error matrices are expressed as estimated area proportions. Map categories are the rows while the reference categories are the columns. Accuracy measures are presented with a 95 % confidence interval. W_i = proportion of area of class i in the map, n_i = number of sample pixels of class i.

	Permanent forest	Permanent non forest	Forest disturbance	Reforestation	W_i	n_i	User Acc.	Prod. Acc.
Study area 1: Overall accuracy = 0.867 ± 0.057								
Permanent forest	0.464	0.009	0.009	0.027	0.509	57	0.912 ±0.074	0.933 ±0.054
Permanent non forest	0.024	0.334	0.008	0.024	0.391	48	0.854 ±0.101	0.914 ±0.060
Forest disturbance	0.002	0.001	0.008	0.000	0.011	20	0.750 ±0.195	0.324 ±0.877
Reforestation	0.007	0.021	0.000	0.061	0.089	25	0.680 ±0.187	0.543 ±0.342
Study area 2: Overall accuracy = 0.912 ± 0.049								
Permanent forest	0.285	0.015	0.007	0.000	0.307	42	0.929 ±0.079	0.891 ±0.092
Permanent non forest	0.029	0.580	0.010	0.010	0.629	65	0.923 ±0.065	0.957 ±0.032
Forest disturbance	0.004	0.000	0.008	0.000	0.012	20	0.700 ±0.206	0.331 ±0.836
Reforestation	0.002	0.011	0.000	0.039	0.053	23	0.739 ±0.183	0.801 ±0.350

Interestingly, the MTC approach confirm that the reforestation in Study area 1 tend to mix with both stable classes, while in Study area 2 it is confused with the permanent non-forest (Table 8). Forest disturbance is, again, the class that is most difficult to map. Even though the results are still unsatisfactory, the MTC performed better than PCC for that class, with User Accuracies over 70 % and Producer Accuracies of 32 %. Note, however that Producer Accuracy are again not statistically significant. The estimated areas of forest change classes are significant (Table 7) but the confidence intervals are quite wide especially for the "Forest disturbance" class. The MTC approach confirm that reforestation prevails over forest disturbance in both study areas. The reforested area in Study area 1 is estimated to 280 km^2 (11 % of the area), while in Study area 2 it is estimated to 137 km^2 (5 % of the area). The disturbed forest area is estimated to 63 km^2 in Study area 1 and to 71 km^2 in Study area 2.

Discussion and conclusions

With this study, we attempted to test the possibility for automatic change detection and mapping of forest cover change in Bulgaria through satellite image processing. Using satellite imagery for change detection has the advantage of large area coverage but with the drawback of results never being perfect. Classification errors are inevitable in all classifications of satellite data into land surface features but the characteristics of the Bulgarian landscape with its hilly, patchy and varying terrain make it especially difficult to map. The relatively poor classification results for the forest cover change classes in this study proved this. As a result, instead of counting pixels in maps, areas need to be estimated by applying unbiased estimators to sample data of observations of reference conditions on the land surface [14]. *A priory* knowledge of the spatial distribution of disturbance and reforestation in the two study areas suggests that the SPOT-derived classifications managed to detect the main forest change events (for example stand replacing wildfires), but still significant misclassifications were observed. Thus, further improvement is needed to make satellite-derived change detection maps more useful, not only for stratification for reference data collection, but for other spatial analyses too. The main findings from this study and implications for monitoring the state of Bulgarian forests are discussed in the following paragraphs.

The SVM classification method has proven successful in classifying multispectral satellite data. It is particularly suitable for binary problems (like forest/non-forest maps) and, in contrast to the traditional parametric algorithms like maximum likelihood, can handle multimodal classes (e.g. non-forest). The results from Approach 1 suggest that SVM is, in most cases, very accurate in discriminating forest from other types of land cover in the two study areas (Table 5) and this can be attributed to a larger extend to the enhanced parameterization procedure implemented in EnMAP-Box [16], which automatically search for the optimal values of the parameters g and C. However, some misclassification may still be observed even in this "simple" binary classifications. For example in Study area 1 the meadows along mountain river courses stay green in autumn because of the great soil moisture. These wet meadows have similar spectral characteristics to the broadleaved forest and are partly misclassified. Most other grasslands can easily be distinguished from forest in this season because their vegetative growth had already ceased. Another problematic vegetation type is the *Juniperus sibirica* communities above the tree line, which are partly misclassified as forest. In Study area 2, we observed errors in the classification of vineyards. Despite these difficulties, the accuracy of the SVM forest/non-forest maps is generally very high (Table 5). As regards the overall accuracy of the forest cover change maps, these are also relatively high. For Study area 1 maximal accuracy of 87 % was achieved and for Study area 2 the corresponding value was 92 %. These are however overall map accuracies that are not of primary interest in a change detection study. Regarding the two change

classes results are worse. Irrespective of the change detection approach, the "Forest disturbance" class had maximal User accuracy of 75 % and maximal Producer accuracy of 32 % in Study area 1. In Study area 2 these values are 71 % and 50 % respectively. The "Reforestation" class had maximal User accuracy of 68 % and maximal Producer accuracy of 54 % in Study area 1. In Study area 2 these values are 74 % and 80 % respectively. These figures show that: 1) the maximal User accuracies for the two change classes that have been achieved are similar for the two study areas and 2) the Producer accuracy tend to be lower than the User accuracy; it is more variable and, in most cases, unsatisfactory. Similar results to those presented here have been reported in literature, for example Baumann et al. [20]. Their accuracies are, however, slightly higher.

The 20 m spatial resolution of the SPOT imagery used in this study seems to be fine enough to allow for even small patches of stand-replacing change to be portrayed in the images. This is important because in Bulgarian forests changes may occur in many small areas rather than in large clear cuts. This spatial resolution also allows for accurate mapping of forest stand borders even if the forest patches are fragmented and complex in shape (e.g. linear features along roads and rivers). Disadvantage of the SPOT imagery is that their precise georeferencing is challenging because of the difficulties in recognizing ground control points on the image. Table 2 shows that the accuracy of the orthorectified SPOT data is half a pixel. Thus the cumulative positional error produced when two imagery are overlaid is at the magnitude of one pixel. This made the detection of changes in the border areas of forest stands problematic and also leads to a large number of false change detections.

In this study, we used two simple and common change detection approaches, namely comparison of thematic maps from two different time points (post classification comparison) and multitemporal classification. From practical point of view, the first approach is probably to be preferred because it does not use training data for the two change classes. The multitemporal approach may appear more challenging because of the small area of forest change and the difficulty in collecting training data representing forest change. In short, binary classification of forest and non-forest is more straightforward than multitemporal classification where an additional time dimension is introduced. However, both approaches are technically feasible if SVM is used because this classification algorithm does not require large training dataset. Our comparison of the two approaches does not provide a definitive answer which of them is more accurate because the two experiments presented here are not directly comparable (different training data are used in each case including such collected manually). Instead we tried to follow literature-derived good practices (where available) to get the maximum performance of each procedure. For example, the advantage of Approach 1 is that large number of randomly distributed forest and non-forest training pixels can be collected in short time and we used between 700 and 1 000 per class (Kuemmerle et al. [9], for example, recommend using minimum

300 to 500 ground truth points per class). As expected, the class-specific accuracies are quite similar for the two stable land cover classes and considerably higher than the accuracy of the change classes. The multitemporal approach performed better in our study areas as evident by the consistently higher class-specific accuracies of the change classes, but still the Producers Accuracies of the "Forest disturbance" class were not significant. More interesting than accuracy is the uncertainty of the estimates of the areas of forest disturbance and regeneration. The margins of error for the area estimates, defined here as the ratio of the 95 % confidence interval to the area estimate, are smaller when using the change map created by multitemporal classification to stratify the study areas. The area estimates of forest disturbance were not significantly different from zero in neither study area when using the change map constructed by post classification comparison as stratification. All area estimates are rather uncertain with no margin of error being less than 40 % but this is consequence of the small sample sizes in addition to the accuracy of the stratifications. A larger sample would have resulted in higher precision. Note that the change map created by multitemporal classification used much smaller training dataset than that used in the post-classification example. It is fair to assume that had more training data been used with the multitemporal approach the difference in accuracy between the two approaches would have been even greater.

Most forests in Bulgaria are actively managed and regularly inventoried and these activities provide statistical data to assess forested area and its change at national scale. For example, the Executive Forest Agency (EFA) reported increase in forest area from 3.14 million ha to 3.72 million ha between 1965 and 2008 [21], which is an annual gain of 0.42 %. However, the effect of some processes like forest removal by illegal logging and forest establishment on abandoned agricultural land (mostly pastures) may not be well accounted for in the EFA reports. The abandoned pastures are not part of the lands managed by the State Forestry Enterprises and their rate of reforestation is thus poorly known. Other problem is that the inventory information is available mainly on paper [21] and geospatial technologies are not used effectively or not used at all. It is also widely acknowledged that the access of society and the research community to information about forest (e.g. metadata, methodology used to collect information, accuracy assessment of data, etc.) is difficult. Another source of information that can be used to evaluate the changes in forest area is the CORINE Land Cover (CLC) dataset [22]. A shortcoming of the CLC change layer is that the minimum area of detected changes is 5 ha as opposed to 1 ha in this study. The methods tested in this study may complement the existing sources of information and further improve our understanding of the rates of forest change in Bulgaria. Remote sensing data are currently not used for this purpose in a systematic way neither by the national or regional forest authorities nor by the research community. In this context, it is important to evaluate the possibilities and the limitations of using satellite data and estimation techniques for assessing forest change from the perspective of the Bulgarian conditions, i.e. forest types, forestry

practices, land use pattern, etc. By examining the performance of two change detection approaches on two contrasting study areas this paper tries to contributes to the development in that direction. Even though we used SPOT images, the same change detection techniques may be applied with free satellite data like Landsat and Sentinel-2. With the perspective of collecting longer time series of Sentinel-2 data in the coming years, the need of capacity building for processing these data became obvious. Efforts and networks as GOFC-GOLD, the establishment of good practice guidelines in forest change detection [12], and the availability of free software (e.g. BEEODA, EnMAP-Box) are valuable for the capacity building in Bulgaria.

Based on the experience gained in this study we can formulate several conclusions and guidelines in support of future studies:

• Comparing highly accurate forest/non-forest maps of the same area does not necessarily yield maps of forest cover change of high accuracy – or even accuracy that is significantly different from zero.

• The magnitude of area and accuracy estimates of forest/non-forest maps should not be used to communicate the accuracy and area bias of change maps constructed by post-classification comparison – an independent assessment of the change map is required.

• The multitemporal classification approach yielded maps that were more accurate and stratifications more efficient compared to the maps created by the post-classification comparison. However, the Producers Accuracy of the "Forest disturbance" class was not significant even with the MTC approach. Larger sample, than that used in this study, should be used to assess accuracy of classes with small areas as the "Forest disturbance" in our two study areas.

• Areas of forest disturbance and regeneration estimated by applying a stratified estimator to sample data were all significantly different from zero when the study areas were stratified using the change maps created by the multitemporal approach, even though just 150 sample units were collected.

• Multitemporal classification by non-parametric algorithms of forest change combined with stratified estimation can be easily implemented in open source software, and can help Bulgarian Universities, NGOs, and Government agencies in monitoring forest and collecting independent, statistically sound data of change rates.

• Possibilities to increase the geometric accuracy of the orthorectified SPOT imagery by using higher resolution/more accurate DEM and higher number of GCPs, etc. should be further evaluated.

• Studies that make use of auxiliary information to separate forest from spectrally-similar vegetation classes (including phenological information and expert knowledge, i.e. manual editing of the classification output) should be attempted in search of improvement of the accuracy of satellite-derived forest change detection maps.

• Relying on training/validation data visually interpreted from the SPOT imagery itself is uncertain in many cases; it is very important to have high resolution archive aerial photographs in order to accurately determine the land cover of the training/validation pixels at the beginning of the studied period.

Acnowlegments

References

1. Nikolov, S.C. 2010. Effects of Land Abandonment and Changing Habitat Structure on Avian Assemblages in Upland Pastures of Bulgaria. Bird Conservation International, 20, 200–213. doi:10.1017/S0959270909990244.
2. Kostov, G., I. Paligorov, S. Petrov, Z. Bogdanov, and P. Hirschberger. 2005. Illegal Logging in Bulgaria. WWW European Forest Programme and Danube Carpathian Programme.
3. Stankova, N., and R. Nedkov. 2015. Monitoring Forest Regrowth with Different Burn Severity Using Aerial and Landsat Data. In: 2015 IEEE Int. Geosci. & Rem. Sens. Symp. (IGARSS), Milan, 2015, 2166–69. doi:10.1109/IGARSS.2015.7326233.
4. Gikov, A., and P. Dimitrov. 2010. Applying Geoinformation Technologies to Assess the Damages and Effects of the Great Fire in the Area of the Malyovitsa Hut, Rila Mountain. In: Proceedings of the 5th Scientific Conference with International Participation "Space, Ecology, Nanotechnology, Safety – SENS`2009", 150–159.
5. Filchev, L., L. Feilong, and M. Panayotov. 2014. An assessment of land-use/land-cover change of Bistrishko Branishte biosphere reserve using Landsat data. 35th Inter. Symposium on Remote Sensing of Environment (ISRSE35). IOP Conf. Series: Earth and Envir. Sci., 2014, 17, 012060, doi:10.1088/1755-1315/17/1/012060
6. Coppin, P., I. Jonckheere, K. Nackaerts, B. Muys, and E. Lambin. 2004. Digital Change Detection Methods in Ecosystem Monitoring: A Review. International Journal of Remote Sensing, 25, 9, 1565–96. doi: 10.1080/0143116031000101675.
7. Kennedy, R.E., Z. Yang, and W.B. Cohen, Detecting Trends in Forest Disturbance and Recovery Using Yearly Landsat Time Series: 1. LandTrendr—Temporal Segmentation Algorithms. Remote Sensing of Environment, 2010, 114, 2897–2910. doi:10.1016/j.rse.2010.07.008.
8. Kozak, J., C. Estreguil, and P. Vogt, Forest Cover and Pattern Changes in the Carpathians Over the Last Decades." European Journal of Forest Research, 2007, 126, 1, 77–90. doi:10.1007/s10342-006-0160-4.

9. Kuemmerle, T., O. Chaskovskyy, J. Knorn, V.C. Radeloff, I. Kruhlov, W. S. Keeton, P. Hostert, Forest Cover Change and Illegal Logging in the Ukrainian Carpathians in the Transition Period from 1988 to 2007. Remote Sensing of Environment, 2009, 113, 1194–1207. doi: 10.1016/j.rse.2009.02.006.

10. Olofsson, P., P. Torchinava, C. E. Woodcock, A. Baccini, R.A. Houghton, M. Ozdogan, F. Zhao, and X. Yang. Implications of Land Use Change on the National Terrestrial Carbon Budget of Georgia. Carbon Balance and Management, 2010, 5, 4. doi: 10.1186/1750-0680-5-4.

11. Olofsson, P., T. Kuemmerle, P. Griffiths, J. Knorn, A. Baccini, V. Gancz, V. Blujdea, R.A. Houghton, I.V. Abrudan, and C.E. Woodcock. Carbon Implications of Forest Restitution in Post-socialist Romania. Environmental Research Letters, 2011, 6, 4, 045202 (10 pp). doi:10.1088/1748-9326/6/4/045202.

12. Jeon, S.B., P. Olofsson, and C.E. Woodcock. Land Use Change in New England: A Reversal of the Forest Transition, Journal of Land Use Science. Journal of Land Use Science, 2014, 9, 1, 105–30. doi:10.1080/1747423X.2012.754962.

13. Mas, J.F. Monitoring Land-cover Changes: A Comparison of Change Detection Techniques. International Journal of Remote Sensing, 1999, 20, 1, 139–52. doi:10.1080/014311699213659.

14. Olofsson, P., G.M. Foody, S.V. Stehman, and C.E. Woodcock. Making Better Use of Accuracy data in Land Change Studies: Estimating Accuracy and Area and Quantifying Uncertainty Using Stratified Estimation. Remote Sensing of Environment, 2013, 129, 122–31. doi: 10.1016/j.rse.2012.10.031.

15. Almutairi, A., and T.A. Warner. Change Detection Accuracy and Image Properties: A Study Using Simulated Data. Remote Sensing, 2010, 2, 1508–1529. doi:10.3390/rs2061508.

16. Van der Linden, S., A. Rabe, M. Held, B. Jakimow, P.J. Leitão, A. Okujeni, M. Schwieder, S. Suess, and P. Hostert. The EnMAP-Box—A Toolbox and Application Programming Interface for EnMAP Data Processing. Remote Sensing 2015, 7, 9, 11249–266. doi:10.3390/rs70911249.

17. Foody, G.M., A. Mathur. Toward Intelligent Training of Supervised Image Classifications: Directing Training Data Acquisition for SVM Classification. Remote Sens. of Envir., 2004, 93, 107–17. doi:10.1016/j.rse.2004.06.017.

18. Czaplewski, R.L. Accuracy Assessment of Maps of Forest Condition – Statistical Design and Methodological Considerations. In: Remote Sensing of Forest Environments: Concepts and Case Studies, edited by M. Wulder and S. Franklin, 2003, 115–42. Norwell, MA: Kluwer Academic Publishers.

19. Olofsson, P., G.M. Foody, M. Herold, S.V. Stehman, C.E. Woodcock, and M.A. Wulder. Good Practices for Estimating Area and Assessing Accuracy of Land Change. Rem. Sens. of Envir., 2014, 148, 42–57. doi: 10.1016/j.rse.2014.02.015.

20. Baumann, M., M. Ozdogan, T. Kuemmerle, K.J. Wendland, E. Esipova, and V.C. Radeloff. Using the Landsat Record to Detect Forest-cover Changes During and After the Collapse of the Soviet Union in the Temperate Zone of European Russia." Rem. Sens. of Envir., 2012, 124, 174–84. doi:10.1016/j.rse.2012.05.001.

21. EFA (Executive Forest Agency). 2009. National Strategy for Sustainable Development of the Forest Sector in Bulgaria 2006–2015. Sofia: Executive Forest Agency, Ministry of Agriculture and Foods (in Bulgarian).

22. Feranec, J., M. Kopecka, R. Vatseva, A. Stoimenov, J. Otahel, J. Betak, and K. Husar. Landscape Change Analysis and Assessment (Case studies in Slovakia and Bulgaria). Central European Journal of Geosciences, 2009 1, 1, 106–19. doi:10.2478/v10085-009-0005-8.

КАРТОГРАФИРАНЕ НА ПРОМЕНИТЕ НА ГОРСКИТЕ ТЕРИТОРИИ ЧРЕЗ SPOT ИЗОБРАЖЕНИЯ С ИЗПОЛЗВАНЕ НА РАЗЛИЧНИ КЛАСИФИКАЦИОННИ ПОДХОДИ

П. Димитров, П. Олофсон, Г. Желев, И. Каменова

Резюме

В настоящето изследване е картографирано изменението на горските територии в два тестови участъка в България (планински и равнинно-хълмист) за приблизително 20-годишен период. Сравнени са два различни подхода при класифициране на мултитемпорални изображения от SPOT HRV/HRVIR с пространствена разделителна способност 20 m. Приложена е спектрална класификация на всяко изображение поотделно и след това са сравнени пиксел по пиксел, за да се открият промените в типа земно покритие („гори" и „извън горски територии"). Приложена е и спектрална класификация директно върху комбинираните данни от двете сравнявани дати. Сравнени са статистическите данни за точността, които показват, че и двата подхода се държат еднакво добре по отношение на общата точност на получените карти на промените (между 85.4 % и 91.8 %). Резултатите от класификациите са доста сходни за двата устойчиви класа земно покритие – „постоянни гори" и „постоянни извънгорски територии", при които точността е относително висока. Точността на класовете променено земно покритие е значително по-ниска от тази на стабилните класове, независимо от подхода за откриване на изменението. Установи се, че спектралната класификация на комбинираните данни (т. нар. мултитемпорална класификация) се представи малко по-добре в избраните тестови участъци, като показа по-висока точност при класифициране на горските нарушения и участъците с повторно залесяване. Като резултат са дискутирани някои проблеми и са дадени някои препоръки при изследване на изменението на горски територии със спътникови изображения.

EVALUATION OF RAPIDEYE VEGETATION INDICES FOR PREDICTION OF BIOPHYSICAL/BIOCHEMICAL VARIABLES OF WINTER WHEAT

Ilina Kamenova[1], Petar Dimitrov[1], Rusina Yordanova[2]

[1]Space Research and Technology Institute – Bulgarian Academy of Sciences
e-mail: petarkirilov@mail.bg, ilina.kamenova@space.bas.bg
[2]Sortovi Semena – Vardim EAD
e-mail: r_yordanova@abv.bg

Abstract
The aim of the study is to evaluate the possibility for using RapidEye data for prediction of Leaf Area Index (LAI), fraction of Absorbed Photosynthetically Active Radiation (fAPAR), fraction of vegetation Cover (fCover), leaf Chlorophyll Concentration (CC) and Canopy Chlorophyll Content (CCC) of winter wheat. The relation of a number of vegetation indices (VIs) with these crop variables is accessed based on a regression analysis. Indices, which make use of the red edge band, such as Chlorophyll Index red edge (CIre) and red edge Normalized Difference Vegetation Index (reNDVI), were found most useful, resulting in linear models with R^2 of 0.67, 0.71, 0.72, and 0.76 for fCover, LAI, CCC, and fAPAR respectively. CC was not related with any of the VIs.

Introduction

RapidEye is a remote sensing mission consisting of a constellation of five small satellites launched in 2008. One of the main applications of the RapidEye satellite data is to provide timely information about the crop condition in support of precision agriculture [1]. To better fulfil this aim, the Multi-spectral Imager on board RapidEye has a band in the red edge spectral region in addition to the visible and the near infrared (NIR) bands.

RapidEye data has been previously used for estimation of crop variables. For example, Vuolo et al. [2] compared physically based (Radiative Transfer Modelling) and empirical (Vegetation Indices) approaches for retrieval of LAI and CCC using RapidEye imagery. In their study, one regression model was applied for a range of crops (fruit trees, maize, and other crops). Using generally calibrated model, however, may not provide equally good estimates for all crops. In this study, we are only interested in winter wheat and the aim is to investigate empirical relations between VIs and biophysical variables that are specific for this crop.

Data and methods

Field data

For this study, measurements of biophysical and biochemical variables of winter wheat are available from fields located in the north-western part of Sofia municipality, close to the residential district of *Trebich*. Measurements of Leaf Area Index (LAI), fraction of Absorbed Photosynthetically Active Radiation (fAPAR), fraction of vegetation Cover (fCover) and leaf Chlorophyll Concentration (CC) were conducted seven times during the growing seasons of 2014–2015 and 2015–2016 (Table 1). During the 2014–2015 growing season, 5 plots in each of 2 fields were measured each time. During the 2015–2016 growing season 5 fields were sampled in a total of 11 plots (one of the plots was not sampled in 18/05/2016, see Table 1). In both seasons, the fields were sown with winter wheat *Enola* variety. In most of these seven field campaigns the full set of variables (i.e. LAI, fAPAR, fCover and CC) were measured; however fCover were not measured on 02/04/2015 and CC was not measured on 15/05/2015. Measurements were made within a plot with size 5 m × 5 m. AccuPAR LP80 (Decagon Devices©) was used for measuring LAI, fAPAR and fCover in 4 "subplots" in each plot. Portable chlorophyll meter CCM-300 was used for measuring CC ($mg\ m^{-2}$) in 5–6 "subplots" in each plot. The averages of the "subplots" measurements were used in further analysis to represent the biophysical/biochemical variables at the plot level. Using the CC and LAI measurements, the canopy chlorophyll content (CCC) was calculated, where CCC ($g\ m^{-2}$) = LAI ($m^2\ m^{-2}$) × CC ($mg\ m^{-2}$) × 0.001. Fig. 1 provide some graphical description of data.

Table 1. Dates of the field campaigns and the corresponding RapidEye images used in this study

Growing season	Field campaign	Development stage	RapidEye image
2014–2015	02/04/2015	Tillering	31/03/2015
2014–2015	15/04/2015	Stem elongation	20/04/2015
2014–2015	04/05/2015	Stem elongation	12/05/2015
2014–2015	15/05/2015	Booting and heading	18/05/2015
2014–2015	20/05/2015	Heading and start of anthesis	21/05/2015
2015–2016	13/04/2016	Stem elongation	13/04/2016
2015–2016	18/05/2016	Heading	23/05/2016
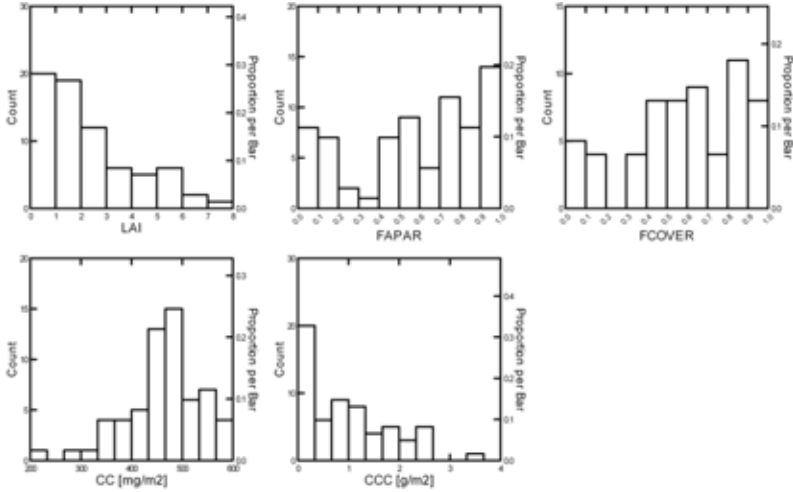
Fig. 1. Histograms of ground measured LAI (n = 71; mean = 2.25), fAPAR (n = 71; mean = 0.58), fCover (n = 61, mean = 0.60), Chlorophyll Concentration (CC) (n = 61; mean = 463) and Canopy Chlorophyll Content (CCC) (n = 61; mean = 0.96)

RapidEye data

Seven RapidEye images were available for this study, which dates roughly corresponded to the dates of the field campaigns (Table 1). The separation between date of field campaign and image acquisition was between 0 and 5 days with only one occasion when the gap was 13 days (Table 1). The images are provided as Level-3A (Ortho product) and showed highly accurate geo-registration as assessed by visual inspection of road vector map superimposed on the images. Each scene consists of five spectral bands: B1-Blue (440–510 nm); B2-Green (520–590 nm); B3-Red (630–685 nm); B4-Red edge (690–730 nm) and B5-Near infrared (760–850 nm). The spatial resolution is 5 m for all bands. The image data were transformed from DN to spectral radiance (L_λ) using the provided scale factor [3]. Then, the top of the atmosphere (TOA) reflectance ρ_λ was calculated using the equation:

(1) $$\rho_\lambda = \frac{\pi \times L_\lambda \times d^2}{ESUN_\lambda \times \cos\theta_S},$$

where L_λ is Spectral radiance [W/(m^2 sr µm)], d is Earth–Sun distance [astronomical units], $ESUN_\lambda$ is Mean exoatmospheric solar irradiance [W/(m^2 µm)], θ_s is Solar zenith angle [degrees] [4]. The values of $ESUN_\lambda$ for each RapidEye band and of θ_s for each acquisition date are available in the image product metadata.

Methods

A database was constructed prior to the analysis, consisting of the biophysical/biochemical measurements, the reflectance values in each RapidEye band and a range of vegetation indices (VIs). The RapidEye reflectance values for a specified plot are extracted using bilinear interpolation, which is a method providing an estimated value that represents a weighted average of the 4 input pixels surrounding the plot centre. This approach was taken, instead of using only the pixel with the closest centroid, in order to account for possible errors in the GPS-measured plot coordinates. As the RapidEye spatial resolution (i.e. 5 m) is comparable with the GPS accuracy this precaution is justified. The list of vegetation indices is presented in Table 2.

Table 2. Spectral vegetation indices calculated in this study using RapidEye data. The RapidEye band numbers are used in the formulas

Vegetation Index	Abbreviation	Formula	Reference
Chlorophyll Index red edge	CIre	(B5 / B4) − 1	[5, 6]
Chlorophyll Index green	CIg	(B5 / B2) − 1	[5, 6]
Normalized Difference Vegetation Index	NDVI	(B5 − B3) / (B5 + B3)	[7]
Simple Ratio	SR	B5 / B3	[8]
NIR/RE	NIR/RE	B5 / B4	
RE/RED	RE/RED	B4 / B3	
Visible Atmospherically Resistant Index	VARI	(B2 − B3) / (B2 + B3 − B1)	[9]
red edge Normalized Difference Vegetation Index	reNDVI	(B5 − B4) / (B5 + B4)	[10]
Wide Dynamic Range Vegetation Index	WDRVI	(0.3 × B5 − B3) / (0.3 × B5 + B3)	[11]
Vegetation Index green	VIg	(B2 − B3) / (B2 + B3)	[9]
Optimized Soil-Adjusted Vegetation Index	OSAVI	(1 + 0.16) × (B5 − B3) / (B5 + B3 + 0.16)	[12]
green Normalized Difference Vegetation Index	gNDVI	(B5 − B2) / (B5 + B2)	[13]
Modified Triangular Vegetation Index 2	MTVI2	$\dfrac{1.5 * \left[1.2 * \left(B5 - B2\right) - 2.5 * \left(B3 - B2\right)\right]}{\sqrt{\left(2 * B5 + 1\right)^2 - \left(6 * B5 - 5\sqrt{B3}\right) - 0.5}}$	[14]
Green Infrared Percentage Vegetation Index	GIPVI	B5 / (B5 + B2)	
green Normalized Difference Vegetation Index1	gNDVI1	(B4 − B2) / (B4 + B2)	
Perpendicular Vegetation Index†	PVA	(B5 − a × B3 − b) / (SQRT(1 + a²))	[15]
Transformed Soil Adjusted Vegetation index †‡	TSAVI	(a × (B5 − a × B3 − b)) / (a × B5 + B3 − ab + X × (1 + a²))	[16]
Soil Adjusted Vegetation index 2†	SAVI2	B5 / (B3 + (b / a))	[17]

† a and b are the slope and the intercept of the soil line (see Fig. 2); ‡ X=0.08

66

The vegetation indices were selected based on a literature review. Special emphasis was placed on the VIs that used bands from the red edge spectral region. Also, three soil adjusted VIs were calculated, Perpendicular Vegetation Index (PVI, [15]), Transformed Soil Adjusted Vegetation index (TSAVI, [16]), and Soil Adjusted Vegetation index 2 (SAVI2, [17]). The soil adjusted VIs used the parameters of the soil line in their formulas. The soil line was derived empirically using manually selected bare soil and stubble pixels (Fig. 2). Stubble pixels were used because crop residue may constitute significant part of the background reflectance in the winter wheat fields.
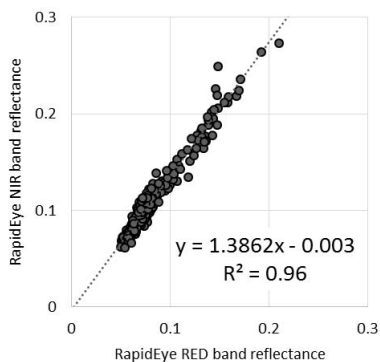
Fig. 2. *Near infrared (NIR) band reflectance regressed on the red band reflectance for soil/stubble pixels from RapidEye (image data 31 March 2015, 20 April 2015 and 13 April 2016)*

We used two approaches to compare the potential of different VIs for prediction of biophysical/biochemical variables. First, the association of each biophysical/biochemical variables with each VI was visually assessed using scatterplots. The second, quantitative, approach was based on the regression analysis. All VIs were systematically evaluated by fitting linear and exponential models with each biophysical/biochemical variable being dependant variable. These two models have the form y=a + bx and y=a × e^{bx} respectively, where *a* and *b* are the regression parameters to be estimated. Literature suggested that, in most cases, the relation between biophysical/biochemical variable of crop and spectral vegetation index can be described by one of these two models. We used regression analysis, instead of some measure of correlation, because the interest is on the prediction capabilities. This approach also permitted us to account explicitly for the type of the relation, i.e. linear or nonlinear. The Root Mean Square Error (RMSE) was calculated for each model using the leave-one-out method:

(2) $$RMSE = \sqrt{\frac{\sum_i (y_i - \hat{y}_i)^2}{n}},$$

where y_i is the measured value for the i-th observation and $\hat{y}_i$ is the predicted value for that observation derived from a model calibrated with all observations except i. The RMSE was used as a criterion for the performance of the VIs. Note that not every model produced in this procedure makes sense. For example, if the relation between a VI and LAI is curve-linear then fitting a straight line to this data would be erroneous. For every given combination of biophysical/biochemical variable and VI the lower RMSE may indicate which model (linear or exponential) might be more appropriate but one should not rely on this. In any case, the scatterplot must be checked.

For this analysis, we did not pay attention for the regression assumptions because the aim was to make some automated and consistent comparison of a number of VIs and found those that may represent interest for further analysis.

Results

The scatterplots obtained from RapidEye VIs against the five winter wheat biophysical/biochemical variables are displayed in Fig. 3. Fig. 4 shows the RMSE of the fitted linear and exponential models for each combination.

The scatterplots suggest that LAI is most strongly correlated with Chlorophyll Index red edge (CIre) (this index is, in practice, equivalent to the NIR/RE ratio (see Table 2)). The form of the relation may be roughly described as linear but some outliers (low LAI values corresponding to high CIre) contradict this general trend. The regression analyses confirm that the best linear predictor of LAI is CIre (RMSE = 1.05). Exponential model is more appropriate to describe the relation of LAI to some of the other VIs such as the red edge Normalized Difference Vegetation Index (reNDVI). The RMSE of the exponential model with reNDVI is 1.06. Thus, similar results are obtained using linear and exponential models.

The fAPAR and fCover behave very similarly with respect to their relation with the VIs. In general, the scatter of data points is high, which indicates relatively poor relationship for most VIs (Fig. 3). The linear models with lowest error are those with reNDVI (RMSE = 0.16 for both fAPAR and fCover), but other indices such as NDVI, TSAVI and OSAVI perform almost equally well. The exponential model form was not appropriate for any of the VIs.

There was no correlation between CC and the tested VIs. This is probably because other factors, such as background reflectance and canopy structure mask the differences in CC at leaf level. CCC showed better association with the VIs but this is not surprising because the variation of CCC is affected mostly by the variation of LAI. As with LAI, the best model is the linear model with CIre which yielded RMSE of 0.47 g m^{-2}.

On Fig. 6 are shown the best performing linear model for each biophysical/biochemical variable. The models explain between 67 % (fCover) and 76 % (fAPAR) of the variability of the dependent variable. In general, the level of uncertainty is too high for these models to provide reliable estimates at pixel level. Even though the predictions are not precise, they are unbiased as indicated by the mean residuals, which are close to zero for all models (data not shown). This may be important if the estimates are to be aggregated at field or regional level.
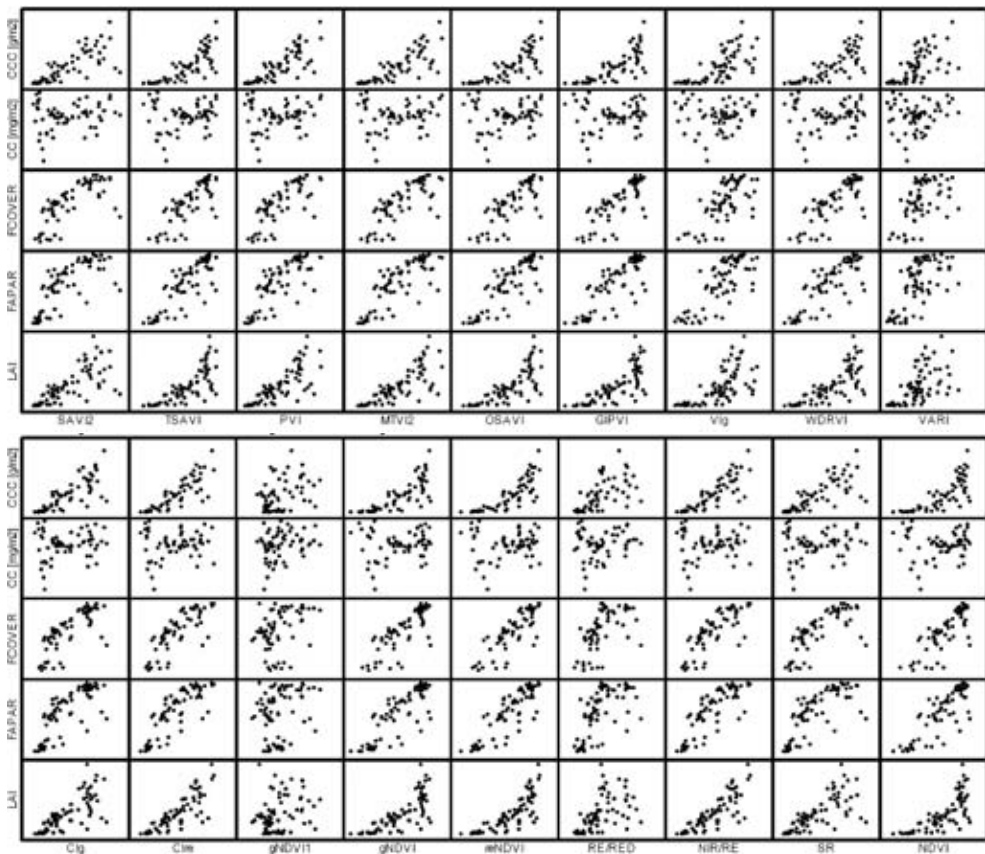
*Fig. 3. Scatterplots of the studied biophysical/biochemical variables
and the RapidEye vegetation indices*

Characteristic for both LAI and CCC is the increasing dispersion with the increase of CIre. Predictions become more uncertain approaching the peak of the growing season in May when winter wheat is in heading and anthesis phenological stages. The team led by Dahms [18] has also found that LAI and FPAR are difficult

to predict at the phenological phase of fruit development, which, according to the authors, is most likely due to canopy closure in combination with accompanied saturation effects in the RapidEye observations.

None of the tested soil adjusted vegetation indices improved significantly the prediction capabilities of the models probably because the variation in background reflectance was not an important factor for the observed prediction uncertainty. A paper by Ali et al. [19] showed that a similar index to those used in our study, the Soil Adjusted Vegetation Index, do not necessarily outperform NDVI in the estimation of LAI with RapidEye. As shown, most uncertainty is related with the closed canopies, while the soil adjusted VIs are designed to improve the relation with the vegetation parameters in open canopies where soil contribution is significant [20].
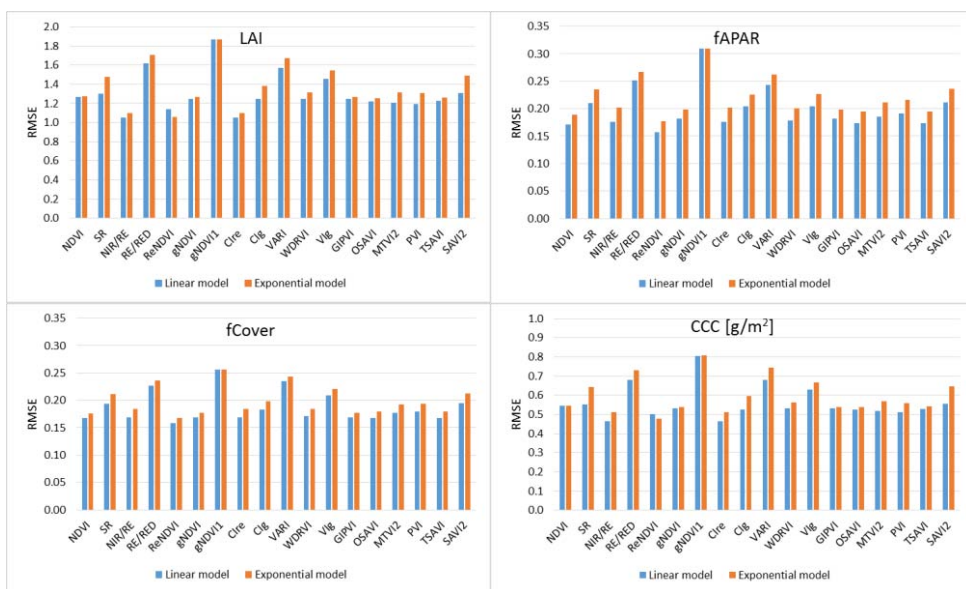
Fig. 4. Comparison of the accuracy (RMSE = root mean square error) of regression models employing different vegetation indices. Both linear and exponential models for prediction of LAI, fAPAR, fCover, and CCC are shown.

The regression models were assessed using the RMSE value. The best models were used for calculation of prediction maps for the targeted biophysical/biochemical parameters. CIre was the index with the lowest RMSE value among other indices for predicting LAI in winter wheat. The RMSE showed relatively low error of 1.05 $m^2\,m^{-2}$.

The LAI maps were calculated using vegetation index map with the spectral values from each RapidEye image, and the coefficients derived from the regression

analysis. On Fig. 5 are represented the LAI maps derived for each of the available RapidEye images from vegetation season 2015.

The resulting map consisted of one layer, whereby each pixel in the map had a value for the predicted LAI. The predicted values based on the linear regression coefficients of the CIre relation resulted in some pixels with negative values. The negative LAI result is of course not possible in the reality, but the values are result of a simple linear mathematical function. However, the fraction of the pixels having negative LAI values, can be attributed to pixels with exposed soil cover. This is the reason to find larger proportion of pixels with negative values during the first two dates (31/03/2015 and 20/04/2015).

In the maps is shown the infield variation of LAI, which could be of interest for the farmers for the management practices. On the other hand, the 6 maps also show the seasonal dynamic of LAI during the vegetation season.
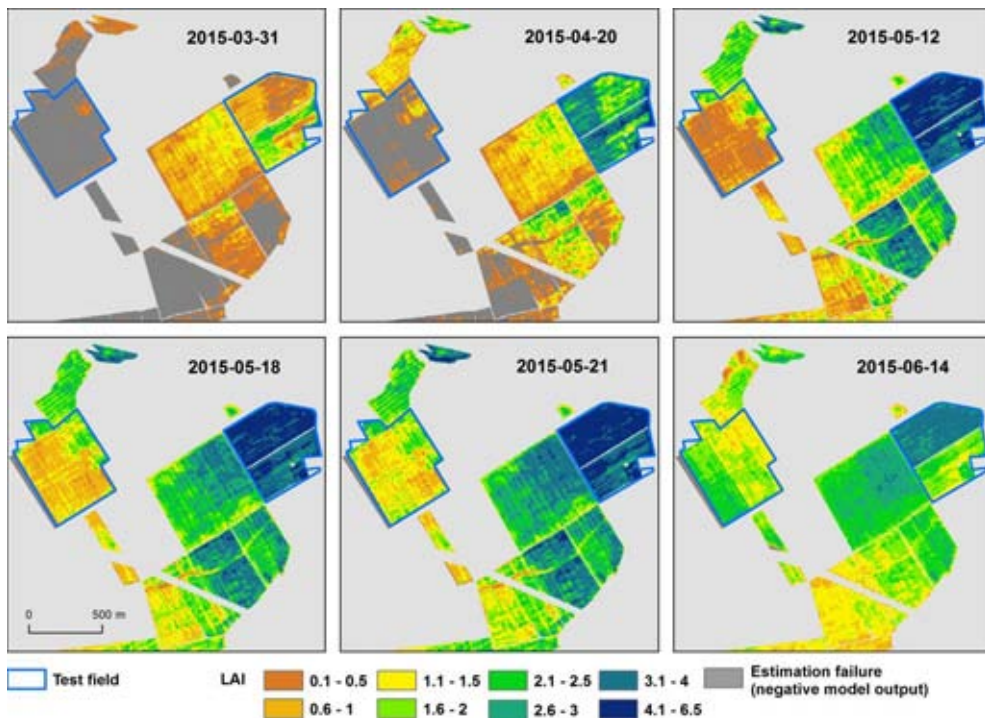
Fig. 5. Predicted LAI (m^2m^{-2}) maps for winter wheat

Conclusions

In this study, we compared a range of VIs calculated from RapidEye data with respect to their potential for prediction of LAI, fAPAR, fCover, CC, and CCC in winter wheat fields (Fig. 6). Of these biophysical/biochemical variables, only CC

was not significantly correlated with any of the tested VIs. For prediction of LAI and CCC, the most useful indices appear to be CIre and reNDVI, for which linear and exponential regression models are appropriate respectively. We found that reNDVI is the best predictor of fAPAR and fCover, but that several other indices perform almost equally well. Both reNDVI and CIre employ the red edge band, which confirm the importance of the red edge spectral region for crop condition characterisation. Note however, that it is possible for several VIs to show similar results and more data are needed to find if given VI should be preferred to the others.
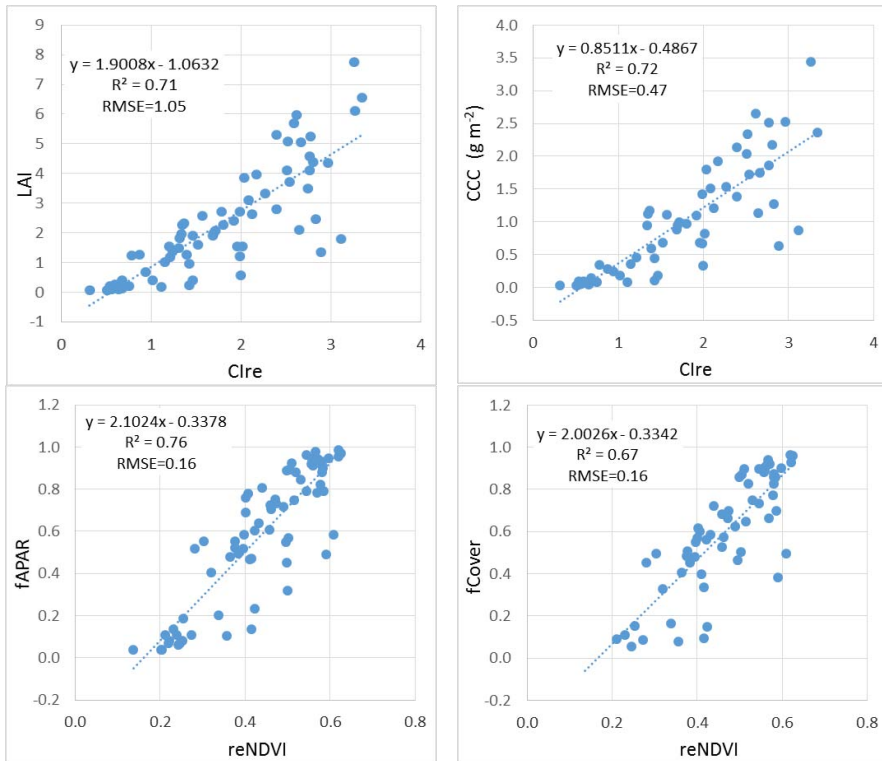
Fig. 6. Linear regression models for LAI, fAPAR, fCover and CCC
with selected VIs from RapidEye

The accuracy of the regression models presented in this study is relatively low. This may be due to atmospheric effects on the satellite data, presence of weeds on the field plots or other factors. In conclusion, VIs from RapidEye employing the red edge band are promising for winter wheat variables characterization, but further experimental work is needed to better understand the sources of uncertainty and eventually increase prediction accuracy of the regression models.

References

1. Tyc, G., J. Tulip, D. Schulten, M. Krischke, and M. Oxfort. The RapidEye mission design. Acta Astronautica, 2005, 56, 213–19.
2. Vuolo, F., C. Atzberger, K. Richter, G. D'Urso, and J. Dash. Retrieval of biophysical vegetation products from RapidEye imagery. In: Wagner W., Székely, B. (eds.): ISPRS TC VII Symposium – 100 Years ISPRS, Vienna, Austria, July 5–7, 2010, IAPRS, Vol. XXXVIII, Part 7A, 281–86.
3. BlackBridge. Satellite Imagery Product Specifications, Version 6.1, April 2015, 48 p.
4. Chander, G., B. L. Markham, and D. L. Helder. Summary of current radiometric calibration coefficients for Landsat MSS, TM, ETM+, and EO-1 ALI sensors. Remote Sensing of Environment, 2009, 113, 893–903.
5. Gitelson, A., Y. Gritz, and M.N. Merzlyak. Relationships between leaf chlorophyll content and spectral reflectance and algorithms for non-destructive chlorophyll assessment in higher plant leaves. Journal of Plant Physiology, 2003, 160, 271–82.
6. Gitelson, A., G.P. Keydan, and M.N. Merzlyak. Three-band model for noninvasive estimation of chlorophyll, carotenoids, and anthocyanin contents in higher plant leaves. Geophys. Res. Lett., 2006, 33, L11402, DOI:10.1029/2006GL026457.
7. Rouse, J.W., R.H. Haas, J.A. Schell, and D.W. Deering. Monitoring vegetation systems in the Great Plains with ERTS. In: Third ERTS Symposium, 1973, NASA SP-351, vol. 1, NASA, Washington, DC, 309–317.
8. Jordan, C.F. Derivation of leaf-area index from quality of light on the forest floor. Ecology, 1969, 50, 663–66.
9. Gitelson, A., Y.J. Kaufman, R. Stark, and D. Rundquist. Novel algorithms for remote estimation of vegetation fraction. Remote Sensing of Environment, 2002, 80, 76–87.
10. Gitelson, A., and M.N. Merzlyak. Spectral reflectance changes associated with autumn senescence of Aesculus hippocastanum L. and Acer platanoides L. Leaves.Spectral features and relation to chlorophyll estimation. J. Plant Physiol., 1994, 143, 286–92.
11. Gitelson, A. Wide Dynamic Range Vegetation Index for Remote Quantification of Biophysical Characteristics of Vegetation. J. Plant Physiol., 2004, 161, 165–73.
12. Rondeaux, G., M. Steven, and F. Baret. Optimization of soil-adjusted vegetation indices. Remote Sensing of Environment, 1996, 55, 2, 95–107.
13. Gitelson, A., Y.J. Kaufman, and M.N. Merzlyak. Use of a green channel in remote sensing of global vegetation from EOS-MODIS. Rem. Sens. Envir., 1996, 58, 289–98.

14. Haboudane, D., J.R. Miller, E. Pattey, P.J. Zarco-Tejada, and I.B. Strachan. Hyper-spectral vegetation indices and novel algorithms for predicting green LAI of crop canopies: modelling and validation in the context of precision agriculture. Remote Sensing of Environment, 2004, 90, 337–52.

15. Richardson, A.J., and J.H. Everitt. Using Spectral Vegetation Indices to Estimate Rangeland Productivity. Geocarto International, 1992, 7, 1, 63–69.

16. Baret, F., G. Guyot. Potentials and limits of vegetation indices for LAI and APAR assessment. Remote Sensing of Environment, 1991, 35, 161–73.

17. Major, D. J., F. Baret, and G. Guyot. A ratio vegetation index adjusted for soil brightness. International Journal of Remote Sensing, 1990, 11, 727–40.

18. Dahms, T., S. Seissiger, E. Borg, H. Vajen, B. Fichtelmann, C. Conrad. Important Variables of a RapidEye Time Series for Modelling Biophysical Parameters of Winter Wheat. PFG, 2016, 5 – 6, 285–99. DOI: 10.1127/pfg/2016/0303.

19. Ali, M., C. Montzka, A. Stadler, G. Menz, F. Thonfeld, and H. Vereechen. Estimation and Validation of RapidEye-Based Time-Series of Leaf Area Index for Winter Wheat in the Rur Catchment (Germany). Remote Sensing, 2015, 7, 2808–31, DOI:10.3390/rs70302808.

20. Bannari, A., D. Morin, F. Bonn, and A.R. Huete. A review of vegetation indices. Remote sensing reviews, 1995, 13, 95–120.

ИЗСЛЕДВАНЕ НА ВЪЗМОЖНОСТИТЕ ЗА ОПРЕДЕЛЯНЕ НА БИОФИЗИЧНИ/БИОХИМИЧНИ ПОКАЗАТЕЛИ НА ЗИМНА ПШЕНИЦА ЧРЕЗ ВЕГЕТАЦИОННИ ИНДЕКСИ ОТ RAPIDEYE

И. Каменова, П. Димитров, Р. Йорданова

Резюме

Целта на изследването е да оцени възможностите за приложение на данни от спътниковата система RapidEye за определяне на индекса на листната повърхност (LAI), дела на погълнатата фотосинтетично активна радиация (fAPAR), проективното покритие (fCover), концентрацията на хлорофил в листата (CC) и хлорофилното съдържание в растенията на единица площ от земната повърхност (CCC) на посеви от зимна пшеница. Връзката на тези показатели с различни вегетационни индекси е изследвана чрез регресионен анализ. Индекси използващи спектралния канал „red-edge“ на RapidEye, като например *Chlorophyll Index red edge (CIre)* и *red-edge Normalized Difference Vegetation Index (reNDVI)* са най-полезни, позволявайки съставянето на линейни регресионни модели с детерминационни коефициенти 0.67, 0.71, 0.72 и 0.76 съответно за fCover, LAI, CCC и fAPAR. Концентрацията на хлорофил в листата не се корелира с никой от използваните вегетационни индекси.

REMOTE ESTIMATION OF CROP CANOPY PARAMETERS BY STATISTICAL REGRESSION ALGORITHMS FOR WINTER RAPESEED USING SENTINEL-2 MULTISPECTRAL IMAGES

Dessislava Ganeva, Eugenia Roumenina

Space Research and Technology Institute – Bulgarian Academy of Sciences
e-mail: d.ganeva@space.bas.bg

Abstract

Estimation of crop canopy parameters is important task for remote sensing monitoring of agriculture and constructing strategies for within-field management. The main objective of this study is to evaluate the retrieval from Sentinel-2 images by parametric and non-parametric statistical models several crop canopy parameters for monitoring before winter and after winter rapeseed crop in real farming conditions of North East Bulgaria. For the calibration of the models in-situ data from three field campaigns is used. For most of the studied parameters models with good accuracy were identified, except for aboveground fresh biomass. The best identified model for vegetation fraction (RMSEcv = 0.14 %) and plant density (RMSEcv = 9 nb/m^2) were parametric models with three band vegetation index (3BSI-Tian) and linear fitting function for the first, three band vegetation index (3BSI-Verreslt) and polynomial for the second parameter. For aboveground dry biomass (RMSEcv = 52 g/m^2), mean plant height (RMSEcv = 4 cm) and nitrogen content in fresh biomass (RMSEcv = 2 g/kg) the best models were non-parametric, Gaussian Processes Regression for the first parameter and Variational Heteroscedastic variant of the Gaussian Processes Regression for the other two.

Introduction

Quick and accurate retrieval of crop canopy parameters is of importance for remote sensing monitoring of agriculture. Rapeseed is one of the most important oilseed crops worldwide [1] and it is monitored by traditional methods [2] as well as by remote sensing [3–5] .

One of the important periods in the development of winter rapeseed crop is the before winter and after winter period [6]. Before winter, the condition of the crop is evaluated regarding its preparation to withstand the winter meteorological conditions. The rapeseed crop should be developed enough before winter, but the plants should not be developed beyond a certain threshold because they are more sensitive to low temperatures and frost. The rapeseed plants compete for light and when there is an uneven plant density or weed development, the plants develop in

height and again become more susceptible to frost. After winter, the condition of the crop is evaluated regarding its plant density, phenological phase and frost damage. A decision is often made to keep the rapeseed crop because enough plants survived the winter and they have good change for a satisfactory yield, or to destroy the rapeseed crop and plant the field with spring crop.

The traditional monitoring is based on parameters like plant density, phenological phase, biomass. This study is focused on remote estimation of several crop canopy parameters of winter rapeseed with the purpose to be able to use them for before winter and after winter monitoring and within-field management.

Historically, Vegetation indices (VI) with regression functions are used to retrieve biophysical parameters, such as aboveground biomass [7] or vegetation fraction [8], agronomical parameters, such as plants density [9], or growth parameters, such as plant height [3]. More recently, VI types of formulas are used with all available wavelength and different regression functions for retrieval of biophysical parameters, such as leaf area index and leaf chlorophyll content, called "spectral index optimization" [10] and retrieval of nitrogen concentration, was obtained by non-parametric models [11–15]. All those methods use in-situ sampled, or simulated, data for the modeled canopy parameters and associated surface reflectance from remote sensing sensor. In our approach we use in-situ sampled data and Sentinel-2 associated surface reflectance.

In order to determine the variability of the fields before the actual collection of the field data [16], the sample locations were determined by calculating VI, Table 1, that correlate with the rapeseed canopy parameters that we are interested in. A VI that was not tested with rapeseed but was specially tested with Sentinel-2 images [17] was also included in the list. The selected VI, Table 1, were calculated on the Sentinel-2 image from 12.11.2017, downloaded from Copernicus Data Open Hub in 2A product (https://scihub.copernicus.eu). The samples were positioned manually to capture the maximum vegetation variability of the test fields and in relatively homogeneous surrounding area of 20 m² in terms of vegetation density and growth phase

The main objective of this study is to evaluate the retrieval from Sentinel-2 images by parametric and non-parametric statistical models several crop canopy parameters for monitoring before winter and after winter rapeseed crop.

Table 1. Vegetation Indices used to position the location of the samples for the field campaign

Estimated parameter	Vegetation Index	Formula	Reference
Aboveground biomass, number of plants per m^2 after emergence	RVI (Ratio Vegetation Index)	NIR / Red	[9]
Aboveground biomass	OSAVI (Optimized Soil Adjusted Vegetation Index)	(1 + L)(NIR − Red) / (NIR + Red + L) (L = 0.16)	[7]
LAI	SAVI (Soil Adjusted Vegetation Index)	(1 + L)(NIR − Red) / (NIR + Red + L) (L = 0.5)	[18]
Canopy chlorophyll and nitrogen	CiredEdge	R783/R705 − 1	[17]
Plan height	EVI (Enhanced Vegetation Index)	EVI = G × ((RNIR − Rred) / (RNIR + C1 × Rred − C2 × Rbleu +L)); G = 2.5; C1 = 6; C2=7.5; L = 1	[3]
Vegetation Fraction	VARIgreen (Visible Atmospherically Resistant Index)	(R550 – R670) / (R550 + R670)	[8]
Number of plants per square meter after emergence	NDVI (Normalized Difference Vegetation Index)	(NIR − Red) / (NIR + Red)	[9]

Materials and Methods

Study area

This study area is part of the East Danube plain in Bulgaria, Fig. 1, and the study period was over one growing season, from September 2017 to July 2018, on three mass fields sown with different hybrids of winter rapeseed. The area is mostly flat, the soil has mainly sandy loam texture, the climate in this region is Moderate Continental with cold winters and hot summers (mean daily temperature 10.2º C), and an annual cumulative rainfall of 540 mm.

The bigger of the field plots (P1) is 137 ha and was planted for three days, from 03.09.2017, with sowing rate of 80 plants/m^2. The other two plots are smaller, one (P2) is 10 ha, planted on 28.08.2017 at sowing rate of 56 plants/m^2 and the other (P3) is 15 ha, planted on 04.09.2017 at sowing rate of 76 plants/m^2.
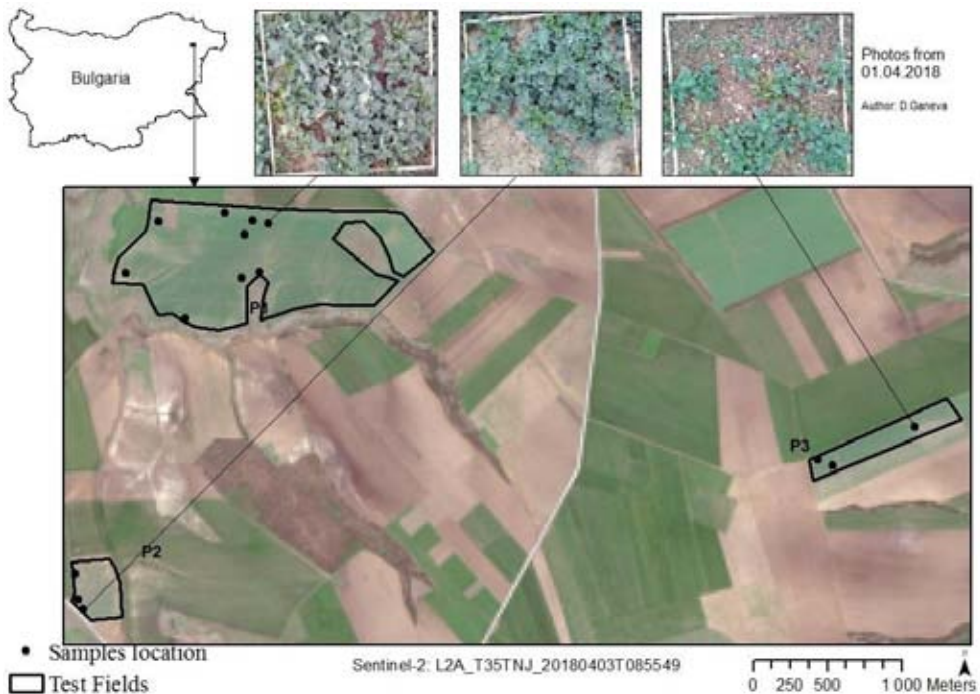
Fig. 1. Location of the field sites near Dobrich, North East Bulgaria

In-situ data

The crop canopy parameters were measured within 1 m^2 elementary sampling units (ESU) at the pre-defined samples location. Each ESU was geo-located by means of a GPS, with an accuracy of ± 3–5 m. For the aboveground fresh biomass (FBM), all plants in the ESU were manually cut, stored in paper bags and transported to a laboratory.

In the laboratory the FBM is weighted (in g/m^2) and then, a sample of it is oven-dried at 105° C until constant weight to obtain the dry biomass (DBM), measured in g/m^2. In each ESU the density (number winter rapeseed per m^2, NbPlant) was counted and recorded. The mean plant height of all plants (PlantH) in an ESU was recorded as well, in cm. The vegetation fraction (VF) as described by [19] was expertly estimated and photographed. The recorded VF includes the rapeseed plants and the weeds. The nitrogen content in g/kg (N) was measured from a sample of the FBM by Kjeldahl method [20]. The crop canopy parameters were measured during three field campaigns, two before winter and one after winter, Table 3. At each field campaign, Table 3, the ESU at a given sample location was positioned near the one from the previous field campaign.

Table 2. Descriptive statistics for the measured crop canopy parameters

Parameters	Number of ESU	Mean	SE Mean	StDev	Minimum	Maximum
FBM (g/m^2)	30	1058.00	151.00	829.00	146	2 761
DBM (g/m^2)	30	124.50	17.80	97.60	18	332
VF (%)	30	0.58	0.05	0.28	0.15	1.00
NbPlant (nb/m^2)	30	36.13	3.18	17.42	10	95
PlantH (cm)	45	15.67	0.83	5.57	9	28
N (g/kg)	30	10.28	0.26	1.39	7.54	13.46

Because of the meteorological conditions, some of the plants started growing immediately after sowing but many had more than a month delay. Particularly the plots P2 and P3 were with plants in very different phonological phases, from BBCH13 to BBCH19 [21], during the before winter field campaign. This difference in the phenological phase was completely reduced after winter, where all plots were at BBCH50/BBCH51.

Remote sensing data

Sentinel-2, sensor S2A and S2B, data was used for the study. Cloud free images closest to the field data collection were selected at Copernicus Open Hub Access (https://scihub.copernicus.eu). All spectral bands of 10 m and 20 m spatial resolution are used, from level 2A products. It provided 10 spectral bands from 490 nm to 2 190 nm, resampled at 10 m spatial resolution.

Methods

Two types of models for crop canopy retrieval are studied: (1) the parametric univariate regression models with a Vegetation index (VI) as independent variable and (2) the non-parametric multivariate regression models with all the 10 spectral bands from the remote sensing data as independent variables. In both models the crop canopy parameter is the dependent variable.

Table 3. Timing of the field campaigns and satellite acquisitions with corresponding measured parameters

Field Plot	Nb of ESU	Before Winter			After Winter		
		Sampling date	Crop Canopy param.	Sentinel-2 image date (sensor)	Sampling date	Crop Canopy param.	Sentinel-2 image date (sensor)
P1	9	23.11.2017	FBM, DBM, VF, NbPlant, PlantH	29.11.2017 (S2A)	01.4.2018	FBM, DBM, VF, NbPlant, PlantH, N	03.04.2018 (S2B)
		13.12.2017	PlantH, N	12.12.2017 (S2A)			
P2	3	23.11.2017	FBM, DBM, VF, NbPlant, PlantH	29.11.2017 (S2A)	01.4.2018	FBM, DBM, VF, NbPlant, PlantH, N	03.04.2018 (S2B)
		13.12.2017	PlantH, N	12.12.2017 (S2A)			
P3	3	24.11.2017	FBM, DBM, VF, NbPlant, PlantH	29.11.2017 (S2A)	01.4.2018	FBM, DBM, VF, NbPlant, PlantH, N	03.04.2018 (S2B)
		13.12.2017	PlantH, N	12.12.2017 (S2A)			

Model Selection

The first step consists in model conceptualization and selection. The selected models are parametric univariate and non-parametric multivariate regression models, as described in [22], and they are applied using the Automated Radiative Transfer Models Operator (ARTMO) package (http://ipl.uv.es/artmo/).

In the first type of models it is not really VI that is selected but rather general formula to be used, because all the top of canopy reflectance of the spectral bands are tested with all formulae, Table 4. Also, different fitting functions are used for the regression: linear, exponential, logarithmic, power and polynomial. The first six VI from Table 4, are the same one used in the preliminary study to determine the

samples location. Two more 3 bands VI were added to the list because they are reported [23–24] to perform better for retrieval of biophysical variables and leaf nitrogen concentration.

The evaluated non-parametric multivariate regression models are Least Square Linear Regression (LSLR), Principal Components Regression (PCR), Partial Least Squares Regression (PLSR), Kernel Ridge Regression (KRR), Gaussian Processes Regression (GPR) and the Variational Heteroscedastic variant of the Gaussian Processes Regression (VHGP). For non-parametric multivariate regression models the "curse of dimensionality" [25] could represent a problem. Therefore, some of the selected models have dimension reduction, like PCR, PLSR, KRR. PCR and PLSR have been developed for cases, as is of this study, where there are many, possibly correlated, predictor variables and relatively few samples [26]. GPR is reported [27] to be a robust model for biophysical variables retrieval. GPR and VHGP are especially valuable [23] because they calculate a Coefficient of Variation (CV = σ/μ), where σ is the Standard Deviation (SD) around the estimated variable and μ the mean estimated variable. CV provides relative uncertainty of the estimated variable in %. Finally, LSLR was selected as the oldest method for comparison with the others.

Model calibration/fitting evaluation and validation

The model calibration, evaluation and selection will be treated together, because model selection is an integral part of the model fitting process and furthermore in the present study, the goal is not to evaluate one model alone, but rather compare and select a model [28].

In the calibration step the parameters will be adjusted to make the model as consistent as the available data [29]. Model evaluation according to [30] consists in preliminary experiments and test of alternative scenarios. This part of the work was done previously in [31] and the results will be used in the development of the models in the present study. Namely, bare soil pixels are included in the input data for the models and the reflectance data is from 1 pixel, corresponding to the sample, without averaging with the pixels around. Because outliers in the data could cause distortion in the models [32], all crop canopy variables were tested for outliers with Grubbs test [33]. No outliers were detected at 5 % level of significance for smallest and largest data values, apart from one sample for NbPlant. The outlier sample is from plot P1, where the sowing rate is 80 plants/m^2 and the measured sample had 95 plants/m^2. The decision was to remove the sample, because it was probably due to local malfunctioning of the sowing machine.

Table 4. Type of VI testes in the study. Ra, Rb and Rc are the reflectance for a given wavelength.

Type index	The formula is from the VI	Formula	Reference
2 bands Simple ratio of reflectances	RVI (Ratio Vegetation Index)	Ra / Rb	[9]
2 bands normalized difference ratios of reflectances	OSAVI (Optimized soil adjusted index)	$1.16 \times (Ra - Rb) / (Ra + Rb + 0.16)$	[7]
2 bands normalized difference ratios of reflectances	SAVI (Soil adjusted vegetation index)	$1.5 \times (Ra - Rb) / (Ra + Rb + 0.5)$	[18]
2 bands Simple ratio of reflectances	CIredEdge (Red-edge Chlorophyll Index)	$(Ra / Rb) - 1$	[17]
3 bands normalized difference ratios of reflectances	EVI (The enhanced vegetation index)	$2.5 \times ((Ra - Rb) / (Ra + 6 \times Rb - 7.5 \times Rc + 1))$	[3]
2 bands normalized difference ratios of reflectances	NDVI (Normalized Difference Vegetation Index)	$(Ra - Rb) / (Ra + Rb)$	[9]
3 bands normalized difference ratios of reflectances	3BSI-Verrelst	$(Ra - Rc) / (Rb + Rc)$	[23]
3 bands normalized difference ratios of reflectances	3BSI-Tian	$(Ra - Rb - Rc) / (Ra + Rb + Rc)$	[24]

In model evaluation there is also the notion of evaluation of uncertainty and accuracy. In the present study there is an uncertainty because of the way the field data is collected (from only $1m^2$, without repetition of the measurements and geo-located with GPS with an accuracy of $\pm 3-5$ m), that could be considered as part of the dependent variables noise, but this uncertainty is not considered in the present study.

Each goodness-of-fit statistic gives certain aspect of the model accuracy [34]. In this study the accuracy of the model will be based on Root Mean Square Error (RMSE), for the magnitude of error, and Coefficient of determination (R^2), for the spatial patterns [34].

Leave-one-out cross-validation (LOOCV) will be used to get the expected prediction error, to help select the best model and to ensure that the model does not overfit. All models will be ranked by Normalized RMSE (NRMSE in %),

NRMSE% = 100 × (RMSE / Range(Obs)), because it is a goodness-of-fit measurement that is suitable for comparison [34].

Table 5. Best parametric and non-parametric models for each studied crop canopy parameter. For all models, pixels with bare soil are included, except model marked by *.

Variable	Model	Best Bands	RMSEcv	R²cv	NRMSEcv %
FBM (g/m²)	EVI / Polynomial	Ra:842, Rb:560, Rc:665	421	0.75	15
	PLSR		429	0.74	16
DBM (g/m²)	EVI / Polynomial	Ra:842, Rb:560, Rc:665	52	0.73	16
	GPR	560;740;490;842	52	0.73	16
VF (%)	3BSI-Tian / Linear	Ra:842, Rb:705, Rc:560	0.14	0.81	14
	PCR		0.15	0.78	16
NbPlant (nb/m²)	3BSI-Verrelst / Polynomial	Ra:665; Rb:842;Rc:560	9	0.73	14
	PLSR		10	0.68	15
PlantH (cm)	3BSI-Verrelst / Power*	Ra:490, Rb:842, Rc:560	4	0.53	20
	VHGR	560;842;665;490	4	0.72	15
N (g/kg)	VHGR	665;842	2	0.74	15

Results and discussion

The best parametric univariate regression models with a VI as independent variable are ranked by NRMSEcv and R^2cv > 0.5, for every variable, Table 5. However, the models for N and PlantH did not perform well with the added bare soil pixels. It was clearly visible in the scatter plot of "residuals vs predicted value" and "measured vs estimated". New models for N and PlantH are fitted without the bare soil pixels. No satisfactory model was found for N. A weaker model was found for PlantH, Table 5.

The best non-parametric multivariate regression models with all the spectral bands from the remote sensing data as independent variables, ranked by NRMSEcv and R^2cv > 0.5, for every variable are in Table 5. All non-parametric models behave correctly with the bare soil pixels included.

The comparison between parametric and non-parametric models for every crop canopy parameter shows, Table 5, that in terms of goodness-of-fit cross-validation statistic the models have comparable performance. To be able to further

distinguish between their performance, each model is applied to the remote sensing images and the estimated values are compared to the measured values. The models that meet the criteria of $R^2 > 0.514$ [36] and slop > 0.6 are considered only, Table 6 and Fig. 2.

Table 6. Comparison between measured/estimated values from models, where $R^2>0.514$ and slop > 0.6

Model	R2	Intercept	Slop	P
S2_03042018_FBM_SI	0.84290	250.43	0.80541	7.86E-08
S2_03042018_ML_PLS_FBM	0.82123	316.59	0.78671	2.23E-07
S2_29112017_ML_GP_DBM	**0.89341**	**13.003**	**0.74553**	**3.44E-09**
S2_03042018_ML_GP_DBM	**0.88951**	**24.134**	**0.84835**	**4.60E-09**
S2_03042018_DBM_SI	0.82875	31.317	0.79268	1.58E-07
S2_29112017_VF_SI	**0.66756**	**0.098277**	**0.76144**	**3.49E-05**
S2_03042018_VF_SI	**0.85872**	**0.079719**	**0.84443**	**3.33E-08**
S2_12122017_ML_VHGP_Ni	**0.91985**	**0.94872**	**0.89149**	**3.47E-10**
S2_03042018_ML_VHGP_Ni	**0.93942**	**0.84355**	**0.9036**	**3.66E-11**
S2_29112017_ML_PLS_NbPlant	0.78664	5.9884	0.81215	9.37E-07
S2_03042018_ML_PLS_NbPlant	0.77134	7.2667	0.70727	3.55E-06
S2_29112017_NbPlant_SI	**0.79727**	**3.9772**	**0.79844**	**6.19E-07**
S2_03042018_NbPlant_SI	**0.73464**	**8.5499**	**0.75636**	**1.11E-05**
S2_29112017_ML_VHGP_PlantH	**0.86076**	**2.2378**	**0.76445**	**2.96E-08**
S2_12122017_ML_VHGP_PlantH	**0.70192**	**3.7626**	**0.63536**	**1.43E-05**
S2_03042018_ML_VHGP_PlantH	**0.87996**	**2.8455**	**0.81848**	**8.96E-09**

No model could estimate, according to the proposed criteria, the FBM before winter, however the DBM is estimated for before and after winter with the GPR model. On the other hand, FBM and DBM are highly correlated with Pearson's correlation (r) of 0.99. For both periods the VF is estimated by 3BSI-Tian/linear, N and PlantH by VHGP. The NbPlant is estimated by the two types of models, the simpler will be considered, namely 3BSI-Verrelst/Polynomial.
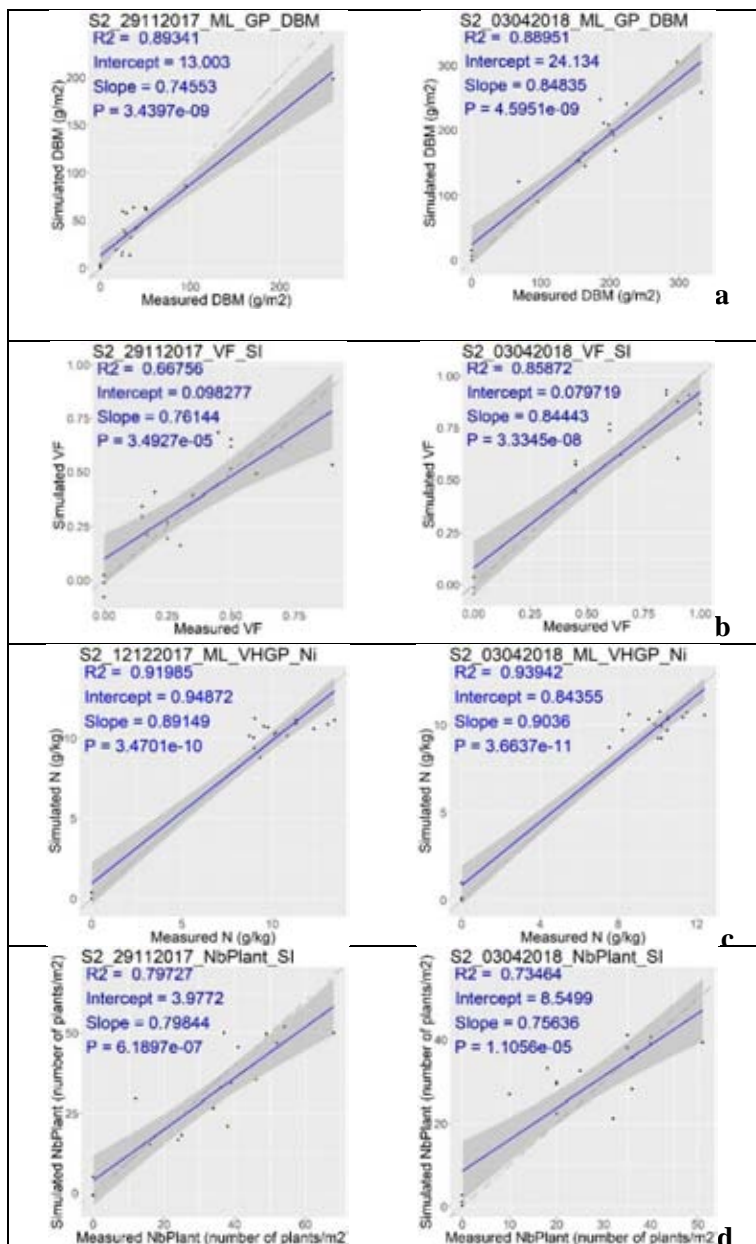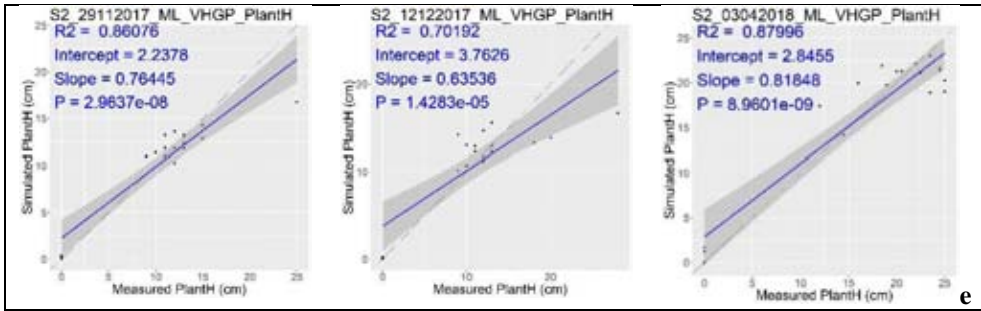
*Fig. 2. Scatter plots of measured/estimated values from models, where R² > 0.514
and slop > 0.6. a) DBM; b) VF; c) N; d) NbPlant; e) PlantH*

It is difficult to make comparison between the retrieval methods from the literature, because the different studies did not evaluate the same variables or used other measurement for accuracy [3, 7]. The DBM was evaluated by fitting parametric models and VIs [7], but the DBM is sampled from the whole growing season of the rapeseed, not only until Inflorescence Emergence stage (BBCH50). The NbPlant was sampled only at emergence and no measurement of accuracy is published [9] or Unmanned Aerial Vehicle (UAV) is used with shape feature recognition or classification [36–37]. The VF is studied with UAV with spatial resolution of 2.5 cm [8]. The model for retrieval of PlantH was evaluated by standard error of the estimate (SEE) [3], which is not one of the goodness-of-fit measurements of the present study. PlantH was also evaluate with RGB camera mounted on a UAV [38–39].

Selected model for each variable

Aboveground Fresh Biomass (FBM) in g/m^2: no model could estimate, according to the proposed criteria, the FBM before and after winter.

Dry Biomass (DBM) in g/m^2: for DBM retrieval, the GPR model is selected with the most relevant bands being the blue, green, middle red-edge and near infrared (λ = 560; 740; 490; 842). In related studies [3, 7, 40, 41] it was found that for crops or grass, DBM is best retrieved with visible and near-infrared reflectance which is in accordance with our results.

The relative uncertainty, expressed by CV, is higher than 10 % for all periods, Fig. 3, meaning that those areas are retrieved with high uncertainty. The higher is the DBM the lower is the relative uncertainty of the model.
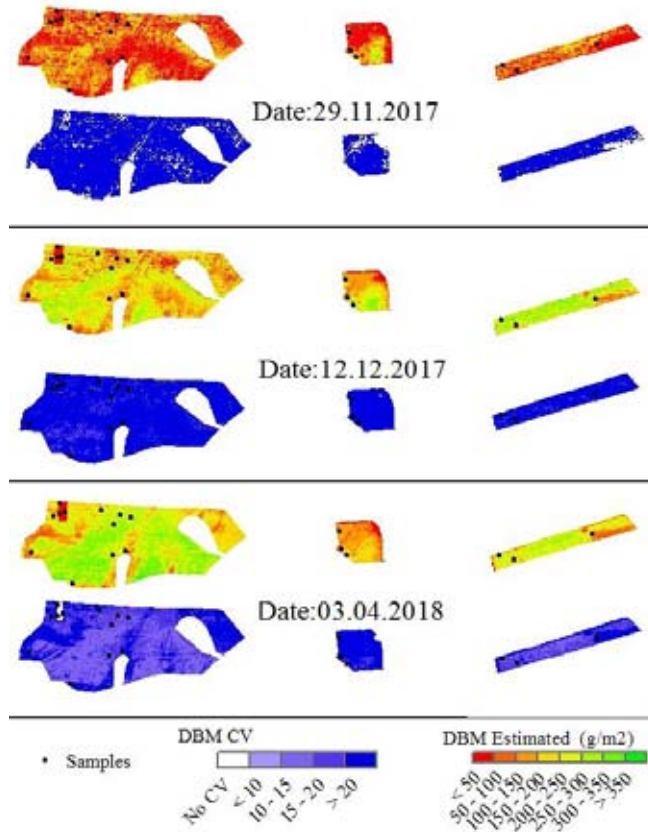
Fig. 3. GPR model for DBM retrieval, applied to the selected remote sensing images before winter and after winter

Vegetation Fraction (VF): for VF retrieval, the 3BSI-Tian VI and linear fitting function is selected with the most relevant bands being the green, shortest red-edge and near infrared (λ = 560; 705; 842). In related studies [8] it is reported that the VF for rapeseed crop before flowering is best correlated with green and red reflectance. For vegetation in general, VF is reported to be characterized [42] by green, red, shortest infra-red reflectance, red and near infra-red [43] or even only by visible reflectance [8]. It was remarked [43] that for higher vegetation cover the estimation is poorer. However, we cannot verify this statement in our study as no model with uncertainty calculation was selected.
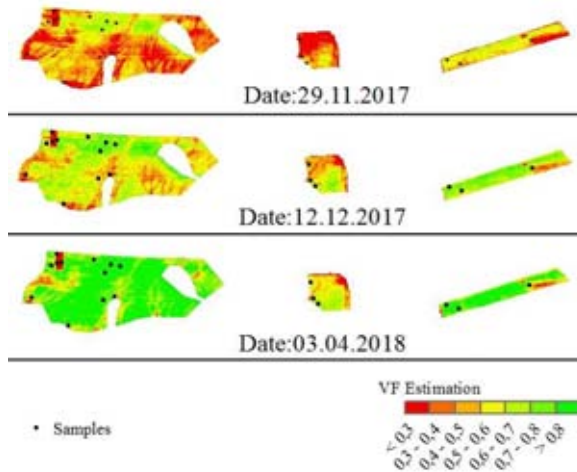
*Fig. 4. 3BSI-Tian VI / linear model for VF retrieval, applied
to the selected remote sensing images before winter and after winter*

Plant density (NbPlant) in nb/m^2: for NbPlant retrieval, the 3BSI-Verrelst VI and polynomial fitting function is selected with the most relevant bands being the green, red and near infrared ($\lambda = 560; 665; 842$). In related studies [9, 44] it is reported that NbPlant is best correlated to red, green and near infrared reflectance which is in accordance with our results. The after winter period shows decrease of the NbPlant, Fig. 5, compared to the before winter period. The sampled measurements show the same trend.
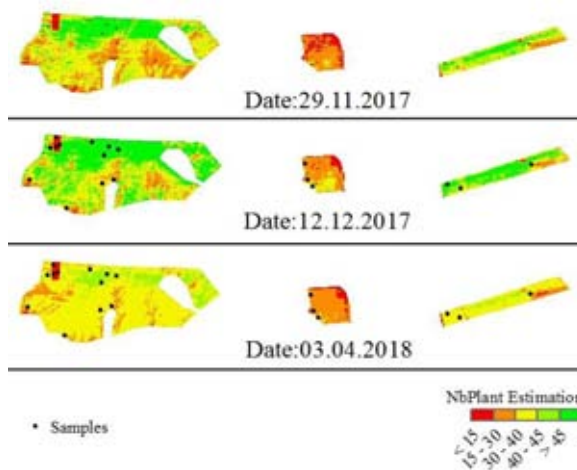
*Fig. 5. 3BSI-Verrelst VI / polynomial model for NbPlant retrieval, applied
to the selected remote sensing images before winter and after winter*

Mean Plant Height (PlantH) in cm: for PlantH retrieval, the VHGP model is selected with the most relevant bands being the visible and near infrared ($\lambda = 490$; 560; 665; 842). In related studies [3] it is reported that PlantH is best correlated to same reflectance as calculated by our model, Fig. 6.

Nitrogen content in fresh biomass (N) in g/kg: for N (g/kg) retrieval, the VHGP model is selected with the most relevant bands being the red and near infrared ($\lambda = 665$; 842). In related studies [12–14, 41] it is reported that N is best correlated to visible and near infra-red. Some of those studies report also correlation to the longer red-edge, others to the shorter red-edge. One of the relevant bands selected by our model is close to the absorption of chlorophyll, located around 675 nm, and reported to characterize the nitrogen status of leaves [45] and the other is the near infrared that is reported [47] to determine the canopy structure. Crop phenology is found to be cause for substantial difference in canopy reflectance vs canopy chlorophyll content [46] and therefore canopy N. This is probably why in our study no parametric model could fit the before and after winter crop stage. However, the selected VHGP model gives almost constant uncertainty, between 10–20 %, Fig. 7, for before and after winter period where the rapeseed crop is in different phenological phases.
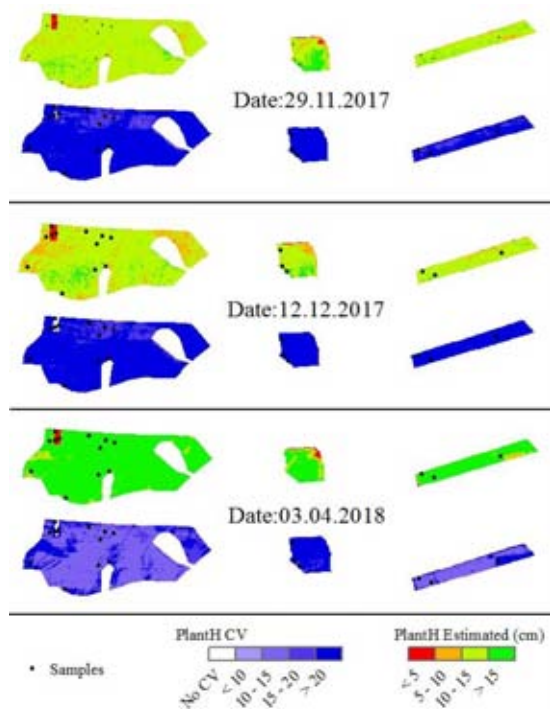
Fig. 6. VHGP model for PlantH retrieval, applied to the selected remote sensing images before winter and after winter

Conclusion

This study demonstrated that rapeseed crop canopy parameters before and after winter, such as, aboveground dry biomass (DBM), vegetation fraction (VF), plant density (NbPlant), mean plant height (PlantH), nitrogen content (g/kg) in fresh biomass (N), can be retrieved directly from remote sensing measurement from Sentinel-2 with good accuracy in real farming conditions of North East Bulgaria.
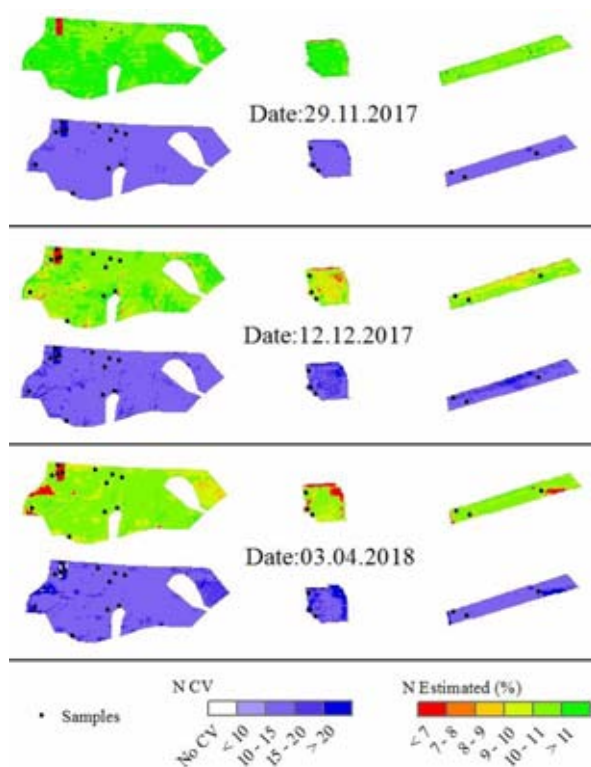
Fig. 7. VHGP model for N retrieval, applied to the selected remote sensing images before winter and after winter

For some of the parameters, VF (RMSEcv = 0.14 %), NbPlant (RMSEcv = 9 nb/m^2), the best models were parametric and for others, DBM (RMSEcv=52 g/m^2), PlantH (RMSEcv = 4 cm), N (RMSEcv = 2 g/kg), non-parametric. It also demonstrated that for FBM no model could be selected for the both periods: before and after winter. The retrieved parameters and classification techniques can be used for delineating within-field units for which to develop different management.

Some of the studies parameters are not independent from one another. For example, FBM, VF and NbPlant, or PlantH, NbPlant and FBM. To be able to increase their retrieval accuracy multi-output regression algorithms can be used [50] in a future work.

Acknowledgment

References

1. FAOSTAT, 2014. Online statistical database of the Food and Agricultural Organization of the United Nations. http://faostat.fao.org
2. Diepenbrock, W., Yield analysis of winter oilseed rape (Brassica napus L.): A review. Field Crops Research, 2000, 67, 1, 35–49.
3. Bartoszek, K., Usefulness of MODIS data for assessment of the growth and development of winter oilseed rape, Zemdirbyste-Agriculture, 2014, 101, 4, 445–52.
4. She, B., J. F. Huang, D. Y. Zhang, and L. S. Huang., Assessing and Characterizing Oilseed Rape Freezing Injury Based on MODIS and MERIS Data. International Journal of Agricultural and Biological Engineering, 2017, 10, 3, 143–57.
5. Wojtowicz, M., A. Wojtowics, and J. Piekarczyk. Application of Remote Sensing Methods in Agriculture. Communication in Biometry and Crop Science. 2015, 11, 1, 31–50.
6. Иванова, Р., Рапицата - култура на настоящето и бъдещето. Второ допълнително и преработено издание. Издателство «Виденов и син», София, 2012. стр. 306. (In Bulgarian)
7. Han, J., C. Wei, Y. Chen, *et. al*. Mapping Above-Ground Biomass of Winter Oilseed Rape Using High Spatial Resolution Satellite Data at Parcel Scale under Waterlogging Conditions. Remote Sensing, 2017, 9, 3, 1–21.
8. Fang, S., W. Tang, Y. Peng, *et. al*. Remote Estimation of Vegetation Fraction and Flower Fraction in Oilseed Rape with Unmanned Aerial Vehicle Data. Remote Sensing, 2016, 8, 416, 1–19.
9. Piekarczyk, J., M. Wójtowicz, and A. Wójtowicz.. Estimation of Agrinomic Parameters of Winter Oilseed Rape from Field Reflectance Data. Acta Agrophysica. 2006, 8, 1, 205–218.
10. Rivera, J. P., J. Verrelst, J. Delegido, F. Veroustraete, and J. Moreno. On the Semi-Automatic Retrieval of Biophysical Parameters Based on Spectral Index Optimization. Remote Sensing, 2014, 6, 6, 4927–51.

11. Yu, X., H. Lu, and Q. Liu. Deep-Learning-Based Regression Model and Hyperspectral Imaging for Rapid Detection of Nitrogen Concentration in Oilseed Rape (Brassica Napus L.) Leaf. Chemometrics and Intelligent Laboratory Systems, 2018, 172, 188–93.
12. Li, L., S. Wang, T. Ren, et al. Ability of Models with Effective Wavelengths to Monitor Nitrogen and Phosphorus Status of Winter Oilseed Rape Leaves Using in Situ Canopy Spectroscopy. Field Crops Research, 2018, 215, 1, 173–186.
13. Li, L., J. Lu, S. Wang, et al. Methods for Estimating Leaf Nitrogen Concentration of Winter Oilseed Rape (Brassica Napus L.) Using in Situ Leaf Spectroscopy. Industrial Crops and Products, 2016, 9, 194–204.
14. Zhang, X., F. Liu, Y. He, and X. Gong. Detecting Macronutrients Content and Distribution in Oilseed Rape Leaves Based on Hyperspectral Imaging. Biosystems Engineering, 2013, 115, 1, 56–65.
15. Wang, F., J. Huang, Y. Wang, Z. Liu, and F. Zhang. Estimating Nitrogen Concentration in Rape from Hyperspectral Data at Canopy Level Using Support Vector Machines. Precision Agriculture, 2013, 14, 2, 172–183.
16. Bohnam, C. D. Measurements for Terrestrial Vegetation Measurements, 2nd edition ed. Wiley-Blackwell, 2013. 246 p.
17. Clevers, J. G. P. W, and A. A Gitelson. Remote Estimation of Crop and Grass Chlorophyll and Nitrogen Content Using Red-Edge Bands on Sentinel-2 and -3. International Journal of Applied Earth Observations and Geoinformation, 2013, 23, 344–351.
18. Hatfield, J. L., and J.H. Prueger. Value of Using Different Vegetative Indices to Quantify Agricultural Crop Characteristics at Different Growth Stages under Varying Management Practices. Remote Sensing, 2010, 2, 2, 562–78.
19. Gitelson, A. A., Y. J. Kaufman, R. Stark, and D. Rundquist. Novel Algorithms for Remote Estimation of Vegetation Fraction. Remote Sensing of Environment, 2002, 80, 1, 76–87.
20. AOAC, Nitrogen (Total) in Fertilizers: Kjeldahl Method No. 978 1990, 02, 18–19
21. Lancashire, P. D., H. Bleiholder, T. Van Den Boom, et al. A Uniform Decimal Code for Growth Stages of Crops and Weeds. Annals of Applied Biology, 1991, 119, 3, 561–601.
22. Verrelst, J., G. Camps-Valls, J. Muñoz-Marí et al.. Optical Remote Sensing and the Retrieval of Terrestrial Vegetation Bio-Geophysical Properties - A Review. ISPRS Journal of Photogrammetry and Remote Sensing, 2015, 108, 273–290.
23. Verrelst, J., J. Pablo, F. Veroustraete, et al. Experimental Sentinel-2 LAI Estimation Using Parametric, Non-Parametric and Physical Retrieval Methods – A Comparison. ISPRS J. of Photogrammetry and Rem. Sens., 2015, 108, 260–272.
24. Tian, Y. C., K. J. Gu, X. Chu, et al. Comparison of Different Hyperspectral Vegetation Indices for Canopy Leaf Nitrogen Concentration Estimation in Rice. Plant and Soil, 2013, 376, 1, 193–209.
25. Bellman, R. Adaptive Control Processes: A Guided Tour. Princeton, NJ: Princeton. University Press. 2016. 276 p.
26. Mevik, B-H., and R. Wehrens. The Pls Package: Principal Component and Partial Least Squares Regression in R. Journal of Statistical Software, 2007, 18, 2, 1–22.

27. Verrelst, J., L. Alonso, G. Camps-valls, J. Delegido, and J. Moreno, Retrieval of Vegetation Biophysical Parameters Using Gaussian Process Techniques, IEEE Transactions on Geoscience and Remote Sensing, 2012, 50, 5, 1832–43.

28. Cawley, G. C., and N. L. Talbot, On Over-Fitting in Model Selection and Subsequent Selection Bias in Performance Evaluation, Journal of Machine Learning Research, 2010, 11, 2079–2107.

29. Rykiel, E. J, Testing Ecological Models : The Meaning of Validation, Ecological Modelling, 1996, 90, 229–244.

30. Gardner, R. H., and R. H., Urban. Models in Ecosystem Science, Canham C. D., Cole J. J. and Lauenroth W. K. Ed. Princeton University Press, Princeton, New Jersey, 2003, Ch. "Model validation and testing: past lessons, present concerns, future prospects", 184–203.

31. Ganeva, D., 'Semiautomatic Retrieval of Biomass Based on Vegetation Index Optimization and Learning Machine Methods for Winter Rapeseed Crops', in Proceedings of the Fourteenth International Scientific Conference – SPACE, ECOLOGY, SAFETY, Sofia, Bulgaria, 7–9 November 2018, 299–305.

32. Obsborne, J. W., and A. Overbay, The Power of Outliers (and Why Researchers Should Always Check for Them), Journal of Chemical Information and Modeling, 2013, 53, 9, 1689–99.

33. Grubbs, F. E., G., Beck, Extension of sample sizes and percentage points for significance tests of outlying observations. Technometrics, 1972, 14, 847–854.

34. Richter, K., C. Atzberger, T. B. Hank, and W. Mauser, Derivation of Biophysical Variables from Earth Observation Data : Validation and Statistical Measures, *Journal of Applied Remote Sensing*, 2012, 6, 1, 1–24.

35. Rogerson, P.A. *Statistical method for Geography*. First edit. London: Sage Publications. 2001. 236 p.

36. Zhao, B., J. Zhang, C. Yang, G. Zhou, and Y. Ding, Rapeseed Seedling Stand Counting and Seeding Performance Evaluation at Two Early Growth Stages Based on Unmanned Aerial Vehicle Imagery, Frontiers in Plant Sci., 2018, 9, 1362, 1–17.

37. Jin, X., S. Liu, F. Baret, M. Hemerlé, and A. Comar, Remote Sensing of Environment Estimates of Plant Density of Wheat Crops at Emergence from Very Low Altitude UAV Imagery, Remote Sensing of Environment, 2017, 198, 105–114.

38. Bendig, J., K. Yu, H. Aasen, et al., Combining UAV-Based Plant Height from Crop Surface Models, Visible, and near Infrared Vegetation Indices for Biomass Monitoring in Barley, International Journal of Applied Earth Observation and Geoinformation, 2015, 39, 79–187.

39. Li, W., Z. Niu, H. Chen, et al., Remote Estimation of Canopy Height and Aboveground Biomass of Maize Using High-Resolution Stereo Images from a Low-Cost Unmanned Aerial Vehicle System, Ecological Indicators, 2016, 67, 637–648.

40. Näsi, R., N. Viljanena, J. Kaivosojab, et al., Assessment of Various Remote Sensing Technologies in Biomass and Nitrogen Content Estimation Using an Agricultural Test Field, The International Archives of the Photogrammetry, Remote Sensing and Spatial Information Sciences, Volume XLII-3/W3, 2017 Frontiers in Spectral Imaging and 3D Technologies for Geospatial Solutions, 25–27 October 2017, Jyväskylä, Finland, XLII, 2017, 25–27.

41. Hansen, P. M., and J. K. Schjoerring, Reflectance Measurement of Canopy Biomass and Nitrogen Status in Wheat Crops Using Normalized Difference Vegetation Indices and Partial Least Squares Regression, Remote Sensing of Environment, 2003, 86, 4, 542–553.
42. Gitelson, A. A., R. Stark, U. Grits, et al., Vegetation and Soil Lines in Visible Spectral Space: A Concept and Technique for Remote Estimation of Vegetation Fraction', International Journal of Remote Sensing, 2002, 23, 13, 2537–62.
43. Purevdorj, T., R. Tateishi, T. Ishiyama, and Y. Honda, International Journal of Relationships between Percent Vegetation Cover and Vegetation Indices, International Journal of Remote Sensing, 1998, 19, 18, 3519–35.
44. Warren, G., and G. Metternicht, Agricultural Applications of High-Resolution Digital Multispectral Imagery, Photogrammetric Engineering & Remote Sensing, 2005, 71, 5, 595–602.
45. Penuelas, J., and I. Filella, Technical Focus: Visible and Nearinfrared Reflectance Techniques for Diagnosing Plant, Trends in Plant Science, 1998, 3, 4, 151–156.
46. Peng, Y., A. Nguy-Robertson, T. Arkebauer, and A. A. Gitelson, Assessment of Canopy Chlorophyll Content Retrieval in Maize and Soybean : Implications of Hysteresis on the Development of Generic Algorithms, Remote Sens, 2017, 9, 226, 1–18.
47. Baret, F., and T. Fourty. Radiometric estimates of nitrogen status of leaves and canopies. In: Lemaire G, ed. Diagnosis of nitrogen status in crops. Heidelberg, Germany: Springer-Verlag, 1997, 201–227.
48. Tuia, D., J. Verrelst, L. Alonso, F. Pérez-Cruz, and G. Camps-Valls, Multioutput Support Vector Regression for Remote Sensing Biophysical Parameter Estimation, IEEE Geoscience and Remote Sensing Letters, 2011, 8, 4, 804–808.

ДИСТАНЦИОННО ОПРЕДЕЛЯНЕ НА ПАРАМЕТРИ НА ПОСЕВА НА ЗИМНА РАПИЦА ЧРЕЗ СТАТИСТИЧЕСКИ РЕГРЕСИОННИ АЛГОРИТМИ С ПОМОЩТА НА МУЛТИСПЕКТЪРНИ ИЗОБРАЖЕНИЯ ОТ SENTINEL-2

Д. Ганева, Е. Руменина

Резюме

Определянето на параметри на посева на земеделски култури е важна задача за дистанционното наблюдение на селското стопанство и за изготвяне на стратегии за управление на полетата. Основната цел на това изследване е да се оцени извличането на параметри на посева на зимна рапица за два периода от растежа: преди презимуване и след презимуване, чрез параметрични и непараметрични статистически модели и Sentinel-2 изображения, в реални условия на земеделие в Североизточна България. За калибрирането на моделите се използват in-situ данни от три полеви кампании. За повечето от

изследваните параметри бяха идентифицирани модели с добра точност, с изключение за надземната свежа биомаса. Най-добрите модели за общо площно покритие (RMSEcv = 0.14 %) и гъстота на посева (RMSEcv = 9 nb/m^2) са параметрични модели с три-канален вегетационен индекс (3BSI-Tian) и линейна функция за първия, 3-канален вегетационен индекс (3BSI-Verrelst) и полиномиялна за втория параметър. За надземна суха биомаса (RMSEcv = 52 g/m^2), средна височина на растенията (RMSEcv = 4 cm) и съдържание на азот в свежа биомаса (RMSEcv = 2 g/kg) най-добрите модели са непараметрични, *Gaussian Processes Regression* за първия параметър и *Variational Hetero-scedastic* вариант на *Gaussian Processes Regression* за другите две.

SCALES FOR MEASURING
UAV MICRO-MOTOR STATIC THRUST

Svetoslav Zabunov, Garo Mardirossian

Space Research and Technology Institute – Bulgarian Academy of Sciences

Abstract

With the advent of micro-sized unmanned helicopters and airplanes weighing under 250 g certain needs for measurement instruments and setups are emerging. The authors have identified the lack of micro-motor measurement instruments and more specifically a static thrust gauge device. For this reason, a scales to measure static motor thrust was advised and further developed as a laboratory setup.

The motors that are subject to testing with the described instrument are the brushed micro-sized coreless electric motors, well suited for micro-drones with total weight under 250 g. The scale is fitting different sizes of micro-motors and appropriate control of the input voltage is provided. The instrument is measuring simultaneously the applied voltage to the motor and the current it consumes, along with the static thrust the motor generates. The scale is versatile – it measures both pusher and tractor propeller configurations. Pusher propellers in micro-drones are gaining significant attention lately due to their better efficiency characteristics.

Introduction

The miniaturization of unmanned aerial vehicle avionics in the last few years has led to increased interest in the design of drones having maximum total weight less than or equal to 250 g [1]. Further, in the legislation of several countries, a registration requirement was recently introduced, applying to drones, as well as drone owners of machines weighing over 250 g.

There is a long list of benefits the micro-UAVs offer in comparison to larger drones. Most important of these are:

- Low cost for manufacturing and maintenance.
- Lower risk for damaging objects and living beings due to less weight and decreased kinetic energy of the rotors.
- Ease of transportation and storage.
- Low visibility due to small dimensions.
- Reduced RADAR signature [2–6].
- Reduced acoustic signature.
- Negotiability through windows and manoeuvrability inside buildings.

The current paper discloses a test instrument, developed by the authors, used to measure the static thrust generated by coreless brushed micro-motors, suitable for micro-drones. The test setup is shown in Fig. 1. The proposed device is a weighing scale with three arms and is designed to be implemented in examining micro-motors having 7 mm diameter of the motor body. There are different motor sizes according to motor body length: 17 mm, 20 mm, etc. Motors with different body diameter are also suitable to be tested with the proposed equipment after minor modifications.

Fig. 1. Scale for measuring static thrust of micro-motors

Fig. 2 presents some of the most frequently used coreless micro-motors for small UAVs. All of the motors up to 8.5 × 20 mm are powered with maximum supply voltage of 3 V. The motor mounted on the scales in Fig. 1 is a 7 × 20 mm type motor (Fig. 2 – left).

Fig. 2. Brushed coreless micro-motors, frequently employed in micro-UAVs.
From left to right: 7 × 20 mm, 7 × 16 mm, 6 × 14 mm, 8.5 × 20 mm.

Construction

The construction of the scales is based on the balanced scales principle – the scales arms have equal length, pivoted on a fulcrum. Nevertheless, unlike the classic balance scales, the instrument proposed here has three, instead of two arms with equal length. The arms are positioned in one plane and are at 90 degree angles from one another.
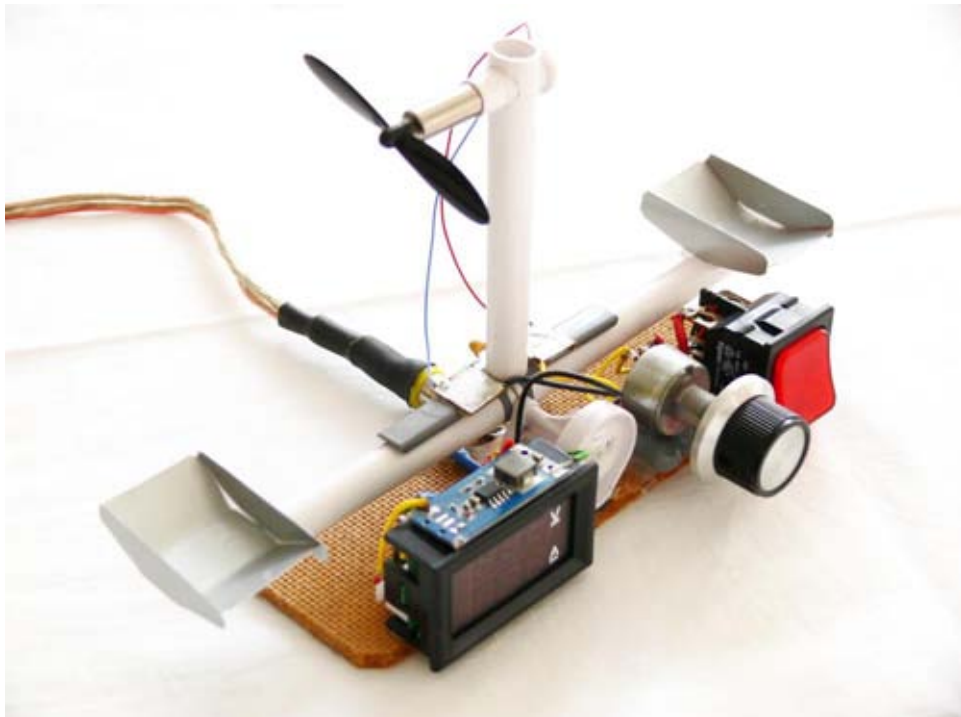
Fig. 3. Static thrust scales in equilibrium

Applying the same moment of force, but with inverse signs, to two of the arms would keep the scales in equilibrium. Due to arms' equal length, in order to generate equal moments of force one should apply equal forces to arms' ends, such that each force is perpendicular to the given arm and lies in the plane, defined by the three arms.

The moving part – the arms structure – is secured to the scales base through a bearing, acting as the scales fulcrum. The friction of the bearing introduces an error of less than 0.1 g.

The instrument in balance is shown in Fig. 3. Two of the arms are horizontal and have weighing dishes where weights may be placed. The third arm is vertical and employs a motor mount.

Electrical schematic

The scales instrument has a socket for supplying electrical power through a cable. The voltage delivered to the device is 3.6 V, coming from a single cell Li-Ion battery. The motor voltage is filtered by a 100 nF capacitor. Further, the voltage is manually regulated by means of a powerful (2 W) 10 ohm potentiometer, connected in series with the motor.
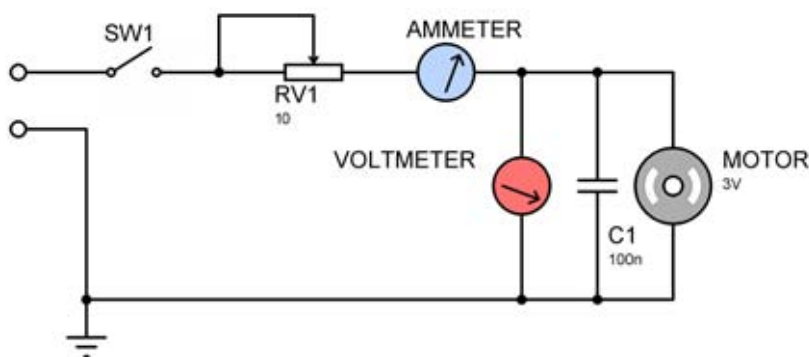
Fig. 4. Scales electrical schematic

A digital voltmeter measures the voltage applied to the motor and displays the result in volts on a red coloured LED digital display (Fig. 1, 4 and 6). The current flowing through the motor is measured by a digital ammeter, displaying the current in amperes on a blue coloured LED digital display (Fig. 1, 4 and 6). Both metering instruments were laboratory calibrated. The electrical circuit is powered on and off using a master switch (the red coloured switch on the right-hand side of the scales – Fig. 1).

Measurements

In Fig. 3 and 6, the motor mount was populated with a 7 × 20 mm coreless brushed motor having shaft diameter of 0.9 mm. On the shaft, a 55 mm tractor propeller was mounted (black coloured propeller). This propeller is standard for the attached motor and generally delivers maximum static thrust in the range of 20–22 g. A common rule for multi-rotor helicopters is to fly at 50 % of the maximum static thrust a rotor is capable of generating. For this reason the given motor has been tested at 10 g static thrust.

For a weight of 10 g two coins of 50 Bulgarian Lev cents (see Fig. 5) were adapted. According to Bulgarian National Bank, each such coin weighs 5 g.

Fig. 5. Used scales weight of 10 g

The process of searching for equilibrium starts by placing the 10 g weight in the right-hand side scales dish (Fig. 6 – left), turning the potentiometer to minimum voltage and switching on the master switch. The pot is then slowly turned such that voltage is increased. The motor is measured to generate 10 g of thrust when the scales has just left balance – but instead of inclining to the side of the weight, it falls to the other side – left inclination – lifting the 10 g weight up.
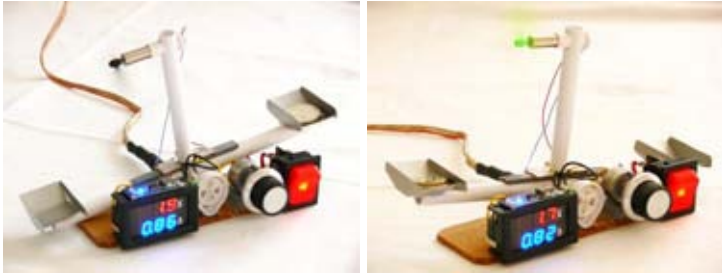
Fig. 6. Tractor versus pusher propeller configuration

The same measurement is taken after mounting a pusher propeller (green coloured propeller) of the same type to the motor shaft (Fig. 6 – right). Now, the weight is moved to the left weighing dish and the process of searching balance is repeated.

The results of the measurements show a definite benefit from using a pusher instead of a tractor propeller. The measurement results are summarized in Table 1. A 14.7 % savings in power drain is observed, which translates directly into the same increase in fight time and range of the unmanned aerial vehicle. On the other hand, this power economy may be used to increase the payload of the UAV.

The decrease of power consumed for creating the needed static thrust comes from the lack of aerodynamic drag (form drag and skin friction) against the beam, holding the rotor – in this case this is the scales arm – and the motor body. In real scenario, a pusher propeller's accelerated airflow will avoid any parts of the aircraft it might encounter, which would, otherwise generate unwanted parasitic drag.

Table 1. Generating 10 g static thrust in tractor and pusher propeller configurations

	Voltage	Current	Power	Thrust efficiency
Tractor propeller configuration	1.9 V	0.86 A	1.634 W	6.12 g/W
Pusher propeller configuration	1.7 V	0.82 A	1.394 W	7.17 g/W
Power gain: 14.7%				

Conclusions

The authors have been in development of unmanned aerial vehicle models since 2014 and have intentions in future continuation of their work [7]. The advent of micro UAVs as a branch of unmanned vehicles is posing significant challenge, but also giving pleasant rewards for the large area of their possible implementation.

References

1. Coffey, T., J.A. Montgomery. The Emergence of Mini UAVs for Military Applications. Defense Horizons Dec. 2002, 22, 1–8.
2. Chenchen, J. Li, H. Ling. Radar Signatures of Small Consumer Drones. AP-S/USNC-URSI IEEE, Puerto Rico, 2016, 1–23.
3. Hammer, M., M. Hebel, B. Borgmann, M. Laurenzis, M. Arens. Potential of LIDAR sensors for the detection of UAVs. Proc. SPIE 10636, Laser Radar Technology and Applications XXIII, 1063605 (10 May 2018); DOI:10.1117/12.2303949.
4. Molchanov, P., R. I.A. Harmanny, J. J.M. de Wit, K. Egiazarian, and J. Astola. Classification of small UAVs and birds by micro-Doppler signatures. Int. J. of Microwave and Wireless Techno., 2014, 6, 3/4, 435–44. Cambridge University Press and the European Microwave Association, 2014, DOI:10.1017/S1759078714000282.
5. Kim, B.-K., J. Park, S.-J. Park *et al.* Drone Detection with Chirp-Pulse Radar Based on Target Fluctuation Models. ETRI Journal, 2018, 40, 2, 188–96.
6. Birch, G.C., J.C. Griffin, and M.K. Erdman. UAS Detection, Classification, and Neutralization: Market Survey 2015. Sandia Report, SAND2015-6365, 1–74.
7. Zabunov, S., P. Getsov, and G. Mardirossian. XZ-4 vertical takeoff and landing multi-rotor aircraft. Asian Journal of Natural & Applied Sciences, 2014, 3, 4, 1–7.

ВЕЗНИ ЗА ИЗМЕРВАНЕ НА СТАТИЧНАТА ТЯГА НА МИКРОДВИГАТЕЛИ ЗА БЛА

С. Забунов, Г. Мардиросян

Резюме

С навлизането на безпилотните летателни апарати (БЛА) с микро-размери и маса не повече от 250 g, се появява и нужда от измервателни средства, адаптирани към тези машини. Тук е констатирана липса на подобни средства и по-конкретно везни за измерване на статичната тяга, генерирана от двигателите. Поради това е разработена лабораторна везна с гореописаното предназначение. Могат да се тестват колекторни двигатели без сърцевина в ротора.

Двигателите, които са предмет на измервания и тестване с описания инструмент, са с миниатюрни размери. Последните са подходящи за приложение в БЛА с микро-размери и маса до 250 g.

Везната работи с различни размери на двигателите и предоставя контрол на захранващото им напрежение, тока на консумация и статичната тяга. Тя е приложима за измерване, както на теглещи, така и на тласкащи витла. Тласкащите витла за микро-дронове придобиват все по-голяма популярност поради по-високата си ефективност.

INVESTIGATION OF THE BASIC HAAR WAVELET-TRANSFORMATIONS IN THE PROBLEM OF DECRYPTION OF SPACE IMAGES ON DETECTION OF WASTE DISPOSAL FIELDS

Maretta Kazaryan[1], Mikhail Shahramanian[2], Svetoslav Zabunov[3]

[1]*Financial University under the Government of the Russian Federation;*
e-mail: marettak@bk.ru
[2]*Research Institute AEROKOSMOS, 105064, Moscow, e-mail: 7283963@mail.ru.*
[3]*Space Research and Technology Institute – Bulgarian Academy of Sciences,*
e-mail: svetoslavzabunov@gmail.com

Abstract

In this paper, we study the use of orthogonal transformations, namely, the basic Haar wavelet transforms, for data processing of the Earth remote sensing.

The internal structure of orthogonal Haar transforms is considered. The Haar matrix is divided into blocks of the same type, so that parallelization of the computations is possible. The expediency of replacing the spectral components corresponding to the whole block (or several blocks) of the original matrix with zeros is asserted. Theoretical and experimental studies are carried out to improve the results of image classification (on the example of cluster analysis). The Haar wavelet expansion coefficients are used as indicators when decoding space images for the presence of waste disposal sites.

The aim of this paper is to describe the approach, on the basis of which an optimal method is established on a class of vectors with real components

$$X_\Delta = \left\{ \bar{x} = (x_0, ..., x_{N-1}) : \max_k |x_{k-1} - x_k| \le \Delta \right\}, \text{ application of two-dimensional discrete Haar wavelet}$$

transformations in the problem of recognition of space images for the presence of waste disposal sites.

General methodology of research. The paper uses elements of mathematical analysis, wavelet analysis, the theory of discrete orthogonal transformations, and methods for decoding cosmic images.

Scientific novelty. Encoding by means of conversion is an indirect method, especially effective in processing of two-dimensional signals, in particular, space images used for remote sensing of the Earth.

We propose the approach that takes into account the structure of the wavelet-Haar matrix, while recognizing waste disposal fields by means of space images.

The article comprises the result of the experimental application of wavelet-Haar transformations for decoding of space images. We consider this case, both with and without the technique of taking into account the structure of the wavelet-Haar matrices.

Introduction

Modern photogrammetry is characterized by digitalization, i.e. wide introduction of information technologies and the creation of automatic and automated information systems for decoding of satellite imagery. It suggests the measuring of the coordinates of the corresponding points and the recognition of objects.

This article continues the research of the creation of an automated system for monitoring the territories for the presence of waste disposal sites (WDSs).

As a matter of fact, we speak about the application of the mathematical apparatus, namely, of wavelet analysis in the subsystem of detecting the unauthorized WDSs, while working with aerospace information, primarily for automated decryption. As different information technologies with multiple characteristics emerge, remote monitoring of various phenomena and objects is now quite possible and is widely used [1, 12, 22–28].

It is, first of all, the satellite systems for Earth observation and large flows of information that enter the scientific laboratories. This leads to the creation of new approaches and methods for organization of the work with information about remote sensing of the Earth (RS), as well as technologies for constructing remote monitoring systems.

The topic of wavelet analysis is quite in demand [4–11, 18, 19]. The wavelet transform is the decomposition of the original signal into wavelet functions using scaling and shift operations. The graphical representation of the result of the wavelet analysis is called wavelet coefficients. The accomplishment of an inverse transformation leads to a convolution of the wavelet coefficients and the wavelet function. If only a part of the coefficients is used for the inverse transformation, a filtered image is obtained, which is later used when recognizing the objects in the image.

There is a relationship between the values of the coefficients of wavelet decompositions and signal deviations [18, 19]. This property is used when working with space images [12].

The visual analysis of wavelet decompositions allows identifying objects of different sizes. This is due to the fact that when the conversion and the shifts are performed in parallel, scaling also occurs. General patterns are determined when small scales are used. Local features in the image are revealed when large scales are used [20].

The use of the wavelet transform makes it possible to exclude from consideration small, minor objects that hinder the visualization of valuable objects in the image. The visualization of WDS, as is known, is carried out with the automated processing of the results of remote sensing of the Earth, as well as in the interactive processing of space images.

When monitoring territories using remote sensing data for the presence of a WDS, one can use the properties of wavelet transforms under consideration.

To detect the changes in the area of study, a periodic monitoring of a fixed area is also necessary. So, in the course of time, it is necessary to identify changes in the terrain for the presence of WDS. When solving such a problem, external factors that interfere with the objective information gathering are in effect: the state of the atmosphere, the season, the position of the sensor, and so on.

The wavelet transform minimizes this effect and improves the accuracy of the decoding of the space image [16].

Let us specifically consider the Haar transformations as one of the varieties of wavelet transforms and carry out theoretical as well as practical studies on deciphering the space images (SI) for the presence of a WDS [20].

Formulation of the problem

The Haar functions belong to the class of piecewise-constant functions. They allow evaluating the local properties of the signals under study and are usually called Haar wavelets. Let us give the main definitions.

Definition 1.

$$\chi_1(t) \equiv 1$$

(1)
$$\chi_{mj}(t) = \begin{cases} 2^{\frac{m-1}{2}}, for\ t \in \left[\frac{j-1}{2^{m-1}}, \frac{2j-1}{2^m}\right) \\ -2^{\frac{m-1}{2}}, for\ t \in \left[\frac{2j-1}{2^m}, \frac{j}{2^{m-1}}\right) \\ 0\ in\ all\ other\ cases \end{cases}$$

where $m = 1, 2, \ldots$; $j = 1, \ldots, 2^{m-1}$, and in case $j = 2^{m-1}$, the right side of the segments is also considered closed on the right. When numbering functions by a single index k, it is assumed $k = 2^{m-1} + j$.

This definition, as it is known, differs from Haar's definition of Haar values [2] at points of discontinuity, but the main property of the Haar system – the uniform aspiration of the Fourier-Haar series of $f(t)$ to $f(t)$ [10] is preserved.

Let's consider the Haar functions from the standpoint of applying them to wavelet analysis. It is known that Haar's functions are now also called Haar wavelets, since they can be described with the help of formal rules adopted in the theory of wavelet analysis [18, 19]. The scaling function and the "Haar mother wavelet" coincide with the first and second functions respectively, of the considered system.

(2) $\varphi(\theta) = \chi_0(\theta) \equiv 1,\ \theta \in [0,1)$;

$$(3) \qquad \psi(\theta) = \varphi(2\theta) - \varphi(2\theta - 1) = \chi_1(\theta) = \begin{cases} 1, & \theta \in \left[0, \tfrac{1}{2}\right); \\ -1, & \theta \in \left[\tfrac{1}{2}, 1\right). \end{cases}$$

Functions of the Haar system are determined according to the theory of wavelets by means of large-scale transformations and transfers of the "mother wavelet":

$$(4) \qquad \chi_{mk}(\theta) = \sqrt{2^m}\, \psi\left(2^{-m}\,\theta - k\right); \; m = 0, 1, 2, \ldots; \; k = 0, 1, \ldots, 2^m - 1$$

It is also known how to move from double numbering to single [19]

$$(5) \qquad n = 2^m + k; \qquad m = 0, 1, 2, \ldots, ; \quad k = 0, 1, \ldots, 2^m - 1$$

There is also a mechanism for using the system of orthogonal Haar functions as the basis for the expansion of a continuous signal defined on an interval.

Haar series of one-dimensional signal $x(t)$, $t \in [0, T)$ have the form

$$(6) \qquad x(t) = \sum_{n=1}^{\infty} c_n\, \chi_n\left(\frac{1}{T}\right)$$

Here the coefficients are calculated by the formula:

$$(7) \qquad c_n = \frac{1}{T} \int_0^T x(t)\, \chi_n\left(\frac{1}{T}\right) dt$$

The truncated Haar series are:

$$(8) \qquad x_N^*(t) = \sum_{n=0}^{N-1} c_n\, \chi_n\left(\frac{t}{T}\right)$$

The latter possess the property of uniform, mean-square convergence and convergence in mean. These series are used to approximate signals described by integrable functions.

The mean square error of approximation for a finite number of orthogonal components of the Haar series is calculated by the formula:

$$(9) \qquad \sigma^2 = \frac{1}{T} \int_0^T \left[x(t) - \sum_{n=0}^{N-1} c_n\, \chi_n\left(\frac{t}{T}\right) \right]^2 dt$$

Or with double numbering, the Haar series has the form:

$$(10) \qquad x(t) = c_0 + \sum_{m=0}^{\infty} \sum_{k=0}^{2^m - 1} c_{mk}\, \chi_{mk}\left(\frac{t}{T}\right)$$

We consider the following problem connected with the structure of Haar functions [3].

As an example, let us consider the Haar matrix of order 8.

106

$$
(11) \quad F_H(8) = \frac{1}{\sqrt{8}}
\begin{vmatrix}
1 & 1 & 1 & 1 & 1 & 1 & 1 & 1 \\
1 & 1 & 1 & 1 & -1 & -1 & -1 & -1 \\
\sqrt{2} & \sqrt{2} & -\sqrt{2} & -\sqrt{2} & 0 & 0 & 0 & 0 \\
0 & 0 & 0 & 0 & \sqrt{2} & \sqrt{2} & -\sqrt{2} & -\sqrt{2} \\
2 & -2 & 0 & 0 & 0 & 0 & 0 & 0 \\
0 & 0 & 2 & -2 & 0 & 0 & 0 & 0 \\
0 & 0 & 0 & 0 & 2 & -2 & 0 & 0 \\
0 & 0 & 0 & 0 & 0 & 0 & 2 & -2
\end{vmatrix}
\begin{array}{l}
\} \ MH_8^0 \\
\} \ MH_8^1 \\
\} \ MH_8^2 \\
\\
\} \ MH_8^3 \\
\\
\\
\end{array}
$$

The notation system is as follows: MH_8^k – a rectangular submatrix of the size $8 \times 2^{k-1}$. This submatrix is formed from the Haar functions of rank r, where $2^{k-1} \le r < 2^k$, $k=1, \ 2, \ 3$.

The Haar matrix of any order $N = 2^{n+1}$ ($n \ge 0$) can be decomposed into submatrices $MH_{2^{n+1}}^k$, $k = 1, \ 2, \ \dots, \ n+1$.

Each submatrix is formed from the Haar functions of rank r, $2^{k-1} \le r < 2^k$. Known matrix operator $\Im$, which makes it possible to create these submatrices with the help of a recurrence relation:

$$
(12) \quad \Im[M] = M \otimes \begin{bmatrix} 1 & 0 \\ 0 & 1 \end{bmatrix} =
\begin{bmatrix}
[M] & \vdots & [0] \\
\cdots & \vdots & \cdots \\
[0] & \vdots & [M]
\end{bmatrix}
$$

Notation system: M is a dimension matrix $m \times p$; $\otimes$ – kronecker product. After the action of the operator $\Im$, we obtain a matrix of dimensions $2m \times 2p$;

It is known that:

$$
(13) \quad MH_{2^{n+1}}^k = \Im\left[MH_{2^n}^{k-1}\right] \ k = 2, \ \dots, \ n+1
$$

The rectangular matrix $MH_{2^{n+1}}^k$ for any n has the following form:

$$
(14) \quad 2^{k-1} \left\{ \left\| \begin{array}{cccccc} \overbrace{+ \ldots +}^{2^{n+1-k}} & \overbrace{- \ldots -}^{2^{n+1-k}} & 0 \ldots 0 & 0 \ldots 0 & 0 \ldots 0 & 0 \ldots 0 \\ 0 \ldots 0 & 0 \ldots 0 & \overbrace{+ \ldots +}^{2^{n+1-k}} & \overbrace{- \ldots -}^{2^{n+1-k}} & 0 \ldots 0 & 0 \ldots 0 \\ 0 \ldots 0 & 0 \ldots 0 & 0 \ldots 0 & 0 \ldots 0 & 0 \ldots 0 & 0 \ldots 0 \\ 0 \ldots 0 & 0 \ldots 0 & 0 \ldots 0 & 0 \ldots 0 & \overbrace{+ \ldots +}^{2^{n+1-k}} & \overbrace{- \ldots -}^{2^{n+1-k}} \end{array} \right\| \right.
$$

Notation system: $+$ means $+\sqrt{2^{k-1}}$; $-$ means $-\sqrt{2^{k-1}}$; where $k = 2, \ldots, n+1$.

Let $F = \left\| \varphi_j(i) \right\|_{j,i=0,N-1}$ discrete orthogonal transformation (DOT) Haar matrix

and let $\overline{x} \in X_\Delta$, where $X_\Delta = \left\{ \overline{x} = (x_0, \ldots, x_{N-1}) : \max_k \left| x_{k-1} - x_k \right| \le \Delta \right\}$. To determine the

most informative elements, let's consider the following optimization problem. Find

$y_j \to extr$ under condition $\overline{x} \in X_\Delta$, where:

$$
(15) \qquad y_j = x_0 \, \varphi_j(0) + x_1 \, \varphi_j(1) + \ldots + x_{N-1} \, \varphi_j(N-1)
$$

For definiteness, let us consider the maximum problem.

$y_j \to \max$ under conditions:

$$
(16) \qquad \left| x_{k-1} - x_k \right| \le \Delta, \ k = \overline{1, \ N-1} \quad \text{where} \quad y_j = \sum_{i=0}^{N-1} x_i \, \varphi_j(i)
$$

j – fixed integer $j = \overline{1, \ldots, N-1}$.

Algorithm for solving the problem (1): In solving this problem, we use the optimality principle in dynamic programming [21]. The initial problem splits into iterative steps, at each step a solution is sought in accordance with the principle of optimality. The decision-making procedure will be carried out starting at the end and going to the beginning.

Let $\hat{x}_0, \ldots, \hat{x}_{N-2}$ in (1) are optimally chosen. Then the last step will be to

find the optimal value of the component x_{N-1}. Given that $\left| x_{N-2} - x_{N-1} \right| \le \Delta$ we

can assume $\hat{x}_{N-1} = \hat{x}_{N-2} + \Delta \, sign \, \varphi_j(N-1)$.

The solution of problem (16) is presented:

$$
\begin{aligned}
(17)\quad \hat{y}_j &= \hat{x}_0\,\varphi_j(0) + \hat{x}_1\,\varphi_j(1) + \ldots \\
&\quad + \hat{x}_{N-2}\,\varphi_j(N-2) + \big(\hat{x}_{N-2} + \Delta\,sign\,\varphi_j(N-1)\big)\varphi_j(N-1) = \\
&= \hat{x}_0\,\varphi_j(0) + \hat{x}_1\,\varphi_j(1) + \ldots + \hat{x}_{N-2}\big(\varphi_j(N-2) + \varphi_j(N-1)\big) + \Delta\,\varphi_j(N-1)
\end{aligned}
$$

Let us now turn to the following problem for a maximum: $y_j \to \max$ on condition:

$$
(18)\quad |x_{k-1} - x_k| \le \Delta,\ k = \overline{1,\ N-2}
$$

where

$$
(19)\quad y_j = \sum_{i=0}^{N-3} x_i\,\varphi_j(i) + x_{N-2}\big[\varphi_j(N-2) + \varphi_j(N-1)\big] + \Delta\big|\varphi_j(N-1)\big|
$$

Let us assume that $\hat{x}_0,\ldots,\hat{x}_{N-3}$ in (19) are optimal. Then

$$
(20)\quad \hat{x}_{N-2} = \hat{x}_{N-3} + \Delta\,sign\big(\varphi_j(N-2) + \varphi_j(N-1)\big)
$$

The solution of problem (19) is

$$
\begin{aligned}
(21)\quad \hat{y}_j &= \hat{x}_0\,\varphi_j(0) + \hat{x}_1\,\varphi_j(1) + \ldots + \hat{x}_{N-3}\,\varphi_j(N-3) + \\
&\quad + \big[\hat{x}_{N-3} + \Delta\,sign\big[\varphi_j(N-2+\varphi_j(N-1))\big]\big]\big[\varphi_j(N-2) + \varphi_j(N-1)\big] + \Delta\big|\varphi_j(N-1)\big| = \\
&= \hat{x}_0\,\varphi_j(0) + \hat{x}_1\,\varphi_j(1) + \ldots + \hat{x}_{N-3}\big(\varphi_j(N-3) + \varphi_j(N-2) + \varphi_j(N-1)\big) + \\
&\quad + \Delta\big|\varphi_j(N-2) + \Delta\,\varphi_j(N-1)\big| + \Delta\big|\varphi_j(N-1)\big|
\end{aligned}
$$

Continuing this process step by step, in the end we will have

$$
(22)\quad \max_{x \in X_\Delta} y_j = x_0 \sum_{i=0}^{N-1}\varphi_j(i) + \Delta\sum_{m=1}^{N-1}\left|\sum_{i=m}^{N-1}\varphi_j(i)\right|,\quad j = \overline{1,\ N-1}
$$

For the Haar matrix, by virtue of orthogonality, we have:

$$
(23)\quad \varphi_j(0) + \varphi_j(1) + \ldots + \varphi_j(N-1) = 0,\quad j = \overline{1,\ N-1}
$$

Taking into account relations (22) and (23), we obtain:

$$
(24)\quad \max_{x \in X_\Delta} y_j = \Delta\sum_{m=1}^{N-1}\left|\sum_{i=0}^{m-1}\varphi_j(i)\right|,\quad j = \overline{1,\ N-1}
$$

If we consider the problem to a minimum, we have:

(25)
$$\min_{x \in X_\Delta} y_j = -\Delta \sum_{m=1}^{N-1} \left| \sum_{i=0}^{m-1} \varphi_j(i) \right| \quad, \quad j = \overline{1, N-1}$$

In general

(26)
$$\max_{x \in X_\Delta} |y_j| = \Delta \sum_{m=1}^{N-1} \left| \sum_{i=0}^{m-1} \varphi_j(i) \right| \quad, \quad j = \overline{1, N-1}$$

This relation leads to the following assertion.

Statement:

The least informative elements, which can be zeroed out in the future, are the elements of the last bundle of vector $\overline{y}$.

Proof. Let $F = F_H(N)$ be the matrix of order

(27)
$$N = 2^{n+1} \ (n \geq 0), \ \overline{x} \in X_\Delta, \ \overline{y} = F_H(N)\overline{x} = (y_0, \ldots, y_{N-1})^T.$$

Based on (26) and starting from the form of the matrix $MH_{2^{n+1}}^k$, we have for

(28)
$$j = 2^{k-1}, \ldots, 2^k - 1:$$

$$\frac{1}{\Delta} \max_{x \in X_\Delta} |y_j| = \frac{1}{\sqrt{N}} \left[\sqrt{2^{k-1}} + 2\sqrt{2^{k-1}} + \ldots + 2^{n+1-k}\sqrt{2^{k-1}} + \left(2^{n+1-k} - 1\right)\sqrt{2^{k-1}} + \left(2^{n+1-k} - 2\right)\sqrt{2^{k-1}} + \ldots + \sqrt{2^{k-1}} \right] =$$

$$= \frac{\sqrt{2^{k-1}}}{\sqrt{N}} \left[1 + 2 + \ldots + 2^{n+1-k} + \left(2^{n+1-k} - 1\right) + \ldots + 1 \right] = \frac{\sqrt{2^{k-1}}}{\sqrt{N}} 2^{2(n+1-k)} = \frac{N^{3/2}}{\sqrt{2^{3k+1}}}$$

It follows that the least informative elements are the elements of the last packets of vector $\overline{y}$, so they can be reset to zero when the image or space image (SI) is further processed.

Experimental research

Let's use the theoretical studies and carry out an experiment related to the application of the cluster analysis algorithm to decipher the SI for the presence of WDS on the basis of the soil.

The state of the soil cover largely depends on anthropogenic factors – industrialization, urbanization, contamination with solid and liquid waste, soil poisoning with pesticides, etc.

As an experimental part of this article, we investigate the problem of using wavelets-Haar for space images obtained from the Landsat artificial satellite (AS), in aerospace monitoring of solid domestic waste. The experiment will consider multispectral imagery, for example, one received from Landsat 4-5 TM satellites for a given observation period (OP), usually at least 10 years long, as well as the data on the amount of precipitation in the study area for the same period. Photographs (SI)

should be geo-linked, atmospherically corrected and without clouds. In the experiment, bands 1–7 are used.

Consider one of the methods for processing of multispectral images that improves the results of decoding – the method of applying orthogonal transformations (Fourier transform, Walsh, Haar, and Karunen-Loeve). In particular, we consider the wavelet-Haar transformation. We also verify assertion 1, which was proved earlier in this article.

It is known [12] that the bands of multispectral images very often turn out to be correlated. The reason for this correlation may be:

- Correlation of spectral properties of objects (this is possible, for example, with low reflectivity of vegetation cover in the visible part of the spectrum);
- Topography (the level of shading due to topographic features can be considered the same in all ranges of registration of reflected solar radiation);
- Overlapping of registration ranges (ideally this factor is excluded when designing the sensor, but in practice this is not always the case).

Such a correlation leads to the emergence of redundant information. The goal that is in front of us in the experiment is to try to get rid of the redundant information with minimal errors using the wavelet-Haar transform property of the transformations stated in Statement 1. First, we consider the representation of a space image by means of orthogonal transformations. Next, let us consider the selection of the most informative coefficients or the selection of certain features by applying wavelet-Haar transformations and performing the filtering in the local area of the image, i.e. we will make the transition to a new basis for measurements in fixed spectral channels.

The transformation matrix of the orthogonal transform under investigation is fixed for a given type of sensor and survey system, therefore, for each new surveying system; new coefficients of the discrete orthogonal transformations (DOT) must be calculated.

Let us consider the point of the proposed method. The physical justification for it is as follows. In multispectral imaging systems, the image is formed in accordance with the reflection from objects of electromagnetic energy in narrow spectral regions.

The image in certain channels fixes the reflection of the spectral brightness of the original object in a given range of the electromagnetic spectrum.
Multispectral image

$$
(29) \qquad P_M = \begin{pmatrix} \overline{P}_{11} & \cdots & \overline{P}_{1M} \\ \vdots & \ddots & \vdots \\ \overline{P}_{N1} & \cdots & \overline{P}_{NM} \end{pmatrix}
$$

consists of k images $P^{(k)}$, each of which represents the values of the brightness measured in narrow spectral regions (k – number of channels of the survey system).

Vector $\overline{P}_{ij} = \left(p^1_{ij}, p^2_{ij}, \ldots, p^k_{ij} \right)$ contains the brightness values of the elements P_{ij} in each channel of the filming system.

For different objects, the spectral brightness in different ranges of the electromagnetic spectrum, although different, is strongly correlated. Measurements in narrow spectral regions (bands) performed by a multispectral imaging system do not eliminate the correlation dependence. Thus, the measurement system does not form an orthogonal basis. Orthogonal transformations make a transition from the space of measurements of the spectral brightness of objects to the space of attributes associated with the properties of a given class of objects.

So, the experiment consists of two steps: the first one is the application of the orthogonal transformation to the original image, which will allow decorrelating the component image vectors and reducing the dimensionality of the image; the second is to build a learning classifier for the task of pattern recognition.

Let us consider the implementation of the first part, namely, the selection of characteristics.

We consider the type of object that undergoes changes in the presence of solid household waste: clean soil, i.e. we are interested in such a characteristic sign as brightness.

The purpose of experimental studies is to assess the accuracy of soil deciphering based on comparing the results of visual decoding of the original image and the image obtained with the use of the ADT. Then, based on comparing the results of classification without learning, using the *k*-means algorithm for this image, and on the image with orthogonal transformation. After segmenting the selected SIs, we define homogeneous clusters.

Description of the algorithm

The further numerical algorithm is defined as follows.
Let us describe the algorithm first for the original one-dimensional vector *x*. The transition to a two-dimensional image is accomplished by applying the experimental results to the rows and columns of the original image, i.e. the SIs, will be discussed in detail below.

Let $x = \left(x_0, x_1, \ldots, x_{N-1} \right)$ be the initial data vector, considered as the realization of some random process with certain properties.

F – discrete orthogonal transformation (wavelet-Haar transform);

F^{-1} – inverse transformation;

k – number of discarded items, $k = \dfrac{N}{m}$;

m – the number of stored items in the new coordinate system;

S – matrix of dimension choice $m \times N$ ранга m, $1 \leq m \leq N$;

W – dimension recovery matrix $N \times m$;

ρ – some metric.

The task of selecting informative elements consists in choosing F, S, W so that

(30) $\rho\left(x, F^{-1} W S F x\right) \rightarrow \min$

The matrices F_0, S_0, W_0 lead to the indicated minimum and are called respectively the optimal basis matrices, optimal choice matrices and optimal recovery matrices.

Substantively, problem (30) reduces to the following. The original vector x of dimension N undergoes an orthogonal transformation F, which leads to a new, more convenient coordinate system. Then, using the selection matrix S, m samples of the signal in the new coordinate system are selected. These samples are intended for image recognition. If necessary, "extrapolation" (restoring the dimension) of these samples by means of the matrix W is carried out. Then, by means of the orthogonal transformation, the original signal is restored.

When solving the SIs decoding problem, we consider a simpler problem. Namely, we fix the transformation F and take $W = S^T$. Then in (30) the minimization is performed only over S.

The value $\rho\left(x, F_0^{-1} W_0 S_0 F_0 x\right)$ is called the recovery error level.

Comment. Let S be a matrix of the form $\left(I_k : 0\right)$, $W = S^T$, ρ - the root-mean-square criterion, then in expression (30) the optimization is carried out only with respect to F. In this case, the optimal basis is the Karunen-Loeve basis [3]. The Karunen-Loeve basis leads to uncorrelated components, but requires a large volume of operations - $o\left(N^3\right)$.

In view of our assertion 1, we can list the main steps of the algorithm under consideration.

Let $x = \left(x_0, x_1, \ldots, x_{N-1}\right)$ be the initial data vector from some metric space (X, ρ), F is an orthogonal matrix of order N (wavelet-Haar);

The algorithm is implemented in three steps.

1. The vector $x = \left(x_0, x_1, \ldots, x_{N-1}\right)$ undergoes a transformation F:

(31) $y = F x = \begin{pmatrix} y_0 \\ y_1 \\ \vdots \\ y_{N-1} \end{pmatrix}$

2. The vector y is replaced by the operator of choice S by a smaller vector $\hat{y}$:

113

(32) $\hat{y} = S\,y = (\,y_0,\,y_1,\ldots,\,y_{m-1})$,

which must be further deciphered.
The matrix S of dimension $m \times N$ has the form:

(33)
$$S = \begin{pmatrix} 1 & 0 & 0 & 0 & 0 & 0 & 0 \\ 0 & 1 & 0 & 0 & 0 & 0 & 0 \\ \vdots & \vdots & \ddots & \vdots & \vdots & \vdots & \vdots \\ 0 & 0 & 0 & 1 & 0 & 0 & 0 \end{pmatrix}$$

k – compression ratio of the original signal, $k = \dfrac{N}{m}$;

3. On the receiving side, the resulting vector $\hat{y}$ is complemented to the dimension N by means of the operation

(34) $\tilde{y} = S^T\,\hat{y} = (\,y_0,\,y_1,\ldots,\,y_{m-1},0,\ldots,0).$

4. The vector $\tilde{y}$ undergoes a reverse transformation F^{-1} i.e.

(35) $\hat{x} = F^{-1}\,\tilde{y}$,

which restores the original data vector with an error $\varepsilon = \rho(x,\,\hat{x})$.

The problem is to determine such a choice of the spectral components replaced by zero, which ensures a minimum of error for a given k.
It follows from Assertion 1 that in the case of a wavelet-Haar transformation, it is necessary to replace the last pack of blocks with zeros.

In more detail, let us consider in detail the case of two-dimensional space images.

Entering the input system of the original image of dimension $N \times N$, we represent them in the form of their scans, namely the $m = N^2$ element vector, i.e. consider a one-dimensional signal.

The coding process is performed in two stages.
1. By means of the transformation $F\,m$, the m-dimensional space of the original vectors f is mapped into the m-dimensional spectral space of vectors $\hat{f}$.
2. The transition to the k-dimensional (k < m) space by means of the operator S reduces the dimension of the vector $\hat{f}$, i.e. the most informative spectral components of the vector $\hat{f}$ are selected.

The most informative are those spectral components whose transmission will allow us to obtain in the decoder an estimate of g of the original vector f with the minimum possible distortions determined by the chosen metric $\rho(f,\,g)$.

The decoding process is performed in two stages:

1. By means of the operator W, a filtering of the noisy truncated vector $\hat{f}$ and a transition from the k-dimensional to the m-dimensional space of the spectral components are carried out.

2. Through the F^{-1} operator m-dimensional space of spectral components is mapped into m-dimensional space of initial vectors.

Let us give a photogrammetric interpretation of the described algorithm, taking into account the research related to the WDS and space images, respectively. The Haar transformation in matrix form can be written as $Y = FX$, $X = F^{-1}Y$, where X and Y are matrices of the halftone image size in the luminance and frequency space, F and F^{-1} are linear operators $N \times N$ of the size of the direct and inverse Haar transform for the corresponding images of X and Y.

The matrix X is obtained by changing the size of the original matrix X from $N \times N$ to $m \times m$, where $N = 2^n$, $n = 1, 2, \ldots$ change in spatial resolution. To do this, an interpolation of the functional $z = X(i, j)$ defined by a grid of values $i = 1 \ldots m$, $j = 1 \ldots m$ with a step $h = 1$ (m values along the abscissa and ordinate axes) into the functional $z = X(i, j)$, given by a grid of values $i = 1 \ldots m$, $j = 1 \ldots m$ with step $h = (m-1)/N$ (N values along the abscissa and ordinate axes). Compression of the matrix Y is provided by the compression matrix $Y' = SFX$ (selection matrix) S.

The effect of the operator S on Y acting as a low-pass filter (from 1 to m) leads to another result of the direct conversion: $Y' = SFX$.

As a result of the inverse transformation of the $(F')^{-1}$ matrix Y' signal $X' = (F')^{-1}Y'$ is restored with accuracy

$$(36) \qquad \varepsilon_1 = \rho_{l_2}(X, X') = \sqrt{\frac{1}{N^2} \sum_{i=1}^{N} \sum_{j=1}^{N} (x_{ij} - x'_{ij})^2} \;,$$

l_2 – standard-mean-square norm; ε_1 – error of restoring a two-dimensional signal.

0.0198	0.0198	0.0198	0.0198	0.0199
0.0130	0.0130	0.0131	0.0131	0.0131
0.0211	0.0211	0.0211	0.0211	0.0212
0.0147	0.0147	0.0147	0.0147	0.0148
0.0238	0.0238	0.0239	0.0239	0.0239
0.0064	0.0064	0.0064	0.0064	0.0064
0.0193	0.0193	0.0193	0.0193	0.0194

$$\begin{matrix}
0.0199 & 0.0202 & 0.0212 & 0.0243 \\
0.0132 & 0.0133 & 0.0141 & 0.0161 \\
0.0213 & 0.0215 & 0.0226 & 0.0259 \\
0.0148 & 0.0150 & 0.0161 & 0.0183 \\
0.0241 & 0.0244 & 0.0259 & 0.0308 \\
0.0064 & 0.0065 & 0.0066 & 0.0072 \\
0.0195 & 0.0197 & 0.0208 & 0.0245
\end{matrix}$$

(a1)   *(b1)*

$$\begin{matrix}
0.1156 & 0.1151 & 0.1092 & 0.1016 & 0.0934 \\
0.0839 & 0.0831 & 0.0786 & 0.0728 & 0.0667 \\
0.1418 & 0.1406 & 0.1339 & 0.1232 & 0.1128 \\
0.0962 & 0.0957 & 0.0902 & 0.0833 & 0.0761 \\
0.1567 & 0.1590 & 0.1515 & 0.1413 & 0.1311 \\
0.0442 & 0.0445 & 0.0427 & 0.0402 & 0.0375 \\
0.1185 & 0.1201 & 0.1142 & 0.1063 & 0.0984
\end{matrix}$$

$$\begin{matrix}
0.0851 & 0.0760 & 0.0757 & 0.0793 \\
0.0604 & 0.0543 & 0.0507 & 0.0508 \\
0.1022 & 0.0914 & 0.0825 & 0.0816 \\
0.0693 & 0.0634 & 0.0592 & 0.0570 \\
0.1221 & 0.1187 & 0.1171 & 0.1299 \\
0.0349 & 0.0323 & 0.0297 & 0.0284 \\
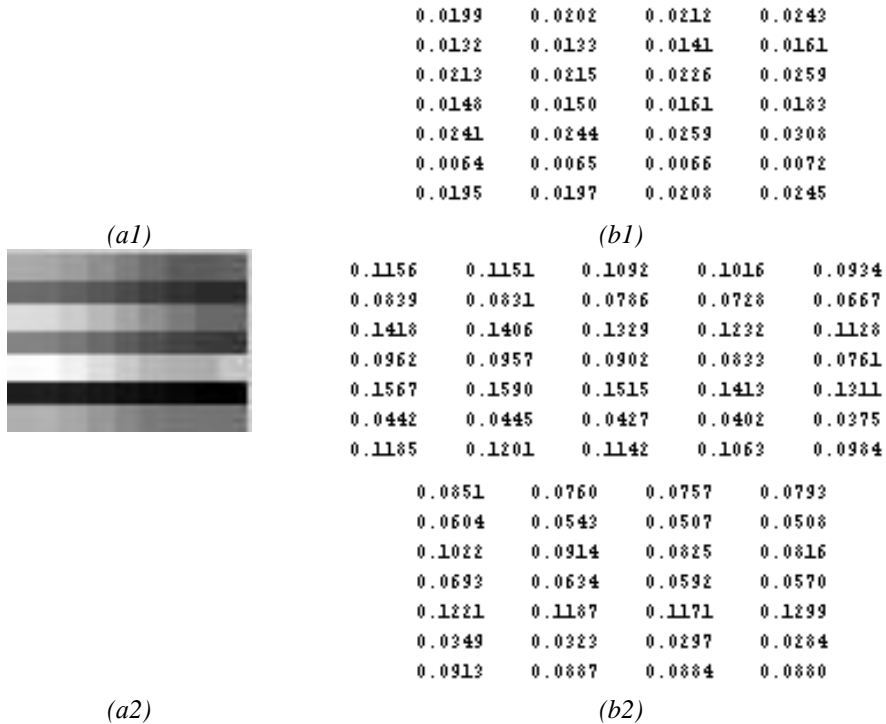0.0913 & 0.0887 & 0.0884 & 0.0880
\end{matrix}$$

(a2)   *(b2)*

*Fig. 1. Recovery errors: 1) ε₁; 2) ε₂; on different channels
and at different compression ratios; b) matrices*

We estimate the recovery errors (without the action of *Statement*) ε'_1, ε'_2 (under the action of the *Statement*) for the Haar transformation with different compression coefficients k and on different channels of the original image X of the litter area (landfill Kuchino, August 2011). We set $n = 10$. In Fig. 1 shows the matrices $E_1 = [\varepsilon_1(i,j)]$, $E_2 = [\varepsilon_2(i,j)]$ of sizes $l \times (N–1)$. We see that the maximum accuracy is observed on the 6 (thermal) bands and it varies little with compression. Matrices $E_1 \approx E'_1$ and the elements of the matrix E'_2 are on the average larger than E_1 for a given value of k. The smaller k, the smaller the recovery error.

In Fig. 2 – an example of signal reconstruction for $n' = n / 2 = 5$ is given. It can be seen from figure (e) that an increase in the spatial resolution and a decrease in the compression ratio have little effect on the recovery result. In other words, the image of littering can be restored both with preservation or even reduction of the spatial resolution, and at its strong compression. This is due to the fact that the litter texture is characterized by a random, random spatial distribution of pixel brightness.
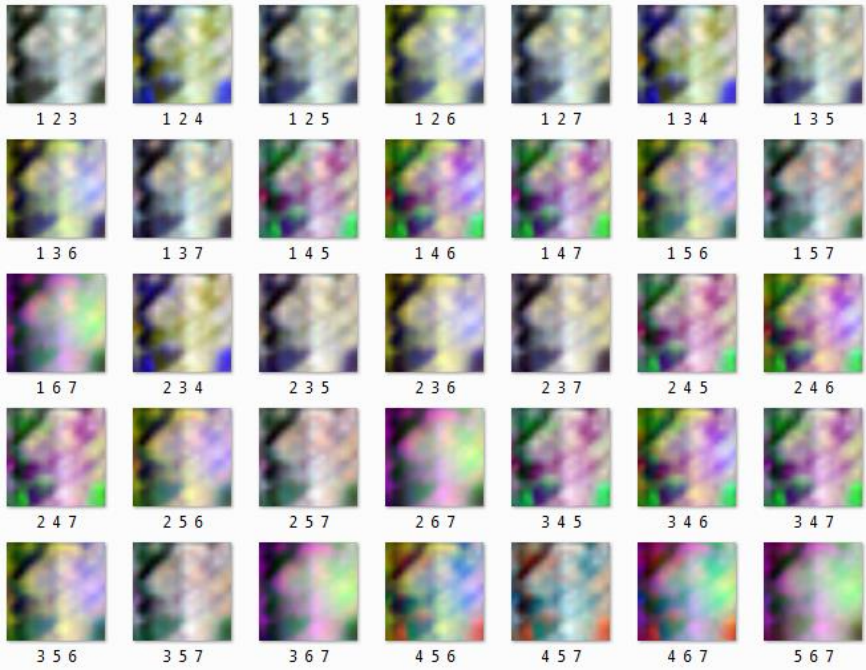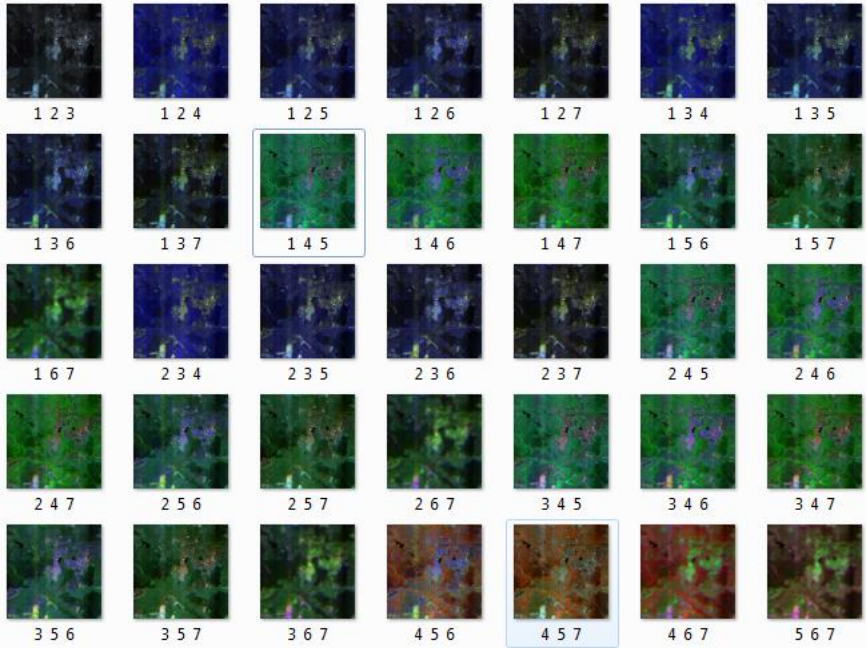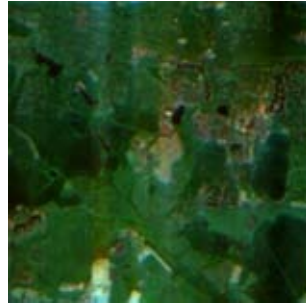
116

(a)

(b)

(c)

117

(d)

(e)

118
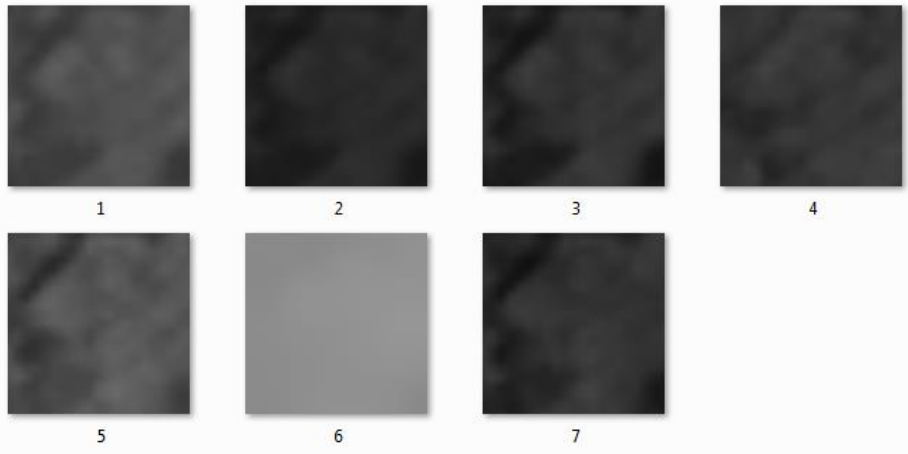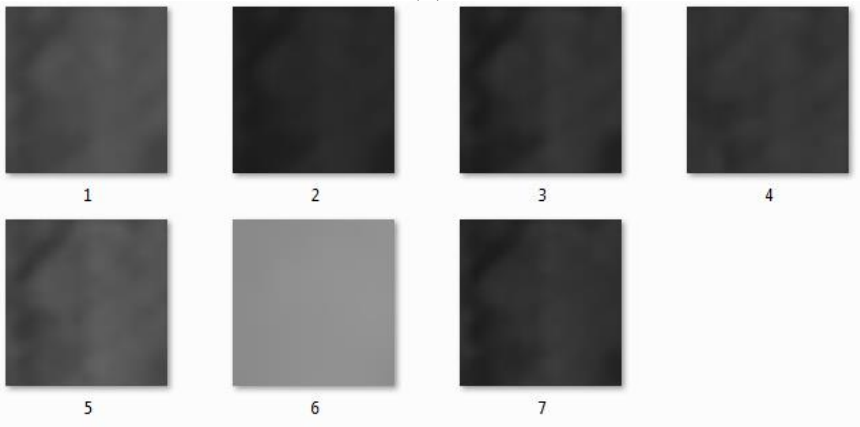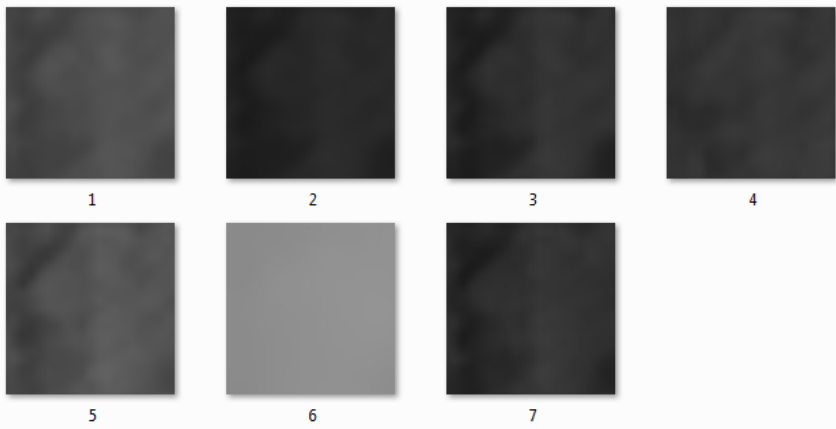
(f1)   *(f2)*

Fig.2. An example of Haar transforming the litter image:
a) source images (with increasing spatial resolution, n = 10);
b) Haar transformation with contraction (n' = 5);
c) Haar transformation with contraction and S (n' = 5);
d) composites of transformations (combination of different channels,
n = 8, n' = 2);
e) the best transformation (combination [3 5 7]);
f) examples of images (1 − n = 8, n'= 2, 2 − n = 10, n' = 3).

Conclusions

In this paper, the Haar wavelet transforms used in the recognition of space images are studied. The assertion about the determination of the selection matrix for a given type of transformation is proved.

An experiment has been carried out that confirms the validity of the asserted statement when decoding space images. This task is included as a component module of the project for aerospace monitoring of WDS facilities. The principle of optimality in dynamic programming, elements of mathematical analysis, the theory of discrete orthogonal transformations, as well as photogrammetric bases of information representation in space images are used in the work.

References

1. Kazaryan, M. L., M. A. Schahramanian, A.A. Richter. Space monitoring of the Earth and Haar wavelet transform. Future Communication Technology and Engineering, Chapter 61, (ed. Kennis Chan) CRC Press 2015, 291–94. Print ISBN: 978-1-138-02777-0, eISBN: 978-1-315-69045-2.
2. Haar, A. Zur Theoria der orthogonalen Funktionsysteme. Math. Fnn. 1910, 69, 331–71.
3. Pratt, W. Digital image processing. M .: Mir, 1982, 312 p.
4. Hyvarinen, A. and Oja, E. Independent component analysis: Algorithms and applications. Neural Networks, 2000, 13, 4–5, 411–430.

5. Cichocki, C., A. Amari. Adaptive blind signal and image processing: Learning algorithms and applications. Wiley, 2002. 555 p.

6. Vincent, E., R. Gribonval, C. Fevotte. Performance Measurement in Blind Audio Source Separation", IEEE Trans. on Speech and Audio Processing, 2006, 14, 4, 1462–69.

7. Percival, D., Walden A. Wavelet methods for time series analysis. London: Cambridge University Press, 2000, 594 p.

8. Donoho, D., Johnstone I. Adapting to unknown smoothness via wavelet shrinkage. J. Amer. Statist. Assoc., 1995, 90, 1200–24.

9. Strang, G., Nguyen T. Wavelets and Filter Banks. Boston: Wellesley-Cambridge Press, 1996, 512 p.

10. McQuarrie, A., Chin-Ling Tsai. Regression and time Series Model Selection. London: World Scientific Publishing, 1998. 455 p.

11. Redfern, A. L., G. T. Zhou. A root method for Volterra systems equalization. IEEE Signal Processing Letters. 1998, 5, 11, 285–288.

12. Robert, A. Showengerdt. Remote sensing / Models and Methods for Image processing. Burlington: Elsevier INC, 2007. 560 p.

13. Aristov, M. A. Monitoring of solid waste landfills and detection of spontaneous garbage disposal according to space survey data. GeoProfil.ru. № 2.

14. Pogorelov, A. V., S. V. Dulepa, D.A. Lipilin. Experience of space monitoring of landfills in the territory of the Krasnodar Territory. Geomatika, 2013, 4, 64–71.

15. Aleksandrovna, L. N., M. L. Glinsky, A. A. Zubkov, V. V. Danilov, and L .G. Chertkov. Monitoring of the state of the subsoil on the LRW burial site. URL: http://www.atomic-energy.ru/articles/2012/02/20/31086

16. Brovkina, O. V. Remote monitoring of anthropogenic disturbances in the taiga zone of the Northwest of Russia / dissertation, 2011, 125 p.

17. Yannikov, I. M., M. V. Sleptsova, K. K. Krivoshapkin. Organization of biomonitoring of chemically hazardous objects and landfills with the use of identification polygons. Bulletin of the NEFU M.K. Ammosov, Yakutsk, 2013, 15–25.

18. Chui, C. K. Wavelets: A Mathematical Tool for Signal Analysis. SIAM, Philadelphia, 1997.

19. Daubechies, I. Ten Lectures on Wavelets. SIAM, Philadelphia, 1992.

20. Gonsales, R. C., R .E. Woods, and S. L. Eddins. Digital Image Processing using Matlab, Pearson Prentice Hall, Upper Saddle River, NJ, 2004.

21. Korolyuk, V. S., N. I. Portenko, A. V. Skorokhod, A.F. Turbine et al. A handbook on probability theory and mathematical statistics. M.: Science. The main edition of physics and mathematics, 1985, 640 p.

22. Nedkov, R. Orthogonal Transformation of Segmented Images from the Satellite Sentinel-2. Comptes rendus de l'Acad´emie bulgare des Sciences, 2017, 70, 5, 687–92. "Prof. Marin Drinov" Publishing House of Bulgarian Academy of Scinces, ISSN 1310–1331.

23. Nedkov, R. Quantitative Assessment of Forest Degradation after Fire Using Ortogonalized Satellite Images from Sentinel-2. Comptes rendus de l'Academie Bulgare des Sciences, 2018, 71, 1. "Prof. Marin Drinov" Publishing House of Bulgarian Academy of Scinces, ISSN 2367–5535.

24. Nedkov, R. Normalized Differential Greenness Index for Vegetation Dynamics Assessment. Comptes rendus de l'Acad´emie bulgare des Sciences, 2017, 1143–46, 70, 8. "Prof. Marin Drinov" Publishing House of Bulgarian Academy of Scinces, ISSN 1310–1331.

25. Nedkov, R., E. Velizarova, I. Molla, and K. Radeva. Application of remote sensing data for forest fires severity assessment. Proc. SPIE 10790, Earth Resources and Environmental Remote Sensing/GIS Applications IX, 107901U (9 October 2018), 10790, SPIE, 2018, DOI:10.1117/12.2325742.

26. Radeva, K., R. Nedkov, and A. Dancheva. Application of remote sensing data for a wetland ecosystem services assessment in the area of Negovan village. Proc. SPIE 10783, Remote Sensing for Agriculture, Ecosystems, and Hydrology XX, 107830Y (10 October 2018); 10783, SPIE, 2018, DOI:10.1117/12.2325767.

27. Stankova, N., R. Nedkov. Monitoring forest regrowth with different burn severity using aerial and Landsat data. Geoscience and Remote Sensing Symposium (IGARSS), 2015 IEEE International, IEEE, 2015, 2166–69. ISBN: 978-1-4799-7929-5, ISSN 2153–7003, DOI:10.1109/IGARSS.2015.7326233.

28. Avetisyan D., R. Nedkov. Determining the magnitude and direction of land cover changes in the semi-natural areas of Haskovo Region, Southeast Bulgaria. Geoscience and Remote Sensing Symposium (IGARSS), 2015 IEEE International, IEEE, 2015, 4637–40. DOI:10.1109/IGARSS.2015.7326862.

ИЗСЛЕДВАНЕ НА ОСНОВНИТЕ ХААР УЕЙВЛЕТ-ТРАНСФОРМАЦИИ В ЗАДАЧАТА ЗА ДЕКОДИРАНЕ НА ПРОСТРАНСТВЕНИ ИЗОБРАЖЕНИЯ ПРИ ОТКРИВАНЕ НА СМЕТИЩА

М. Казарян, М. Шахраманян, С. Забунов

Резюме

В настоящата статия ние изследваме използването на ортогонални трансформации, а именно основните Хаар уейвлет трансформации с цел обработката на данни от дистанционни изследвания на Земята.

Използва се вътрешната структура на ортогоналните Хаар трансформации. Хаар матрицата се разделя на блокове от един и същи тип, така че да е възможна паралелизация на изчисленията. Установява се целесъобразността на заменяне на спектралните компоненти, съответстващи на целия блок (или няколко блока) на ортогоналната матрица с нули. Проведени са теоретични и експериментални изследвания с цел подобряване на резултатите при класификация на изображения (чрез примери от клъстерния анализ). Коефициентите на разширение на Хаар уейвлета се използват като индикатори при деко-дирането на пространствени изображения в търсенето на сметища.

Цел на тази публикация е да опише подхода, на базата на който се установява оптимален метод върху клас от вектори с реални компоненти

$$X_\Delta = \left\{ \bar{x} = (x_0, ..., x_{N-1}) : \max_k |x_{k-1} - x_k| \leq \Delta \right\},$$ приложение на двумерни дискретни Хаар

уейвлет трансформации върху задачата за разпознаване на сметища в пространствени изображения.

Обща методология на изследването. Материалът използва елементи на математическия анализ, уейвлет анализа, теорията на дискретните орто-гонални трансформации и методите за декодиране на космически изобра-жения.

Научна новост. Кодирането чрез преобразуване е индиректен метод особено ефективен при обработката на двумерни сигнали, най-вече про-странствени изображения, използвани за дистанционни изследвания на Земята.

Ние предлагаме подход, който взема под внимание структурата на Хаар уейвлет матрицата, като в същото време разпознава сметища в пространствени изображения.

Статията обхваща експерименталното приложение на Хаар уейвлет трансформациите за декодиране на пространствени изображения. Ние разглеждаме случаите, както с, така и без техниката на вземане предвид структурата на Хаар уейвлет матриците.

HYBRID PROPULSION OF MULTI-COPTER TYPE UAVS, FEASIBILITY AND CURRENT STATE OF THE ART

Petar Getsov[1,2], Ruslan Yanev[2], Wang Bo[1]

[1]*Ningbo University of technology – China*
[2]*Space Research and Technology Institute – Bulgarian Academy of Sciences*
e-mail: office@space.bas.bg

Abstract
A limiting factor in further development of the electrically driven multicopter type UAVs is their low flight endurance – up to 1 hour with a real payload. It depends, on the limited specific energy of the batteries that multicopters carry on board. One of the solutions to the problem is the use of an energy source with higher specific energy – gasoline. Through it, electricity is generated onboard, which feeds the drive motors and the payload. In theory and in practice, hybrid drives allow the flight endurance of multicopters to reach 4 hours.

Attempts to create multirotor aircraft, powered by internal combustion engines, date back to the beginning of the last century. In general, they are all unsuccessful. The main reason is the inability to manage effectively the thrust of the individual rotors.

The idea of multicopters was successfully implemented about 10 years ago, with the development of unmanned aerial vehicles with electric propulsion (MCP_{ep}).

Nowadays MCP_{ep} are separate, independent and fast growing class in the aviation technique, with good perspectives and application capabilities. They have flight characteristics, robotic and automation potential, with which they are superior to other heavier than air unmanned aerial vehicles – airplanes and helicopters.

The modern MCP_{ep} are powered by propellers with low weight, high aerodynamic efficiency and specific thrust that reach up to 19.0 kg/kW. They are mounted directly on the shafts of brushless electric motors with an efficiency of $95 \div 98$ % and specific power of $3.0 \div 4.0$ kW/kg.

The control of MCP_{ep}s flight is carried out by precise and rapid change of the thrust, that create the lifting propellers, via varying of their electric motors *rpm*.

This is done by Electronic speed controllers (ESC), which have efficiency of about 95 % and a relative weight of 0.15 kg/kW.

The MCP_{ep} are mainly powered by lithium-polymer (Li-Po) batteries. At present, they have specific energy (C_pE_c) up to 350 Wh/kg. Their operating life is relatively short – no more than 1 000 charging cycles, while through this time their capacity is constantly decreasing. Their theoretical maximum is 400 Wh/kg. The next generation in the development of lithium batteries is lithium-sulphide (Li–S) and lithium-air (Li-Air) batteries. It is expected their C_pE_c to reach $600 \div 1\ 000$ Wh/kg. Now on the market are available Li-S batteries with C_pE_c – 380 Wh/kg. However, they quickly lose their capacity and still have a very limited number of charge-discharge cycles. This makes it difficult to use them for propulsion of MCP_{ep}.

Modern MCP_{ep} are made of composite and other materials with high strength characteristics and low relative weight. Modern technologies are used and effective constructive solutions are being implemented. This allows their empty weight (EW) (with engines and propellers, without batteries and payload (PL) to be reduced to $30.0 \div 40.0$ %, and the payload to reach $10.0 \div 15.0$ % of the maximum takeoff weight of the vehicle (MTOW).

The MCP_{ep} fly in high thrust-to-weight ratio. When hovering and maneuvering in calm air they need a thrust (T) that exceeds $1.2 \div 1.4$ times the MTOW of the vehicle. In dynamic air environment the thrust-to-weight ratio T/MTOW may exceed 2.0. To achieve these parameters, MCP_{ep} must carry on board batteries with high capacity and weight.

The main problem with the modern MCP_{ep} is the limited flight duration (T_{flight}). There are different formulas and electronic calculators for calculating the flight duration of electric driven multicopters. In all of them T_{flight} is a function of the following parameters:

(1) $T_{flight.} = f(\eta_{pwr}; C_pE_c; C_pT_{prop}; T/MTOW)$,

where: η_{pwr} – efficiency of the electric power transformation (a product from the multiplication of the efficiency of electric motors and controllers ≈ 0.9);

C_pT_{prop} – propeller specific thrust (for existing multiscopers – an average of 11.5 g/W);
T/MTOW – thrust-to-weight ratio $1.4 \div 2.0$.

The T_{flight} of the multicopter depends mainly on the specific energy of the battery C_pE_c. When using existing lithium-polymer batteries with C_pE_c – 350 Wh/kg, the maximum flight duration of MCP_{ep} with PL (carrying on board a payload representing 10 % of the MTOW) is achieved when the weight of the battery is twice as much as the empty weight of the aircraft. However, it may not be more than 45 minutes (with thrust-to-weight ratio – 1.4), regardless of the MTOW. After this flight duration limit, MCP_{ep} become very heavy, reduces their

payload and generally they lose their specific advantages over the airplanes and helicopters.

A solution of the existing problem, while retaining the advantages of the electric propulsion of the lifting propellers, is the generation of electricity on the board of MCP_{ep}, using internal combustion engines – ICE, that work with fossil-type liquid fuels or such, produced from renewable energy sources containing hydrocarbons.

The feasibility of the hybrid propulsion of MCP_{ep} is based on the high specific energy of the widely used liquid fuels, which exceeds many times that of the best batteries. C_pE_c for the diesel and kerosene is about 12 000 Wh/kg. For the gasoline this value is over 12 200 Wh/kg. This is a chemical energy. In order to be used to fuel MCP_{ep} it should be converted into electric. For hybrid propulsion of multicopters, it is best to do this indirectly – using heat engines. In them, the heat produced by the fuel becomes into a mechanical energy that drives power generators.

The specific energy of such a hybrid power plant – $C_pE_cH_y$ depends on the following parameters:

$C_pE_cH_y = f(C_pF; \eta_{he}; C_pW_{he}; \eta_{eg}; C_pW_{eg}; C_pE_cB_h)$

C_pF – fuel specific energy – for the gasoline 12 220 Wh/kg;

η_{he} – heat engine efficiency – $5.0 \div 45.0$ %, depending on type and power range;

C_pW_{he} – specific weight of the thermal engine, exhaust system and control unit $0.450 \div 5.0$ kg/kW, depending on the type of the engine and power range;

η_{eg} – efficiency of the electric generator, rectifier and control unit ≈ 0.9;

C_pW_{eg} – total specific weight of the electric generator, rectifier and control unit, their cooling system and the connecting node with the heat engine ≈ 1.10 kg/kW;

$C_pE_cB_h$ – specific energy of the Buffer battery – 350 Wh/kg.

The main factors that determine the specific energy of the hybrid power plant are the thermal engine efficiency of and its specific weight. They are vastly dependent on the power, required for the multicopter flight. Modern MCP_{ep} should have a payload of over 2 kg. This means that their MTOW must start at about 20.0 kg. The upper limit on which this type of aircraft loses its advantages is about 50.0 kg (payload – 5 kg). With a specific thrust of the propellers – C_pT_{prop} – an average of 11.5 g/W, the power required by the electric motors is within the range $1.8 \div 4.3$ kW. Taking into account their efficiency and the efficiency of their power controllers (0.9), a minimum of $2.0 \div 4.8$ kW should be supplied from the hybrid system. Assuming that the peak loads will be absorbed by the buffer batteries and they provide an average of 5.0 % of the total power ($0.1 \div 0.24$ kW), the capacity of the power generators should be in the range $2.1 \div 5.0$ kW. With total efficiency

of the electric generators, their rectifiers and control blocks ≈ 0.9 – the power of the thermal engines should be 2.3 ÷ 5.5 kW.

For the calculated power range, the most relevant technical specifications have the two-stroke, gasoline internal combustion engines – ICE_{gts}. Their specific weight, fully equipped (with ignition system, exhaust pipe and cooling system) is 1.10 ÷ 1.80 kg/kW, power per liter (80 ÷ 110 kW/dm^3), efficiency (11.0 ÷ 15.0 %).

The dependence between the Brake Thermal Efficiency – BthE – η_{th} and specific fuel consumption – bcfc (g / kW / h) is as follows:

$$\eta_{th} = \frac{100 \times 10^6}{bcfc \times C_pF} \qquad ; \qquad bcfc = \frac{100 \times 10^6}{\eta_{th} \times C_pF}$$

For ICE_{gts} with η_{th} (11.0 ÷ 15.0 %), the specific fuel consumption – bcfc will be in the range (750.0 ÷ 550.0 g/kWh).

In order to achieve maximum flight duration, a battery powered MCP_{ep} with a maximum take-off weight of 20.0 kg and a payload of 2.0 kg, must have a battery with weight of not less than 10.0 kg. To replace this battery, the hybrid power plant – with the same weight should have a weight:

ICE_{gts} (with power 2.3 kW and efficiency 10 %) with its systems – 2.6 kg;
fuel tank – 3.8 kg (empty – 0.3 kg + fuel – 3.5 kg);
electric generator with rectifier and control unit – 2.4 kg;
buffer battery – 0.4 kg;
supporting structure for mounting the engine, generator and other equipment – 0,8 kg;
total – 10 kg.

With the fuel of 3.5 kg, available on board, the hybrid-powered MCP_{ep} will have flight duration of about 2 hours – more than 2.5 times greater than the maximum possible with batteries. For the above example, the energy density provided by the hybrid power plant – C_pE_cHy is about 1 500 Wh/kg.

The practical realization of the idea of hybrid propulsion of MCP_{ep} starts in 2015. The first multicopter with hybrid drive is the quad-copter HYBRIX.20, Fig. 1. It is created by the Spanish start-up company *Quaternium* based in Valencia. It is assigned to it by the Spanish Ministry of Defense with the Vantex project in the middle of 2015. The same year, in November, a prototype was made and tests began. On December 26, 2017, HYBRIX.20 establishes a flight duration record – a 4 h and 40 min hovering.

Main characteristics of HIBRIX.20:

1. MTOW:	20.0 kg
2. Empty Weight:	13.5 kg
3. Payload:	+ 2.5 kg
4. Flight duration with maximum payload:	2.0 h
5. Cruise speed:	50 km/h
6. Max. speed:	80 km/h
7. Propellers:	30"
8. Operational temperature:	$-10 + 45°C$
9. Propulsion system:	hybrid
10. Heat engine:	Two-stroke gasoline ICE
11. Fuel:	Gasoline, 95 octane + 4 oil
12. Batteries:	LiPO 12S

In 2016, after improvements, the maximum payload of the multicopter was increased to 5.0 kg.

HIBRIX.20 is powered by a single cylinder, gasoline, carbureted two-stroke ICE with spark ignition, air cooling and a conventional exhaust system. The shaft of the engine is located horizontally across the longitudinal axis of the multi-copter. By means of an increasing rpm belt drive with a toothed belt and a gear ratio of about 1: 3, it drives a brushless electric motor running in the generator mode. The engine turn over manually, by Pull starter.

Analysis of HIBRIX.20 Flight Duration Results – at full load, with and without payload, show that its engine's specific fuel consumption is around 840 g/kWh. This corresponds to η_{th} of about 9.6 % and means that this ICE is likely to have a working volume below 30 cc.

With the same aerodynamic configuration as the HIBRIX.20 and with very close flying characteristics is the hybrid quadcopter Tailwind – Fig. 1, developed by the US company *Skyfront*, located in the State of California.
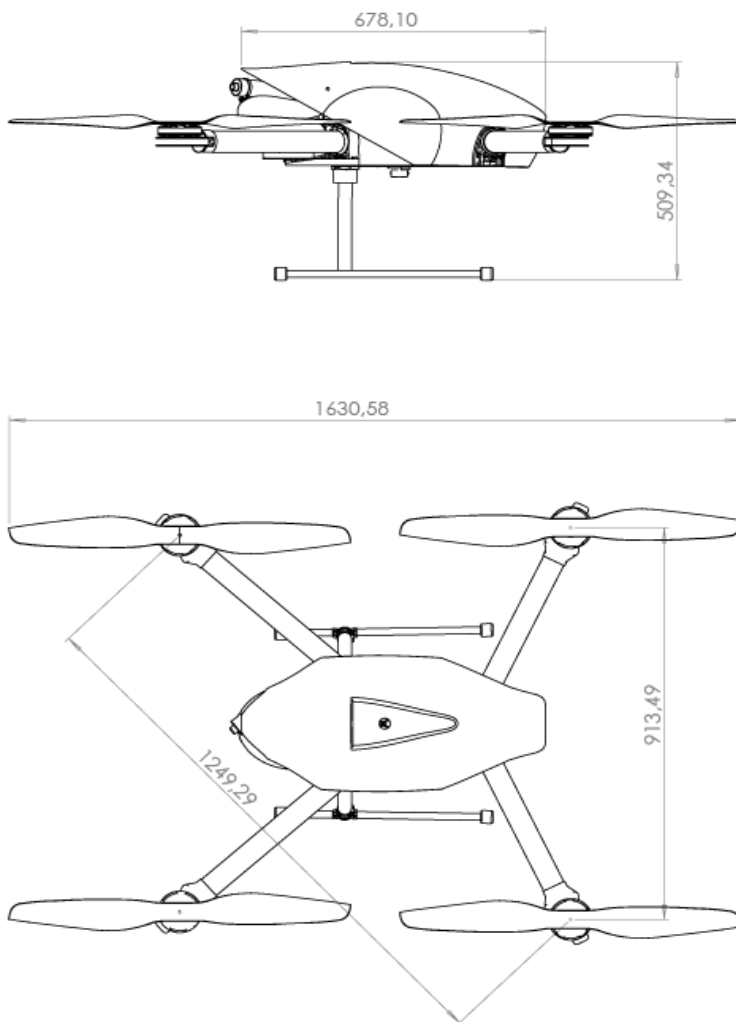
Fig. 1. Main view of HIBRIX.20

Fig. 2. Main view of Tailwind

Main characteristics of *Tailwind*:

1. MTOW:	12.0 kg
2. Payload:	3.0 kg
3. Flight duration with 1.0 kg payload:	3.5 h
4. Flight duration without payload:	4 h 34 min
5. Max. speed:	50 km/h
6. Flight range:	250 km
7. Operational temperature:	$0 + 45^o C$
8. Propulsion system:	hybrid
9. Heat engine:	two-stroke gasoline ICE

The *Tailwind* engine is gasoline, single-cylinder, carbureted. Its shaft is located parallel to the vertical axis of the multi-copter. Its shaft is oriented in parallel to the vertical axis of the multi-copter. It directly drives a three-phase, brushless electric motor that initially starts the ICE and then operates in a generator mode. Fuel consumption of the ICE is about 930 g/kWh. The engine's efficiency is around 8.8 %. Probably it has a working volume of 25 cc.

Chinese company Richen Power has developed a Hybrid Power Plant – NOVA 2000 Generator System H2 – Fig. 3. It is in the form of a separate module for installation into electrically driven multicopters.
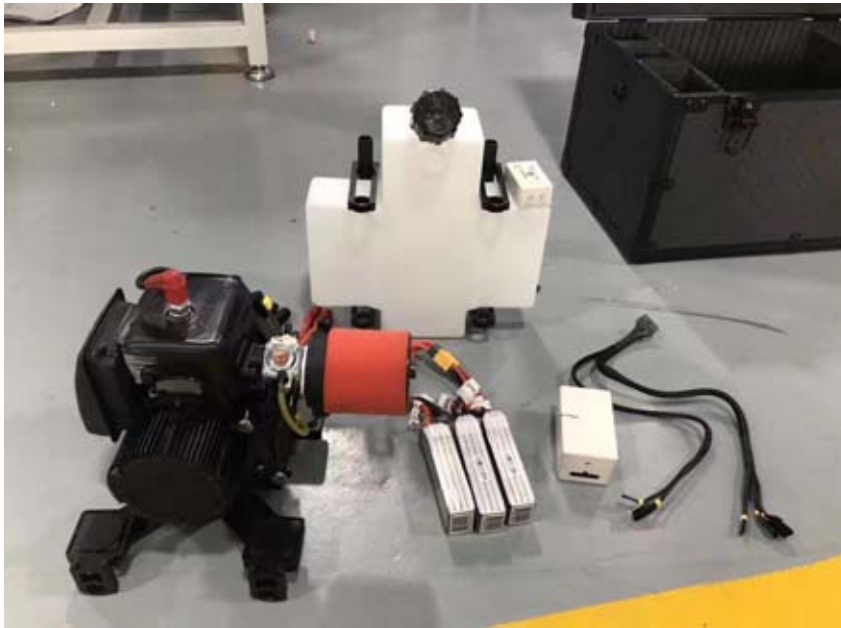
Fig. 3. Main view of NOVA 2000

The engine is two-stroke, gasoline, with carburetor and spark ignition. Its displacement is 32 cc, with a cylinder diameter of 38 mm. The bsfc, depending on the flight regime, is 560 ÷ 750 g/kWh with efficiency 14.6 ÷ 11.0 %. It turns over with an external electric starter. The electric generator is connected to the ICE directly – on one axis. It is three-phase with stationary coils. Its maximum power is 2.0 kW and the nominal – 1.8 kW. The voltage that H2 generates is 48 V. Peak loads in turbulent conditions, when maneuvering and in emergency situations are provided by 3 pcs. LiPo batteries – 1 800 mAh, 75C, 4S. The total weight of the NOVA 2000 Generator System H2, without tank, buffer battery and frame is 5.2 kg. The module is designed to supply with energy quadcopters with total take-off weight up to 18 kg and hexacopters with MTOW – 21 kg.

The NOVA 2000 price is $ 4 660.

GAIA 160 – Hexacopter – Fig. 4 and *Bumblebee* – quadcopter are multi-copter systems with hybrid drive and both are developed by the Chinese company FoxTech. They use NOVA 2000 Generator System H2. The hybrid unit is located under the aircraft along their vertical axis.

Fig. 4. Main view of GAIA 160

The MTOW of GAIA 160 is 19.5 kg. The fuel tank capacity is 6.5 l. With a payload of 2 kg, it provides flight duration of 4 hours. When the payload is 5 kg, GAIA 160's flight duration is 2 h. The maximum flight speed is over 15 m/s. The electric motors are T – MOTOR U8II KV85. The lifting capability of each hexacopter arm is 6.5 kg. This enables GAIA 160 to fly with 5 moto-propeller groups when one of the engines is off.

The GAIA 160 price is $ 20,000.

Chinese company *Guangzhou Walkera Technology* Co. Ltd. uses NOVA 2000 Generator System H2 hybrid module in its hexacopter – QL1200 Gas-Electric Hybrid Drone, Fig. 5.

QL1200 has MTOW of 18 kg at a payload of 3.0 kg. At full load, the flight duration of the multi-copter is 2 h.

Fig. 5. Main view of QL1200

The US company *Top Flight Technologies*, based in Boston, develops the heavyweight *Airborg™* H8 10K hybrid multi-copter, Fig. 6. It is an 8-rotor quadcopter. On each of the 4 shoulders, coaxial, one above the other are located 2 pcs. electric motors with directly coupled 34" air propellers.

Fig. 6

The multi-copter has the following dimensions: 1 950 mm (L) × 1 600 mm (W) × 1 500 mm (H). It has MTOW of 54 kg and its empty weight is 33 kg (without fuel and payload). At 4 kg payload, its flight duration is 3 h and at 10 kg payload – 1 h. Its maximum speed is 40 mph and the flight range is 100 miles. It can fly at wind speeds up to 35 km/h. The hybrid drive includes a two-stroke, two-cylinder boxer gasoline ICE weighing 7.7 kg and a rated power of 10 kW; Engaged directly to the engine electric starter – generator; fuel tank with a capacity of 19 liters and 50 V, 6 000 mAh, LiPo battery. ICE is mounted under the platform of the multi-copter. Its shaft is directed along the vertical axis of the MCP_{ep}. The generator is above it.

Analysis of flight data of H8, 10K at a payload of 4 kg shows that in this flight regime, the *bsfc* of the ICE is an average of 566 g/kWh – efficiency 14.5 %.

Acknowledgements

References

1. Getsov, P., W. Bo , D. Zafirov, G. Sotirov, St. Nachev, R. Yanev, P. Gramatikov, V. Atanassov, H. Lukarski, and S. Zabunov. An unmanned aerial surveillance system in urban environments, Aerospace research in Bulgaria, 2017, 29, 94–110.

ХИБРИДНО ЗАДВИЖВАНЕ НА БЕЗПИЛОТНИ ЛЕТАТЕЛНИ АПАРАТИ МУЛТИКОПТЕРЕН ТИП, ОСЪЩЕСТВИМОСТ И АКТУАЛНО СЪСТОЯНИЕ НА ТЕХНИКАТА

П. Гецов, Р. Янев, В. Бо

Резюме

Ограничаващ фактор в бъдещото развитие на безпилотните летателни апарати мултикоптерен тип е тяхната ниска продължителност на полета – до 1 час с реален полезен товар. Тя зависи от ограничената специфична енергия на батериите, които мултикоптерите носят на борда си. Едно от решенията на проблема е използването на енергоизточник с по-висока специфична енергия – бензин. Чрез него на борда на мултикоптерите се генерира електроенергия, която захранва задвижващите електродвигатели и полезния товар. На теория и на практика хибридните задвижвания позволяват продължителността на полета на мултикоптерите да достигне 4 часа.

SECONDARY POWER SYSTEMS
FOR VIDEOMETRIC COMPLEX "FREGAT"

Pavlin Gramatikov, Roumen Nedkov, Doino Petkov

Space Research and Technology Institute – Bulgarian Academy of Sciences
e-mail: pgramatikov@space.bas.bg; rnedkov@space.bas.bg; dpetkov@stil.bas.bg

Abstract

The power supply for the video-spectrometric complex (VSC) "Fregat" is being considered. This secondary power supply systems have the following functions: Reception and switching of the voltages; Protection from overload and short circuit in the internal circuits and the exit circuits; Transformation of primary voltage in stabilized secondary voltages; Galvanically untethered secondary circuits by primary and Hull; Protection of the users from the electromagnetic noises; Provision of "Cold " and "Hot " reserve, etc. A set of technical documentation and test-measuring equipment for testing were created. Four sets of Secondary Power Systems for "Fregat" are designed and implemented for two flights to planet Mars.

1. Introduction

The VSC "Fregat" [5, 7] must perform two basic stages when photographing Phobos, Fig. 2: long-range photos and detailed photos with centimetre permission. VSC is managed from the Earth and then with the autonomous system itself solves the problems of convergence, hovering and flyby of 50 m from the surface of Phobos.

Eight blocks constructively shape VSC on the Fig. 1:

- Video Camera and Spectrometer (VCS), (1)
- Control System for VSC (CS VSC), (2)
- Video Storage Device for VSC (VSD VSC), (3)
- Secondary Power Supply System for VSC (SPSS VSC), (4)
- Electronics Block of the Video Storage Device (EB VSD VSC), (5)
- Block of the Tape Mechanism for VSD VSC (BBM VSD VSC), (6)
- Secondary Power Supply Unit for CS VSC (SPSU CS VSC), (7)
- Secondary Power Supply Unit for VSD VSC (SPSU VSD VSC), (8)

The functional elements of VSC "Fregat" are four blocks: (1), (2), (3) and (4). The two wide-range video camera channels at a distance of 50 m are authorized 50 mm and the spectral ranges of blue-green ($0.4 \div 0.6$ μm) and of the nearby infrared radiation ($0.8 \div 1.1$ μm). A narrow-angle channel shoots from a remote distance with an authorization of 20 m at a distance of 100 km. In this channel is used the full range

of matrix, which is 0.4 ÷ 1.1 µm. The spectrometer has an overall spectral clearance of 0.01 ÷ 0.02 µm. On flyby to Phobos (once every 7 days) from orbit, 3–5 series of 3 images must made, each with an interval of 75 s. In a convergence stage with Phobos, a series of footage containing altitude information must made. With hovering and a movement of 50 m above the surface of Phobos must be obtained 180 frames with centimetric permission and 120 panoramic frames, which occupy a volume of 1.5 Gbit and are emitted for 30–60 sessions to the Earth. The planet Mars provides 120 frames of elliptical orbit and multiple photos of individual areas [7]. The block (2) provides automatic testing of VSC; applies the reservation logic according to the technical condition of the elements of the VSC and realizes the reconfiguration of the structure of the VSC in case of failure situations. The block (5) record and store video and spectrometric data and at appropriate times transmit it to the Earth with 200 ÷ 500 times lower speed data to the telemetry channel [7]. Unit (6) performs the mechanical movement of the data media-magnetic tape.
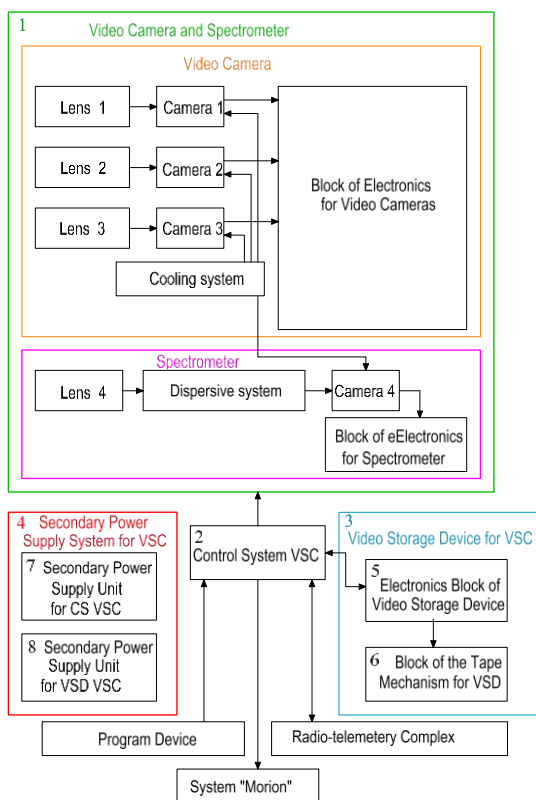

Fig. 1. Functional scheme of VSC "Fregat"

Fig. 2. Phobos in the background of Mars

Fig. 3. Appearance of SPSU CS VSC and SPSU VSD VSC

135

2. Materials and methods

2.1. Secondary Power Supply Unit for CS VSC

According to the technical specifications [1], the output voltages of SPSU CS VSC should be in the following ranges: + 5 V_{VSK} +/– 0.25 V; +18 V_{VSK} + 3/– 1.5 V; –18 V_{VSK}; +3 /–1.5 V and +27 V_{VSK} +/– 4 V. The stability of the output voltages of SPSU CS VSC must be according to the Table 1, where the maximum permissible K_{stab} values are shown, under specified conditions.

Table. 1. Parameters of SPSU CS VSC

Conditions of measurement of K_{stab}		K_{stab}			
Change of BN	Change of output current	+5 V_{VSK}	+18 V_{VSK}	-18 V_{VSK}	+27 V_{VSK}
24 ÷ 30 V	100 %	0.5 %	3 %	0.5 %	0.5 %
27 V	20 ÷ 100 %	5 %	15 %	5 %	5 %
24 ÷ 30 V	20 ÷ 100 %	6 %	20 %	8 %	8 %

The overall appearance of SPSU CS VSC is given in Fig. 3 [3]. The front panel has dimensions 202 × 100 mm, and the width of the shell is 140 mm. The time of establishment of the nominal values of the output voltages of SPSU CS VSC at start should be up to 0.1 s. Constructive SPSU CS VSC is executed by two identical modules (SPSU CS1 VSC and SPSU CS2 VSC) and one common Relay Board (RB), Fig. 4. In case of failure of the module SPSU CS1 VSC or SPSU CS2 VSC, it must be disconnected from the BN for a time not exceeding 0.05 s by fuse. In the laboratory tests according to the space methodology for the EMC (created by SPSU CS VSC) unacceptable meanings of noises with high frequencies were measured. This requires the installation of an additional filter FEMC1, Fig. 4.

Relay board (RB) performs the following functions:
- Inclusion of SPSU CS1 VSC or SPSU CS2 VSC;
- Simultaneous inclusion of SPSU CS1 VSC and SPSU CS2 VSC;
- Simultaneous exclusion of SPSU CS1 VSC and SPSU CS2 VSC;
- Telemetry data for operating temperatures; command for switching of SPSU CS VSC and presence of +5 V_{VSK}.

Constructively SPSU CS1 VSC is in a separate box and consists of four PCB:
- CSF1 Unit serves three functions: limit the starting current by circuit of a smooth start CSS; filtration of the internal and external noises by FEMS2 and voltage stabilization (VS1) for voltage +12V_{bs}.
- Controller1 Unit – performs the management functions of SPSU CS1 VSC;

136

- PTR1 Unit – realize the functions for: power amplifier (PA); transformer (Tr); rectifiers Rt1 ÷ Rt4 and voltage stabilization (VS2) for voltage +27V$_{vsk}$;
- FB1 Unit – board of negative voltage feedback.

Controller1 unit has the following functions: generates impulse voltage U$_{q1}$ and U$_{q2}$ for PTR1; monitors and limits the current of the PTR1 by the signal I$_{FB1}$ and ensures smooth charging of the capacitors in PTR1. He also monitors the tension of the BN and decides to exclude SPSU CS1 VSC when BN is less than 20 V or above 34 V.
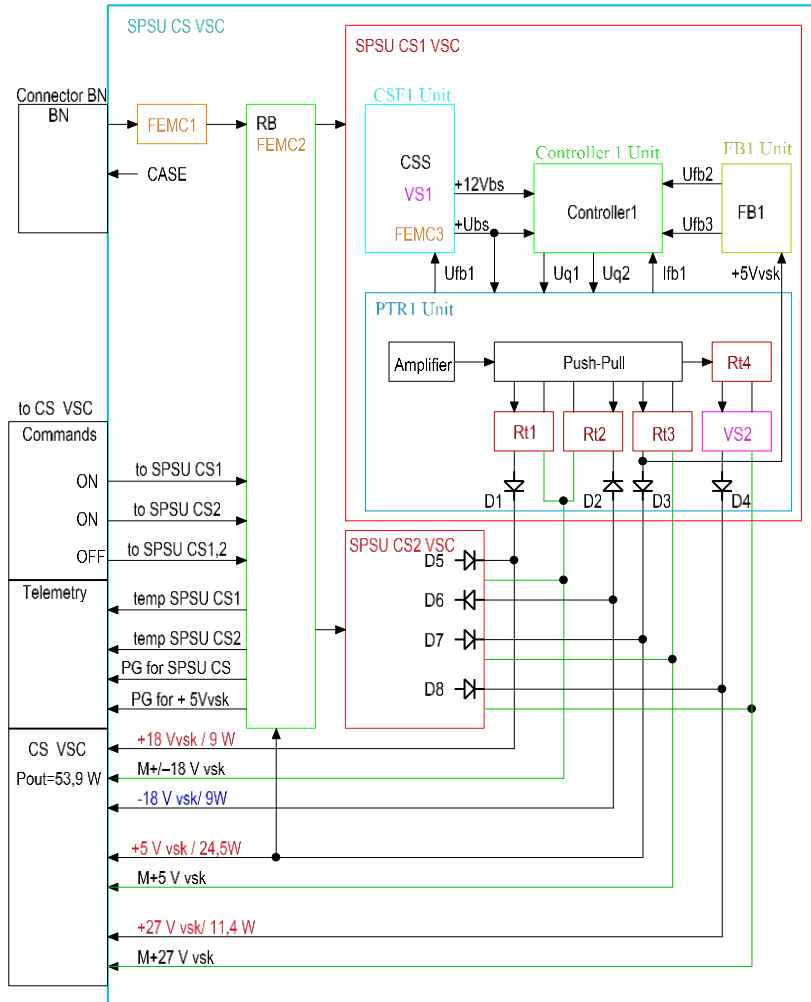

Fig. 4. Functional scheme of SPSU CS VSC

The PCB FB1 monitors and stabilizes by U_{fb2} voltage + 5 V_{VSK} for powering the digital part of CS VSK. One of the nodes of the FB1 traces for short surges of + 5 V_{VSK} and submits command U_{fb3} for rapid reduction of the output voltages of the SPSU CS VSC. The primary requirement for the design of space research equipment is the creation and use of Control and Measurement Equipment (CME). Through the CME the working capacity of the scientific devices is checked, the acceptance and executing of the commands are measured, the parameters of SPS in the Ground Based Autonomous and Complex Tests [24]. For the SPSU CS1 VSC and SPSU CS2 VSC, the CME is made according to [4] and is used for measurements according to [2–4]. At full load and at three different voltage values of BN with KIA, the starting currents of SPSU CS1 VSC LK-1 and SPSU CS1 VSC LK–2 are measured, Fig. 5 and Fig. 6. From BN at time $\Delta t = 0 \div 50$ ms becomes charge of the primary capacitors. The secondary capacitors are charged in the interval $\Delta t = 100 \div 350$ ms. There is a large identity of the parameters of the two channels of (SU1 and SU2) and the starting current does not "exceed 5 times the nominal time less than 0.2 s", according to the electrical requirements [2, 3]. The UFB1 voltage serves to saturate the transistor in CSF1, which reduces thermal losses. To the +27 V_{VSK} connect to about 0.2 s the windings of the relays, switching the primary spare boards of CS VSC, i.e. the cargo in this chain is highly dynamic and requires the use of VS2. In order to make the "hot" mode of SPSU CS VSC are used diodes D1, D2, D3, D4, D5, D6, D7 and D8, which worsens the K_{stab}. In case of overload or short circuit (in PTR1 or CS VSC) the voltage proportional to the current Ifb1 is used to limit the current SPS CS1 VSC consumption.
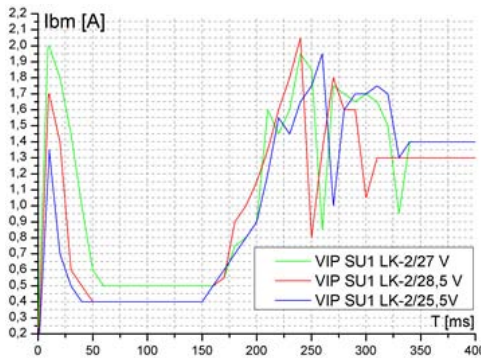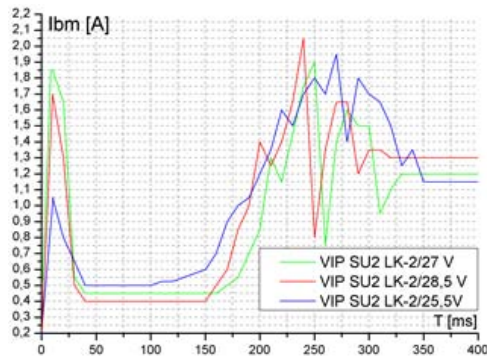

*Fig. 5. Starting current
of SPS CS1 VSK LK-2*

*Fig. 6. Starting current
of SPS CS2 VSK LK-2*

2.2. Secondary Power Supply Unit for VSD VSC

In Fig. 7 is given the functional scheme of SPSU VSD VSC [4]. The loads of SPS VSD VSK in different modes are given in Table 2. In "Standby" mode +5 V_a only works and SPS consume from BN only 1.125 W.

Table. 2. Loads of the SPS VSD VSK in different modes

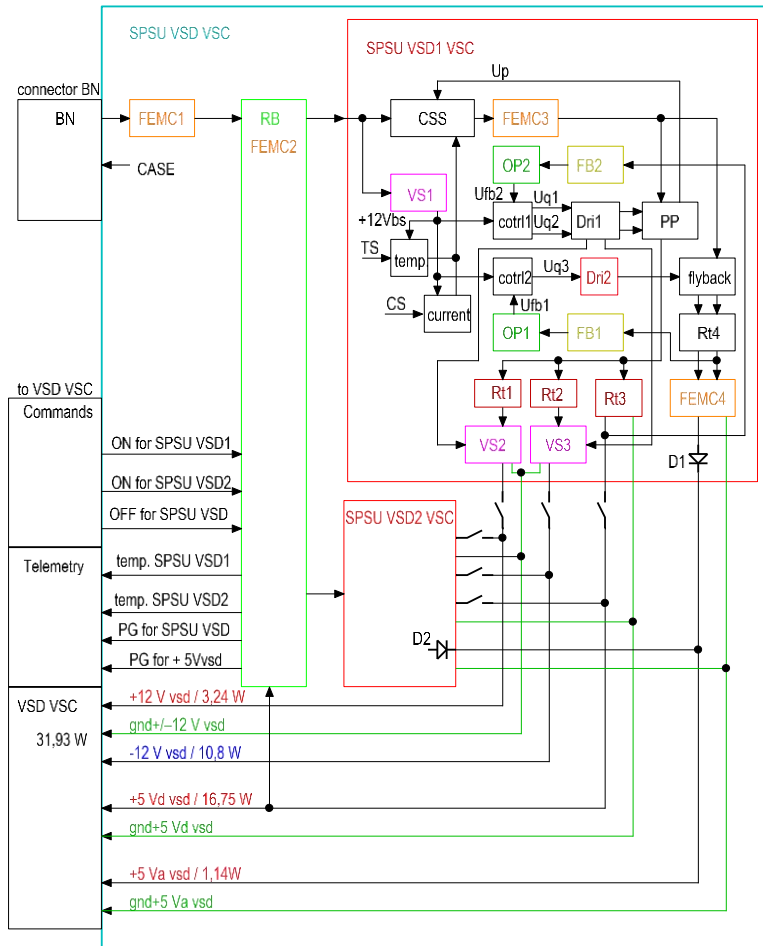| Mode	Dimensions	+5 Va VSD	+12 V VSD	-12 V VSD	+5 Vd VSD	Pout
Record	[W]	0.825	2.52	7.92	16.75	28.015
Play	[W]	0.825	3.24	10.80	12.50	27.365
Delete	[W]	0.825	2.40	8.16	10.00	21.385
Rewind	[W]	0.825	2.40	7.92	16.75	27.895

Fig. 7. Functional scheme of SPSU VSD VSC

139

The appearance and dimensions of SPSU VSD VSC are similar to SPSU CS VSC. The difference is in the functional and principle scheme: there is a "hot" reserve only for Standby mode $+5V_{VSD}$, and the contacts of the relays are used for the "cool" reserve of the remaining voltages. The mode off duty cycle is carried out with a Flyback converter (UDR, OPTV, S, ovn1, FEMS4, Ovn1, Or1, D1) and the main mode–with the other blocks. In comparison with SPS CS VSK in SPS VSD VSK are added TC and ZKSP with functions of temperature control and protection against short circuit.

2.3. Parallel Stabilizer for VSD VSC

When was first connection on the technological specimen of SPSU VSD VSC to the technological model of VSD VSC, an unacceptable noise of the video data is obtained. It is found that the low-frequency engine current of the tape recorder induces a surge in voltage -12 V_{VSD}, where are connected sensitive amplifiers of the video signals. The problem is solved by a copyright solution by attaching a current stabilizer in the chain of -12 V_{VSD} [6]. Scheme of parallel stabilizer of current PS-VSD-VSC is given on Fig. 8. The signal "ITM" enabled VSD VSC in the mode "recording" and "playback" (Table 2) characterized by unacceptable noise of the video data. For saving electricity in the remaining modes, PS-VSD-VSC is in standby mode.
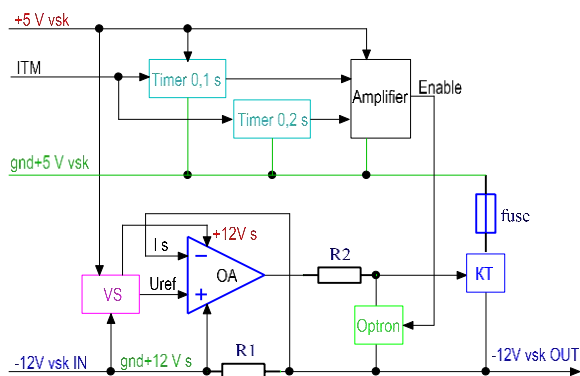

Fig. 8. Functional scheme of PS-VSD-VSC, Project „PHOBOS"

3. Results

Phobos images are captured at a distance of $320 \div 440$ km. There are 5 series pictures of Phobos from distance $184 \div 223$ km. The total number of photos of Phobos are 37, of which 8 in the background of Mars [24]. The Scientific program

52 days (flight 83 days) is performed by "Phobos-1" mission and 200 days (flight 255 days) from "Phobos-2" mission.

4. Discussion

VSC provides the special task of the spacecraft – the main navigational task of space mission during flight to planet Mars, in orbital flight and convergence to Phobos. When flying to Mars and conducting the navigation sessions for the "Phobos-2" becoms one instability of the operation of the TV channels 1 and 2. After reconfiguration of VSK with switching the additional SPS CS2 VSC and automatically transitioning to a backup subordinate processor, the reliable operation of these channels is restored.

References

1. Основные технические характеристики автоматической универсальной орбитальной станции АУОС и техническе требования для устанавливаемой на ней научной аппаратуре, АН СССР, ИНТЕРКОСМОС, 1982.
2. Инструкция по эксплуатации ВИП ВЗУ ВСК, ВС'\К.30.039.ИЭ, ИКИ-БАН, 1987 г.
3. Вторичный источник питания системы управления, проект „Фобос", Техническое описание ВИП СУ ВСК, ВСК.30.038.ТО, ВИП СУ ВСК ЛК-1, ИКИ-БАН, 1987.
4. Частный протокол приемо-сдаточных (ПСИ) и конструкторо-доводочных (КДИ) испытаний, ВИП ВЗУ ВСК ЛК-2, ВИП ВЗУ ВСК ЛК-3, Недков Р., П. Граматиков, Р. Тодоров, В. Янков, М. Иванов, И. Иванова, В. Шаламанов, Техническое и технологическое обеспечение медико-биологической программы проекта „Шипка", Экспрес отчет БАН, София, 1988.
5. Avanesov, G. A., B. I. Bonev, et al. Television observations of Phobos, Nature, 1989, 341, 6243, 585–87.
6. Граматиков, П., Метод за подтискане на нискочестотни токови пулсации в захранването на цифровото видеозапомнящо устройство на видео-спектрометричния комплекс „Фрегат" от проекта „Фобос", 2-ра национална конференция „Аерокосмос и екология", Шумен, 19-20 април 1990 г.
7. Аванесов, Г. А., и др., Телевизионные исследования Фобоса. К.Н.-М.: Наука, 1994. 168 с. ISBN 5-02-000298-4.
8. Граматиков, П., Р. Недков, Д. Петков, Вторична електрозахранваща система на видео запомнящо устройство от видео спектрометричен комплекс, In: 6th International scientific and technical conference, "Engineering, technologies, education, security", 2018, Veliko Tarnovo, 191–93.

ВТОРИЧНИ ЕЛЕКТРОЗАХРАНВАЩИ СИСТЕМИ
ЗА ВИДЕОСПЕКТРОМЕТРИЧЕН КОМПЛЕКС „ФРЕГАТ"

П. Граматиков, Р. Недков, Д. Петков

Резюме

В настоящата статия се разглежда системата за вторично електрозахранване на Видео-спектрометричен комплекс "Фрегат" и параметри на първичното захранване (ПЗ). Тя се състои от две вторични електро-захранващи системи (ВЕС) и един паралелен стабилизатор, които имат следните функции: приемане и превключване на ПЗ; защита на ПЗ от претоварване и късо съединение във вътрешните вериги и изходните вериги на ВЕС; трансформация на първичното напрежение в стабилизирани вторични напрежения (галванично развързани от ПЗ и корпуса); защита на ползвателите на ВЕС от шумовете на ПЗ; ограничаване на нивото на шума, създаден от ВЕС в ПЗ; осигуряване на "студен" и "горещ" резерв и др. Предложеното решение за ВЕС доказва себе си при нещатна полетна ситуация. Създадени са комплект техническа документация и контролно-измервателна апаратура за изпитания. Проектирани, разработени и реализирани са по четири броя от ВЕС за "Фрегат" за два полета до планетата Марс. Спътникът Фобос на планетата Марс е заснет от разстояние $320 \div 440$ km. Направени са 5 серии снимки на Фобос от разстояние $184 \div 223$ km. Общият брой на снимките на Фобос са 37, от които 8 на фона на планетата Марс.

COMPOSITE METAL-CERAMIC AND METAL-POLYMERIC MATERIALS FOR FRICTION ASSEMBLIES OF NATIONAL CIVIL AIRCRAFTS

Andrii Bychkov[1], Olha Nechyporenko[2]

[1]State Scientific and Research Expert-Forensic Center of the MIA of Ukraine. Kyiv
[2]State enterprise "ANTONOV". Ukraine, Kyiv

Abstract

Experience of using of metal-ceramic and metal-polymeric materials in friction assemblies of aeronautical engineering is generalized. Characteristics and conditions of operation of the sintered friction and antifriction materials are presented. Peculiarities of metal-fluoroplastic tapes of foreign production are considered. Efficiency of using of sintered and metal-polymeric materials in friction assemblies of modern civil aircrafts is shown.

One of the reasons of failure of components and units is wear, at that about 75 % cases of failure are stipulated exactly by wear of the friction pairs. As far as the aircraft control systems, landing gear, hydraulic system, etc. are the systems working due to movement of their elements, importance of ensuring their reliable functioning becomes obvious [1].

Increased wear of the components in the friction assemblies in some cases violates air-tightness of the working space, in other cases normal conditions of lubrication, in third cases it causes loss of the mechanism precision, which worsens aircraft control and affects flight safety. Wear and damage of the surfaces reduce fatigue resistance of the components and may be reason of their failure even at insignificant stress concentrators and low nominal loads. Violation of normal interaction of components in the friction assemblies due to their wear may cause vibrations and impacts in the joints, and jamming and seizing of components – emergency situations. In this connection materials for work under friction conditions are referred to the most important in aircraft construction [1, 2].

In the context of triboengineering, the powder metallurgy is one of the most efficient methods of production of the materials (metal-ceramic and metal-polymeric materials) because it allows joining in one material different components specially selected for solution of a specific task. Materials of triboengineering designa-

tion are able to meet whole complex of frequently contradictive requirements stipulated by specific conditions of the aviation engineering operation, which is practically impossible when using traditional materials [3, 4].

In structures of friction assemblies of national civil aircrafts the metal-ceramic iron-based (FMK-79) and copper-based (FMKM-1) friction materials are used. Use of sintered friction materials allows increasing longevity, reliability and efficiency of the friction assemblies, and creating new structures with high power intensity, wear resistance, heat resistance and high and stable values of the friction factor.

Sintered friction materials not just improve technical characteristics of aeronautical engineering, but also ensure its high economic efficiency due to increase of longevity of the friction assemblies and reduction of the operation expenses. In addition, in majority of cases safety of passengers and the crew depends upon reliable work of the aircraft friction assemblies [3, 4].

Items of friction designation represent a steel basis with sintered to it on one or two sides metal-ceramic linings from friction materials. Low-carbon (steel 20), medium-carbon (steel 45), chromium (12Cr13, 20Cr13) and low alloy steel (high-grade steel 30CrMnSi) are used as the basis. For protection against corrosion and ensuring strong adhesion of the metal-ceramic linings to the steel basis, surface of the latter is galvanically nickel-plated.

For optimization of the friction material properties, different metal and non-metal components are introduced into their composition, which, depending upon the created by them effect, may be divided into two groups:

- the components, which reduce predisposition of the friction couple to jamming;

- the components, which create and stabilize certain conditions [3].

For improvement of the antiscuffing properties and increasing wear resistance of the friction materials, the metals with low melting point (lead, tin) and non-metal substances (graphite, boron nitride, barite) are introduced into their composition. During friction without lubrication, when temperature of the friction surface exceeds melting point of the low-melting-point metal, lead and tin melt and form on the friction surface a lubrication film, which reduces friction factor. Due to this friction temperature reduces, molten metal again solidifies, which causes increase of the friction factor up to the initial level (principle of self-regulation). Formation of a liquid lubrication film enables smooth and stable slipping, which is especially important at increased temperatures, when metal matrix is more inclined to seizure [5].

Lubrication action of solid lubricant with laminated structure (graphite, boron nitride) is connected with presence of adhesion of the solid lubricant particles to the metal and difference in the bonding force between atoms and molecules in the elementary crystal layer and between separate layers [5].

Introduction of solid lubricants reduces wear of the metal-ceramic, enables more stable work of the friction pairs, however at that friction factor reduces. For the friction factor increase up to the required level, friction additives are introduced into composition of the materials – silicon oxide and molybdenum oxide, silicon carbide. Main task of the friction additives is ensuring of optimum level of the material adhesion to the working surface of the counter-body without its abrasive wear [5, 6].

Friction metal-ceramic FMKM-1 on basis of copper is used in friction electromagnetic and safety couplings of aviation units at dry friction and temperatures up to 200 ºC. Friction factor of such material in pair with a chrome-plated steel at slip velocity up to 6.0 m/s is 0.28÷0.30 [6].

In comparison with the iron-based materials, the copper-based metal-ceramic scuffs significantly less mated component from steel or cast iron. Copper has high heat conductivity, which ensures good heat removal during friction [5].

After sintering the material FMKM-1 has hardness 300÷400 *HB*, after machining – 400÷600 *HB*. In sintered state at room temperature the metal-ceramic FMKM-1 has $\sigma_\text{в} = 50÷60$ MPa, $\sigma_{\text{в. bend}} = 70÷80$ MPa, $\sigma_{\text{в. compr}} = 140÷150$ MPa [1, 6, 7].

From the friction material FMKM-1 the brake shoes, friction disks for the onboard loading cranes of transport aircrafts, etc. are made (Fig. 1, *a*).

Friction disks with the metal-ceramic FMKM-1 are used in the limiting coupling of the mechanism located in the civil aircraft crew seats. Such mechanism ensures vertical movement of the set and its fixing in any place of the working movement range. At that, reliability of the mechanism with sintered friction disks is 45 flight hours, longevity is 30 years [8].

Friction metal-ceramic FMK-79 stands on the friction surface temperature up to 1000 ºC, and volumetric heating – up to 600 ºC, which is ensured due to the material basis – iron. Iron is pressed well, and relatively low cost makes use of iron economically advisable. For removal of the seizure and increase of heat conductivity up to 10 % copper is introduced into composition of the material [8].

The friction factor of the metal-ceramic FMK-79 in pair with cast iron ChNMKh (ЧНМХ) at slip velocity 20 m/s is 0.3÷0.4 [1, 6, 7].

At room temperature the FMK-79 metal-ceramic has hardness 800 ÷1050 *HRF*, $\sigma_\text{в} = 40÷50$ MPa, $\sigma_{\text{в. bend}} = 110÷120$ MPa, $\sigma_{\text{в. compr}} = 250÷260$ MPa. At temperature 600 ºC mechanical characteristics of the material are on average 1.3÷1.5 times lower [1, 6, 7].

Brake disks with the metal-ceramic material FMK-79 are used in the combined wing extendable devices drive and in the brakes designed for braking of the flap and the slat control transmission in case of their mismatch.

From the material FMK-79 the friction washers for the onboard loading cranes of transport aircrafts, load beams of the ground maintenance facilities, etc. are manufactured (Fig. 1, *b*) [6, 8].
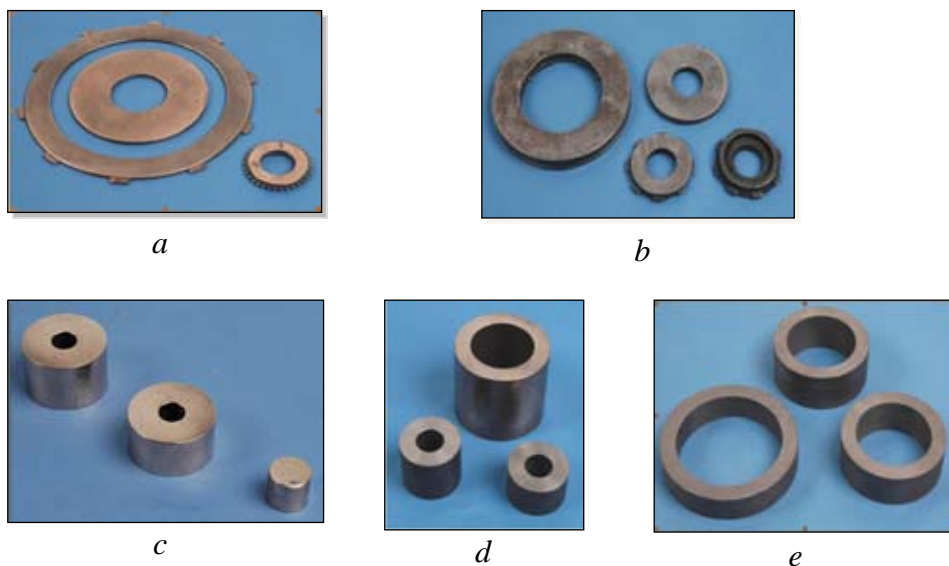

Fig. 1. Metal-ceramic billets of components with friction materials
FMKM-1 (a), FMK-79 (b) and from antifriction materials
AMK-1 (c), AMK-4 (d), AMK-5 (e) [6]

Another class of tribotechnical materials for aeronautical engineering are powder (composite) antifriction materials.

Antifriction materials are the materials with low friction factor, which are used for work in units-carriers or in guiding units (sliding bearings). Such materials must be wear resistant, have good running-in ability, high tribotechnical properties, big carrying capacity, self-lubrication, volumetric and surface strength, high heat conductivity, corrosion resistance, sufficient endurance and fatigue resistance, good technological properties, low wear of conjugated with them surfaces, not seizure, stand the load, speed and temperature without failure and change of the shape and the quality. Such complex of properties is not peculiar for a separate metal or non-metal. The task was solved due to creation of sintered composite materials, in which separate phases fulfil the assigned specific functions, ensuring, as a whole, a set of properties for the material necessary for specific conditions of work of the aviation unit friction assemblies [2, 4].

One of the main advantages of sintered antifriction materials is their self-lubrication. It is ensured both due to the lubrication located in pores of the sintered

materials, and due to the substances located directly in composition of the material, which play role of solid lubricant [6].

Use of the sintered antifriction materials as intermediate inserts is the most optimum structural decision for ensuring working ability of the friction assembly. In this case, structural materials, which practically do not participate in friction, ensure structural strength, and intermediate inserts, which are worn, may be easily replaced during the repair [1].

In friction assemblies of aeronautical engineering metal-ceramic materials on basis of copper (AMK-1, AMK-4) and nickel (AMK-5) and metal-polymeric materials (BFG-50M, metal-fluoroplastic tape) are used.

Antifriction sintered material AMK-1 represents a tin bronze with additives of graphite. In process friction graphite gradually forms a film on surface of the counter-body, which constantly restores in separate sections of the friction surface in case of a mechanical damage. Bronzografite works more reliably than materials without graphite and replace cast bronze and brass in friction assemblies.

The AMK-1 material has hardness after sintering 250÷350 *HB*, and after machining or calibration – 300÷450 *HB* [1, 6].

From the bronzografite AMK-1 different friction components are manufactured which work under conditions of self-lubrication at slip velocity up to 1 m/s and load 4÷5 MPa. At that, effect of self-lubrication is ensured both due to presence of graphite in composition of the material and due to lubricant present in the pores after its impregnation [6].

It should be noted that impregnated metal-ceramic bearings have a number of advantages in comparison with the cast ones, in particular:

- high running-in ability and smoothness of movement;

- possibility of use in the cases, when lubrication process using conventional methods is impeded or impossible and when it is impossible to remove products of attrition of the friction pair;

- possibility of using during cyclic movement and rotation with low speeds, when cast bearings have not integrated lubrication film;

- possibility of installation in vertical and inclined positions (in such positions oil just escapes from the cast bearings);

- reduction of oil consumption;

- reduction of the friction pair wear [3, 6, 8].

Bushings from the sintered antifriction material AMK-1 working under self-lubrication conditions are used in landing searchlights of the aircraft, simulators of different aviation units, etc. (Fig. 1, *c*).

For friction assemblies of aeronautical engineering working at increased loads and temperatures use of liquid lubrication substances is not advisable, because

they either are squeezed out or burn out. In these cases sintered bronzes are used, properties of which are significantly improved by introduction of alloying metals and substances playing role of solid lubricants [6, 8].

Bushings from the *sintered complexly alloyed bronze AMK-4* are installed in "dry" friction zones with working temperature up to 350 °C (Fig. 1, *d*). The material contains up to 10 % solid lubricant of layered structure, which enables reduction of the friction factor, wear and probability of the conjugated components seizure. Within temperature range 300÷350 °C at load up to 5 MPa and slip velocity 0.5 m/s in pair with counter-body from steel 9Cr18 (9X18 in Russ.) without lubrication the metal-ceramic friction factor is 0.20÷0.24 [6].

At room temperature the metal-ceramic AMK-4 has hardness 550÷750 *HB*, $\sigma_{B. bend}$ = 130-140 MPa, $\sigma_{B. compr}$ = 250-280 MPa; at temperature 350 °C – hardness is 400÷650 *HB*, $\sigma_{B. bend}$ = 70÷90 MPa, $\sigma_{B. compr}$ = 160÷180 MPa [1, 6, 7].

Sintered nickel-based antifriction materials are used for manufacturing of friction assemblies working under especially hard conditions. In pure form, nickel is characterized by high plasticity and very low antifriction properties during work without lubrication. That is why for manufacturing friction assembly components multicomponent nickel-based alloys containing strengthening and antiscoring additives are used. Part of the nickel in such alloys is replaced by iron and copper. Alloys with high content of nickel have good corrosion resistance [4, 6].

During flights in clouds, in majority of cases ice formation occurs, which is connected with presence in the atmosphere of water in dispersed liquid state at negative temperatures. At that, flight characteristics of an aircraft significantly worsen (vertical rate of climb reduces, ceiling and maximum flight speed reduce, increases fuel consumption and required power for flight at the assigned speed), and jamming of the aircraft control systems is possible. For protection of aircraft against ice formation, the anti-icing systems have been developed, the action of which is based on heating of the surface, which it is necessary to protect, by hot air. For compensation of the pipeline length change, special compensators are used at significant temperature differentials, which admit linear and angular movements [6, 8].

Nickel-based bushings from the *antifriction metal-ceramic AMK-5* enter into composition of the compensators made from titanium alloys or corrosion resistant steels (Fig. 1, *e*). At temperature 550 °C, slip velocity reduces up to 0.2 m/s and at the load 1.5 MPa in pair with the counter-body from steel 9Cr18 (without lubrication) the friction factor of the antifriction metal-ceramic AMK-5 equals 0.20÷0.24. At temperature 450 °C the metal-ceramic AMK-5 has $\sigma_{B. bend}$ = 120÷170 MPa, $\sigma_{B. compr}$ = 200÷270 MPa [6].

Bushings from the metal-ceramic AMK-5 are used in the non-return valve design, which ensures protection of the aircraft airline system against return airflow (air temperature at the inlet is 500 °C).

In mobile connections of aeronautical engineering seamless and wrapped *metal-fluoroplastic bushings* with flange (Fig. 2) and without flange may be used. Depending upon standard size, number of such bushings in the aircraft may achieve hundreds and sometime thousands pieces.

Operating life of metal-fluoroplastic bushings working without lubrication at reciprocating-rotary motion with average slip velocity up to 0.04 m/s, load 100 MPa and deviation angle $\pm 30^\circ$ is not less than 10^5 cycles; friction factor after 10^5 cycles does not exceed 0.12. Metal-fluoroplastic bushings stand static load not less than 300 MPa; at that, residual deformation does not exceed 0.02 mm (or 0.25 mm, if internal diameter of the bushing is more than 12 mm). Metal-fluoroplastic bushings preserve their working capacity in the process after cyclic change of the temperature from –60 to +250 $^\circ$C as well [6].

Mentioned complex of properties is stipulated by structure of the metal-fluoroplastic tape, which is used for making bushings. Metal-fluoroplastic tape (MFT) represents a three-layer composition consisting from the base (a bimetal copper-plated tape from carbon steel), a porous layer (spherical particles of tin bronze sintered on one side of the copper-plated base) and antifriction layer (fluoroplastic filled by molybdenum disulfide, which covers by a thin film spherical particles of the bronze and fills voids of the porous layer) (Fig. 3) [9].

Fig. 2. Metal-fluoroplastic bushings with flange

Fig. 3. Metal-fluoroplastic tape structure (Russia) [1]

Such material integrates high strength of the basis with good antifriction properties of the filled fluoroplastic, which is strongly held on the working surface by the porous bronze layer, which, in its turn, also imparts to the material certain antifriction properties [10].

During fabrication of MFP, a layer of spherical tin bronze particles is sintered to the steel copper-plated basis, then the tape is calibrated and fill pores with fluoroplastic with molybdenum disulfide. Then the paste from the filled fluoroplastic is dried at temperature 80÷90 $^\circ$C and sintered at temperature 380÷390 $^\circ$C

with simultaneous calibration by the rolls heated to the same temperature. The final operation is additional calibration of MFP after its cooling [4].

Before starting the production, MFP pass obligatory metallographic control and control of strength and quality of sintering, stamping capacity according to Erickson method [6].

It should be noted that although composition of MFP of different producers is, as a whole, similar, in relation to the structure, dimensional parameters of the MFP constituents and chemical composition of the basis material (steel brand) significant differences exist (Fig. 4).
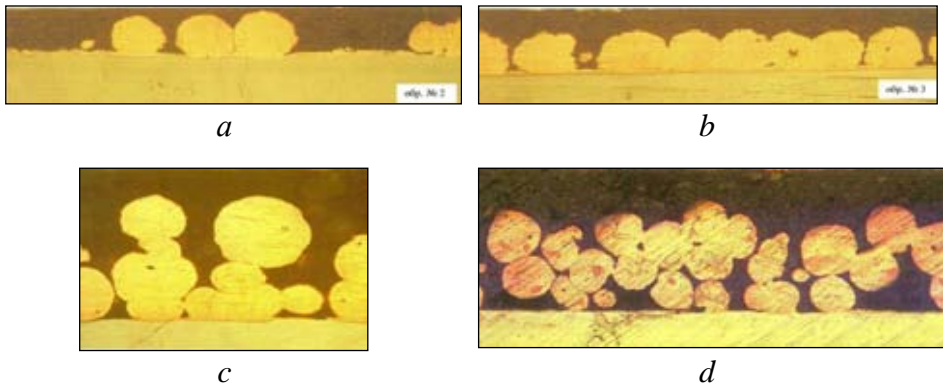

a   *b*

c   *d*

Fig. 4. Metal-fluoroplastic tape structure:

a) MFP of DU grade (Slovakia);   *b) MFP of DP4 grade (Slovakia);*
c) MFP of MU grade (Italy);   *d) MFP of SF-1 grade (China) [11]*

So, for example, MFP samples of the DU and the DP4 grades (Fig. 4, *a*, *b*) of Slovakian production have big general thickness, a thinner bronze layer and smaller average dimensional deviations from those established in the normative-technical documentation used in the national aircraft construction. At that, porous layer is characterized by non-uniform single-row distribution of the bronze spherical particles: both their fusion with each other and placement at significant distance from each other is observed. Nevertheless, control of working capacity of the wrapped bushings from MFP of the DP4 grade within the volume of periodic tests showed their correspondence to the standard requirements adopted in national aircraft construction: friction factor after 10^5 test cycles equaled 0.065, wear – 0.001÷0.02 mm per a side [11, 12].

Metal-fluoroplastic tape of the SF-1grade (Fig. 4, *d*) of Chinese production is characterized by satisfactory sintering of the bronze layer, qualitative sintering of the bronze granules and corresponds to the quality criteria established during tests according to Erickson method. Bushings from the mentioned tape passed without

remarks longevity (friction factor after 10^5 tests – 0.039, wear – 0.01÷0.05 per a side) and deformation tests, as well as the resistance tests at cyclic change of the temperature according to the standard, which regulates methodology of the type tests [11, 12].

Type tests of bushings from MFP of the SF-1 grade in composition of universal joints working without renewal of the lubrication also confirmed their correspondence to requirements of the standard on wear resistance (wear after $2 \cdot 10^6$ test cycles was not more than 0.16 mm, the norm being not more than 0.20 mm) and moisture resistance [11].

Positive results of the complex of investigations allowed using MFP of the SF-1 grade in production of assemblies and units of aeronautical engineering.

Despite high operation properties of metal-fluoroplastic bushings, a serious problem of their corrosion damage exists. One of the options of solution of this problem is replacement in the MFP of the basis from carbon steel for the corrosion-resistant steel [11].

From MFP of the SF-1SS grade (China) on basis from the corrosion-resistant steel the inserts into the hinge bearings working without lubrication are made.

Self-lubrication material BFG-50M represents a three-layer composition consisting from the base (tin bronze), a sintered porous bronze layer from non-spherical particles of tin bronze and antifriction layer from fluoroplastic filled with graphite. Such material is designed for work at slip velocity up to 1 m/s and load 100 MPa within wide range of temperatures (from –60 to +250 ºC) and vibrations. The material friction factor is 0.06÷0.09 [6, 7].

This material was developed for fabrication of components with friction surface of complex configuration – nuts (Fig. 5). Use of such nuts allowed reducing weight and overall dimensions of the slipping friction assemblies in structures of propeller mechanisms of the aircraft and excluding time of scheduled maintenance and preflight preparation [6, 7].

In addition to the details with a screw friction surface, the material BFG-50M is also used in other aircraft friction assemblies. So, inserts into the control column, rollers of the cargo door shutters of transport aircraft, sliding bearings for the wing extendable devices control, thrust washers for limiting couplings, etc. are made from it [6].

Efficiency of using sintered bushings from the BFG-50M material instead of similar bushings from metal-fluoroplastic is confirmed by positive results of the complex of tests according to the standard requirements, which establish volume and methodology of the tests for metal-fluoroplastic bushings (friction factor after 10^5 cycles of tests is 0.079, wear is 0.01÷0.05 per a side) [6, 9].

Advantages of the powder metallurgy technology during fabrication of bushings from the material BFG-50M in comparison with the traditional technology

of bushing fabrication from MFP by the method of deep drawing are relative simplicity of the technology and the fixtures and equipment; absence of a set of transitions like during drawing of the bushings; possibility of simultaneous sintering of a big number of the bushing ingots of one or several unit sizes depending upon the furnace load; possibility of removal of the sintered porous layer in case of presence of defects in it and its repeated sintering [9].

The powder metallurgy technology allows manufacturing sintered bushings from the self-lubricating material BFG-50M both with flange and without a flange (Fig. 6).

Fig. 5. Billets of nuts from the material BFG-50M

Fig. 6. Bushing without a flange (to the left) and with a flange (to the right) from the material BFG-50M [9]

Use of *fluoroplastic-based antifriction coatings* allows simplifying design of the compensators used for compensation of thermal, mounting and other movements during mounting of "hot" pipelines of the aircraft air system (Fig. 7). Absence of a crossbar in such compensators due to its replacement for a spherical element with antifriction fluoroplastic coating (Fig. 8) allowed reducing total hydraulic resistance in mounting of the aircraft air preparation system and reducing the compensator mass, which is especially important in aircraft construction. Power schemes of the pipelines with use of the hinge compensators with fluoroplastic-based antifriction coatings reduce loads on the system fixing elements and therefore, the aircraft framework [13].

152

Fig. 8. Spherical elements of compensator with fluoroplastic-based antifriction coating [11]

Fig. 7. Hinge compensator [1]

So, experience of operation of the metal-ceramic and metal-polymeric materials proves efficiency of these materials for ensuring reliability, quality and service life of the aeronautical engineering friction assemblies. The powder metallurgy technology has huge potential in the field of creation of the materials with unique properties, the use of which will allow solving principally new tasks connected with ensuring of flight safety.

Reference

1. Molyar, A. G., A .A. Kotsyuba, and A.S. Bychkov, O.Yu. Structural materials in aircraft construction / Nechyporenko – Kiev: KVITS, 2015. 400 p.
2. Garkunov, D. N. Tribotechnics: Textbook for High Schools / D.N. Garkunov. - Moskow: Mashinostroenie, 1989. 328 p.
3. Powder metallurgy. Sintered composite materials: Trans. for German (Edited by V. Shatt), Moskow: Metallurgy, 1983. 520 p.
4. Mitin, B. S., Vasiliev V. A. Powder metallurgy of amorphous and microcrystalline materials. Moskow: Metallurg, 1992. 128 p.
5. Fedorchenko, I. M., V. M. Kryachek, and I. I. Panaioti. Modern friction materials. Kiev: Naukova Dumka, 1975. 336 p.
6. Kotsyuba, A. A., A. S. Bychkov, O. Yu. Nechyporenko, and I.G. Lavrenko. Powder materials for aviation and rocket-space technology. Kiev: KVITS, 2016. 304 p.
7. Semenchenko, V. P., S. G. Kushnarenko, S. A. Bychkov, and O. Yu. Nechyporenko. Technological processes of receiving   details of planes by method of powder metallurgy: Textbook. Kharkiv: KhAI, 1992. 64 p.
8. Molyar, A. G., O. Yu. Nechyporenko, V. P. Semenchenko, and I. M. Romashko. Metal-ceramic of triboengineering designation in aircraft structures "AN". Technol. systems. 2006, 4, 18–22.

9. Bychkov, A. S., I. G. Lavrenko, O. Yu. Nechyporenko et al. Assessment of operation characteristics of bushings from the material BFG-50M instead of metal-fluoroplastic in aircraft friction assemblies. Bulletin of machine building and transport. 2016, 1, 4–11.

10. Fedorchenko, I. M., Pugina L. I. Composite sintered antifriction materials. Kiev: Naukova dumka, 1980. 404 p.

11. Bychkov, S. A., I. G. Lavrenko, O. Yu. Nechyporenko et al. Present status and prospects of using MFP of new producers in aircraft friction assemblies. Technolog. systems. 2014, 4, 9–21.

12. Bychkov, S. A., I. G. Lavrenko, and O. Yu. Nechyporenko et al. Investigation of the metal-fluoroplastic characteristics of different producers for elements of aviation structures. Open information and computer integrated technologies. Kharkiv: KhAI. 2013, 59, 343–53.

13. Kostornov, A. G., A. G. Molyar, A. V. Nenakhov, and O. Yu. Nechyporenko. Polytetrafluorethylene-based antifriction materials for swing joints of pipelines. Phys.-chem. mechanics of materials. 2005, 1, 111–13.

МЕТАЛОКЕРАМИЧНИ И МЕТАЛОПОЛИМЕРНИ МАТЕРИАЛИ ВЪВ ФРИКЦИОННИ ВЪЗЛИ НА САМОЛЕТИТЕ ОТ ГРАЖДАНСКАТА АВИАЦИЯ

А. Бичков, О. Нечипоренко

Резюме

Обобщен е опита в използването на металокерамични и металополимерни материали във фрикционни възли в аеронавтиката. Представени са характеристиките и условията на работа на синтеровани триещи и антифрикционни материали. Разглеждат се особеностите на металофлуоропластичните ленти, чуждестранно производство. Показана е ефективността на използването на синтеровани и металополимерни материали в триещите се детайли на съвременните граждански самолети.

MODELING OF THE CATASTROFIC VERSION
OF A TRANSPORT AIRPLANE

Petar Getsov[1,2], Dimitar Jordanov[2], Wang Bo[1]

[1]*Ningbo University of Technology - China*
e-mail: bo305@hotmail.com
[2]*Space Research and Technology Institute –BAS, Bulgaria*
e-mail: director@space.bas.bg

Abstract
Under the description of the crash is modeled the main crash-version. On the basis of a model of the "pilot-control system-airplane" system, the pilot actions in case of failure of the damping machine from the directional steering control system are analyzed.

Problem under investigation

The specific problem that is explored in the development is related to the following questions:
- Can a damping automat (DA) failure in the transport plane management system cause destructive overloads for the structure?
- What should be the pilot's actions in the developing emergency situation to prevent the crash?

Introduction

The flight safety theory has the task of responding to important operational issues of aircraft operation. Airborne disasters usually lack many of the facts that have to confirm or reject work versions in the investigation process. In such conditions, flight modeling and crew work in the process of developing the situation can give very important details to clarify the real causes of catastrophes. To illustrate this, modeling has attempted to analyze a Tu-134 plane crash in the 1970s over the territory of Croatia. The circumstances of this mysterious catastrophe are described by one of the leading investigators – Leonid Seliakov, chief designer at Tupolev's desk and author of the book "Man, Environment, Machine". The airplane has left parts of the airborne version, but the real reason is revealed years later when was found installation mistake on another plane: in one of the channels for the angular rate of risk (the reserve channel), the electrical signal goes to the reverse polarity

DA. This means that if, at any given moment, the backup channel starts operating after the main one is canceled (to increase the reliability this channel is reserved), the DA will command a rudder to reverse the demand for normal operation. A large-scale check is being carried out and such an error is detected on several other planes. Then, the most likely cause of the crash was the incorrect operation of DA due to an installation error.

The load and operation of the vertical stabilizer construction is limited to transport planes to breakdown overloads of 3.5 ... 4. If, for any reason, this overload is reached during the operation, airborne damage occurs in the air starting from the vertical stabilizer. For the Tu-134, with a T-shaped taillight, breaking the vertical stabilizer means total loss not only of lateral stability and manageability but also of longitudinal. The emergency situation is short (10 ... 15 s), but with the horizontal stabilizer on the body, the pilot can prevent the whole plane from being destroyed. Such a favorable outcome of the situation was registered in 1964, a B-52 aircraft of the US Air Force. The plane continues flying for another 6 hours with a destroyed vertical stabilizer and landing successfully. Fig. 1 shows a photo (from the Internet) of this unique aviation case.

Fig. 1. During a test flight, the vertical stabilizer of the B-52H, flying at a height of about 5 000 feet above New Mexico, is cut off in the event of large overloads. Six hours later, the crew managed to make the first and only B-52 landing without a vertical stabilizer [6].

Solution of research problem

A model in standard GOST 20058-80 of the "Matlab-Simulink" emergency situation based on the "pilot-control-airplane" contour was developed [1, 5]. Different consequences of failures in the damping machine (DM) from the rudder of

control system and the action of a pilot model for pedal operation and the control lever in the lateral movement of the aircraft are analyzed.

The most important actions in creating a flight model are to select the means to fully reflect the peculiarities of the particular situation. In this case, the modeling is limited to Simulink's contours for coordinated controls with the ailerons and the rudder of the pilot models on these channels. The sideways airplane model is developed in the GOST 20058-80 standard on lateral motion equations known from flight dynamics [2, 4] with the coordinate system and designations specific to that standard.

$$mV(\frac{d\beta}{dt} - \omega_x\alpha - \omega_y) = Z + G\,\cos\vartheta\,\sin\gamma\,;$$

$$I_x\,\frac{d}{dt}\,\omega_x = M_x\,;$$

$$I_y\,\frac{d}{dt}\,\omega_y = M_y\,,$$

where: $Z = Z^\beta\beta + Z^{\delta n}\delta_n$; $\delta_n = \delta_{n\ pilot} + \delta_{n\,damper}$;

$M_x = M_x^\beta\,\beta + M_x^{\omega x}\omega_x + M_x^{\omega y}\omega_y + M_x^{\delta e}\delta_e + M_x^{\delta n}\delta_n;$

$M_y = M_y^\beta\,\beta + M_y^{\omega x}\omega_x + M_y^{\omega y}\omega_y + M_y^{\delta n}\delta_n$.

The behavior of a hypothetical transport airplane, close to its size, aerodynamics and a Tu-134 control system is modeled. For simplicity in modeling, the control wheel grip has been replaced with a central lever, with the stiffness of the aileron pointing to the handle. The main work channel is the pedaling control of the "yaw-motion" movement. This movement is leading in the interdependent fluctuations of the glide and slope angles of the Dutch-roll. The rudder steering system sums up the pilot and the damping machine.

The emergency situation begins after a model wind laterally disturbance at a speed of 30 m/s at a height of 5 000 m and a flight velocity of 860 km/h, failure of the main channel to form a signal proportional to the angular rate of risk and automatic switching of the reserve channel "mounting error" (supplying to the DM signal with reverse polarity).

The general appearance of the model for coordinated control of the airplane after failure of the DM is shown in Fig. 2.
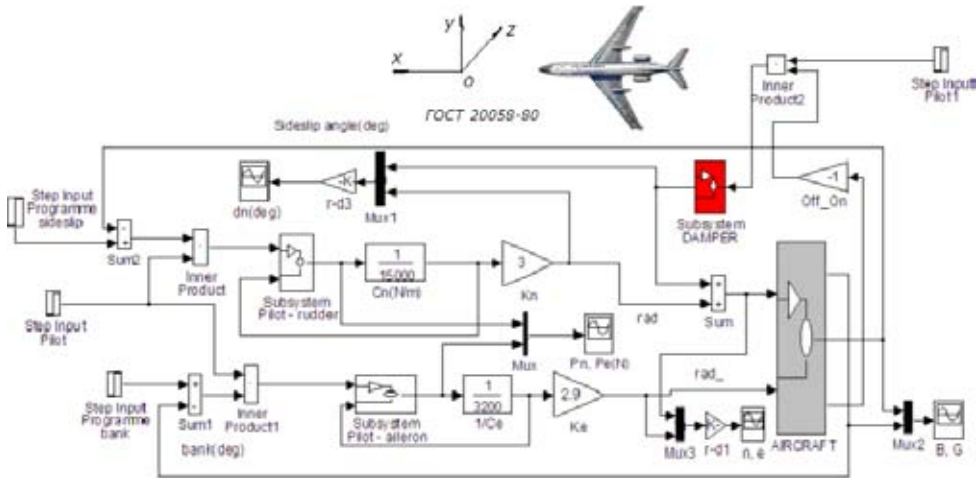
*Fig. 2. Outriggers: Subsystem: DAMPER – model of the damping machine
(Yaw damper); Pilot-rudder-pilot model Subsystem for steering with directional steering;
Pilot-ailerons Subsystem – Pilot model for ailerons operation.*

     The figure shows the two contours for coordinated lateral movement control with ailerons and rudder. The prototype aircraft and model are equipped with a damping machine. The DA works with the rudder for a hydraulic actuator. In the case of an inoperative damping machine, the pilot should strive to maintain, above all, a steady control loop. The pilot's task is to recognize the refusal and to balance the airplane with zero roll and slip angles in the conditions of disruption and failure. Two modes of operation are tested in modeling: first – attempting to balance with a faulty DA and second – excluding a DA and then balancing the airplane.

     On Fig. 3 is shown the pilot models and pilot co-pilot damping (DA). Under normal operation of the DA, the commands from it are opposed to the pilot's commands. Upon receiving a reverse polarity angular velocity, the pilot commands and the DA are unidirectional.
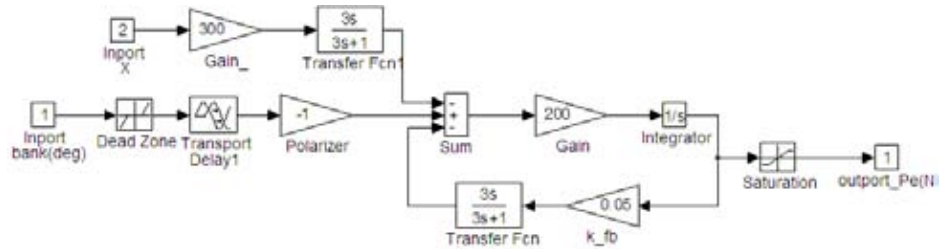
    a)   An aesthetic pilot model in the ailerons control channel

158
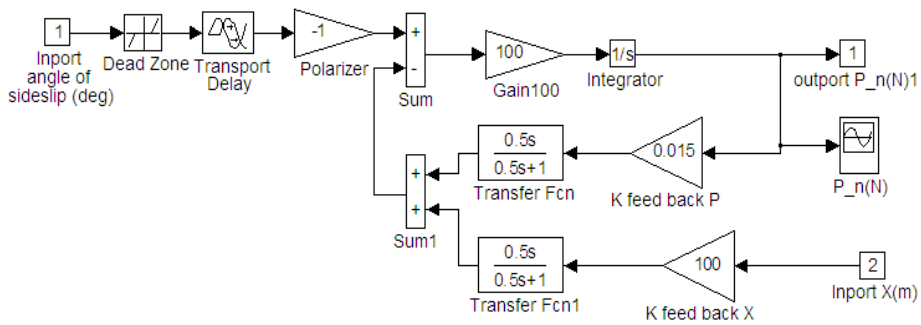
b) *Aesthetic (with flexible feedback) pilot model for pedaling*
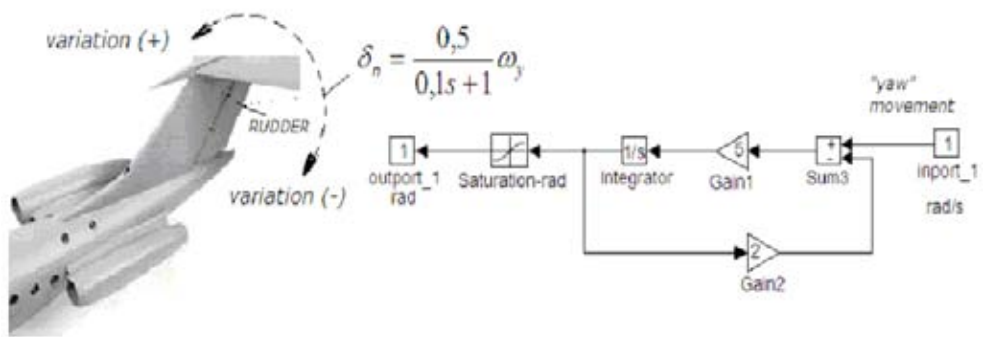
c) Model of the Yaw damper: The rudder deflection signal in DA operation is determined by the angular rate of risk at GOST 20058-80.

Fig. 3. Pilot and Damping Models in the channel to command the ailerons end rudder

Results

In Fig. 4 and Fig. 5 are represented the results of the variation of the basic parameters after failure of the main channel for forming an electrical signal to the executive of the DA and automatic switching of the reserved channel with an installation mistake leading to return of a revers polarity signal. This situation, as well as switching on and off, is achieved by adjusting the Off-On amplifier of the model in Fig. 1. For reverse polarity, this amplifier is set to "−1", for normal operation of "+1", and for OFF when "0" is set.
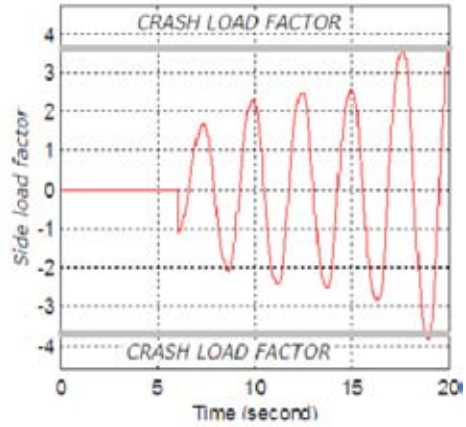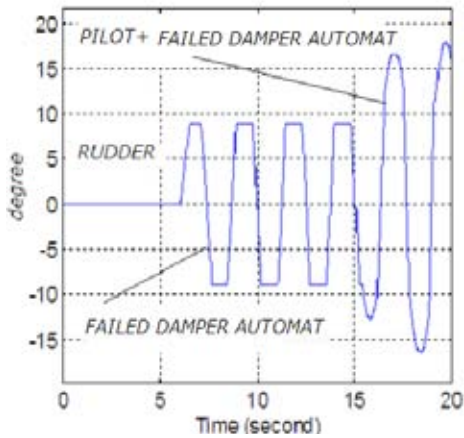
*a) Deviation of the rudder and lateral overload in the event of incorrect pilot actions −
Faults the interference without excluding the failure DA*
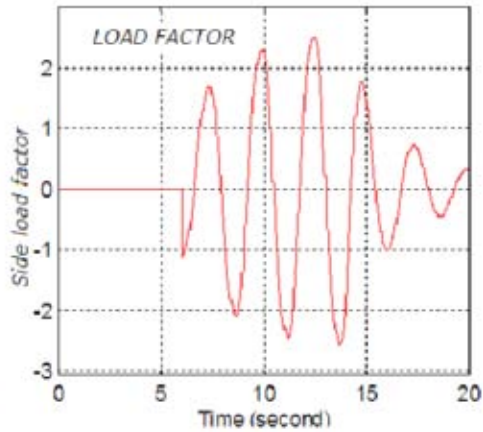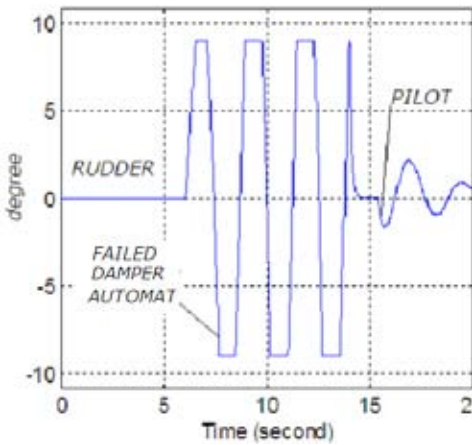
*b) Deviation of rudder and lateral overload with correct pilot actions −
Fails the interference after shutting down the failure DA*

**Fig. 4. Deviation of rudder and lateral overload after failure (Reverse Polarity Type)
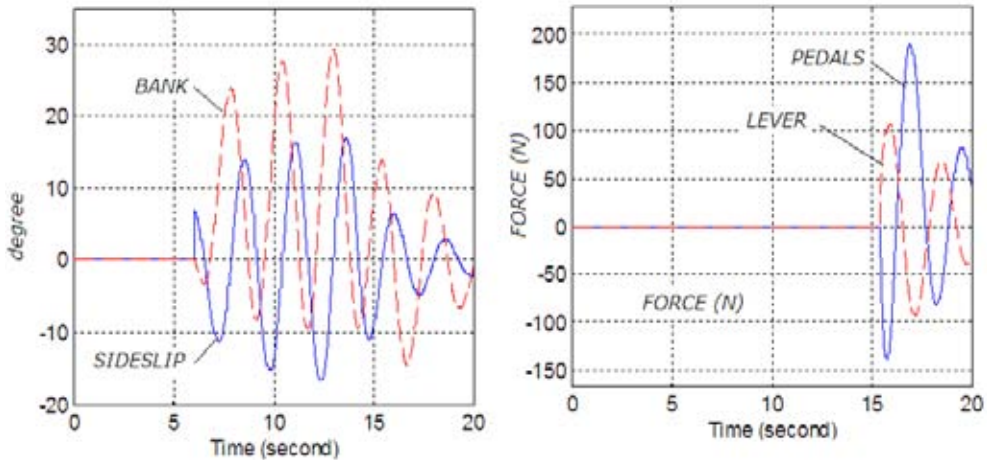of the DA for correct and incorrect operation of the pilot**

160

*Fig. 5. Basic flight parameters (roll and slip angles) and pedal effort and
the lever control for correct actions in the reverse polarity emergency situation of the DA;
the pilot model starts working in t_{pilot} = 15 s after a turbulent
from strong lateral wind modeled in the seventh second ($t_{disturbans}$ = 7 s).*

Conclusion

• The modeling shows that pilots intervention (switch on DA) if the polarity of damping automat is incorrectly connected, the lateral overload may exceed the breakdown. It is result from the oscillating instability of the control loop (over control).

• In the case of correct pilot actions (switch off DA immediately), even in the case of an 8-second delay, no catastrophic situation occurs.

• In the event of a failure of feedback on the rudder machine (RM), the constructive limitations of the RM operation prevent the vertical stabilizer and the airplane from degrading overloads.

• It is most appropriate for the pilot to fix the controls around the neutral position until the fault is detected and to turn off the DA. The aircraft itself stops the fluctuations.

References

1. Jordanov, D., P. Gecov. Unmanned aircraft – modeling and control. Third Scientific Conference with International Participaton "Space, Ecology, Nanotechnology, Safety", 27–29 June 2007, Varna, Bulgaria, http://www.space.bas.bg
2. Бороденко, В.А. и др. Самолет Ту 134, Транспорт, Москва, 1972.
3. Бадягин, А.А., С.М. Егер, В.Ф. Мишин, Ф.И. Склянский, Н.А. Фомин Проектирование самолетов, изд. "Машиностроение", Москва, 1972.
4. Галашев, Е.С., Н.М. Лысенко и др. Аэродинамика и динамика полета маневренных самолетов, ВИ, Москва, 1984.
5. Гультяев, А.К. MATLAB 5.2 – Имитационного моделирования в среде Windows – практическое пособие, Санкт Петербург, изд. "Корона принт", 1999.
6. Димов, Н., Поразен от мълния бомбардировач B-52 каца успешно в базата си. сп. "Клуб КРИЛЕ". http://www.pan.bg/view_article-1-418653-porazen-ot-mylniya-bombardirovach-B-52-kaca-uspeshno-v-bazata-si.html

МОДЕЛИРАНЕ НА ВЕРСИЯ ЗА КАТАСТРОФА НА ТРАНСПОРТЕН САМОЛЕТ

П. Гецов, Д. Йорданов, В. Бо

Резюме

В работата е моделирана основната версия за катастрофата на транспортен самолет по нейното описание от експертите. На базата на модел на системата "пилот-управление-самолет" се анализират действията на пилотите при аварийна ситуация в резултат на повреда на автомата за демпфериране от системата за управление.

DATA LOGGING BY AD7656 ANALOG TO DIGITAL CONVERTER

Konstantin Metodiev

Space Research and Technology Institute – Bulgarian Academy of Sciences
e-mail: komet@space.bas.bg

Abstract

In the paper hereby is presented, an exemplary algorithm of data logging by means of Analog Devices' AD7656 analog to digital converter. Converted data are transmitted further to ATmega644P microcontroller unit through Serial Peripheral Interface. The microcontroller, in turn, sends data to a PC through FTDI's FT232 UART to USB chip.

What motivates the current study is a source code development for the microcontroller unit. The source code is available for download at the quoted link. The main technique used in the code is external interrupt. The development environment used is MikroC Pro for AVR.

The presented study is a part of software developed for space project "Resonance".

1. Introduction

Analog Devices' AD7656 is six channel, bipolar, 16-bit analog to digital converter capable of simultaneous parallel sampling at rate up to 250 kSPS. It can accept bipolar input signals and handle input frequencies up to 12 MHz. The AD7656 has a high speed parallel and serial interface that let the device connect with microprocessors or DSPs. The AD7656 also accepts true bipolar input signals within $\pm 4 \times V_{REF}$ range and $\pm 2 \times V_{REF}$ range and maintains an on-chip 2.5 V reference voltage, [1].

The AD7656 has been used by the project "Resonance" research team as a circuit element included in the control and measuring equipment. As a whole, readily available software for AD7656 application is difficult to encounter which is why both presented study and source code in the appendix section may serve to fill up the gap.

2. Materials and methods

The experimental setup is depicted in Fig. 1. The AD7656 is powered by unipolar voltage of +5 V DC, so is the microcontroller unit. In addition, pin selectable bipolar voltage range of ±12 V DC is provided by AIMTEC's AM3D-0515DH30Z at 100 mW DC/DC converter and 78L12, 79L12 voltage regulators.

A 20 MHz external crystal oscillator clocks the MCU. Auxiliary equipment used is USBASP v.2.0, [2], in-system serial programmer as well as AVRDUDE utility, [3], to write to flash memory of the AVR chip.

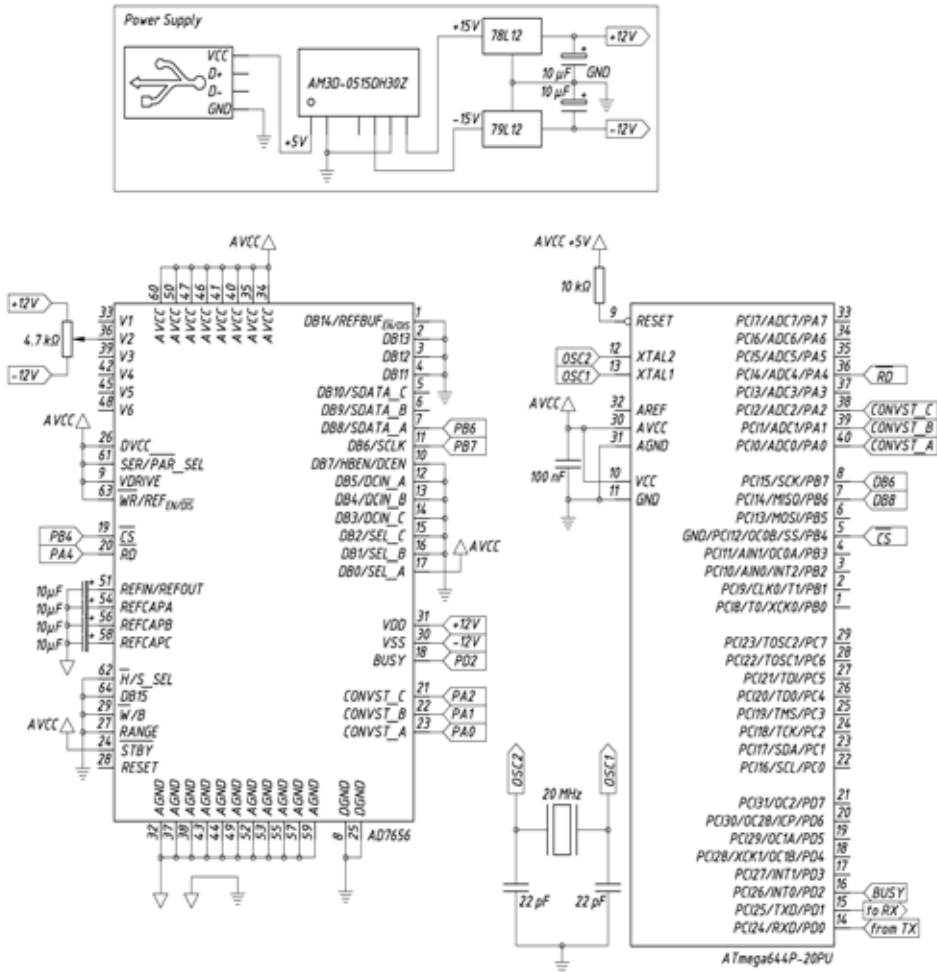
Fig. 1. AD7656 and ATmega644P wiring diagram, serial hardware mode, single output

During the initialization step, the MCU pins PA0, PA1, and PA2 are set to output. They are connected to CONVST_A, _B, _C pins on the AD7656 chip respectively. The CONVST pins are used to start conversions on the channel pairs. Initially, they are set to 1, i.e. idle state HIGH. Having set as input, the MCU pin

PA3/INT0 is connected to BUSY pin on the ADC. The latter returns state LOW whenever conversion is complete; hence, user is allowed to read data from the ADC, [4]. The Interrupt Sense Control bits ISC01 and ISC00 of the External Interrupt Control Register EICRA are set to 1 and 0 respectively, so that the falling edge of INT0 pin generates asynchronously an interrupt request, [5]. The external interrupt request is enabled by setting INT0 bit of the External Interrupt Mask Register EIMSK. Finally, global interrupt is enabled by setting I bit of the Status Register SREG.

In order to get AD7656 to start sampling, a one μs wide negative logic rectangular pulse, must be sent to CONVST pins. During the conversion process, BUSY pin is set to HIGH automatically which prevents the user from accessing the ADC data registers. It takes the ADC about three μs to succeed in converting voltages at all six channels. The conversion completes as soon as the BUSY pin goes back to state LOW. Thus, the falling edge arriving at INT0 pin, Fig. 2, triggers external interrupt request and an Interrupt Service Routine (ISR) starts. Essentially, the ISR reads converted data through SPI interface at frequency Fosc/128 ≈ 160 kHz. Finally, a data processing function sends text strings further via UART to the PC.

Data reading process, performed by the ISR, is implemented by means of SPI interface as follows. The CS (chip select) and the RD (ready) pins are set to state LOW to address ADC. The MCU exchanges data with the ADC like shift register. For this reason, SPI Data Register SPDR has to be written to initiate data transmission. After transmission completion, SPIF bit is set to HIGH by the hardware. The result is brought from the ADC and stored back in the SPDR register. This sequence is repeated twice to obtain data two bytes long (function "write2bytes" in the Appendix). Data transfer initiates by simply writing to the SPDR register twice in a row. It is not necessary to connect the MOSI line. Finally, both CS and RD pins are restored to state HIGH to deselect the ADC.

The reader is advised to examine closely the included source code at the Appendix section so as to apprehend the underlying idea.

3. Results

An exemplary scanning of all six channels by a logic analyzer is depicted in Fig. 2. In addition to generic SPI channels – MISO, CLK, and CS, the ADC pins BUSY, CONVSTA, and RD are also examined. The start pulse and the falling edge triggering an external interrupt are visible in the zoomed window.
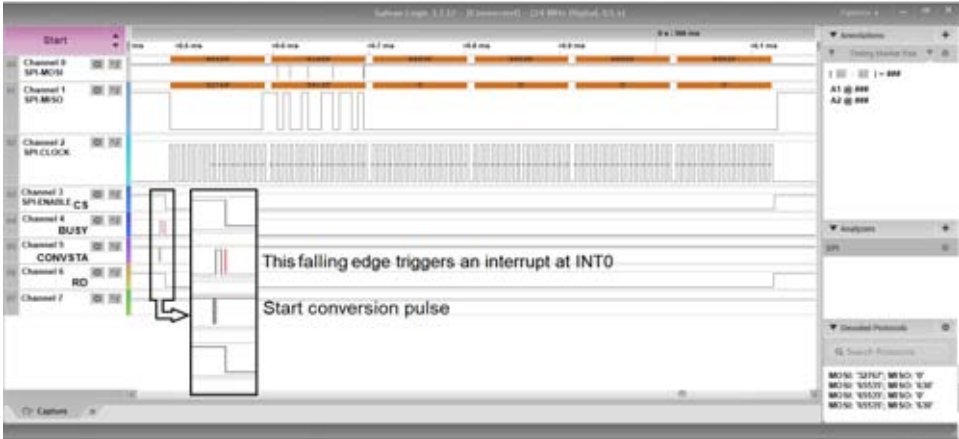
Fig. 2. Reading all six channels (two bytes each) of AD7656 via SPI, Saleae Logic session

In Fig. 3, an exemplary terminal session is shown. The input voltage feeds channel V2. The converted value, denoted by a red arrow, varies within –32 768 to +32 767 quantization levels, so does the input voltage, i.e. from –12 V to +12 V DC. In this study case, the first two input channels solely produce meaningful results according to following states of pins SEL_A = HIGH, SEL_B = LOW, SEL_C = LOW, SER/PAR = HIGH, H/S = LOW, Fig. 1 [4].

Fig. 3. Yet Another Terminal session, SDATA_A output channel

4. Discussion

The external interrupt technique used in the current study proved to be versatile enough. It lets user read data as soon as the conversion completes. The advantage of the presented interrupt technique over the so-called polling technique is evident. In the latter ("polling") case, the user is compelled to scan the MISO pin on a regular basis whilst, in the former ("interrupt") case, data are transferred to the MCU automatically whenever the conversion is done.

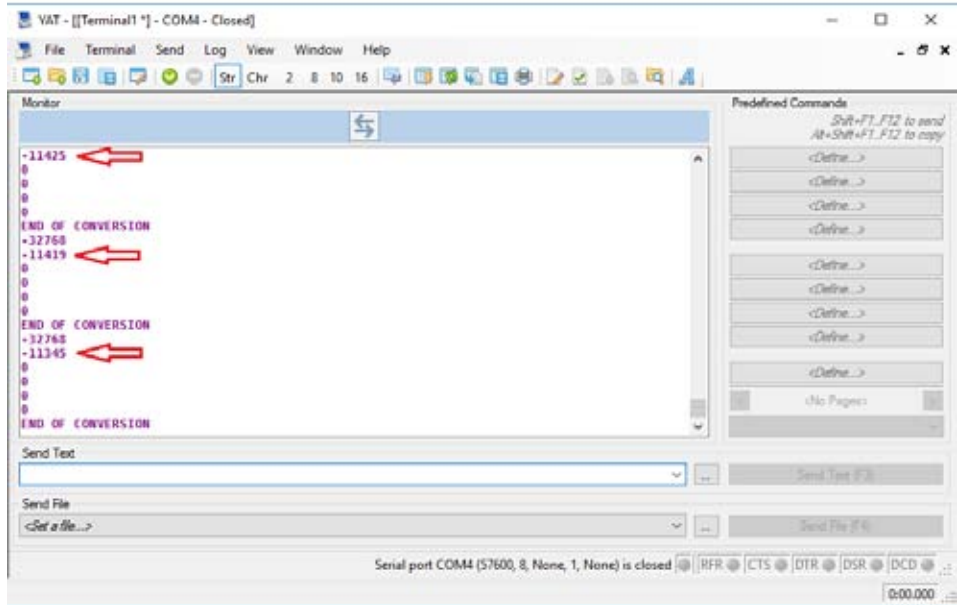In the Appendix section, reader may find source code, which is uploaded in the MCU. The development environment is Mikroelektronika's MikroC Pro for AVR, v.7.0.1 [6]. The presented source code might be downloaded at link [7].

A 3D model of sensing element and data logger used in project "Resonance" is shown in Fig. 4. The model is created in Autodesk Inventor IDE v.2018, [8]. The AD7656 used in the current study is an essential part of the corresponding control and measuring equipment.

Fig. 4. Electric potential measurement equipment, project "Resonance"

According to experience, it is very rare for the AD7656 to go silent. The reason this happens is that the BUSY pulse does not occur. Should it happen, it is necessary to reset the AD7656 (pin 28 to GND, Fig. 1) to restore its functionality.

Further project development might be using multiple ADCs configured in daisy-chain mode as it is described in [4].

References

1. AD7656/AD7657/AD7658 datasheet, Analog Devices
2. https://www.fischl.de/usbasp/
3. https://www.nongnu.org/avrdude/
4. Croke, C., Configuring the AD7656/AD7657/AD7658 for Serial and Daisy-Chain Interface Modes of Operation, Application Note AN-893, Analog Devices
5. ATmega644P/V, datasheet complete, Atmel
6. https://www.mikroe.com/mikroc-avr
7. https://libstock.mikroe.com/projects/view/2015/atmega644p-ad7656-in-serial-mode
8. https://www.autodesk.com/products/inventor/overview

Appendix 1. Source code.

```c
typedef unsigned short uint8_t;
typedef unsigned int uint16_t;
typedef signed int int16_t;
sbit Chip_Select at PORTB4_bit;
sbit Chip_Select_Direction at DDB4_bit;
int16_t VBs[] = {0, 0, 0, 0, 0, 0};

int16_t write2bytes(uint16_t command) {
uint8_t higherByte, lowerByte;
int16_t result;

higherByte = (uint8_t)((command &
            0xFF00) >> 8);
lowerByte = (uint8_t)(command & 0x00FF);
SPDR = higherByte; // sending high byte
while(!(SPSR & (1<<SPIF))); // wait
result = SPDR & 0xFF;
result <<= 8;
SPDR = lowerByte;  // sending low byte
while(!(SPSR & (1<<SPIF))); // wait
result |= SPDR;

return result;
}//write2bytes

uint8_t SPI_init(void) {

DDB6_bit = 0; // Set PB6 pin as input MISO
DDB5_bit = 1; // Set PB5 pin as output MOSI
Chip_Select = 1; // Deselect ADC
Chip_Select_Direction = 1; // Set CS# pin
SPI1_Init_Advanced(_SPI_MASTER,
    _SPI_FCY_DIV128, _SPI_CLK_LO_LEADING);

return 0;
}//SPI_init

uint8_t sendThroughUART(char *text_) {

UART1_Write_Text(text_);
UART1_Write(13); UART1_Write(10);

return 0;
}//sendThroughUART

uint8_t startSampling(void) {

PORTA.F0 = 0; // CONVSTA = LOW
// PORTA.F1 = 0; // CONVSTB = LOW
// PORTA.F2 = 0; // CONVSTC = LOW
Delay_us(1);
PORTA.F0 = 1; // CONVSTA = HIGH
// PORTA.F1 = 1; // CONVSTB = HIGH
// PORTA.F2 = 1; // CONVSTC = HIGH

return 0;
}//startSampling

uint8_t readADC(void) {
uint8_t j;

Chip_Select = 0; // Select chip
```

```c
PORTA.F4 = 0; // Select RD pin
for (j = 0; j < 6; j++)
    VBs[j] = write2bytes(0x0000);
PORTA.F4 = 1; // Deselect RD pin
Chip_Select = 1; // Deselect chip

return 0;
}//readADC

uint8_t processData(void) {
uint16_t result = 0;
uint8_t j;
char buffer[16];

for (j = 0; j < 6; j++) {
    result = VBs[j];
    sprintf(buffer, "%d", result);
    sendThroughUART(buffer);
}//for_j
UART1_Write_Text("End of conversion");
UART1_Write(13); UART1_Write(10);

return 0;
}//processData

void interrupt_ISR () org IVT_ADDR_INT0 {

SREG_I_bit = 0; // Disable interrupts
readADC();
SREG_I_bit = 1; // Enable interrupts

return;
}//interrupt_ISR

uint8_t init(void) {

DDA0_bit = 1; // PA0 as output (CONVSTA)
DDA1_bit = 1; // PA1 as output (CONVSTB)
DDA2_bit = 1; // PA2 as output (CONVSTC)
// DDA3_bit = 0; // PA3 as input (BUSY)
DDA4_bit = 1; // Set PA4 as output (RD)
SPI_init();
UART1_Init(57600);
Delay_ms(100);
PORTA.F0 = 1; // CONVSTA = idle HIGH
// PORTA.F1 = 1; // CONVSTB = idle HIGH
// PORTA.F2 = 1; // CONVSTC = idle HIGH
EICRA = 0b00000010; // Falling edge of INT0
EIMSK = 0b00000001; // External interrupt
SREG_I_bit = 1; // Enable interrupts

return 0;
}//init

void main() {

    init();
    while (1) {
        startSampling();
        processData();
        Delay_ms(100);
    }//while

return;
}//main
```

СЪБИРАНЕ НА ДАННИ ПОСРЕДСТВОМ АНАЛОГО-ЦИФРОВ ПРЕОБРАЗУВАТЕЛ AD7656

К. Методиев

Резюме

В настоящата статия е представен примерен алгоритъм за събиране на данни с помощта на аналого-цифров преобразувател AD7656. Преобразуваните данни се предават към микроконтролер ATmega644P по сериен интерфейс SPI. Микроконтролерът, на свой ред, предава данните към компютър по USB чрез преобразувател FT232.

Това, което мотивира настоящето изследване, е създаването на програмно обезпечение за микроконтролера. Изходният код може да бъде изтеглен от цитираната препратка. Основната програмна техника, използвана в кода, е външно прекъсване. Развойната среда е MikroC Pro for AVR.

Представеното изследване е част от програмното обезпечение, разработвано за космически проект „Резонанс".

THE RISK IN AEROSPACE PROJECTS

Nadia Marinova

New Bulgarian University
e-mail: nmarinova@nbu.bg

Abstract

The risk of inconsistencies in any public activity is a determining factor in the behavior of each subject. What are aerospace projects that involve large material, technological and human resources.

The first step in the risk analysis involves tabling the different stages or phases of the design system and determining the risks for each of them, whether technical, human or economic. The time at which the event occurs may significantly affect the consequences. For example, the collapse in the air traffic control system at a major airport can cause disruption to local air traffic much more than if it occurs during the week than on Sunday morning. Similarly, an accident at the chemical plant can be far more dangerous if it causes an immediate chemical reaction that generates toxic gases than in the final phase where the waste products are less dangerous.

Introduction

For engineers and managers, the main task of risk analysis (defining the stages of a mission, examining the interconnection between the parts of the system and quantifying the probability of failure) is to identify weaknesses in construction and to indicate those that contribute most – much for delay or loss. The evaluation process may even recommend ways to minimize or mitigate the risk. An example of probable risk analysis is that made for NASA by the engineering consultancy firm Packard, Lowe & Garrick inc. in connection with the Space Shuttle's external missile accelerators. NASA engineers and management, through the qualitative performance of the analysis, conclude that fuel leaks from the three external accelerators are "unlikely" and the risk is acceptable without fully understanding the amount of risk they are taking (although the worst, one of the problems with qualitative analysis is that the subjective interpretation of words such as "probable" and "incredible" creates preconditions for mistakes in risk assessment, for example NASA uses the term "unlikely" for risks, degree from 1:250 to 1:20 000.

Probability risk analysis shows that despite the fact that the individual risk of individual leakage is negligible, there are many places where leakage is possible. In fact, there were 5 leakages in the first 24 shuttle flights, and on 28 November 1983

the leaking fuel self-ignites when the shuttle landed and exploded after landing. Probability risk analysis shows that there is more likely to be explosion during landing than during take-off. The analysis recommends several possible ways to reduce the risk, for example, by replacing the fuel or placing explosive barriers between the different power plants.

The theoretical basis for risk analysis is the theory of probabilities and their applications in the safety and reliability of space flights. A quantified risk statement for piloted programs is the credibility of the crew. For Apollo, the probability of a safe return of the crew was 0.999, which means a 1.10^{-3} risk (1 in 1000). Risk analysis uses mathematical models for estimation and forecasting. For example, in the United States, from 1965 to 1970, the maturity model MARCEP (Maintainability and Reliability Cost Effectiveness Programm) was used to optimize the distribution of operational and emergency reservations. The model optimizes the system for the minimum weight, volume, and value when reaching a definite requirement for the mission and crew safety performance.

Risk-benefit analysis is a generic concept of risk-pricing techniques and the risk, cost and benefits of alternative projects or policies included in this assessment. Like other quantitative methods, the stages of this analysis include: defining objectives and tasks of the project alternative; identification of limiters; defining the scope and limits of the analysis itself and developing effective and feasible alternatives.

The main purpose of these techniques is to give a digital expression, if possible, of the risks and benefits of a project. Calculating these parameters requires scientific methods or simulation programs to assess the probability of failure or error. Finally, a complex assessment is made by aggregating the individual assessments of the different alternatives. Conclusions should contain the results of the sensitivity analysis where each important component or parameter changes according to its effect on aggregate risk, costs and benefits.

One of the possible approaches is based on the three main stages outlined in Fig. 1, which are formulating, analyzing and interpreting the impact of alternatives and institutional and value perspectives. When formulating risk, we determine or identify the type and amount of risk we take. Methods such as: nominal group techniques are applicable here; brainstorming; the Delphi method and others. Only the elements of risk and those elements that identify the needs, limitations and alternatives associated with risk mitigation with or without technological innovations are identified.
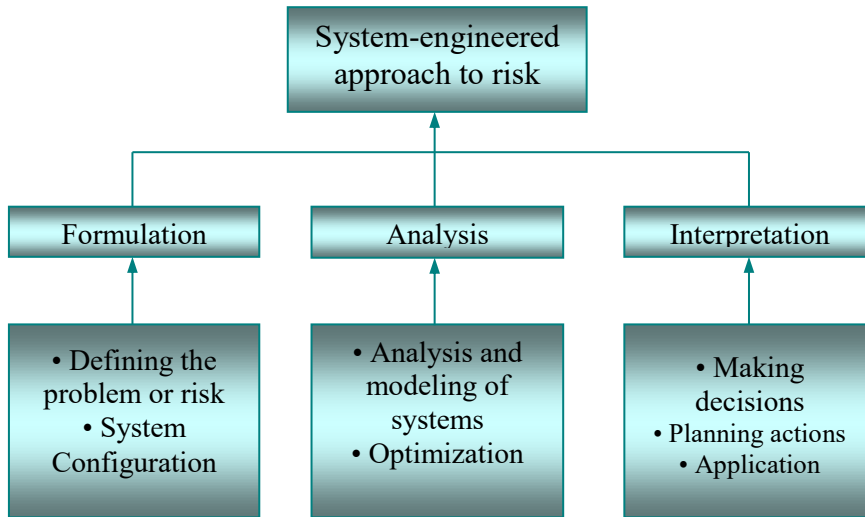
Fig. 1. Engineering System Approach to Risk Assessment

At the analysis stage, the errors, deviations and other consequences that may follow from the design and implementation of the project are predicted. This means assessing the probabilities associated with a result and the resulting fluctuations.

At the final stage, an organizational and political interpretation of the impact of the risk is given. This includes the individual and group mechanisms for the final evaluation, and then follows the decision-making process. Cost-benefit and cost-benefit analyzes are best suited for this purpose. Attempts to include the results of the risk analysis in these schemes are successful. The underlying problem arises from the fact that the risk and benefits are measured with different parameters and are therefore not always compatible.

For the interpretation of the results, a risk graph is drawn up – similar to the cost-benefit ratio. Risk profiles can also be useful. For example, projects 1 and 2 are likely to generate a total profit of approximately USD 150 000 000 and USD 200 000 000, respectively. For this reason, project 2 should be accepted by managers due to a better benefit/cost ratio. However, the data should be reviewed a little more thoroughly. Project 2 is likely to give a zero score of 15 % and only 43 % probability of generating a profit of $ 2 million.

There is also a 20 % probability that the return on project 2 will be less than project 1. This is an additional risk if project 2 is selected.

Based on this information, managers willing to reject the risk will be willing to accept Project 1, which has a good chance (83 %) to bring a modest profit of $ 150 000 000, with little chance of a greater or lesser profit , i.e. project 1 has a limited standard deviation. The professional would, however, prefer Project 2, which has little chance of making more profits.

172

The type of risks makes the results of the risks more transparent and thus allows the decision-maker to make choices according to his or her attitude to risk, whether it is more conservative or looser. Generally speaking, the data needed to compile the graph are limited in number, and examples from the history of such projects can easily be given. Engineers and marketing staff familiar with such projects can provide similar data. If there is no collective experience within the organization, freer or subjective assessments may be used for this purpose. There is a set of software to solve this problem.

The primary responsibility for project selection and implementation exceeds the risk assessment and lies mainly in the functions of senior management. In our opinion, notwithstanding the fact that formal analysis may imply some unexpected problems with large complex projects, it remains an academic exercise until the managers take its results seriously and ensure the proper management of the projects. Security has to be embedded in the system from the outset and good operational experience is essential to the success of any long-term risk management program.

In order to properly understand and manage the risk in certain systems, it is necessary for the managers to evaluate them at the stage of engineering projects. It is often said that the efficiency of a system can be reduced due to poor quality control, but it is not possible to improve a poor construction or design through good quality control. From the moment the project managers are in charge of making important decisions, risk assessment is one way of assessing alternatives so that their choice is more justified than isolated or, worse, repeat past errors.

Possible risk assessment methods based on multiplication criteria

Often, in the public sector, goods and services are either "complex", for example defense or space exploration, or so subsidized that their market price is an unrealistic measure of the real cost to society. Finding a way to determine the "undeformed" price of those goods and services, that is to limit the financial risk. When the analysis reaches such quantifiable parameters as security, health, quality of life, it is rarely possible to find a single variable, whose direct measurement gives an acceptable indicator. Frequently, substitutes are used. For example, the urban environmental code can be measured by an index composed of air pollution levels, noise level, traffic frequency, pedestrian density. Another index may include criminal background, fire index. At national level, it is accepted to quote unemployment rates, consumer price indices and producer prices, and the Dow Jones index. Each of these indicators is composed of multiple elements of different relative weight, which are then summed in an attributive way. Major and complex projects require more systematic and rational procedures.

The success and risk of a technical project depends on a set of criteria, the most important of which is the ability to take action to meet the project requirements. But the success and risk of the project also depend on the likelihood that the project

will remain within the set budget and timetable, technological possibilities beyond the immediate applicability of technology, the attitude of the user to the long-term goals of the organization. In order to balance all these factors, a model of value is needed to give the decision-maker the framework to carry out these actions.

The paradigm of the analysis of each solution is shown in Fig. 2. In the process of making the decision, the person responsible for the decision must choose the "preferred" alternative of a finite set of options, so the system model can be simplified to a spreadsheet or to a dynamic mathematical simulation, and attention must be paid to the full range of economic, technological and policy aspects of the project, each alternative, along with the prevailing uncertainty, should be set on the model of the system and the result is affected.

In the paradigm of solution analysis, the results of a system give the input parameters of the value model. The output parameters are the result of the decision-maker's preference regarding the order of the output parameters or the numerical values that show the preferences and their arrangement.
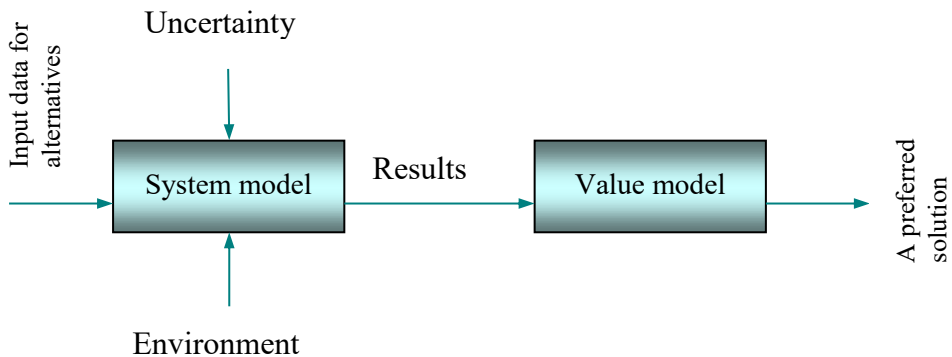

Fig. 2. Analysis of the decision

The Analytic Hierarchy Process (AHP) was developed by Thomas Saaty in order to obtain a simple yet robust methodology for multi-criteria analysis of alternatives and risks. The process can be applied to such decisions as portfolio selection, transport planning, production system design, artificial intelligence, etc. The merits of the AHR consist in the ability to structure a complex, interpersonal, multi-attribute, hierarchical problem, and to examine each level of the hierarchy by combining the results with the progress of the analysis. Comparing the individual pairs of factors (which may be alternatives, attributes or criteria depending on the context) is done by using a specific scale indicating the power a factor dominates over the others, taking into account the priority factors. The staging process can then be transformed into priority weights or alignment of alternatives.

The AHP begins by compiling a hierarchy of goals. At the top is the wording of the problem. At the next level, in general terms, the main considerations are formulated, usually followed by a list of criteria for each consideration. Depending on how detailed the model will be, each criterion can be divided into individual parameters whose values are either evaluated or determined by experiments or measurements. The lowest level of the hierarchy contains alternatives or scenarios containing the problem being solved.

The basis of the problem is "choice of orbital mounting system" and the four main criteria are: human factor productivity, economy, design and functionality. Five alternatives include an astronaut to work outside the station, a mechanical manipulator, man-operated, a complex manipulator with computer control, a maneuverable teleworking system with a control module or a visual control and manipulator manipulator. In fact, in the analysis process, each of the Level 2 criteria is further detailed to cover the date little necessary for precise comparisons. In terms of human performance, load necessary support, team compatibility and other aspects of interaction "man-machine" included several additional factors.

Once the hierarchy is structured, local priorities must be formulated for each individual factor at a certain level, taking into account the factors directly above the survey factor. This procedure is performed by comparing factors in pairs to determine their relative weight or priority. Because this approach is primarily a qualitative comparison, it is easier to apply than Keeney and Raiffa's multi-attribute approach. This will define the functions of the preferences. Nevertheless, the theory requires the following conditions to be met in the form of axioms:

Axiom 1. If we take two alternatives (or below criterion) i and j from the many alternatives A, then the decision maker will be able to make pairwise comparison (a_{ij}) when applying criterion c by a set of criteria

$$(1) \qquad c, a_{ij} = \frac{1}{a_{ij}} \text{ for everyone } i, j \in A$$

Axiom 2. When comparing two alternatives, the decision maker never evaluates one alternative as infinitely better than the other, taking into account criterion c, i.e. for each.

Axiom 3. The task can be formulated in a hierarchical form.

Axiom 4. All alternatives and criteria that matter to a task can be ordered hierarchically, i.e. the intuition of the decision maker must be included (or excluded) from the structure of the criteria or alternatives.

These axioms can be used to describe the two main tasks of AHR - formulating and solving a problem such as hierarchy (3 and 4) and providing assessment in the form of pairs (1 and 2). Such an assessment is an accent on results in conflicting criteria and is often too subjective. Saaty proposes to use a ratio of 1:9

in the quantitative assessment of the decision-maker's ability to "feel" the differences between two alternatives in relation to a given criterion.

The affiliation or transitionality of items is verified by confirming the circumstance.

$$(2) \qquad a_{ij} = a_{ik}\, a_{kj} \quad \text{for all } i,\, j,\, k$$

In practice, decision-makers assess only "real" elements a_{ij} by giving certain values so that perfect continuity of the equation is unlikely to occur. Therefore, approximation is possible elements of A can be represented as satisfying $a_{ij} = w_j / w_j + e_{ij}$, where e_{ij} is a factor error inconsistency of decision maker when compared with factors $i\, j$. If we continue the analysis one step further, one can see that the highest intrinsic value of matrix a, λ_{max}, Udo inserts $\lambda_{max} \geq n$, where equality means complete continuity, which leads to the determination of the sequence index:

$$(3) \qquad CI = \frac{\lambda_{max} - n}{n - 1},$$

which can be used for qualitative evaluation of matrix A. To have a basis for further analysis, we compare the index CI with a random matrix whose records are also randomly selected. Through Saaty's simulation, the results are as follows:

n	1	2	3	4	5	6	7	8	9	10
Rl	0.00	0.00	0.58	0.90	1.12	1.24	1.32	1.41	1.45	1.49

Here n represents the parameters of the respective matrix, and RI determines the arbitrary index calculated arbitrarily based on the average CI for a large matrix. Thus, it is possible to determine the sequence ratio. Practice shows that the CR should be less than 0.1 if we want to be completely sure of the results obtained (there is a certain degree of uncertainty in assumptions related to regression analysis). With an increase in the number of factors, less sensitive to the values of the matrix, and it can be shown that the priorities derived from the main considerations are 0.521 for human productivity, 0.205 for the economy, 0.227 for the development, 0.047 for the operation. SECTOR above the rest, probably due to the extreme importance of the program for space station itself. Coefficient of 0.045 sequence is within acceptable limits.

The next step in the analysis is to determine the global priorities for the third level factors compared to the second level factors. In the above example, the five predefined alternatives are compared with each of the key criteria. Let us assume that the necessary data are obtained and the calculations for the four comparative matrices made, the results are shown in Table 1. The first four columns represent the local priorities derived from the input data provided by the decision maker. Global

priorities are obtained by weighing each of the values of the local priorities and then summed up.

Table 1. Local and global priorities for the choice of an orbiting system

Alternative	Local priorities				Global priorities
	Labor productivity (0.521)	Economy (0.205)	Development (0.227)	Evaluation (0.047)	
1	0.066	0.415	0.122	0.389	0.165
2	0.212	0.309	0.224	0.151	0.232
3	0.309	0.059	0.206	0.178	0.228
4	0.170	0.111	0.197	0.105	0.161
5	0.243	0.106	0.251	0.177	0.214

1 - a cosmonaut with instruments outside the ship;
2 - a man-operated universal manipulator;
3 - a special manipulator under computer control;
4 - teleoperator with a set of manipulators;
5 - versatile sensor with touch feedback.

Global priorities at level I are derived from the following equation:

(4) $$W_i^I = \sum_{i=1}^{n_I-1} W_{ij}^I W_j^{I-1} \quad .$$

The values listed in the last column represent the final priorities of the problem, therefore (according to the decision of the decision-maker) alternative 2 appears to be the most acceptable.

In order to complete the analysis, it is desirable to see how sensitive the results are to the changes in the assessment and to the criteria values, ie. to determine how the changes in matrix A will affect the priorities between levels, common priorities and continuity. These parameters are listed in the Exprert Choice – the most popular rule for performing AHP analyzes.

HIPRE 3+ also have such opportunities. When there is uncertainty in the values of the individual factors, additional attributes can be defined to describe it. In general, the declared benefits of the AHP are as follows:

1. The method is easy to understand and easy to apply.

2. The construction of the target hierarchy of criteria, alternatives and attributes allows the problem to be combined and the recommended solutions.

3. Enables the use of unique techniques for quantitative evaluation and sequence of measurements.

In case of particularly important risk projects (development of a new product or business venture) requiring a long time and full dedication by a group, their implementation can be controlled by a project team. Fully recruited staff are

committed to the project and deployed to other members of the team. The project has its own management structure and budget, but it can also be a department in the company structure.

When the project is particularly complex, protracted, risky and involves multiple individual organizations, it is advisable to give one person full control over all the elements necessary to achieve the objectives. For example, when NASA was awarded a multi-million dollar contract (Apollo Command and Service Module and Saturn's second-stage rocket) to Rockwell International, two spatially separated programs were developed. Each program was subordinate to a vice president of a department with its own production facilities and a team of specialists. This formulation applies the idea in its finished form and is called the organization of the project.

The organizational structure is related to a particular product of each organizational unit. Here the separate functions are realized within a single structural unit. This organizational structure implies duplication of resources as similar activities and processes are carried out by different structural units for different projects. The second disadvantage due to the limited lifecycle of a project is the fact that the hierarchy in the work and reporting system is constantly changing.

What are the advantages of this approach:
- strong control through specific project management;
- fast reaction;
- stimulates productivity, keeping track of schedule, reducing costs;
- staff are loyal to a particular project;
- better cooperation with other "external" organizational units;
- good customer relationship.

What are the drawbacks:
- inefficient use of resources;
- does not develop promising technologies;
- does not prepare for future orders;
- poor opportunities for exchanging technical and technological information between projects;
- minimum career opportunities for staff;
- a difficult balancing of load in the individual phases.

As an example, the project-oriented structure of the TERRA project, part of NASA's EOS program, can be mentioned.
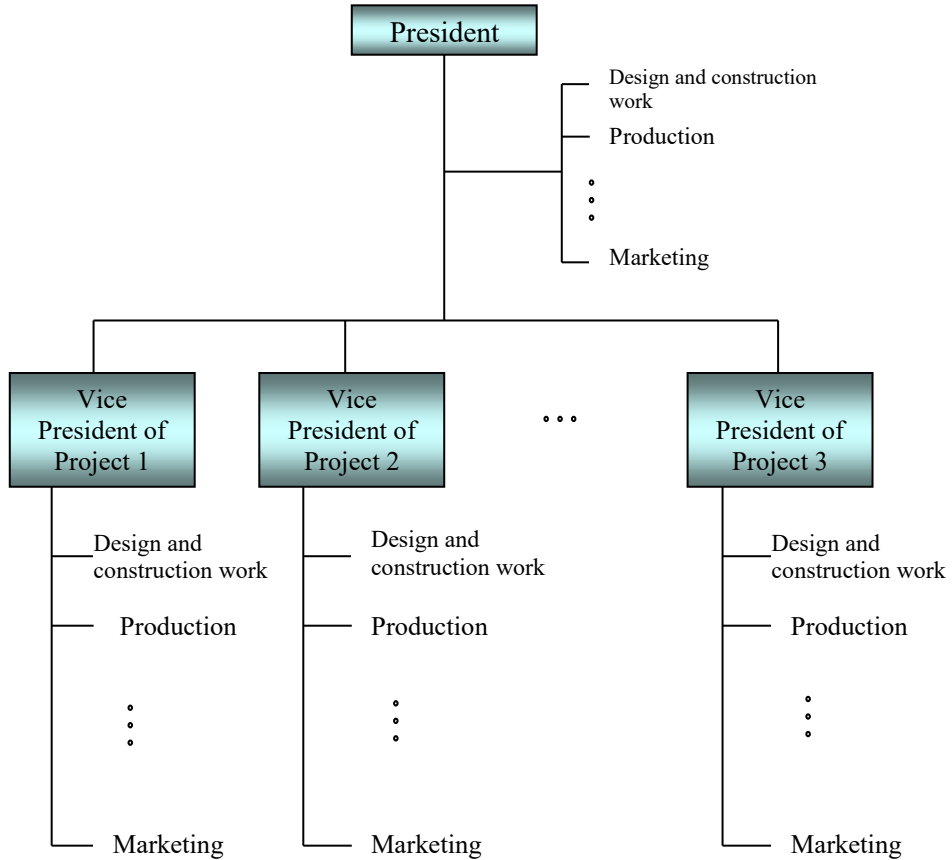
Fig. 3. Project-oriented organizational structure

Conclusion

What is the risk of identifying the project manager? The relationship between uncertainty, lack of experience and difficulties in gathering information makes project management a combination of art, science and above all logical thinking. A good project manager should be familiar with a variety of scientific disciplines and techniques. Most projects have technical, financial, marketing, and organizational subtleties that are also able to break down the best plan.

The participation of the supervisor can begin at different stages of the life cycle of a project. Some executives are engaged from the beginning, helping to identify the project, form the team, negotiate contacts. Others can start at a later stage to implement a plan they did not participate in. At a certain stage, however, most project managers face the main project activities – planning, resource finding,

resource management, staffing, and negotiation. Especially important and perhaps most difficult for a project manager is to have a good overview of the project without losing control over the critical elements. It should eliminate the difficulties whenever decision-making is needed. Issues such as "how important the budget is compared to the timetable" or "whether additional resources need to be mobilized at the expense of budget overruns or possible deviations from the results to the extent that the project is on schedule" are typical [6] .

What basic functions and skills should the project manager have?

The Project Management Institute (US) defines six key functions pertaining to the project manager:

1) Manage the volume of the project by defining objectives and activities that need to be accomplished – with sufficient detail to facilitate understanding and implementation, as well as making adjustments when need arises;

2) Manage the human resources involved in the project;

3) Manage communications so that participating countries have sufficient information to implement the project;

4) Manage time by planning and executing schedules;

5) Manage quality so that the results of the project are satisfactory;

6) Manage costs in such a way that the project is realized at a minimum of actual costs and, if possible, within the budget.

Managing a project is a complex undertaking. Since projects are unique ventures, experience, working relationships, established procedures to guide the participants in it are not particularly useful. The project manager will have to direct many different efforts and activities to achieve the project goal. People with different qualifications and from different parts of an organization who have never worked together will be involved in the project for a different length of time. Subsidiaries who are not familiar with the organization must perform important tasks. The project may contain thousands of interrelated activities performed by staff hired by different subcontractors or by one of the leading organizations. The project manager, even under the influence of pressure and stress, has to deal effectively with changing client priorities, the fears of his executives, eliminate conflicts, and find the optimal balance between counterproductive impacts.

Generally speaking, the project manager needs enthusiasm, excitement, and desire for hard work to resist the emerging problems. Wherever possible, he / she must occupy a leading position by working with the function manager.

For these and other reasons, it is especially important that project management have effective means of identifying and conveying planned activities and their interconnection. A system of computerized planning and monitoring is needed. Network techniques such as CPM (Critical path method) or PETP (program evaluation and change technique) are extremely useful in such systems.

References

1. Alvin, J. Silk (2006) What is marketing? Harvard Business School Publishing Co.
2. Barnes, J. G. (2000) Secrets of Customer Relationship Management, McGraw-Hill, NY.
3. Buckley, R., Caple, J. (2009). The Theory & Practice of Training, Kogan Page.
4. Dibb, S., L. Simkin, W. M. Pride, and O.C. Ferrell (1994) Marketing – Concepts and Strategies, Houghton Mifflin Company, Boston.
5. Gargarov, Z. (2009) Economics and Market, Sofia.
6. Gray, C.F., E.W. Larson (2000) Project management. The managerial process. McGraw. Hill International Editions.
7. Khan, M.Y. (2004) Management of Financial Services, McGraw Hill.
8. Kleiner, G.B. (1997) Enterprise in an unstable economic environment: risk, strategy, security.
9. Marinova, N. (2017) International marketing, New Bulgarian University, Sofia.
10. Marinova, N. (2008) Management and leadership, New Bulgarian University, Sofia.
11. Marinova, N., A. Bliznakov, and Z. Gargarov, (2011) Ecology and economics – economy and ecology, New Bulgarian University, Sofia.
12. Marinova, N. (2012) Project management – instrument for achieving sustainable development, New Bulgarian University, Sofia.
13. Mirchev, A. (1996) Production Management, Princeps, Sofia.

РИСКЪТ В АЕРОКОСМИЧЕСКИТЕ ПРОЕКТИ

Н. Маринова

Резюме

Рискът от несполуки във всяка една обществена дейност е определящ фактор за поведението на всеки субект. Това с особена сила се отнася към такива дейности каквито са аерокосмическите проекти, в които се ангажират големи материални, технологични и човешки ресурси.

Първата стъпка при анализа на риска включва представянето в табличен вид на различните етапи или фази на проектната система и дефиниране на рисковете за всяка една от тях, били те технически, човешки или икономически. Времето, когато се проявява събитието, може съществено да повлияе на последствията. Например, срив в системата за контрол на въздушния трафик на голямо летище може да предизвика смущения в местния въздушен трафик много повече, ако стане през седмицата, отколкото в неделя сутрин. По подобен начин авария в химически завод може да бъде много по-опасна, ако предизвика непосредствена химическа реакция, от която се получават токсични газове, отколкото на един краен етап, където отпадъчните продукти са по-малко опасни.